

UNIVERSITY OF CALIFORNIA,

IRVINE

Macroscopic Electromagnetic Properties of the
Irvine Field-Reversed Configuration:
Equilibrium, Power Balance and Fluctuations

DISSERTATION

submitted in partial satisfaction of the requirements

for the degree of

DOCTOR OF PHILOSOPHY

in Physics

by

Erik Harold Trask

Dissertation Committee:
Professor William Heidbrink, Chair
Professor Norman Rostoker
Professor Roger McWilliams
Doctor Eusebio Garate

2010

DEDICATION

To my family and friends that have kept me smiling over these many years, I thank you from the bottom of my heart. Most especially, I dedicate this work to my wife Kimberly, my son Samuel, and my parents Grant and Lila. Thank you for your love and support!

TABLE OF CONTENTS

LIST OF FIGURES	v
LIST OF TABLES	viii
LIST OF SYMBOLS AND ACRONYMS	ix
ACKNOWLEDGEMENTS	xi
CURRICULUM VITAE	xiii
ABSTRACT OF THE DISSERTATION	xvii
Chapter 1: Introduction	1
Chapter 2: Field Reversed Configurations.....	4
2.1 FRC EQUILIBRIUM.....	5
2.2 FORMATION AND FAILURE.....	8
Chapter 3: Machine Description	10
3.1 PHYSICAL PARAMETERS	11
3.2 DATA ACQUISITION	17
3.3 OPERATIONAL OVERVIEW	19
3.4 DATASETS.....	23
Chapter 4: Diagnostics	25
4.1 MAGNETIC FIELD PROBES	25
4.2 FLUX LOOPS	31
4.3 ELECTRIC PROBES	33
4.4 FARADAY CUPS	39
4.5 ROGOWSKI COIL.....	40
4.6 SPECTROSCOPY.....	43
Chapter 5: Numerical Methods	46
5.1 B-DOT DATA STRUCTURES	46
5.2 NUMERICAL INTEGRATION	47
5.3 ORTHOGONALIZATION AND CALIBRATION	49
5.4 ROTATION.....	50
5.5 FILTERING.....	51
5.6 DATA INTERPOLATION.....	52
5.7 CORRELATION METHODS.....	53
5.8 SPECTRAL METHODS	56
Chapter 6: Basic Plasma Parameters.....	64
6.1 MAGNETIC FIELDS	65
6.2 MAGNETIC FLUX	75
6.3 CURRENT DENSITY	83
6.4 INDUCTIVE ELECTRIC FIELD	93
6.5 PLASMA TEMPERATURE.....	96
6.6 FARADAY CUP	104
6.7 SUMMARY OF BASIC PARAMETERS.....	109

Chapter 7: Secondary Quantities	111
7.1 PLASMA PRESSURE	111
7.2 AVERAGE BETA	118
7.3 POYNTING VECTOR.....	120
Chapter 8: Plasma Resistivity and Power Balance	122
8.1 PLASMA RESISTIVITY	122
8.2 POWER BALANCE	129
8.3 CONFINEMENT TIMES	137
8.4 DISCUSSION	138
Chapter 9: Spectral Analysis.....	140
9.1 MAGNETIC FIELD SPECTRA: RADIAL ARRAY	140
9.2 MAGNETIC FIELD SPECTRA: RF B-DOT.....	151
9.3 CAPACITIVE PROBE SPECTRA	156
9.4 DISCUSSION	160
Chapter 10: Correlations	161
10.1 MAGNETIC FIELD AND FARADAY CUPS	162
10.2 MAGNETIC FIELD CORRELATIONS	176
10.3 MAGNETIC FIELD AND DERIVED QUANTITY CORRELATIONS	184
Chapter 11: Conclusions and Final Remarks.....	188
11.1 SUMMARY.....	188
11.2 DISCUSSION	190
11.3 FUTURE WORK	192
Bibliography	194

LIST OF FIGURES

Figure 2.1: Two Dimensional FRC Magnetic Field Profiles	4
Figure 2.2: Equilibrium plots from rigid-rotor profile for typical IFRC parameters.....	7
Figure 3.1: Irvine FRC	10
Figure 3.2: Irvine FRC Schematic	12
Figure 3.3: Plasma Gun Circuit	14
Figure 3.4: Field Coil Circuit.....	17
Figure 3.5: Current distributions in limiter coil	21
Figure 3.6: Typical IFRC current traces and axial magnetic field.....	22
Figure 4.1: Example of B-dot integration and field reversal	26
Figure 4.2: B-dot Circuit.....	27
Figure 4.3: Loop voltage and axial flux for vacuum and plasma discharges	33
Figure 4.4: Electric Probe Potential Circuit.....	34
Figure 4.5: Single tip probe trace and Capacitive probe trace.....	35
Figure 4.6: Double Probe Circuit.....	37
Figure 4.7: Current drawn by a floating double probe at R=23 cm.....	37
Figure 4.8: Sample I-V trace from a Langmuir probe	38
Figure 4.9: Example of Faraday cup data	40
Figure 4.10: Rogowski coil.....	41
Figure 4.11: Plasma current measured by the Rogowski coil.....	43
Figure 5.1: Effects of rotation on two B_z probes at the axial midplane.....	51
Figure 5.2: Example of numerical filtering on magnetic data	52
Figure 5.3: Example of auto, cross and total correlation	55
Figure 5.4: Example of spectra derived by FFT and Wavelet transforms	59
Figure 5.5: Wavelet spectral analysis methods, with cone of influence.....	60
Figure 5.6: Wavelet bispectral analyses with log spaced frequencies	62
Figure 5.7: Wavelet bispectral analyses with linearly spaced frequencies.....	63
Figure 6.1: Process steps for magnetic measurements.....	65
Figure 6.2: Evolution of the axial magnetic field at the midplane.....	66
Figure 6.3: Magnitude of B at 43 microseconds.....	67
Figure 6.4: Magnetic field components in 2D plane, with strong toroidal field.....	68
Figure 6.5: (a) B_θ scale lengths at 43 microseconds. (b) B_θ scale lengths averaged over the FRC lifetime.....	71
Figure 6.6: B_θ data from shot 5672, with approximate B_z null position	73
Figure 6.7: Evolution of average B_θ spectrogram, with the period being defined as the inverse frequency.....	74
Figure 6.8: Average period of B_θ for the entire dataset.	75
Figure 6.9: Axial Magnetic Flux At 43 Microseconds	77
Figure 6.10: (a) Measured and (b) analytic magnetic field magnitudes	79
Figure 6.11: Theoretical and measured axial flux profiles	80
Figure 6.12: Excluded (trapped) flux estimates.....	82
Figure 6.13: J_θ in the z-r plane at 43 microseconds.....	84

Figure 6.14: Axially averaged J_θ as a function of time and radial position.....	85
Figure 6.15: Comparison of toroidal currents measured directly	87
Figure 6.16: Floating potential measurement	88
Figure 6.17: Total currents flowing into the plasma volume.....	90
Figure 6.18: Axial and radial current density estimates at 43 microseconds.....	92
Figure 6.19: E_θ measurement at 43 microseconds	94
Figure 6.20: Axially averaged E_θ as a function of time and radial position	95
Figure 6.21: Average loop voltage.....	95
Figure 6.22: Theoretical loop voltage.....	95
Figure 6.23: Theoretical E_θ based on measured currents at 43 microseconds.....	96
Figure 6.24: Effective temperatures measured by Doppler shifts for (a) singly ionized carbon and (b) neutral hydrogen and (c) electrons	97
Figure 6.25: Average intensities for various spectral lines.....	99
Figure 6.26: (a) Estimates of fluid velocities that give rise to erroneously large ion temperatures. (b) Ion temperatures after subtraction of line of sight broadening.....	101
Figure 6.27: Doppler broadened profiles for two analytic densities.....	104
Figure 6.28: Faraday cup data at $r = 16$ cm (a) <i>FCUP</i> dataset (b) <i>FCUP16k</i>	105
Figure 6.29: Radial and temporal evolution of average Faraday cup signals.....	107
Figure 6.30: Particle loss out one end plane for two datasets	109
Figure 7.1: Plasma pressure	113
Figure 7.2: Plasma density and ion saturation current comparison	116
Figure 7.3: Density profile in R-Z plane at 43 microseconds.....	117
Figure 7.4: Particle inventory	118
Figure 7.5: Volume averaged beta.....	119
Figure 7.6: Spatial structure of the radial Poynting vector at 43 microseconds	121
Figure 7.7: Time evolution of the axially averaged radial Poynting vector	121
Figure 8.1: Plasma resistivity estimates vs Spitzer.....	124
Figure 8.2: Spatial and temporal scales of the magnetic flux	126
Figure 8.3: Magnetic diffusivity at the field null vs Spitzer value	126
Figure 8.4: Ratio of measured resistivity to Spitzer value.....	127
Figure 8.5: Variation of density at the null to resistivity estimates.	128
Figure 8.6: Average plasma resistance estimates	129
Figure 8.7: Power and energy estimates from the entire plasma volume	133
Figure 8.8: Power and energy estimates inside the separatrix.....	135
Figure 8.9: Comparisons of thermal losses.....	137
Figure 8.10: Confinement times	138
Figure 9.1: Magnetic spectra for (a) B_r , (b) B_θ , and (c) B_z	141
Figure 9.2: Average spectrograms for the three magnetic field components	143
Figure 9.3: Example of wavelet cone of influence.	144
Figure 9.4: Amplitude of magnetic fluctuations in three frequency bands as a function of time and radial position.....	145
Figure 9.5: Spatial variation of magnetic fluctuations in three frequency bands as a function of axial and radial position at 43 microseconds.	146
Figure 9.6: Relative spatial variation of the normalized magnetic spectra in three frequency bands as a function of time and radial position.....	148

Figure 9.7: Relative spatial variation of the normalized magnetic spectra in three frequency bands as a function of axial and radial position.....	149
Figure 9.8: Four chirps present in Shot 5672 at $r = 32.5$ cm	150
Figure 9.9: Spectrogram of RF B-dot data, averaged from 1 to 20 MHz and radial distribution of spectrum at $t = 40$ microseconds. The lower hybrid, hydrogen cyclotron, and carbon cyclotron frequencies are also plotted.....	152
Figure 9.10: Total power at the local (a) hydrogen cyclotron frequency and (b) lower hybrid frequency as a function of position and time.....	154
Figure 9.11: Absolute value of ∇B^2 . Approximate null position is shown by the dashed line. Edge effects at $r > 30$ cm can be ignored.....	155
Figure 9.12: Comparison of magnetic fluctuation spectra measured by two different probe types. Spectra measured at $t = 40$ microseconds.	156
Figure 9.13: Spectrogram of capacitive probe data, averaged from 1 to 20 MHz, and the radial distribution of the spectrum at $t = 40$ microseconds. The lower hybrid, hydrogen cyclotron, and carbon cyclotron frequencies are also plotted.....	158
Figure 9.14: Total power near the local (a) hydrogen cyclotron frequency and (b) lower hybrid frequency as a function of position and time.....	159
Figure 10.1: Average velocities between components of B^2 and Faraday cup signals from the same dataset	164
Figure 10.2: Average velocities between averaged components of B^2 and average Faraday cup signal	167
Figure 10.3: Average velocities between axial gradients of the averaged components of B^2 and average Faraday cup signal	169
Figure 10.4: Average velocities between components of the Poynting vector and the average Faraday cup signal.....	170
Figure 10.5: Example of the characteristic velocity linking spatially separated probes for fake data at two different signal to noise ratios and velocities	172
Figure 10.6: Spatial variations of the correlation at maximum correlated velocity between the average Faraday cup signal for (a) B_z^2 , (b) B_θ^2 , and (c) B_r^2	173
Figure 10.7: Spatial variations of the correlation at maximum correlated velocity between the average Faraday cup and (a) S_r and (b) S_z	174
Figure 10.8: Correlations between particle losses and magnetic fluctuations. Linking velocity is 2.5 cm/microsecond.....	1780
Figure 10.9: Correlations between magnetic field components. Time period for correlation is from 35 to 60 microseconds.....	178
Figure 10.10: Possible B_z mode structure at 230 and 270 kHz.....	180
Figure 10.11: Time evolution of possible mode structure at 235 kHz compared with total power at 235 kHz	183
Figure 10.12: Spatial correlation of magnetic field and current density components ...	185
Figure 10.13: Spatial correlations of E_θ with B and J components	186

LIST OF TABLES

Table 3.1: Rise times and peak values for field coils	12
Table 3.2: Field coil physical parameters	12
Table 3.3: Force Balance Parameters.....	16
Table 3.4: Capacitor Bank Parameters.....	17
Table 3.5: Digitizer Parameters	18
Table 3.6: <i>NCP</i> timing and charging parameters.....	23
Table 3.7: Description of datasets.....	24
Table 4.1: Probe positions.....	25
Table 4.2: B-dot Circuit Impedances and Values	27
Table 4.3: Average B-dot calibration values	31
Table 4.4: Calibration Matrix for the radial B-dot cluster at $r = 20$ cm	31
Table 6.1: Plasma Parameters	64
Table 6.2: FRC Phases	66
Table 6.3: Curl components of \mathbf{B} in cylindrical coordinates	83
Table 9.1: Chirp parameters.....	151

LIST OF SYMBOLS AND ACRONYMS

A_i	Einstein transition probability
a_1	Magnetic gradient scale length
a_2	Density gradient scale length
B	Magnetic Field
B_0	Peak magnetic field
B_r	Radial magnetic field
B_θ	Toroidal magnetic field
B_z	Axial magnetic field
$B\text{-dot}$	Magnetic pickup loop
C	Capacitance
COI	Cone of influence for wavelet transform
c_s	Ion sound speed
D_B	Magnetic diffusivity
e	Charge of electron
eV	Electron volts
E	Electric field
E_r	Radial electric field
E_θ	Toroidal electric field
E_z	Axial electric field
E_{xy}	Cross spectrum between signals x and y
f	Frequency
f_0	Start frequency
f_j	Particle distribution function, absorption oscillator strength
FFT	Fast Fourier transform
FRC	Field-reversed configuration
H_α	Hydrogen's Balmer alpha transition
H_β	Hydrogen's Balmer beta transition
H_z	Frequency in Hertz
$IFRC$	Irvine Field-Reversed Configuration
I_p	Plasma current
I_{sat}	Ion saturation current
J	Current density
J_r	Radial current density
J_θ	Toroidal current density
J_z	Axial current density
k	Boltzmann's constant
K_r	Radial wave number
K_z	Axial wave number
m_j	Mass of particle species j
n_0	Peak density
n_j	Density of species j
N	Particle inventory
p	Plasma thermal pressure

P_{xy}	Correlation between signals x and y
r	Radial position
r_{null}, r_0	Null radius
r_s	Separatrix radius
Δr	Radial width of plasma current channel
R_p	Plasma resistance
S	Poynting vector
t	Time
T_b	Bounce period
T_j	Temperature of particle species j
v	Particle velocity
V_A	Alfvén velocity
V_{loop}	Loop voltage
W	Total energy in the plasma
W_{EM}	Electromagnetic energy
W_{TH}	Plasma thermal energy
WV	Wavelet transform
x_i	Energy level of atomic transition
z	Axial position
Z	Impedance or ion charge state
β	Plasma beta
γ_{xy}	Coherency between signals x and y
ϵ_0	permittivity of free space
ϵ_i	Emissivity
η	Resistivity
θ	Toroidal angle
λ	Wavelength
λ_{dB}	deBroglie wavelength
λ_0	Wavelength at zero Doppler shift
$\Delta\lambda$	Wavelength spread
μ_0	Permeability of free space
ρ	Mass density
ρ_0	Peak mass density
τ	Flux diffusion time
τ_E	Energy confinement time
τ_N	Particle confinement time
ϕ	Magnetic flux
ϕ_c	Magnetic flux at the separatrix
ϕ_{ex}	Excluded or trapped magnetic flux
ω_e	Electron rotation frequency
ω	Angular frequency

ACKNOWLEDGEMENTS

Firstly, I would like to thank Drs. William Heidbrink, Roger McWilliams, and Eusebio Garate for their countless hours of instruction and guidance. You have all helped me immeasurably over the years.

Bill, you've been a wonderful model of excellence, both as a professor of physics and an example of the kind of man that I'd like to be. Thank you for your emphasis on good science, your Christian witness, and for sharing your home with my wife and me so often.

Roger, you exemplify the curiosity and work ethic that will serve me well if I can but follow you. Thank you for always refocusing me when I wander down paths that may not be fruitful. I greatly appreciate the many discussions that we have had over the years as well, from talk of Wall Street to smoked salmon. It has been a pleasure.

I thank you, Eusebio, for introducing me to what I can only call the 'dirty hands' approach to science. Throughout high school and college, book knowledge was my primary source of learning physics. I highly value your emphasis on a description of nature by experimentation.

To my fellow graduate students Wayne Harris and Thomas Roche, I offer my grateful thanks. I especially appreciate the many hours of discussion, of bouncing ideas off of each other, and talking through difficult concepts. Thank you for being my sounding boards. Thank you also for the effort you have both contributed to the Irvine experiment, from finding vacuum leaks to building diagnostics and analyzing their results. It has been very enjoyable working with you both, though the work may have

been painful at times. Here's to hoping that we never have to clean another diffusion pump or wind another B-dot probe array!

Finally, I'd like to especially thank Tri Alpha Energy for their support over the years. Thank you for the machinery, technical aid, and your financial support. In particular, I'd like to thank Alan van Drie for his efforts in creation and maintenance of our data acquisition system. Thanks go out to Sam Armstrong as well for his help in designing and building electronic circuits.

CURRICULUM VITAE

Erik Harold Trask

EDUCATION

Doctor of Philosophy in Physics **2010**

University of California, Irvine *Irvine, California*

Bachelor of Science in Applied Physics **2001**

Pacific Lutheran University *Tacoma, Washington*

SELECTED AWARDS AND HONORS

Graduate Assistance in Areas of National Need **2007**

PUBLICATIONS

- F. Brandi, F. Giammanco, W. S. Harris, T. Roche, E. Trask, “Electron density measurements of a field-reversed configuration plasma using a novel compact ultrastable second-harmonic interferometer”, *Review of Scientific Instruments* **80**, 113501 (2009)
- W.S. Harris, E.P. Garate, W.W. Heidbrink, R. McWilliams, T. Roche, E. Trask, Y. Zhang. “Time-of-Flight Neutral Particle Analyzer and Calibration”, *Review of Scientific Instruments* **79**, 10F313 (2008).
- J. M. Taccetti, T. P. Intrator, G. A. Wurden, S. Y. Zhang, R. Aragonz, P. N. Assmus, C. M. Bass, C. Carey, S. A. deVries, W. J. Fienup, I. Furno, S. C. Hsu, M. P. Kozar, M. C. Langner, J. Liang, R. J. Maqueda, R. A. Martinez, P. G. Sanchez, K. F. Schoenberg, K. J. Scott, R. E. Siemon, E. M. Tejero, E. H. Trask, M. Tuszewski, and W. J. Waganaar, “FRX-L: A field-reversed configuration

plasma for magnetized target fusion”, *Review of Scientific Instruments* **74**, 4314 (2003)

PRESENTATIONS

- “Macroscopic Electromagnetic Properties Of The Irvine Field-Reversed Configuration: Equilibrium, Power Balance And Fluctuations.” E. Trask. University of California, Irvine. May 26, 2010
- “Focus On Correlations And Ohm’s Law.” E. Trask. University of California, Irvine. July 24, 2009
- “Progress And Summary Of Work.” E. Trask. University of California, Irvine. July 10, 2009
- “Review of Irvine FRC.” E. Trask, T. Roche, W. S. Harris, Tri Alpha Energy. September 27, 2007
- “Lower Hybrid Wave Propagation in a Field Reversed Configuration.” E. Trask, University of California, Irvine. December 17, 2004.

POSTERS

- E. Trask, E. P. Garate, W. S. Harris, W. W. Heidbrink, R. McWilliams, T. Roche , “Dispersion Measurements on the Irvine FRC in the Lower Hybrid Frequency Range,” poster presented at the 2008 American Physical Society Division of Plasma Physics Meeting, Dallas, TX
- W. S. Harris, E. P. Garate, W. W. Heidbrink, R. McWilliams, T. Roche , E. Trask, “Ion Energy Distribution Functions in the Irvine FRC,” poster presented at the 2008 American Physical Society Division of Plasma Physics Meeting, Dallas, TX
- T. Roche , F. Brandi, E. P. Garate, F. Giammanco, W. W. Heidbrink, W. S. Harris, R. McWilliams, E. Paganini, E. Trask, “Density Profiles in the Irvine Field Reversed Configuration,” poster presented at the 2008 American Physical Society Division of Plasma Physics Meeting, Dallas, TX
- E. Trask, E. P. Garate, W. S. Harris, W. W. Heidbrink, R. McWilliams, T. Roche, “Triple Probe Array on Irvine FRC,” poster presented at the 2007 American Physical Society Division of Plasma Physics Meeting, Orlando, FL

- J. M. Little, E. P. Garate, W. S. Harris, W. W. Heidbrink, R. McWilliams, T. Roche, E. Trask, “Spectroscopic Diagnostics of the Irvine FRC,” poster presented at the 2007 American Physical Society Division of Plasma Physics Meeting, Orlando, FL
- W. S. Harris, E. P. Garate, W. W. Heidbrink, R. McWilliams, T. Roche, E. Trask, “Ion Energy Distribution Function Measurements in the Irvine FRC,” poster presented at the 2007 American Physical Society Division of Plasma Physics Meeting, Orlando, FL
- T. Roche, E. P. Garate, W. S. Harris, W. W. Heidbrink, R. McWilliams, E. Trask, “Irvine FRC Magnetic Field Structure,” poster presented at the 2007 American Physical Society Division of Plasma Physics Meeting, Orlando, FL
- E. Trask, W.S. Harris, E. P. Garate, W. W. Heidbrink, A. Van Drie, J.M. Little, “Irvine FRC Equilibria Measurements,” poster presented at the 2006 American Physical Society Division of Plasma Physics Meeting, Philadelphia, PA
- W.S. Harris, E. P. Garate, W. W. Heidbrink, E. Trask, “A Time-of-Flight Neutral Particle Detector for the Irvine FRC,” poster presented at the 2006 American Physical Society Division of Plasma Physics Meeting, Philadelphia, PA
- J.M. Little, E. P. Garate, W. W. Heidbrink, R. McWilliams, E. Trask, W.S. Harris, “Spectral Diagnostics of Plasma Confined within a Field Reversed Configuration,” poster presented at the 2006 American Physical Society Division of Plasma Physics Meeting, Philadelphia, PA
- E. Trask, E. P. Garate, W. W. Heidbrink, A. Van Drie, “Irvine FRC Characterization and Upgrades,” poster presented at the 2005 American Physical Society Division of Plasma Physics Meeting, Denver, CO
- D. T. S. Cook, E. P. Garate, W. S. Harris, W. W. Heidbrink, E. Trask, “Passive spectrographic measurement of plasma electron temperatures using impurity line emissions,” poster presented at the 2005 American Physical Society Division of Plasma Physics Meeting, Denver, CO
- W. S. Harris, E. P. Garate, W. W. Heidbrink, E. Trask, A. Van Drie, “Current Diagnostics in an FRC with a Toroidal Electric Field,” poster presented at the 2005 American Physical Society Division of Plasma Physics Meeting, Denver, CO
- E. Trask, W. W. Heidbrink, E. P. Garate, R. McWilliams, “Lower Hybrid Heating of FRC Plasmas,” poster presented at the 2004 American Physical Society Division of Plasma Physics Meeting, Savannah, GA

- E. Trask, E. P. Garate, W. W. Heidbrink, “Injection of Neutralized Ion Beams as a Possible Heating, Refueling, and Current Source in FRC Plasmas,” poster presented at the 2003 American Physical Society Division of Plasma Physics Meeting, Albuquerque, NM

ABSTRACT OF THE DISSERTATION

Macroscopic Electromagnetic Properties of the
Irvine Field-Reversed Configuration:
Equilibrium, Power Balance and Fluctuations

by

Erik Harold Trask

Doctor of Philosophy in Physics

University of California, Irvine 2010

Professor William Heidbrink, Chair

The plasma parameters and characteristics of the Irvine Field-Reversed Configuration (IFRC) are summarized in this thesis. Particular emphasis is placed on the development of the different diagnostics used to make measurements in the experiment, as well as the measurements themselves. Whenever possible, actual measurements are used in lieu of theoretical or analytical fits to data. Analysis of magnetic probes (B-dots) comprises the bulk of what is known about the IFRC. From these B-dot probes, the magnetic field structure in a two dimensional plane at constant toroidal position has been determined, and has been found to be consistent with a field-reversed configuration. Peak reversed fields of approximately 250 Gauss have been observed.

Further analyses have been developed to extract information from the magnetic field structure, including components of the electric field, the current density, and plasma pressure in the same two dimensional plane. Electric field magnitudes reach 600 V/m, concurrent with current densities greater than 10^5 Amps/m² and thermal pressures over 200 Pa. Spectroscopic analysis of hydrogen lines has been done to make estimates of the electron temperature, while spectroscopic measurements of the Doppler broadening of the H_α line³¹ have allowed an estimate of the ion temperature. Particle losses out one axial end plane measured by an array of Faraday cups quantify the how well the configuration traps particles. Spectral information derived from B-dot probes indicates that there is substantial power present at frequencies lying between the hydrogen cyclotron and mean gyrofrequency. These various measurements are used to find the following parameters that characterize the Irvine FRC:

- Electromagnetic and thermal stored energies as functions of time.
- Power balance, including input power from the field coils, resistive heating, power lost by particle transport and radiation, and particle and energy confinement times.
- Strong correlations between magnetic fluctuations and particle loss.

Chapter 1: Introduction

World energy demand is forecast to rise at an average annual rate of 1.5%, and will probably be 44% higher than the 2006 level by 2030.¹ Current projections of oil reserves² are approximately 1.2 trillion barrels; at current rates of usage³, these reserves will last about 36 years, with the assumptions of no new sources found. Since oil provides⁴ approximately 39% of the total energy used in the world, this (highly simplified) exercise indicates a looming problem in our world: where will we get our energy? Population growth, industrialization of the undeveloped world, and a finite supply of fossil fuels are a recipe for a paradigm shift not too far in the future.

One possible new source of energy is fusion, the same process that powers the sun. Excess energy is produced when light elements fuse together to produce heavier elements. The primary benefit of this energy source is an almost unlimited fuel supply. Unfortunately, fusion has yet to be practically implemented, due to four main aspects of energy flows in fusion experiments. These issues include:

- Heating of the plasma to thermonuclear temperatures.
- Control of energy loss channels that cool the plasma.
- Extraction of energy produced by fusion products.
- Protection of plasma facing surfaces.

Many different machines have been built in attempts to induce controlled fusion reactions. Concepts range from blasting pellets of frozen hydrogen with immense lasers,

to twisting magnetic fields in complicated three dimensional structures. The most heavily studied artificial controlled fusion confinement concept is that of magnetic confinement, of which the Field-Reversed Configuration (FRC) is one instance. Machines that use magnetic fields to confine plasmas include Z-pinches, θ -pinches, Reversed-Field pinches, tokamaks, stellarators, spheromaks, and FRCs. These various machine types differ by their manner of formation, their magnetic field topology, and various instabilities that they are susceptible to. The experiment at UC Irvine was done on the Irvine Field-Reversed Configuration (IFRC), and further discussion will be limited to the FRC topology and the IFRC in particular.

FRCs address the four problems of fusion in a unique manner. They do not depend on large external magnetic fields nearly as much as other fusion concepts, such as tokamaks and stellarators. This means that for a given amount of input energy, more can go to heating the plasma. FRCs also possess a simple cylindrical geometry, which makes construction relatively uncomplicated. Magnetic field lines are open at the edges of the confinement region; these open lines provide a pathway for unconfined charged particles to quickly leave the plasma edge and be directed towards an energy generation region of a machine. The separation of energy source and sink regions also greatly simplifies machine design.

It has not proved easy to keep FRCs hot however. Energy loss channels, such as particle transport, are larger than in other machine designs like tokamaks and stellarators. Minimization of these losses is the goal of most FRC research today. To do this, accurate

measurements of basic plasma quantities are needed, such as the spatial and temporal evolution of the magnetic field, plasma density, temperature and particle losses.

This thesis is intended to address what is known the equilibrium properties of the IFRC, how energy moves in the plasma, and possible causes of particle transport. Chapter 2 discusses the fundamentals of the FRC topology, while Chapter 3 describes the Irvine FRC in particular. Chapter 4 introduces the particular diagnostics that are used to measure plasma parameters. Chapter 5 details some of the numerical methods that are used to find the basic plasma parameters described in Chapter 6. Chapter 7 introduces secondary quantities that are found by various manipulations of our basic parameters. The heart of the thesis is covered in Chapters 8-10. The plasma resistivity, stored energy, loss terms and confinement times are found in Chapter 8, while an analysis of the spectral content of different diagnostics is covered in Chapter 9. Chapter 10 identifies strong correlations between these magnetic fluctuations and particles losses, and Chapter 11 summarizes the physics results and offers some conclusions.

Chapter 2: Field Reversed Configurations

Field-Reversed Configurations (FRCs)⁵ describe a subset of magnetic fusion experiments where the magnetic field that confines the plasma is primarily formed by currents that flow in the plasma itself. This differentiates it from other experiments such as tokamaks and stellarators, which have large magnetic fields formed by external currents. FRCs are further defined by a cylindrically symmetric current loop with self-generated fields that have no toroidal components. This separates FRCs from spheromaks, which are also self-organized but have magnetic field components in all three dimensions. This chapter will cover the equilibrium field structure of FRCs, how they are formed and confined, and how they tend to die.

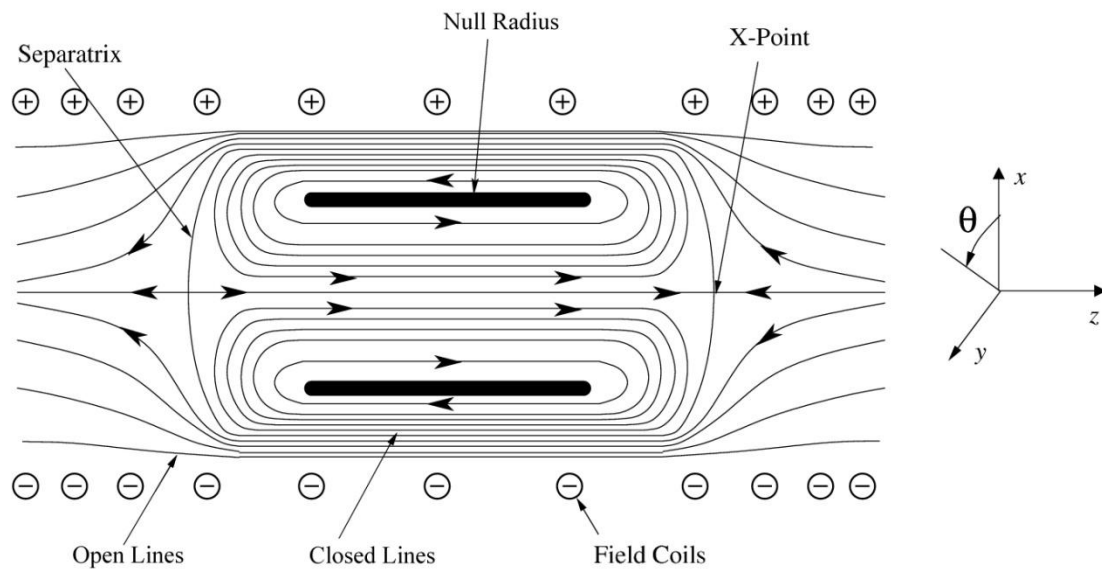


Figure 2.1⁶: Two Dimensional FRC Magnetic Field Profiles

2.1 FRC Equilibrium

FRCs are cylindrically symmetric magnetic field structures that have a finite axial extent, with a poloidal cross section depicted in Figure 2.1. Equilibrium profiles of the magnetic field consist of nested toroidal surfaces that are surrounded by straight field lines. The center of the current channel that forms the closed magnetic field surfaces is located at a radius r_{null} where the axial magnetic field switches signs. The boundary where closed field lines become open field lines is called the separatrix, denoted r_s . There are several different analytical models that describe FRCs, ranging from one dimensional rigid-rotor profiles⁷ to refinements of two dimensional Hill's vortex solutions⁸. The model that this thesis will use is the one dimensional rigid-rotor profile because of its similarities to observed plasma parameters, and further comparisons and discussions will be based upon it alone.

The one dimensional rigid-rotor profile distribution function f_j for particle species j is given by

$$f_j(r, \vec{v}) = \left(\frac{m_j}{2\pi T_j} \right)^{\frac{3}{2}} n_j(r) \exp\left[-\frac{m_j}{2T_j} |\vec{v} - \vec{\omega}_j \times r|^2 \right], \quad (2.1)$$

where r is the radial coordinate, v the velocity, and m_j , T_j , n_j , and ω_j the particle mass, temperature, density, and angular velocity respectively. This distribution function has been shown⁷ to satisfy the Vlasov-Maxwell system of equations, which can be written as:

$$(\vec{v} \cdot \nabla) f_j + \frac{e_j}{m_j} (\vec{E} + \vec{v} \times \vec{B}) \cdot \nabla_v f_j = 0, \quad (2.2)$$

$$\nabla \times \vec{E} = 0, \quad (2.3)$$

$$\nabla \times \vec{B} = \mu_0 \sum_j e_j \int \vec{v} f_j d\vec{v}, \quad (2.4)$$

$$\sum_j n_j e_j \sim 0. \quad (2.5)$$

In the system above, E and B are the electric and magnetic fields, e_j is the particle charge, and μ_0 is the vacuum permeability. These equations describe a system that is quasi neutral and in equilibrium, with no temporal gradients. The rigid-rotor profile is a solution to these equations when spatial gradients in the azimuthal and axial directions are assumed to be zero. Equilibrium profiles for B_z , E_r , and n can be found after substitution of the rigid-rotor distribution into the Vlasov-Maxwell system of equations and are given by

$$B_z(r) = B_0 \left(1 + \sqrt{\beta} \tanh\left\{ \frac{r^2 - r_0^2}{r_0 \Delta r} \right\} \right), \quad (2.6)$$

$$E_r(r) = -r\omega_e B_z - \frac{T_e}{e} \frac{d \ln n(r)}{dr} + \frac{m}{e} r\omega_e^2, \quad (2.7)$$

$$n(r) = \frac{n_0}{\cosh^2\left\{ \frac{r^2 - r_0^2}{r_0 \Delta r} \right\}}. \quad (2.8)$$

In the previous equations, r_0 is the null radius, n_0 is the peak density, and B_0 is a constant that measures the asymmetry between peak magnetic fields inside and outside of the null.

The ratio of thermal to magnetic energy is given by the variable β , written analytically as

$$\beta \equiv \frac{2\mu_0 n_0 \sum_j T_j}{B_0^2}. \quad (2.9)$$

These profiles are plotted in Figure 2.2 for $B_0 = -9.5$ Gauss, $T_i + T_e = 6$ eV, $n_0 = 2.6E14$ cm^{-3} , $r_0 = 21.3$ cm, $\Delta r = 10.4$ cm, and $\omega_e = 2E4$ rad/sec.

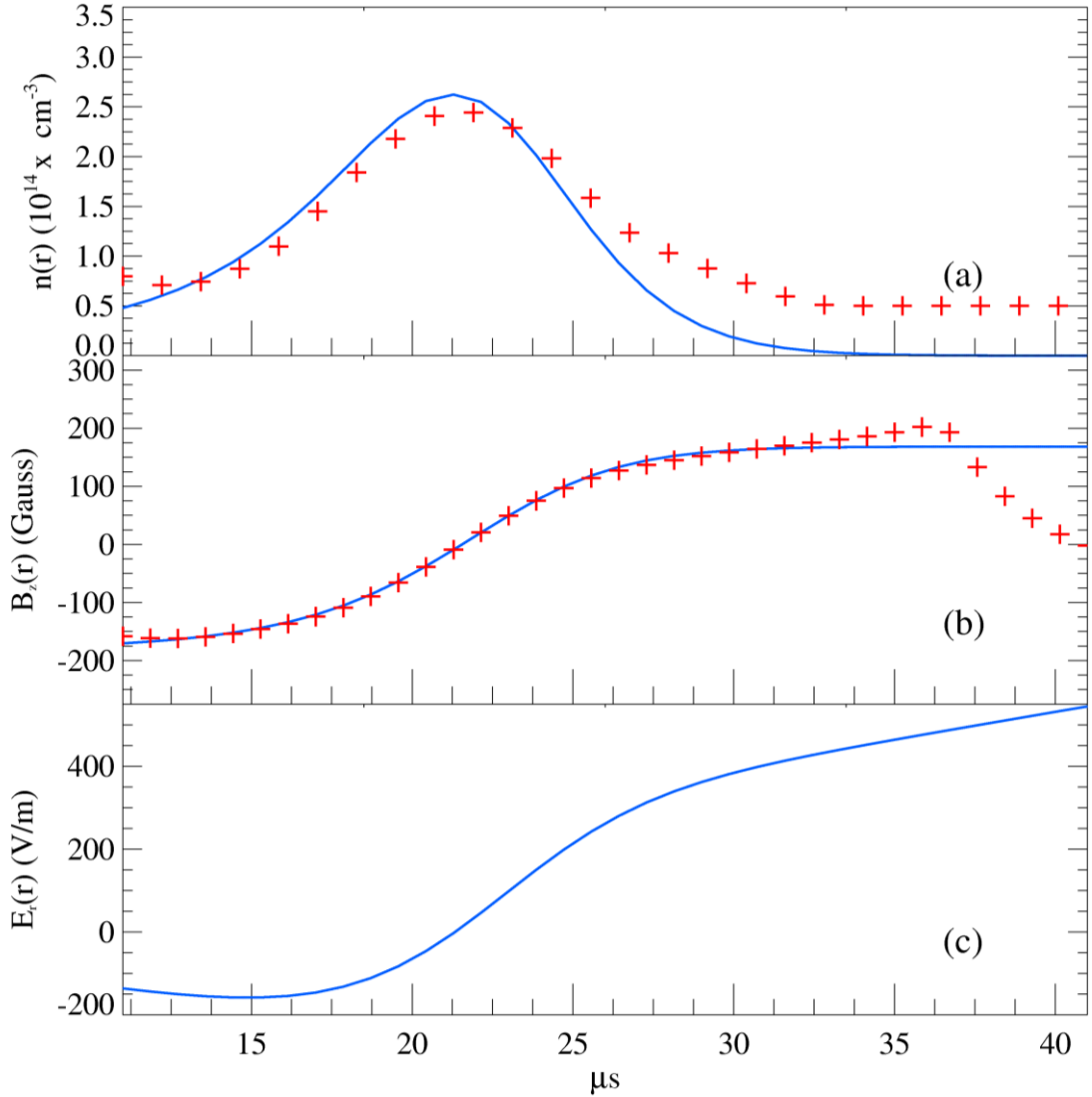


Figure 2.2: Equilibrium plots from rigid-rotor profile for typical IFRC parameters, showing the (a) plasma density, (b) axial magnetic field, and (c) radial electric field. Theoretical profiles are plotted with the solid lines, with experimentally measured data in crosses. Data are from the *NCP* dataset at 36.2 microseconds and $z = -3$ cm. See Chapter 3.4 for the dataset description.

2.2 Formation and Failure

The key component to any FRC is a confined axisymmetric toroidal current that flows in plasma. There are several methods that have been used in experimental devices to generate and confine this current. The most common method is an inductively generated electric field that drives the plasma current. The electric field can be produced by transformer action from an interior solenoid, rapid current reversal in a θ -pinch, or by rotation of a radial magnetic field (RMF). Experiments that use interior solenoids include TS-4^{9 46}, CSS^{10 11} and IFRC. Field-reversed θ -pinch experiments include the FRX series at Los Alamos^{12 13} and the LSX¹⁴ experiment at the University of Washington. The TCS machine^{15 16}, also at the University of Washington, creates FRCs by the RMF method. Other formation methods include the merging of spheromaks such as MRX^{17 18} and SSX-FRC^{19 20} and the trapping of neutralized ion beams in a reverse θ -pinch at the FIX^{21 22} experiment in Japan.

A current ring cannot confine itself radially, due to an innate radial pressure imbalance in the absence of other external forces. Radial confinement is generally accomplished by currents that point in the opposite direction of the plasma current and are located at a larger radius than the plasma current. These confinement currents can be induced in a flux conserving shell or can be driven in external coils. Axial confinement is maintained by field line tension, and can also be aided by passive or active external mirror field coils.

There are a number of ways that FRCs can fail. The most basic is caused by force imbalances in the formation period, which cause the current ring to expand radially (blow out) and hit the vacuum vessel. This is a failure in equilibrium control, and is very common on the IFRC when currents in the flux and limiter coils are not balanced properly. Judicious choices of current distributions practically eliminate this failure mode. Several MHD instabilities have been observed and studied²³; the most common of these are the $n = 1$ tilt mode²⁴ and the $n = 2$ rotational instability.⁵ The tilt mode has proved to be a relatively minor problem in current FRC research, probably due to finite Larmor-radius effects. The $n = 2$ instability has been documented on a number of different experiments, and is usually seen experimentally as a periodic oscillation in the line density as measured by interferometers.

Chapter 3: Machine Description

The Irvine Field Reversed Configuration (IFRC), shown below, is a machine housed at the University of California, Irvine. Work has been done on this experiment since 2004, with between two and three graduate students working on it full time as well as numerous undergraduate summer students. This chapter will cover the physical description of the vacuum chamber and supporting auxiliary systems, the power storage and delivery systems, the field coils, and the data acquisition system.

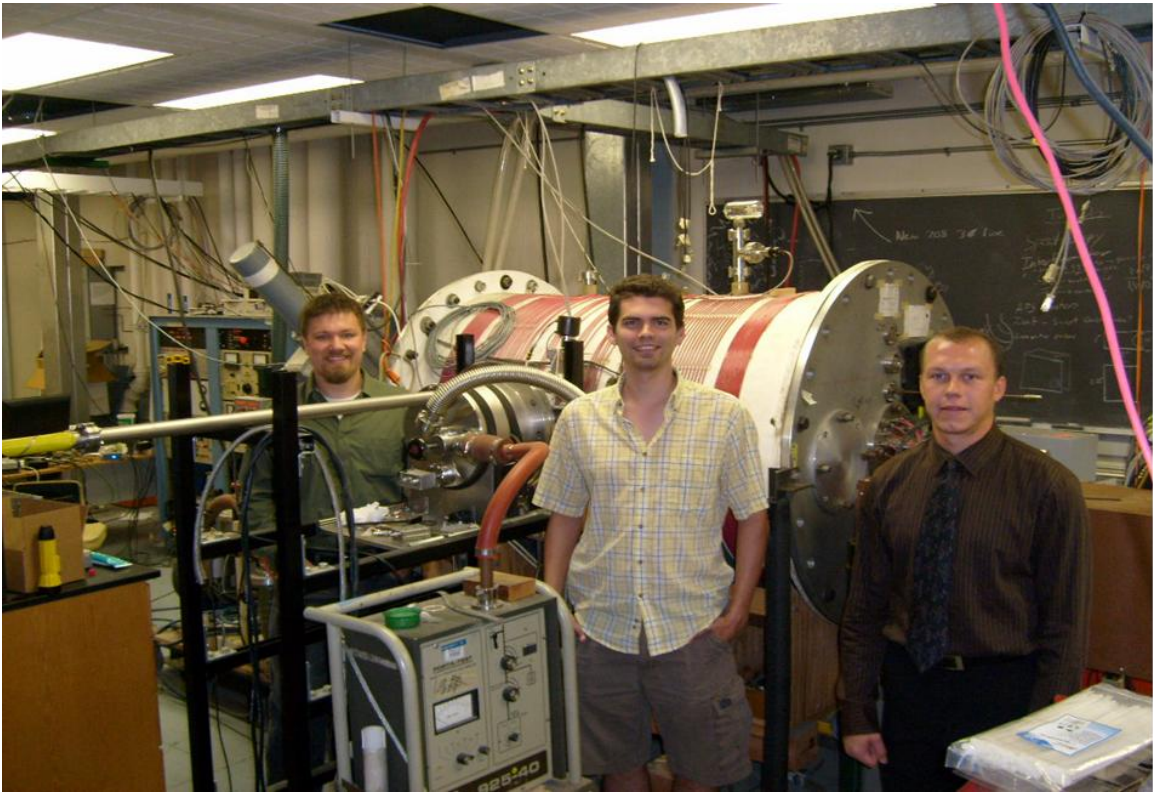


Figure 3.1: Irvine FRC

From left to right: Erik Trask, Wayne Harris, and Thomas Roche

We use a right handed cylindrical coordinate system on the IFRC with variables (r, θ, z) . The origin is at the geometric center of our vacuum chamber, with the axial

direction, denoted by variable z , measuring the distance along the cylindrical axis of the machine. The $+\hat{z}$ direction points towards the north end of our machine; the $+\hat{\theta}$ direction points in a counter-clockwise manner when looking at the origin from positive axial positions. The positive radial direction is defined in the usual sense, with the radial coordinate r increasing with increased distance from the z axis. Though this machine and thesis generally use cylindrical geometry to describe spatial locations, there are some terms borrowed from toroidal geometry. The word poloidal is sometimes used to describe features that lie in a 2D plane at constant angle θ ; for example the amount of axial trapped flux in the FRC is called the poloidal flux. The words toroidal and azimuthal describe quantities that vary or point in the $\hat{\theta}$ direction; for example the main plasma current points in the $-\hat{\theta}$ direction and is called the toroidal or azimuthal current.

3.1 Physical Parameters

The IFRC machine is similar to the initial design the Coaxial Slow Source experiment at the University of Washington,¹⁰ with two concentric solenoids that are not connected in parallel with each other. There are four separate physical windings that make up the IFRC field coils, as shown in Figure 3.2. The two concentric solenoids define the machine center and symmetry direction. The inner (flux) coil has dimensions of 1.3 meters and a radius of 10 cm; there are four parallel windings with a pitch of 20 turns per meter for a total of 80 turns. The outer (limiter) coil is made up of six aluminum straps connected in parallel to each other, with a radius of 40 cm and an axial extent of 60 cm. Each strap is 5 cm wide and 3 mm thick, and is separated from the next by a gap of 5 cm. The last two windings are the mirror coils which define the axial limits

of the plasma volume. They are centered on $z = \pm 30$ cm, and extend from $r = 15$ to $r = 38$ cm. Currents in the flux and limiter coils flow in the $+\hat{\theta}$ direction; magnetic fields in the interior of each solenoid are induced in the $+\hat{z}$ direction. The mirror coils are not actively driven. Induced currents create magnetic fields with a mirror-type topology that usually is anti-aligned with the limiter field.

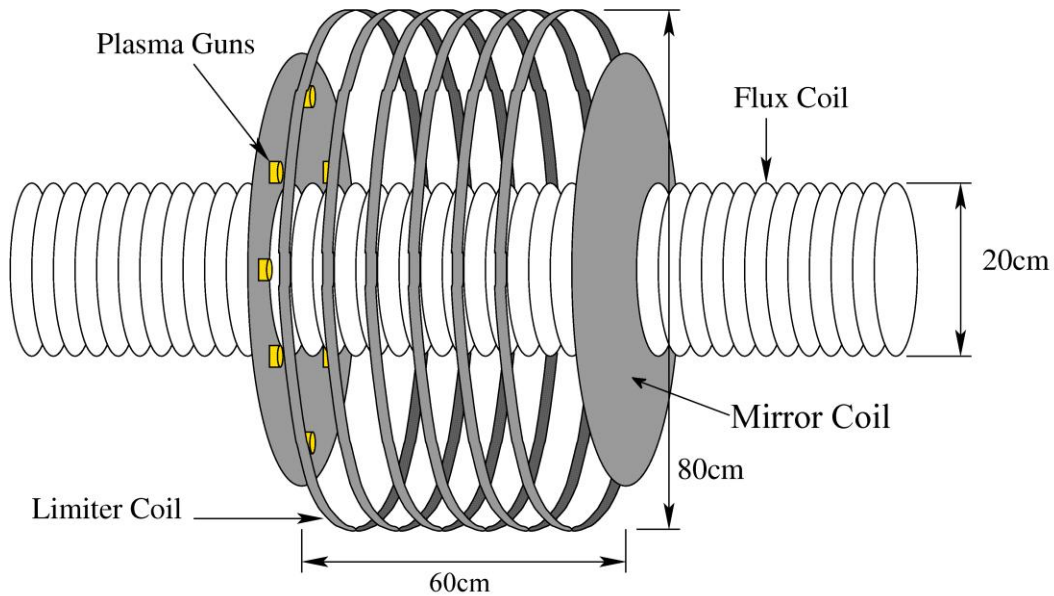


Figure 3.2: Irvine FRC Schematic³¹

Coil	Rise Time	Peak Current	Peak Field
Flux	110 μ s	14000	6000 Gauss
Limiter	110 μ s	15000	600 Gauss

Table 3.1: Rise times and peak values for field coils

Coil	Radius (cm)	Length (cm)	Inductance
Flux	10	130	19 μ H
Limiter	40	60	3.1 μ H

Table 3.2: Field coil physical parameters

The chamber that houses the field coils is a cylindrical vessel that is approximately 1.5 meters long, and 1 meter in diameter. It is made of fiberglass, with a smooth epoxy coating on its interior. The end plates are made of aluminum and have multiple ports for attachment of feedthroughs, pumps, and windows. There are also ports mounted on the sides of the chamber that allow for access perpendicular to the machine \hat{z} axis. The chamber is pumped by two diffusion pumps, Varian models VHS-6 and VHS-10, backed by two mechanical valves. Each pump is connected to the chamber by pneumatically controlled gates. The base pressure that can be reached currently is about 4×10^{-6} Torr. Pressures ranging from atmospheric down to 1 mTorr are monitored by four ConvecTorr gauges, while pressures from 1 mTorr down to the base pressure are measured by a Bayard/Alpert ionization gauge. The gauges are controlled by a Multi-Gauge Controller²⁵ that has the ability to control all five gauges and has a Set Point board installed as well. The set points are set so that high pressure events will cause an interlock system to shut the vacuum valves, isolating the diffusion pumps from the rest of the chamber. This mechanism reduces the chances of cooking or burning the diffusion pump oil.

Plasma is created primarily by arcs across plastic dielectric ‘plasma guns’. Each plasma gun, of which there are 16, consists of a copper center conductor, high density polyethylene dielectric, brass retaining cap, outer tinned-copper braid, and ballast resistor. The dielectric material and inner conductor are taken from RG-8/U cable, similar to Belden model 8237. An arc is formed by a high voltage discharge between the center and outer conductors across the polyethylene insulator; this ionizes the plastic and

produces plasma that is approximately two parts hydrogen to one part carbon. The 16 ballast resistors are made of water and copper sulfate. They have a resistance of approximately 2.5Ω , which is much larger than any other resistance in each plasma gun circuit. This relatively large resistance limits the current that may flow through any particular plasma gun, and effectively ensures that no one gun takes an excessively large amount of current. The guns are mounted on the mirror coils, with eight at each end. They are spaced every 45° at a radius of 20 cm; the two sets of eight are offset from each other by 22.5° to minimize spatial variations of the initial plasma density. Figure 3.3 illustrates the main components of the plasma gun circuit elements.

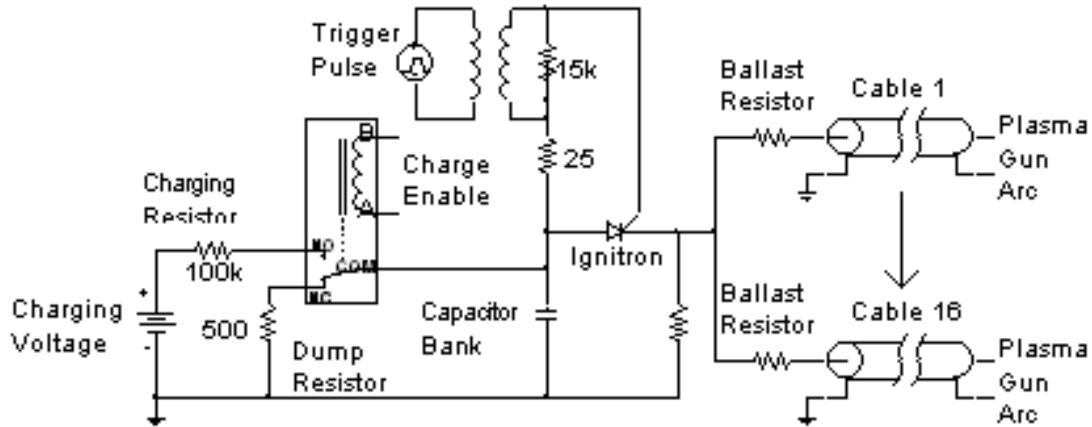


Figure 3.3: Plasma Gun Circuit

The plasma is expelled through the brass retaining caps by a combination of magnetic and thermal expansion forces. The current density \mathbf{J} and magnetic field \mathbf{B} produce a force that can be modeled as

$$\mathbf{J} \times \mathbf{B} \sim \frac{\mu_0 I^2}{a_1^3}, \quad (3.1)$$

where μ_0 is vacuum permeability, I is the current flowing in one plasma gun, and a_1 is a length that describes the size of the spatial gradients in the current and magnetic field.

The force due to the gradient of the thermal pressure ∇p can be modeled by

$$\nabla p \sim \frac{N_T kT}{16V_{gun} a_2}. \quad (3.2)$$

Here N_T is the total particle inventory, kT is the plasma temperature, V_{gun} is the volume inside one gun, and a_2 is the gradient scale length. Estimates for the variables are listed in Table 3.3. For the parameters listed, the magnetic force density is approximately $3 \times 10^8 \text{ Nm}^{-3}$, while the thermal force density is approximately $2 \times 10^9 \text{ N m}^{-3}$. It was initially assumed that the magnetic force was responsible for plasma expulsion; this does not actually seem to be the case, as the plasma velocity is predominately thermal.

With the assumption of a mass density ρ equal to

$$\rho = \frac{m_p N_T}{16V_{gun}}, \quad (3.3)$$

Equations 3.1 and 3.2 can be rewritten as

$$\mathbf{J} \times \mathbf{B} \sim \rho \frac{V_A^2}{a_1} \quad (3.4)$$

and

$$\nabla p \sim \rho \frac{C_s^2}{a_2}. \quad (3.5)$$

The final velocity V_f due to these two forces is estimated by assuming an accelerating distance Δz over which the forces act and an initial velocity of zero. This is written as

$$V_f \sim \sqrt{\left(\frac{V_A^2}{a_1} + \frac{C_s^2}{a_2}\right) 2\Delta z}, \quad (3.6)$$

where the V_A is the Alfvén speed, C_s is the sound speed, and a_1 and a_2 are the previously mentioned scale lengths. The Alfvén and sound speeds are defined in the usual way

$$V_A = \frac{B}{\sqrt{\mu_0 \rho}}, \quad (3.7)$$

and

$$C_s = \sqrt{\frac{kT_e}{m_i}}, \quad (3.8)$$

where local values of the variables are used whenever possible.

We assume that the distance Δz is of the same order as the two scale lengths, and the Alfvén and sound speeds are evaluated inside of the plasma gun. Actual time of flight measurements of the plasma indicate that the axial velocity is approximately 5×10^4 m s⁻¹. This is quite close to the velocity estimated by Equation 3.6, which is 1×10^4 m s⁻¹, given an accelerating distance of 2 cm and the rough approximations of the various quantities that enter into the force models.

Current - I	~1.5 kA
Scale length - a_1	~0.2 cm
Particle Inventory - N_T	~3E19
Temperature - kT	10 eV
Gun volume - V_{gun}	0.1 cm ³
Scale length - a_2	~1 cm

Table 3.3: Force Balance Parameters

The energy necessary to create the magnetic fields and plasma is stored in three groups of capacitor banks. High voltage power supplies charge arrays of capacitors, with

parameters listed in Table 3.4. Each capacitor bank is connected to their respective load by an ignitron switch and a transmission line, as illustrated in Figure 3.4.

Bank	Capacitance (μF)	Voltage (kV)	Energy (kJ)
Flux	240	5.4	3.5
Limiter	2200	1.3	1.9
Plasma Guns	100	16	12.8

Table 3.4: Capacitor Bank Parameters

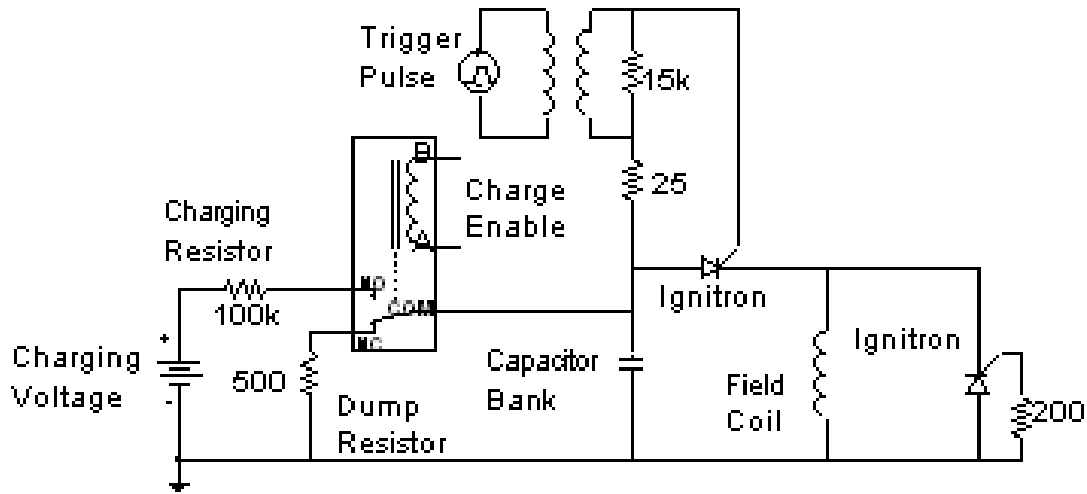


Figure 3.4: Field Coil Circuit

3.2 Data Acquisition

Our data acquisition system consists of three main components: primary acquisition, transmission, and final storage. We have a total of 26 four-channel Bitscopes²⁶, 3 four-channel Tektronix TDS2014 scopes, and 1 two-channel ZT431⁴⁹, for a total of 118 channels available for signal acquisition per shot. The depth, sampling rates, and record length of each scope are listed in Table 3.5. The Tektronix scopes and Bitscopes are housed inside of a Faraday cage that is isolated from earth ground. Signals enter the cage through a breakout panel; common mode chokes are included at the signal

entry point to prevent noise propagation from reaching the digitizers. Transmission of data is by UDP protocol over Ethernet cables and a fiber optic line. All oscilloscopes in the Faraday cage are connected to several Ethernet switches which are linked in turn to an Ethernet to fiber optic converter. The optical signals are transmitted by a fiber optic line to an Ethernet converter which is connected to the computer that stores the data.

Scope Name	Bit Depth	Max Sampling Rate	Record Length
Bitscope	8	40 MS/s	1-128 ksamples
TDS2014	8	100 MS/s	2.5 ksamples
ZT431	12	200 MS/s	4 Msamples

Table 3.5: Digitizer Parameters

A software program called Lab2000 has been written to allow remote interaction with the digital storage oscilloscopes.²⁷ It is written in Visual Basic™ and Excel™, and is a collection of many macros and functions that organizes and collects data received from the scopes. Each scope may be queried with the software, allowing changes to be made to internal scope settings such as the sampling rate or record length. Lab2000 also stores calibration factors for each probe in our system, and maintains assignments of probes to digitizer channels. Arming of our scopes is controlled by the software, as is data downloading. A basic graphical display of the data saved from each shot is also included. The files are saved as Excel files (.xls) and as comma separated value (.csv) files, with both time and data arrays saved for each probe. Further processing is done with IDL™ software, written in house for specific applications.

3.3 Operational Overview

Field reversed configurations are formed when expansionary and compressional forces on a current ring in the plasma are balanced. The flux coil is the primary source of current drive, with peak inductive fields of approximately 250 Vm^{-1} . This large electric field drives current in the toroidal ($-\hat{\theta}$) direction. In the absence of other forces, the magnetic pressure inside of the current loop will be larger than that on its outside which will cause the current loop to expand radially outwards. This expansion can be counteracted by a sufficiently strong magnetic pressure, provided by currents in the limiter coil.

Confinement of the FRC is maintained by a balance between the self organized magnetic field of the plasma current and the fields produced by static field coils such as the limiter and mirror coils. Relatively stationary formations can be maintained on the IFRC for approximately 50 microseconds. Current drive is maintained as long as the flux coil is producing an electric field, which is limited by its rise time.

There are three basic ways that field-reversal ceases on the IFRC. The first and most common is failure due to lack of current drive. The inductive electric field goes to zero, and then reverses in direction as the flux coil current reaches its peak and begins to decay. Plasma resistivity quenches the current, which causes a radial implosion as the magnetic pressures are no longer balanced. The second two failure modes are due to improper balancing of the external and induced magnetic field pressures. If the plasma

current is too small when compared to the limiter current, the FRC may ‘bounce’ off of the limiter fields and fail by hitting the flux coil. Evidence of this mode is given by an initial outward motion of the current channel, followed by a rapid inward motion. The other failure mode occurs when the limiter magnetic pressure is not sufficient to balance the outward force. This ‘blowout’ regime is characterized by a constant outward propagation of the position of the current ring.

A fourth failure mode occurred during early operation of the IFRC but no longer is present. Magnetic fields formed by the limiter coil had a large axial gradient which caused the plasma to acquire an axial velocity and exit the confinement region. This asymmetric magnetic mirror topology was caused by improper transmission line connections to the limiter coil. Current distributions in the six straps of the limiter coil were measured before and after the changes to the transmission line connections were made. The profiles are shown below in Figure 3.5 and are from vacuum shots; note especially the large differences between the two end coils in the initial design.

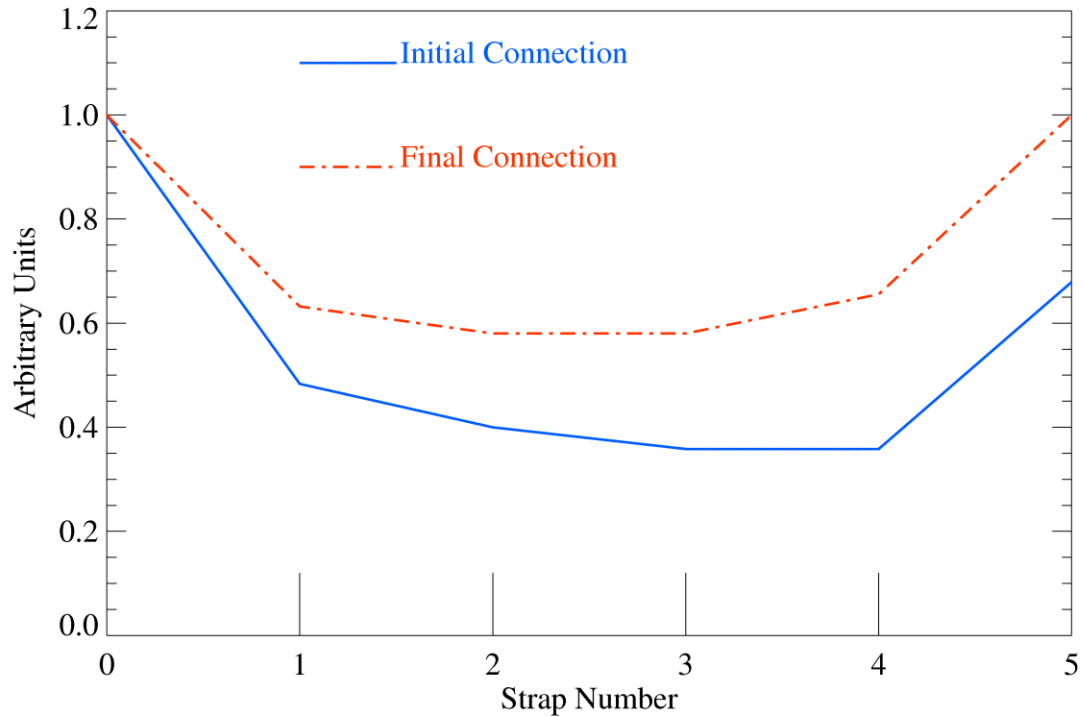


Figure 3.5: Current distributions in limiter coil

A typical shot consists of the following steps. First, each capacitor bank is charged to a desired voltage by manually controlling the output of high voltage power supplies. When all banks are fully charged, an electrical trigger signal is sent to a series of delay boxes which control when each bank fires. The outputs of the delay boxes go to high voltage pulse drivers that transmit a $5 \mu\text{s}$ voltage pulse of approximately 900 volts to a 2:1 step up transformer. The amplified voltage pulse causes each ignitron to begin conduction, closing the switch between each capacitor bank and their load. The banks then discharge through their respective load. Figure 3.6 shows the timing of our various banks and average waveforms for typical shots.

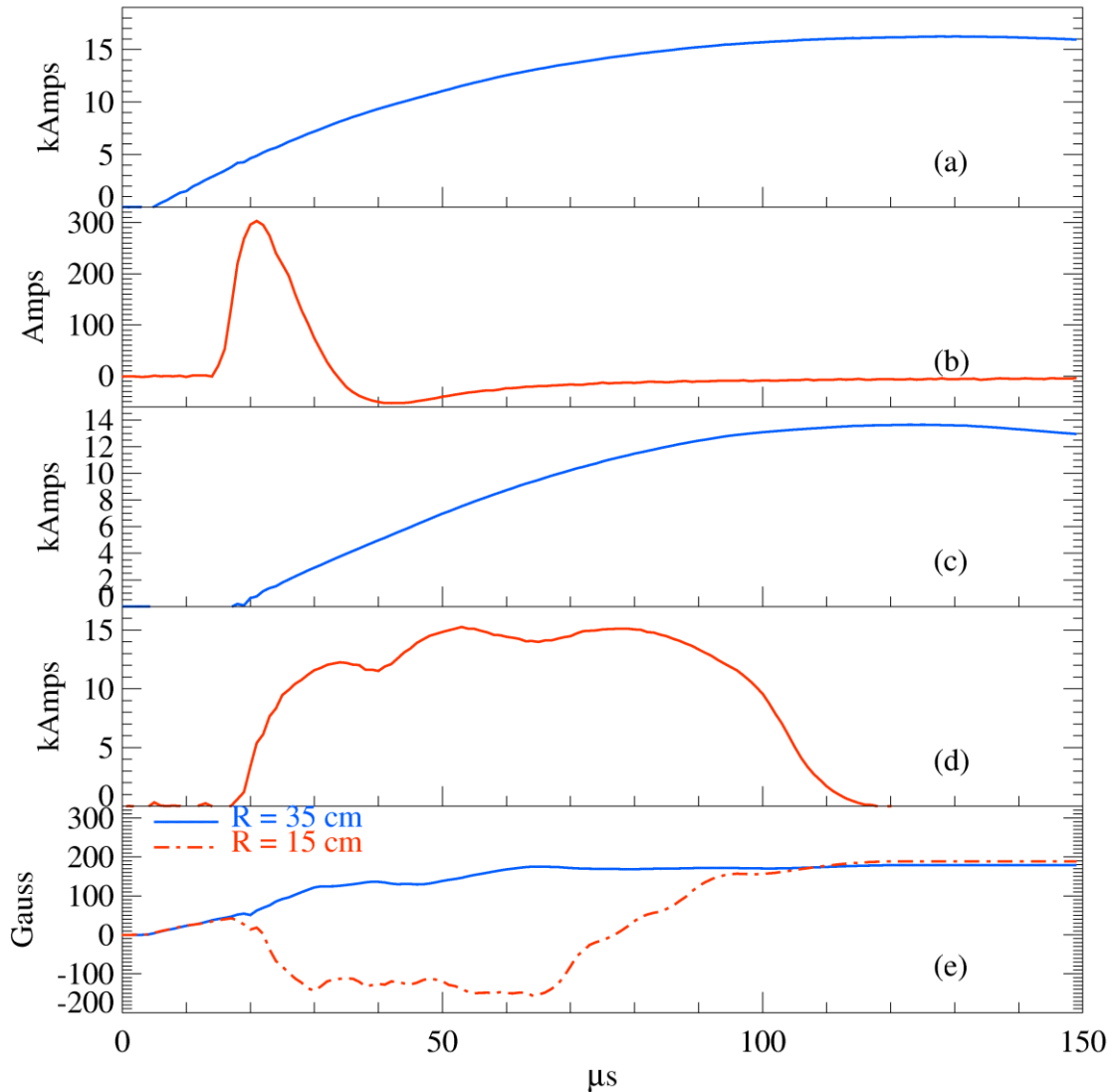


Figure 3.6: The limiter current (a), average plasma gun current (b), and flux coil current (c) are shown for typical charging parameters. (d) is the resultant plasma current as measured by the Rogowski coil, and (e) shows typical axial fields at two radii at the midplane. Note: Plasma gun current trace is not properly integrated, due to an incorrect monitoring circuit.

Control of when each bank fires and how much energy is stored in it are the basic controls that can be used to affect FRC formation and evolution. Table 3.6 lists normal operating parameters. The manner in which the three banks interact can be thought of as two forces that are both pushing on a deformable mass. The flux coil provides a force that is directed radially outward. It ‘pushes’ on the plasma that is formed by the plasma

guns. The amount of plasma is controlled by the charging voltage of the plasma gun bank. Counteracting the outward force from the flux coil is that provided by the limiter coil.

Even	Start Time	Charging Voltage
Limiter Fires	4 μ s	1300 Volts
Plasma Guns Fire	10 μ s	16 kVolts
Flux Coil Fires	19 μ s	5.4 kVolts

Table 3.6: *NCP* timing and charging parameters

3.4 Datasets

There are five different datasets on which analysis is performed in this thesis. The main dataset, named *NCP* for *normal charging parameters*, is a compilation of 153 different shots (discharges) and consists of data describing the magnetic field, field coil currents, flux loop voltage, and plasma current. All twelve possible axial locations are covered by the radial B-dot array, with at least 10 shots at each location for averaging purposes; the data from the two axial B-dot arrays are also recorded for all 153 shots. The *NCP* dataset is used to study the basic structure of the IFRC, such as the magnetic field, current density, magnetic flux, spectra, resistivity, and power balance. High frequency magnetic (*RF B-dot*) and capacitively coupled voltage (*CAP*) measurements are made at one axial location, $z = -10$ cm, and cover a radial extent from $r = 13.7$ to 35.7 cm. The *RF B-dot* dataset consists of 84 shots covering nine radial positions, while the *CAP* dataset has 33 shots covering 11 radial positions. These high frequency datasets are used to describe fluctuations in a frequency range of 10 kHz to 40 MHz. The last two datasets (*FCUP* & *FCUP16k*) are made up of 80 and 107 shots respectively that consist of Faraday cup measurements at $z = -30$ cm and five radial positions from $r = 11$ to 31 cm. The difference between the two datasets is the charging voltage of the plasma gun

capacitor bank, which was increased from 12 kV to 16kV. Magnetic field data is present for the *FCUP* dataset with the radial B-dot array at three axial locations, $z = -8.5, -1.5,$ and 1.5 cm. The *FCUP16k* dataset only has magnetic data at $z = -1.5$ and 8.5 cm. The magnetic measurements are used for correlation studies between magnetic fluctuations and particle losses measured by the Faraday cups.

Dataset	# of Shots	Variables
<i>NCP</i>	153	$\mathbf{B}, I_p, V_{loop},$ coil currents
<i>RF B-dot</i>	84	High frequency B_z
<i>CAP</i>	33	High frequency V
<i>FCUP</i>	80	Faraday cups + NCP vars.
<i>FCUP16k</i>	107	Faraday cups + NCP vars.

Table 3.7: Description of datasets

The *NCP* dataset with charging and timing parameters listed in Table 3.6 is the dataset used for all analyses, unless otherwise noted.

Chapter 4: Diagnostics

This chapter will describe the various diagnostics with which we measure plasma parameters. The diagnostics discussed are magnetic probe arrays (B-dots), flux loops, electric probes, Faraday cups, Rogowski coil, and plasma spectroscopy. Probe positions are listed in Table 4.1.

Diagnostic	Radial Positions (cm)	Axial Positions (cm)
Outer Axial B-dot Array	R = 37	Z = [-24.5, -17.5, -10.5, -3.5, 3.5, 10.5, 17.5, 24.5]
Inner Axial B-dot Array	R = 11	Z = [-27, -20, -15, -12, -9, -6, -3, 0, 3, 6, 9, 12, 15, 20]
Radial B-dot Array	R = [11, 13, 15, 17, 19, 20.5, 22, 23, 24, 25.5, 27.5, 30, 32.5, 35, 38, 41]	Z = [-28.5, -21.5, -18.5, -11.5, -8.5, -1.5, 1.5, 8.5, 11.5, 18.5, 21.5, 28.5]
Flux Loops	R = 38	Z = [-25, 5, 25]
RF B-dot and Capacitive Probes	R = 11→38 cm with 0.5 cm resolution	Z = -10
Double Probe	R = 11→38 cm with 0.5 cm resolution	Z = 0
Faraday Cups	R = [11,16,21,26,31]	Z = -30
Rogowski Coil	R = 11→38	Z = -30→30

Table 4.1: Probe positions
Note: Radial array has only one axial position per shot

4.1 Magnetic Field Probes

There are three arrays of magnetic field probes (B-dots) in the IFRC. Two arrays measure the axial component of the magnetic field along different axial chords, while the third array measures three orthogonal components of the magnetic field along a radial chord that may be changed from shot to shot. Typical B-dot and B traces are shown in Figure 4.1.

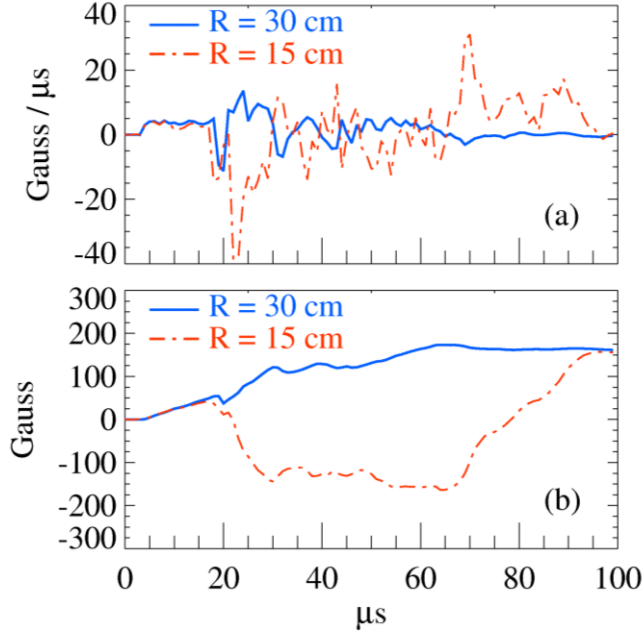


Figure 4.1: (a) B-dot data from two B_z probes at the axial midplane
(b) Integrated traces from the same two probes showing time evolution of the inner and outer axial magnetic field

The arrays are contained in glass or plastic tubing and sealed with low vapor pressure epoxy to protect the probes and wiring from damage. The probes in each axial array consist of small, closely spaced loops of wire, with the area vector of each loop pointing in the \hat{z} direction. The B-dot probes in the radial array are commercial chip inductors, arranged in clusters of three probes.²⁸ The three orthogonal directions that the probes point in are the $\hat{z}, \hat{r}, \hat{\theta}$ directions. Twisted pairs direct received signals through common mode chokes to the data acquisition system. The relationship between the measured output voltage V_{out} and the modeled B-dot voltage V_{B-dot} can be described by

$$V_{out} \sim \frac{V_{B-dot} * Z_T}{Z_{B-dot} + Z_{Line} + Z_{C-DM} + Z_T} + V_{error} , \quad (4.1)$$

where V_{error} is the sum of all error voltages and the various Z_i are impedances in the circuit. The overall circuit for each B-dot is shown in Figure 4.2, with all the impedances and typical values of the components listed in Table 4.2.

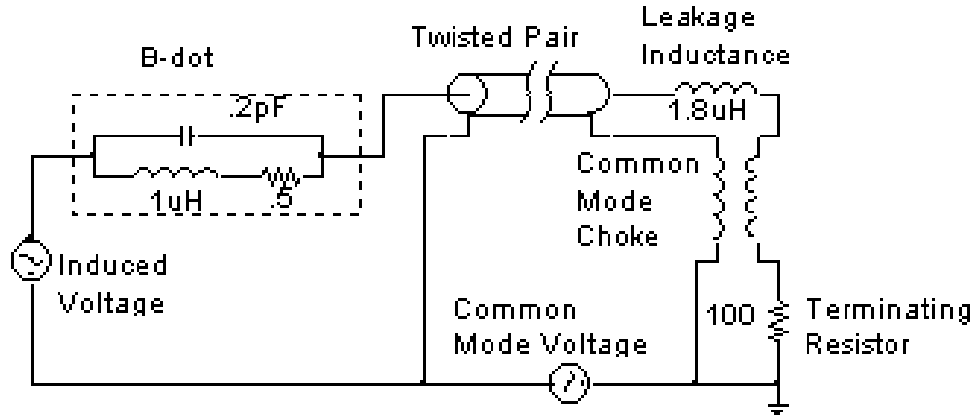


Figure 4.2: B-dot Circuit

Z_{B-dot}	$\frac{R + i\omega L}{1 + i\omega RC - \omega^2 LC}$	$R \sim .5\Omega, L \sim 1\mu, C \sim .5pF$
Z_{Line}	$\sqrt{\frac{R + i\omega L}{G + i\omega C}}$	$R \sim 5\Omega, G \sim 0, L \sim 1\mu H, C \sim 400pF$
Z_{C-DM}	$R + i\omega L$	$R \sim 5\Omega, L \sim 1.8\mu H$
Z_{C-CM}	$R + i\omega L$	$R \sim 1\Omega, L \sim 4.2mH$
Z_T	R	$R \sim 100\Omega$

Table 4.2: B-dot Circuit Impedances and Values

The induced voltage on each B-dot is proportional to the time rate of change of magnetic flux through the B-dot loops (Faraday's Law.) The flux Φ through each probe is an integral of the dot product of the magnetic field \mathbf{B} and the area vector $d\mathbf{A}$ of the N loops of wires that form the probe. If we look at our magnetic signal in the frequency domain with $\frac{dB}{dt} = \omega B$ and an average probe cross sectional area A , the induced voltage may be represented as

$$V_{B-\dot{}} = -\frac{d\Phi}{dt} = -N \frac{d}{dt} \int \mathbf{B} \cdot d\mathbf{A} \sim -NA\omega B_i . \quad (4.2)$$

The reactive portions of the impedances can be ignored in Equation 4.1 if they are much smaller than the resistive components. This requirement may be satisfied by restricting the angular frequency ω to be less than 10^8 for the component values listed in Table 4.2. This simplifies the relationship between the magnetic field and the output voltage to

$$V_{out} \sim K \frac{dB}{dt} + V_{error} , \quad (4.3)$$

where K is a constant. The output voltage is now proportional to $\frac{dB}{dt}$ plus any error signals which we will try to minimize.

Unwanted signals are usually present in addition to the desired magnetic signal. One major source of unwanted signals is fluctuations in the plasma floating potential. These fluctuations are transmitted as common mode signals V_{CM} on the transmission lines. Common mode signals are passively filtered from our signal by passing the transmission lines through common mode chokes. These chokes are composed of twisted wires that are wound on ferrite cores. They present an inductive impedance $j\omega L_{Choke}$ to signals present on both lines, while faithfully passing the desired differential signals from our B-dot probes. The error voltage measured across the terminating resistance R_T can be represented as

$$V_{error} \sim \frac{V_{CM} * R_T}{R_T + j\omega L_{Choke}} + E(t). \quad (4.4)$$

$E(t)$ is a lump sum of all other error signals, such as those due to switching noise from our high voltage ignitron switches and those due to numerical integration (see Chapter 5.2). The purpose of the common mode choke is immediately apparent from the Equation 4.4. Large choke inductances lead to attenuation of the common mode error voltages. For our measurement circuit, effective attenuations are greater than 10 for $\omega > 2.25 \cdot 10^5 \frac{\text{radians}}{\text{second}}$.

Calibration of the different B-dot probes consists of the following steps. Produce a known magnetic field that varies in time. Measure the response of each probe or group of probes to the input field. Integrate the measured signal in time. Find the ratio of the integrated probe signal to magnetic field. A known magnetic field is produced by a Helmholtz coil. Magnetic fields produced in such a coil are known analytically, provided that the coils are built carefully. Currents are driven in the Helmholtz coil by discharge of a high voltage capacitor, and are monitored by a calibrated current probe. The coil is designed to have a small inductance and capacitance; this ensures that measurement of the current and magnetic field are in phase with each other. Probes are placed as close to the geometric center of the two coils as possible. The fields are approximately constant as long as they are within ± 1 cm axially and ± 0.5 cm radially of the actual center. The rise time of the current waveform is approximately 20 microseconds, which is similar to typical timescales in the FRC.

The axial arrays are the simplest to calibrate, as a single measurement of the output voltage measurement of the output voltage and magnetic field is enough to

produce the calibration coefficient for one B-dot probe. Each probe is sequentially placed in the center of the Helmholtz coil, and current is then pulsed through the coil. The calibration coefficient for that B-dot is the constant of proportionality that relates its integrated output signal to the magnetic field waveform.

The 3-D radial array is more difficult to calibrate properly due to the resolution of the magnetic field into three orthogonal components. Misalignments in construction of the array as well as gaps in the twisted pair transmission line cause each probe to be slightly sensitive to magnetic field components that are not in the primary direction of each probe. This is equivalent to each area vector not pointing exactly in one of the three main directions in the lab frame. Calibration is done in a similar manner as that of Romero-Talamás²⁸ et al. Each cluster of three B-dots is placed in the calibration region of the Helmholtz coil with the magnetic field aligned with probe \hat{r} axis. The output voltages of the three B-dots are measured, as well as the current that forms the magnetic field. This process is repeated with the probe array $\hat{\theta}$ axis aligned with the magnetic field, and finally with the \hat{z} axis aligned with the field. These three sets of three output voltages are each integrated and then averaged in time. The three magnetic field measurements are also averaged over the same time period. The nine constants from the B-dots form a two dimensional 3x3 matrix, $\mathbf{B}_{measured}$, which relates the measured voltages to the orthogonal field components present at each probe. The input field constants are stored in a diagonal 3x3 matrix, $\mathbf{B}_{orthogonal}$. The calibration matrix \mathbf{C} is found by matrix multiplication as

$$\mathbf{B}_{orthogonal} \cdot \mathbf{B}_{measured}^{-1} = \mathbf{C}. \quad (4.5)$$

Applying the calibration matrix to recorded data converts the three measured voltages of a cluster into three orthogonal B-dot measurements. This can be written analytically as

$$\mathbf{B}_{orthogonal} = \mathbf{C} \cdot \mathbf{B}_{measured}, \quad (4.6)$$

where $\mathbf{B}_{measured}$ is the 3x1 array of initial measurements from a cluster and $\mathbf{B}_{orthogonal}$ is the resultant 3x1 array.

We call this process ‘orthogonalizing’ the data. Average calibration coefficients for each of our three B-dot arrays are listed in Table 4.3, while a sample calibration array for the radial array is shown in Table 4.4. Uniformity between probes is quite good, with typical variations of 5% or less.

Array Name	Average Coefficient	Misalignment
Outer Axial	$.85 \pm .02 \frac{G}{V * \mu S}$	Unresolved
Inner Axial	$27 \pm .8 \frac{G}{V * \mu S}$	Unresolved
3-D Radial	$57 \pm 2.5 \frac{G}{V * \mu S}$	$2.5 \pm 2.6^\circ$

Table 4.3: Average B-dot calibration values

C_{ij} Elements	j=r	j=θ	j=z
i=r	59.81	1.33	1.36
i=θ	-.04	58.00	-5.02
i=z	.02	.05	56.85

Table 4.4: Calibration Matrix for the radial B-dot cluster at $r = 20$ cm

4.2 Flux Loops

A flux loop is just a loop of wire that encompasses a particular area through which magnetic fields pass. They are quite similar to B-dot probes in their theoretical

operation, though are physically quite different in their size and use. Both probes respond to changes in magnetic fluxes; their difference is that flux loops are used to estimate the electric field along and the magnetic flux through a large loop while a B-dot is used to estimate the value of the magnetic field in a much smaller region of space. Integration in time of the flux loop voltage V_{Loop} gives an estimate of the magnetic flux Φ passing through the area of the flux loop, while the voltage itself is proportional to the average electric field \bar{E}_θ along the loop path. These two properties can be summarized by

$$V_{Loop} = -\frac{d\phi}{dt} = -\oint_L \mathbf{E} \cdot d\mathbf{l} \sim \bar{E}_\theta * 2\pi r_{loop}. \quad (4.7)$$

In Equation 4.7, the path length $d\mathbf{l}$ is defined as a circular loop at a radius r_{loop} .

The three flux loops are made of RG-178 coaxial cable, Belden 83265 50 ohm 30 AWG. Each cable is formed into a loop and fixed to the inside surface of a limiter coil strap. The center conductor is soldered to the outer conductor at the point where it meets the rest of the cable. The solder joint is covered by an insulating plastic sleeve that restricts plasma access to either bare conductor. The outer shield braid isolates the inner conductor from electrostatic fields by covering the great majority of the path length. The voltages induced on each flux loop can be as large as 400 volts. This magnitude of voltage is much too large for our acquisition system to monitor directly. A resistive voltage divider is used to provide a smaller voltage to each digitizer. The dividing ratio is 100:1, with a total series impedance of approximately 1500 Ohms. This impedance level is a compromise between a short L / R time and minimization of the overall impedance. The frequency response of the circuit is greater than 1 MHz, comparable to

that of a Tektronix P2220 voltage probe. The shot averaged loop voltage and flux are shown in Figure 4.3.

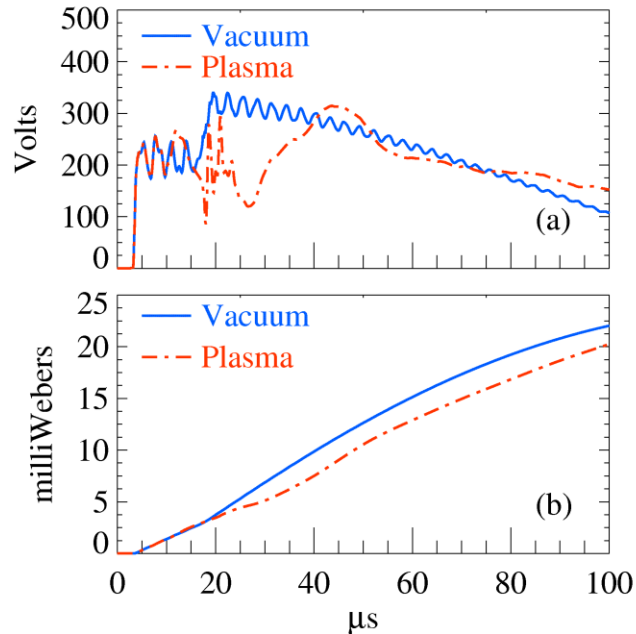


Figure 4.3: (a) Loop voltages at $R = 38$ cm for vacuum and plasma shots. (b) Magnetic fluxes through the same loop. The excluded (trapped) flux of the FRC is given by the difference in flux between vacuum and plasma shots, and has a value here of approximately 2.5 mWebers.

4.3 Electric Probes

If two electrodes are in different positions in plasma, currents may flow through the circuit that connects them. The current that flows between the different electrodes depends on the impedance between them, as well as local values of the plasma temperature, density, and potential. This dependence of the probe current on plasma characteristics can provide valuable information; however the relationship between the probe current and plasma characteristics is a complicated one. The trick to obtaining useful information from these basic probes rests in the design and interpretation of the connecting circuit and the resulting currents.

There have been four different types of electric probes that have been used on the IFRC. The first is just a single conductive electrode exposed to the plasma, with the reference at earth ground. This is called a Langmuir or single tip probe (STP). The second type has a single tip that is capacitively coupled to the plasma (CTP). The third type consists of two bare electrodes in close proximity to each other and the plasma. Unsurprisingly, this is called a double probe (DP). The last type is called a triple probe, with three (or four) probes in contact with the plasma at a particular location (TP). The circuit diagrams of all four probe types can be summarized in Figure 4.4; judicious choices of impedances and potentials differentiate the various probe functions.

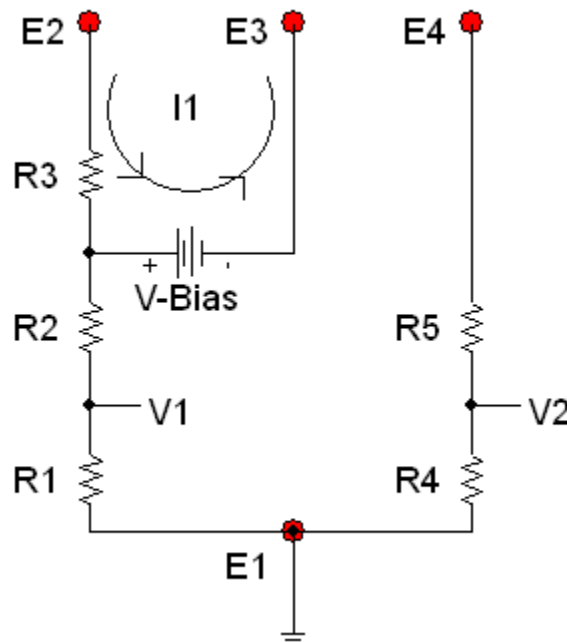


Figure 4.4: Electric Probe Potential Circuit

The STP is used to measure the floating potential in our plasma. E_1 is at the ground potential of our measurement devices, while E_4 is in direct contact with the plasma. E_2 and E_3 are not used, nor is V_{bias} . A large impedance $R_4 + R_5$ is placed

between the two electrodes to restrict the flow of current. The voltage V_2 is then proportional to the floating potential at E_4 . This probe was simply the bare center tip of a piece of semi-rigid coaxial cable. The outer ground electrode was insulated from the plasma by a glass sheath. Currents were restricted by various high pass filtering circuits outside of the vacuum chamber.

The CTP was a simple modification of the STP, formed by insulation of the bare tip E_4 by low vapor pressure epoxy (Hysol). This insulation caused the plasma tip to become capacitively coupled to the plasma, which can be modeled as an impedance $Z_4 = \frac{1}{j\omega C}$ where C is the capacitance between the tip and ω is the angular frequency. The voltage V_2 is still proportional to the floating potential, but no longer has a constant relationship between amplitude and frequency. Figure 4.5 shows typical data from both the STP and CTP.

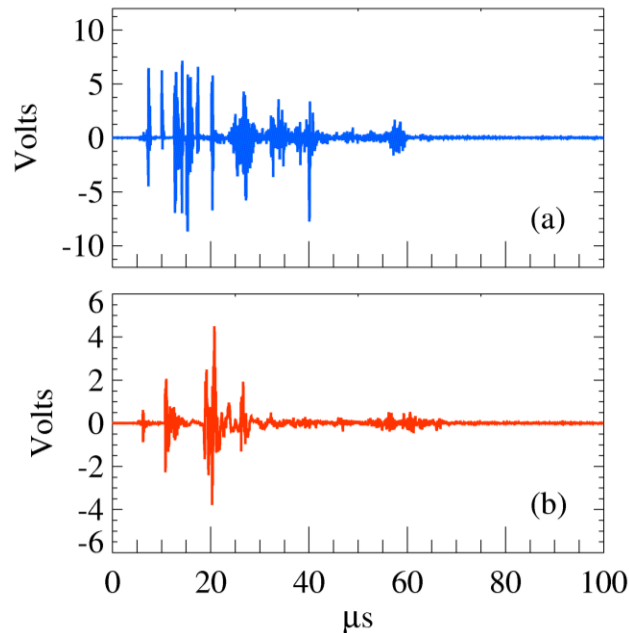


Figure 4.5: (a) Single tip probe trace (b) Capacitive probe trace
Location is $z = -10$ cm, $R = 23.7$ cm

The double probes used primarily on the IFRC differ from single tip probes in one main way; very little current is drawn from either probe to a ground potential, while large currents may flow from one probe to another. This setup is called a floating double probe. Only electrodes E₂ and E₃ are used from Figure 4.4; V_{bias} is approximately 45 volts, while R₁ and R₂ go to infinity and R₃ is on the order of one ohm. The current I₁ is proportional to the ion saturation current, I_{sat} , where

$$I_{sat} \cong en_e c_s A_{probe} , \quad (4.8)$$

as long as the bias voltage is larger than about three times the plasma temperature. In Equation 4.8, e is the elementary charge, n_e is the electron density, c_s is the plasma sound speed, and A_{probe} is the area of one probe tip. The probe current may be measured by any method that isolates the primary circuit from the grounded secondary side, such as a transformer or optical isolator. In practice, this is usually done by an isolation transformer, with the current measured by the voltage drop across a small sense resistor. This resistance enters the measurement circuit as R₃.

The double probe was mostly used to estimate density profiles, since the induced current is usually proportional to the density, with a small temperature dependence in the sound speed c_s . The circuit that was used most often is shown in Figure 4.6. It consists of a low impedance bias voltage and a current monitoring transformer. Sample data are shown in Figure 4.7.

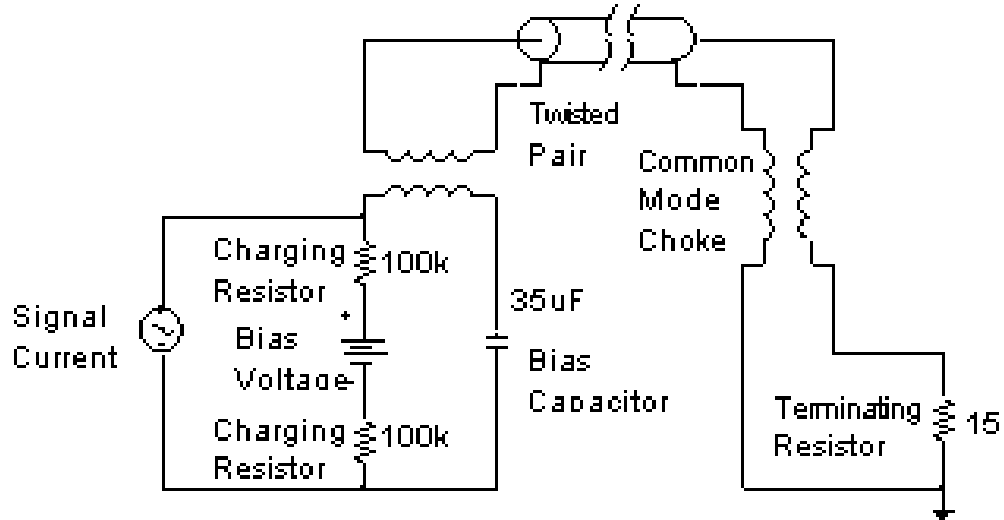


Figure 4.6: Double Probe Circuit

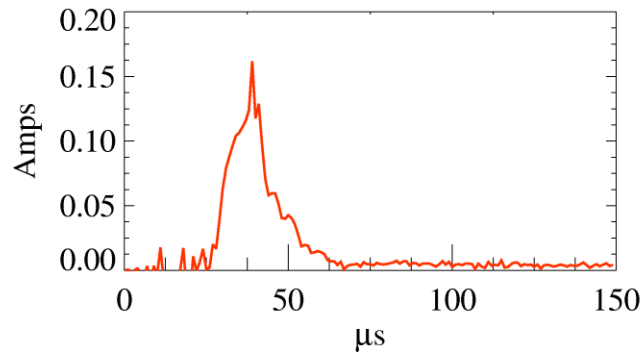


Figure 4.7: Current drawn by a floating double probe at $R=23$ cm. Data comes from shots 4383-4392.

The third probe type used is the triple probe (TP). This type of Langmuir probe is defined primarily by its ability to estimate both the plasma density and temperature with fast time resolution. It can be thought of as a combination of a floating double probe and a single tip probe. Three measurements are necessary to deconvolve the density and temperature relationship. I_{sat} is measured by the current that flows between E_2 and E_3 in the same way as the floating double probe. V_2 is proportional to floating potential, while V_1 is proportional to slightly higher potential. The higher potential of V_1 can be explained by remembering that the total current drawn from the floating pair to ground is

equal to zero. This means that the ion saturation current drawn by E_3 must be balanced by a net electron current on E_2 . As illustrated in Figure 4.8, the electron current grows exponentially as the floating potential is exceeded. The difference in potential, $V_1 - V_2$, is actually proportional to the electron temperature. We can then find the plasma sound speed and infer the local density measurements from I_{sat} .

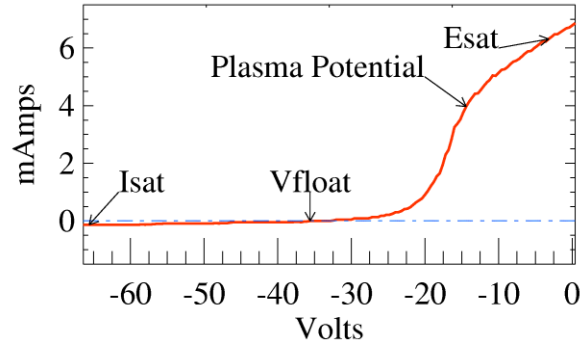


Figure 4.8: Sample I-V trace from a Langmuir probe²⁹

Though much work was done with different triple probe designs, no usable data was ever obtained on IFRC. Reasonable temperatures and densities were measured on another machine in the lab (Mini-Q with a filament discharge in argon); when placed into the IFRC, inferred temperatures usually were negative. This is believed to be because of the large changes in floating potential relative to earth ground, which caused the electronic measuring circuit to malfunction. The temperature at various points in the plasma was thus unable to be measured, leaving spectroscopy as our only method of temperature measurements. Local values of the density are measured by the floating double probe, with spatial profiles determined by pressure balance with the magnetic fields

4.4 Faraday Cups

Faraday cups are actually just a specialized form of a double probe. The first electrode is essentially a hollow can, with a small hole allowing particle access to its interior. The inner electrode is an electrically conductive cup that catches the particles that pass through the entrance hole. The outer electrode is usually at the floating potential due to its relatively large contact area with the plasma. The inner electrode may be biased or not with respect to the outer, depending on the purposes of the experimenter. Figure 4.6 also describes the important aspects of the Faraday cup circuit.

Our experiment uses an array of five Faraday cups. They are located at $z = -30$ cm, and radially spaced every five centimeters starting at $r = 11$ cm. The bias between the outer shell and the inner cup ranged from -90 to $+90$ volts, with the most common bias being -48 volts. The rationale for choosing -48 volts is that it is much greater than the electron temperature in our plasma. This voltage is sufficient to repel almost all electrons that may enter the cup. The measured currents are then due primarily to ion capture. There may be some secondary electron emission; low energy protons impinging on graphite give a secondary electron emission coefficient of only³⁰ 0.058 which is relatively negligible. 80 shots have been averaged together from the five Faraday cups; these data are shown in Figure 4.9.

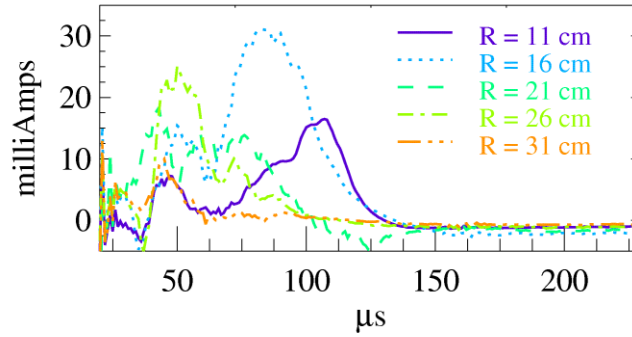


Figure 4.9: Faraday cup data

4.5 Rogowski Coil

A typical Rogowski coil is shown in Figure 4.10. It is a spirally wound coil of wires, with a return wire passing back along its axis. Its purpose is to produce an output voltage that is directly related to any currents that pass through it. Firstly, the induced signal can be represented once again as a sum of contributions from N small loops of wire, connected in series to each other. The total magnetic flux once again is described by Equation 4.2 where $d\mathbf{A}$ is the cross sectional area of each wire loop; the difference lies in the distribution of the N loops. They can be represented by a turn density n along a path L that describes the location of each loop. The total signal produced by the Rogowski coil can then be represented by

$$V = -\frac{d\phi}{dt} = -n \frac{d}{dt} \oint_L dl \int_A \mathbf{B} \cdot d\mathbf{A}. \quad (4.9)$$

If the Rogowski coil is shaped into a closed loop of any shape, the path integral becomes a loop integral and $d\mathbf{l}$ points in the same direction as $d\mathbf{A}$. The order of integration can then be switched, and Ampere's Law, written as

$$\oint_L \mathbf{B} \cdot d\mathbf{l} = \mu_0 * I_{enclosed} , \quad (4.10)$$

can then be used to relate the magnetic field \mathbf{B} to the enclosed current $I_{enclosed}$ that produces it. We are then left with our desired result: an induced voltage that is related to the current by

$$V = -\mu_0 n A \frac{d}{dt} I_{enclosed} . \quad (4.11)$$

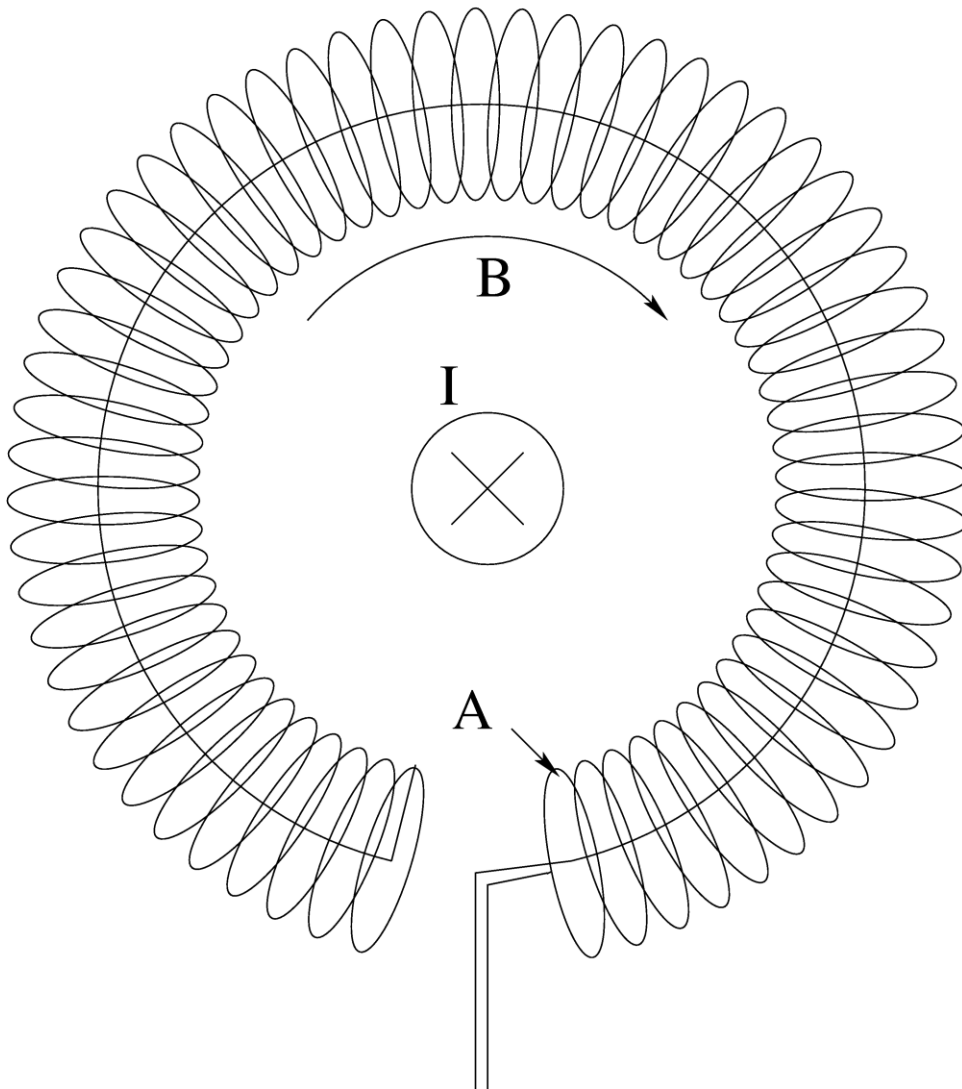


Figure 4.10: Rogowski coil³¹
The current direction and measured B field component are also shown.

We would much rather create a circuit that produces an output voltage that is proportional to I , rather than its time derivative. To do this, we can use Equation 4.1 again, with $Z_T \rightarrow \frac{1}{j\omega C}$, $Z_{Line} \rightarrow R$, $Z_{B-dot} \rightarrow j\omega L$, and $Z_{Choke} \rightarrow 0$. Upon substitution of these values, the resulting relationship between the output and induced voltages is described by

$$V_{out} = \frac{V_{induced}}{1 + j\omega RC - \omega^2 LC} = \frac{-j\mu_0 n A \omega I}{1 + j\omega RC - \omega^2 LC}, \quad (4.12)$$

which is that of a band pass filter.

The current that is measured by the Rogowski coil is the plasma current in the $-\hat{\theta}$ direction, an example of which is shown in Figure 4.11. The loop is rectangular, and located in a two dimensional $\hat{R} - \hat{Z}$ plane at approximately $\theta = -120^\circ$. The details of construction and calibration are quite similar to that of the B-dot arrays, and are covered well in the thesis of W.S. Harris.³¹ The RC high pass filter, with $R = 2.01 \text{ k}\Omega$ and $C = 1.96 \text{ }\mu\text{F}$, has been used to passively integrate the signal. The combination of the integrator and self inductance of $351 \text{ }\mu\text{H}$ produces the band pass filter with approximate corner frequencies of 30 Hz and 1.2 MHz. This means that as long as the frequency content of the recorded voltage from the Rogowski coil satisfies $30 \leq f \leq 1.2E6$, the output will be proportional to the current that passes through the enclosed loop. The constant was determined by comparison of the Rogowski coil output to the output of a calibrated current monitor for a current that passed through each device. This constant was found to be 4.19×10^4 Amps/Volt for the Rogowski coil as currently implemented.

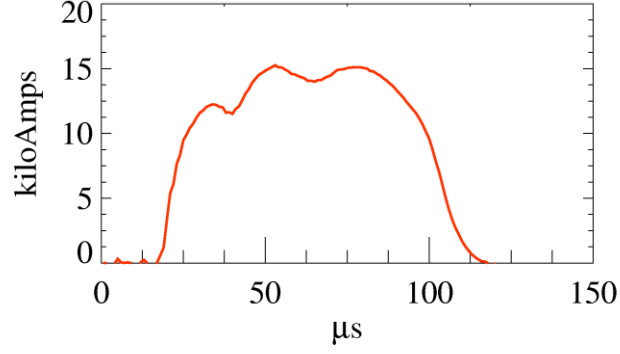


Figure 4.11: Plasma current measured by the Rogowski coil

4.6 Spectroscopy

Light emitted by ionized and neutral atoms in the IFRC is brought to a SPEX 1702 Czerny-Turner spectrometer by a bundle of approximately one hundred 150 μm fibers and dispersed onto a Hamamatsu R5900U-20-L16 photomultiplier array. The bundle is used instead of a single fiber in order to maximize the amount of light coupled from the plasma to the spectrometer. For more details of the spectrometer theory and design, see the thesis of Harris.³¹

Electron temperatures are estimated by taking the ratio of intensities of two hydrogen spectral lines under the assumption of Maxwellian distributions, an optically thin plasma, coronal equilibrium, and the repeatability of plasma discharges. Since the IFRC satisfies all of these criteria³¹, the electron temperature kT_e can be written as

$$kT_e = \frac{x_\beta - x_\alpha}{\ln\left(\frac{\epsilon_\alpha}{\epsilon_\beta}\right) - \ln\left[\frac{\lambda_\beta f_\alpha x_\beta A_\alpha \sum_j A_{\beta j}}{\lambda_\alpha f_\beta x_\alpha A_\beta \sum_j A_{\alpha j}}\right]}, \quad (4.13)$$

where x_i , ϵ_i , λ_i , f_i , and A_i , are the energy level, emissivity, wavelength, absorption oscillator strength, and Einstein transition probability for each of the two lines used to

derive the temperature. The emissivity ϵ is given by the average line intensity measured by the spectrometer for each of the two species that are used to estimate the temperature.

The specific lines used to estimate the electron temperature are the H_α and H_β lines at 6562.81Å and 4861.34Å. Substitution of the appropriate constants into Equation 4.13 leads to a much simpler formula describing the electron temperature, namely

$$kT_e \cong \frac{1.9 \text{ eV}}{\ln(H_\alpha/H_\beta) - 2.011}, \quad (4.14)$$

where H_α and H_β line intensity data are recorded as a function of time for a number of discharges, although not simultaneously. The intensities are combined to produce average signals that are then input into Equation 4.13, giving us an estimate of the average electron temperature.

Ion temperature measurements are based on estimates of Doppler broadening of several different spectral lines. H_α at 656.2 nm and CII at 657.8 nm are the two lines that have been most heavily analyzed, though other impurity ionic lines from helium, argon, krypton, and xenon have also been measured. Other sources of line broadening, including instrumental and Stark broadening, have been accounted for and removed from resultant signals. Instrumental broadening is found to be 0.3 Å, while Stark broadening has a maximal value of 0.27 Å for hydrogen with insignificant values for more massive particles at typical IFRC densities.

One caveat on the temperatures measured by spectroscopy: they are line averaged along one spatial chord. Resolution of spatial variations of the temperature is possible

through the use of multiple sight lines and inversion techniques, none of which have been done here. We will assume that the plasma temperature is isotropic, with no spatial variation inside of the separatrix. This temperature profile does fit the rigid-rotor profile for radii less than approximately 25 cm as shown in Figure 2.2. Deviations at larger radii could be explained by a decreased temperature outside of the separatrix, though the flat experimental profile also may be due to finite resolution of the gradients of the magnetic field and the subsequent integration errors on solving for the plasma pressure.

Chapter 5: Numerical Methods

Several programs have been written in the IDL computer language to aid in the processing and manipulations of the large amounts of data that are produced on the IFRC. This chapter describes the format in which B-dot data are stored and specific functions that manipulate data such as integration, orthogonalization, rotation, and filtering. It also describes the interpolation methods by which we populate a two dimensional grid used for further processing.

5.1 B-dot Data Structures

Signals are downloaded from the digital storage oscilloscopes by Lab2000 software and recorded as .csv files before further processing with IDL code. The .csv files are not terribly easy to deal with and so are reformatted as an IDL structure variable. The most basic structure contains a time and voltage array for a B-dot probe, as well as the radial and axial positions of the probe. Each probe structure is grouped into a larger structure that describes the orientation, which is then added to a structure that groups together all data from one probe array. Next, probe array structures are combined into shot structures, which can finally be assembled into a dataset structure. As an example, data for a particular probe can be accessed from a dataset variable with the following command in IDL:

$$\text{Data} = \text{dataset.Shot06276.Radial3.z.n1.d} \quad (5.1)$$

Likewise, the axial position, radial position, or time array may be accessed by the tags *zpos*, *rpos*, and *t*. Periods demarcate different levels of the structure; the items found between periods are structure tag names which are used to organize and identify data. This structure format makes passing data between functions and programs simple, and uniquely specifies the pertinent information for every B-dot probe.

5.2 Numerical Integration

Any integration of signals is done with an in house IDL program that implements multiple order Newton-Cotes methods. The order of integration determines the number of points necessary for a numerical estimate of the integral. The first points in the integration are integrated with progressively higher Newton-Cotes methods until the fifth point has been reached. After this, the order is no longer increased and integration of the rest of the time signal is done by the fourth order method. If h is the separation between sample points, and f_i is the function evaluated at the i^{th} point, then the numerical integral can be approximated by the following steps:

$$\begin{aligned}
 F(0) &= 0 & (5.2) \\
 F(1) &= \frac{h}{2}(f_0 + f_1) \\
 F(2) &= \frac{h}{3}(f_0 + 4f_1 + f_2) \\
 F(3) &= \frac{3h}{8}(f_0 + 3f_1 + 3f_1 + f_1) \\
 F(4) &= \frac{2h}{45}(7f_0 + 32f_1 + 12f_2 + 32f_3 + 7f_4) \\
 F(i > 4) &= \frac{2h}{45}(7f_{i-4} + 32f_{i-3} + 12f_{i-2} + 32f_{i-1} + 7f_i) + F(i-4).
 \end{aligned}$$

Numerical integration does have the same drawback as analog integration when there is a residual average offset in data. Integration can lead to growing signals that are not proportional to a desired physical quantity. Consider functions $F(x)$ and $Y(x)$, where

$$F(x) = a \frac{dY(x)}{dx} + b, \quad (5.3)$$

and a and b are both constants. After integration in x , the straightforward results are given by

$$G(x) = \int F(x)dx = aY(x) + bx. \quad (5.4)$$

Ideally, the constant b is equal to zero, and we need not worry about any linearly growing terms in our integrated equation. Equation 5.3 is exactly the same as that which describes the induced voltage in a B-dot probe, with the simplest error voltage added in. As we can see, there are parameter ranges for which the error voltage may actually contribute an excessively large amount to the integrated signal.

In reality, the error voltage is not usually constant in time and may change from shot to shot. We still assume that there is a linearly growing error signal due to some small amount of residual offset voltage in our B-dot signals. The procedure for removal of this signal rests on several assumptions. The first is that while plasma discharges may vary from shot to shot, the magnetic fields present in our chamber after the plasma current has gone to zero will be identical, given identical charging voltages on each capacitor bank. This essentially means if we are given the magnetic field structure at a relatively late time, we can find the linear trend that must be subtracted to make data from each shot fit. The second assumption is that there will be no magnetic fields present

in our chamber when no currents are flowing in our field coils. This gives us boundary conditions which can also be used to find some linear trend that must be subtracted.

Integration error correction then proceeds with the following specific steps. B-dot probe voltages are recorded for 2 milliseconds while only our field coils are discharged. This is long enough to ensure that the fields are approximately zero at the last sampling time. After integration and orthogonalization, we enforce the boundary conditions of zero field at the start and end times by subtracting off a linearly growing trend. We then record the values of the magnetic field at 235 microseconds after the start time. The field structure at this time will serve as the boundary condition for actual plasma shots. Linear trends based on the difference between this final condition and the actual recorded data are then removed from data at each spatial position for every shot.

5.3 Orthogonalization and Calibration

The orthogonalization and calibration processes are done at the same time. The inputs to this process are data from the B-dot arrays and the calibration factors that were found for each probe in the initial calibration process. Data from each axial B-dot probe are multiplied by their scalar calibration factor. The data from each cluster of probes on the radial B-dot array are multiplied by the matrix that was found by the calibration procedure described in Section 4.1. Essentially, voltages from three roughly orthogonal probes located in close proximity to each other are added or subtracted from each other to produce the three dimensional magnetic field measurements at the position of the probe cluster.

5.4 Rotation

Orthogonalization of B-dot data produces magnetic field measurements that are aligned with the radial probe axes; however the probe axes are not necessarily aligned with the machine coordinate system. The probe array is kept radially aligned by two parallel sets of guide holes that are mounted on the machine. There still may be an arbitrary rotation about the radial axis since the array is not fixed in that plane. We can align the two sets of axes by looking at the orthogonalized probe signals in the \hat{z} and $\hat{\theta}$ directions during a period of time where we assume that only axial (\hat{z}) and radial (\hat{r}) fields are present. There is a small period of time at the beginning of every discharge where only currents are flowing in the limiter coil; the symmetry of this coil is such that there should be no toroidal ($\hat{\theta}$) fields. If no toroidal fields are actually present, any measured B_θ signal must be due to a small rotation. This rotation can be corrected by finding the angle that minimizes the measured B_θ for the entire probe array during that time period. Application of a standard rotation matrix to the B_z and B_θ data aligns the probe axes with the machine axes. Shown below in Figure 5.1 are the effects of the rotation matrix on two different probe pairs, located at the axial midplane and separated by 15 cm radially. The effect of the rotation is to reduce the B_θ signal and increase the B_z signal at both locations.

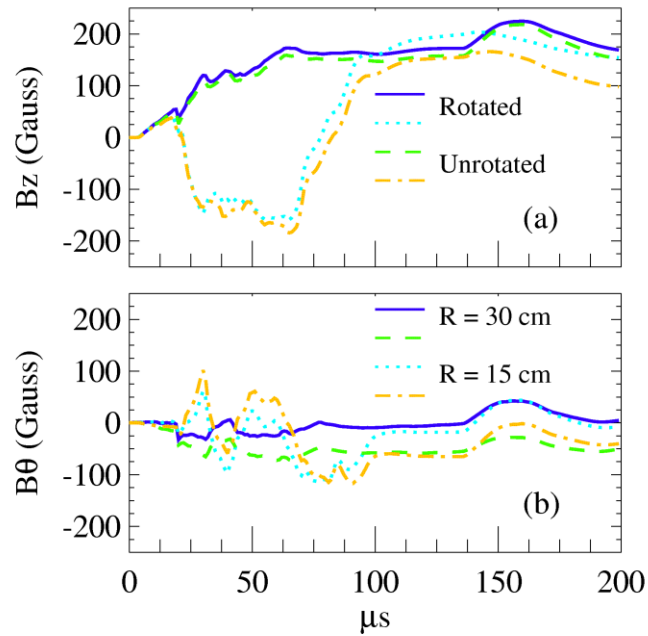


Figure 5.1: (a) Effects of rotation on two B_z probes at the axial midplane
 (b) Rotation effects on B_θ traces at the same positions

5.5 Filtering

Filtering software is used in conjunction with analog filters. IDL has a built in program called *digital_filter* that allows low pass, high pass, and bandpass filters to be constructed relatively easily. The filtering scheme that we use most often is to remove frequencies below 1 kHz and above 1 MHz from all B-dot probe data. The frequency response of the B-dot probes was measured to be $\sim 1\text{MHz}$, which is why 1 MHz was chosen to be the low pass break frequency. A dataset structure is passed into the filtering function, and data from each probe in the dataset are filtered and then returned to the calling program. Sample traces are shown below in Figure 5.2.

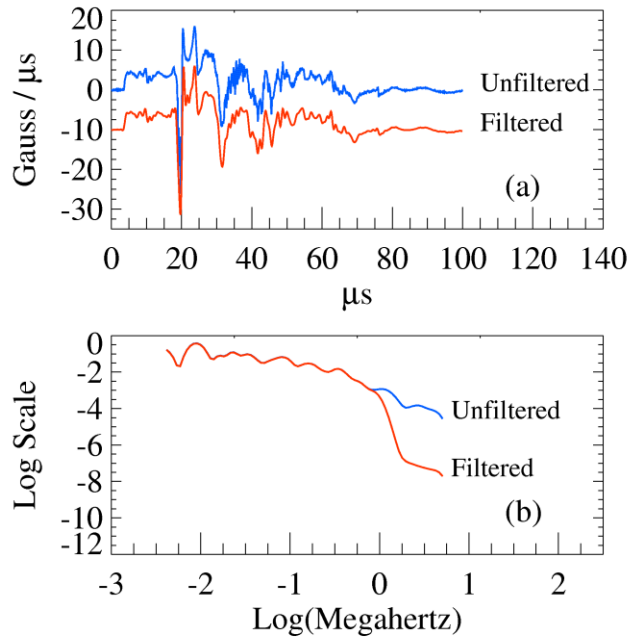


Figure 5.2: (a) Filtered and unfiltered B-dot traces (b) Power spectrum of the entire time series. Note: Filtered data is offset for clarity

5.6 Data Interpolation

B-dot datasets are a compilation of time records from many probes that are then averaged over many shots. The positions at which the B-dots are found do not lend themselves to most numerical methods, such as plotting, integration, or gradient taking. Evenly spaced spatial points are much easier to deal with. The method that we use is an IDL function called *GRIDDATA*; inputs to this function are B-dot data arrays, the two dimensional positions at which the data were recorded, and the requested interpolation points. The function can use any one of ten different methods to fit smooth curves between the input data points; the most common ones are *KRIGING* and *LINEAR*. The smooth curves are used to estimate values of the magnetic fields at the interpolation

points. The output of the function is a two dimensional array of values at the new grid points.

Interpolation points generally have a smaller spacing between their neighbors in both the radial and axial directions than do the input data points. The output grid is usually 24 axial points by 36 radial points. These points are spaced to cover the actual distances of 57 centimeters by 30 cm.

5.7 Correlation Methods

The similarity between any two data arrays can be quantified by a number called the correlation coefficient, P_{xy} . The process of determining P_{xy} consists of picking a particular ‘window’ or portion of two vectors X and Y, subtracting their respective means \bar{X} and \bar{Y} , multiplying the shifted signals together, summing them, and normalizing by their standard deviations σ_x and σ_y ; this is written much more concisely as

$$P_{xy} = \frac{\sum(X - \bar{X}) * (Y - \bar{Y})}{\sigma_x \sigma_y}. \quad (5.5)$$

A similar function is called the delayed cross correlation, which shifts one of the signals relative to the other and finds the correlation as a function of the amount of shift. A shift or ‘lag’ of zero is the same thing as P_{xy} . If one signal is used as both inputs to the cross correlation function, the output is called the autocorrelation. This can reveal periodicities in the input signal that may be obscured by noise. Correlate, auto correlate, and cross correlate are all implemented in IDL, with the inputs specified by the user.

Typical analyses done in this thesis consist of correlating magnetic probe signals with other quantities, such as Faraday cup measurements. Figure 5.3 is an example of the various correlation methods. The inputs to the analysis are shown in Figure 5.3 (a) and are from Shot 6500. The position of the B-dot probe is $r = 17$ cm, $z = -8.5$ cm, while the Faraday cup is located at $r = 16$ cm, $z = -30$ cm. The auto and cross correlations are done over the smaller window from 30 to 70 microseconds, while the overall correlation is found for the entire time period. Each unit of lag corresponds to the sampling period of 0.1 microseconds. The cross correlation analysis shows that the two signals line up best when the magnetic probe data is delayed approximately 6 microseconds. This implies that the average velocity of particles from the B-dot probe to the Faraday cup is approximately 3.6 cm/microsecond. This velocity is higher than the thermal velocity of ~ 2 cm/microsecond given by spectroscopic temperature estimates, but is not out of the realm of possibility.

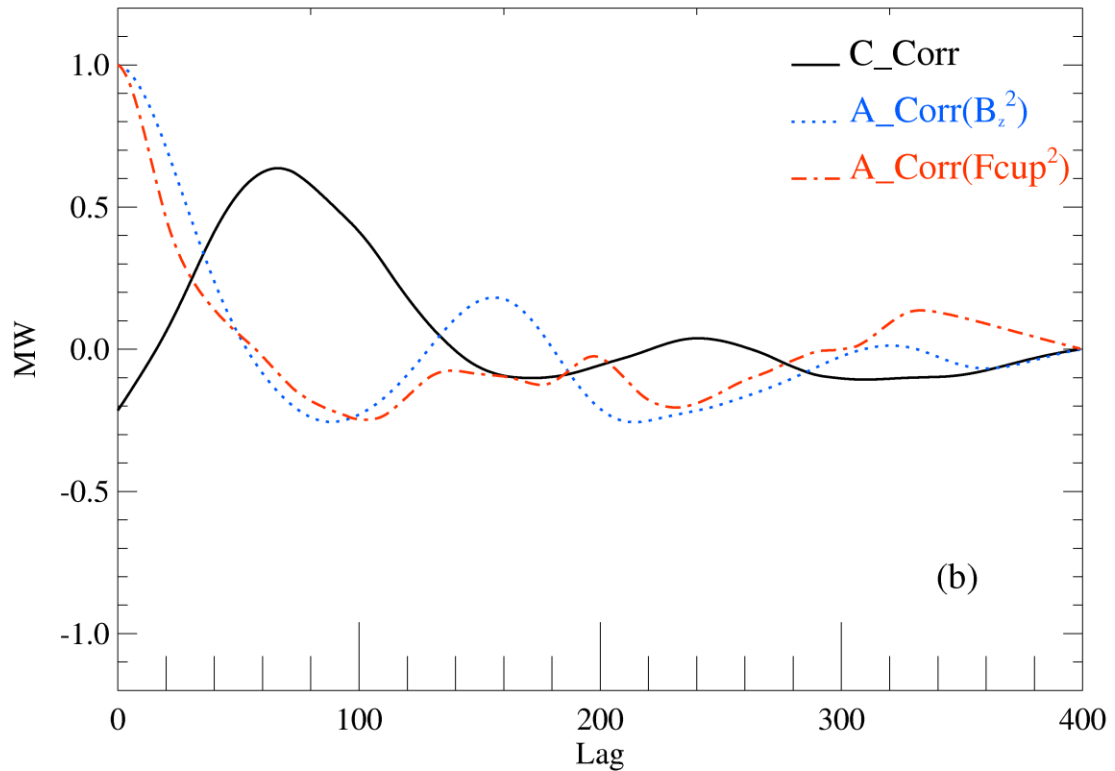
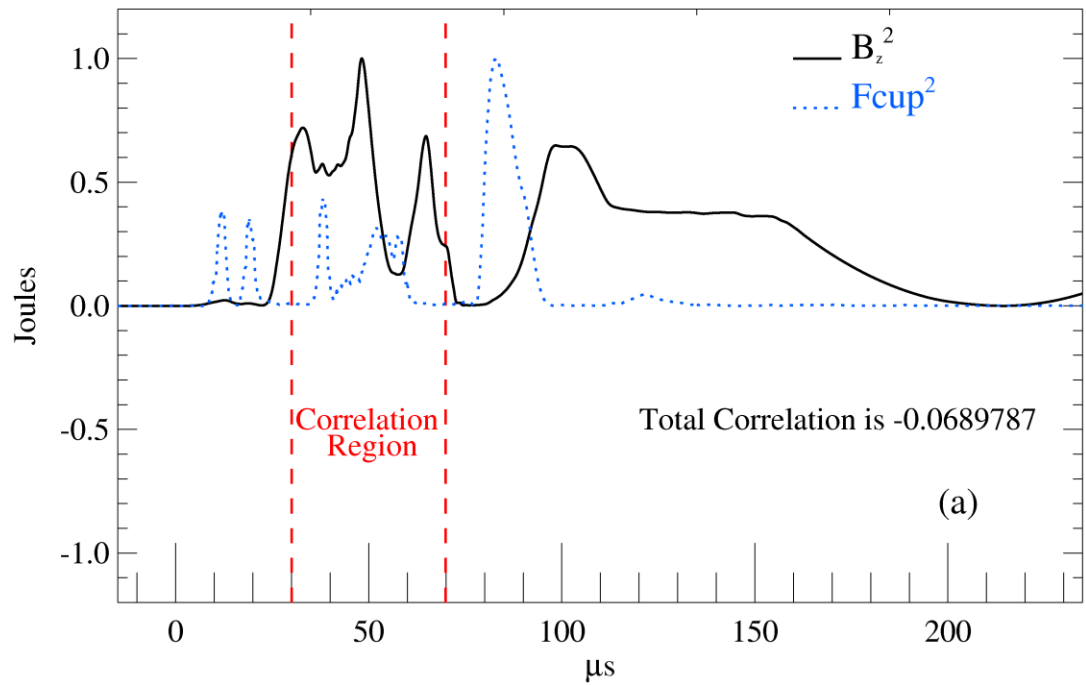


Figure 5.3: (a) Two time series, with overall correlation of -0.069. (b) Cross and auto correlations of the two signals for a restricted window from 30 to 70 microseconds. The large peak in cross correlation near a lag of 65 (6.5 microseconds) indicates the similarity of the two input signals. (See Chapter 10)

5.8 Spectral Methods

The frequency content of time signals is found by two different methods in this work, fast Fourier transforms (FFT) and wavelet transforms (WT). FFT is a basic function in IDL, which returns the discrete Fourier transform $F(u)$ of an input $f(x)$.³² It allows a temporal signal to be characterized by *how* the energy carried by that signal is distributed in frequency. The wavelet transform^{33 34 35} characterizes a temporal signal by both *how* and *when* energy at particular frequencies is present in the original signal. This transform, denoted WV , is a complex function of time. It can be thought of as the convolution of a test pulse with the signal to be analyzed. The test pulse has a characteristic frequency that lasts for a few cycles, six in our case, with an amplitude that goes to zero smoothly at the edges of the six periods. The wavelet used in this thesis is a plane wave modified by a Gaussian function. The frequency of the plane wave and the width of the Gaussian determine the frequency and time in the transform. By varying the frequency and repeating the convolution, a map can be made of when the analyzed signal matches the test pulse as a function of frequency. Due to the finite number of cycles in the test waveform, power in the analyzed signal must be present for a long enough length of time to be unambiguously determined. This minimum resolution in time is a function of frequency and is called the cone of influence (COI). Reference 35 is a particularly good guide to the definitions and mathematical formalisms of the transform as well as its abilities and limitations, and should be referred to for further study of the wavelet transform details.

There are many ways to analyze the frequency content of a signal, all of which can be performed by either Fourier or wavelet transforms. The simplest is the energy spectral density (auto spectrum) of a signal x is defined here as $X \cdot X^*$, where the $*$ denotes the complex conjugate and X is the transform into frequency space of the signal. Normally, the absolute value of the auto spectrum is plotted as a function of frequency to illustrate how the energy of a signal is distributed in frequency space. The cross spectrum E_{xy} between two different signal x and y is calculated quite similarly to the auto spectrum of an individual signal, with

$$E_{xy} = X \cdot Y^*. \quad (5.6)$$

This method finds frequencies where both input signals have significant energy. A quantity called the coherency is also useful to find frequency overlaps between two signals. It is defined as

$$\gamma_{xy}^2 = \frac{E_{xy}^2}{E_{xx} E_{yy}}, \quad (5.7)$$

where γ_{xy} is the coherence, E_{xy} is the cross spectrum, and E_{xx} and E_{yy} are the two auto spectra for signals x and y .

Plots of the energy of a signal as a function of time and frequency are called spectrograms. The wavelet transform produces this type of display by definition, though it can also be done by performing a Fourier Transform on a small window of the signal and then repeating as the window is advanced. The auto and cross spectrograms are defined in the same manner as the auto and cross spectra, as is the coherency.

Variations of the cross spectrogram and cross coherency when one signal is delayed in time by a certain amount are called the delayed spectrogram and delayed coherency. This is analogous to the cross correlation, defined in the previous section. This function is used to find whether variations at a particular frequency in one location look similar at another location later in time, and can be used in conjunction with the delayed cross correlation to estimate a time of flight between fluctuations in magnetic probes and particle losses.

Examples of the auto spectrum and auto spectrogram derived by both Fourier and wavelet transforms are shown in Figure 5.4 for sample B-dot data. This figure is significant because it shows that both transforms produce very similar results. An advantage of the wavelet transform is that it does not sample frequencies evenly over its range; it has logarithmically spaced frequencies with more at the low range and fewer as the frequency increases. Contrast this with the Fourier spectrum, which has evenly spaced frequencies. The properties of fluctuations depend more on ratios than on arithmetic differences, i.e. the difference between 10 and 20 kHz is usually more significant than the difference between 1210 and 1220 kHz.

The cross spectrum, cross coherency, cross spectrogram, delayed cross spectrum and delayed coherence are shown in Figure 5.5 between a magnetic probe signal and a Faraday cup signal separated by 22 cm. The delayed coherence identifies a possible link between the two signals at a frequency of 300-400 kHz and a delay between 10-30

microseconds. This suggests a velocity of approximately 1 cm / microsecond between the two probes, a topic that will be discussed further in Chapter 10.

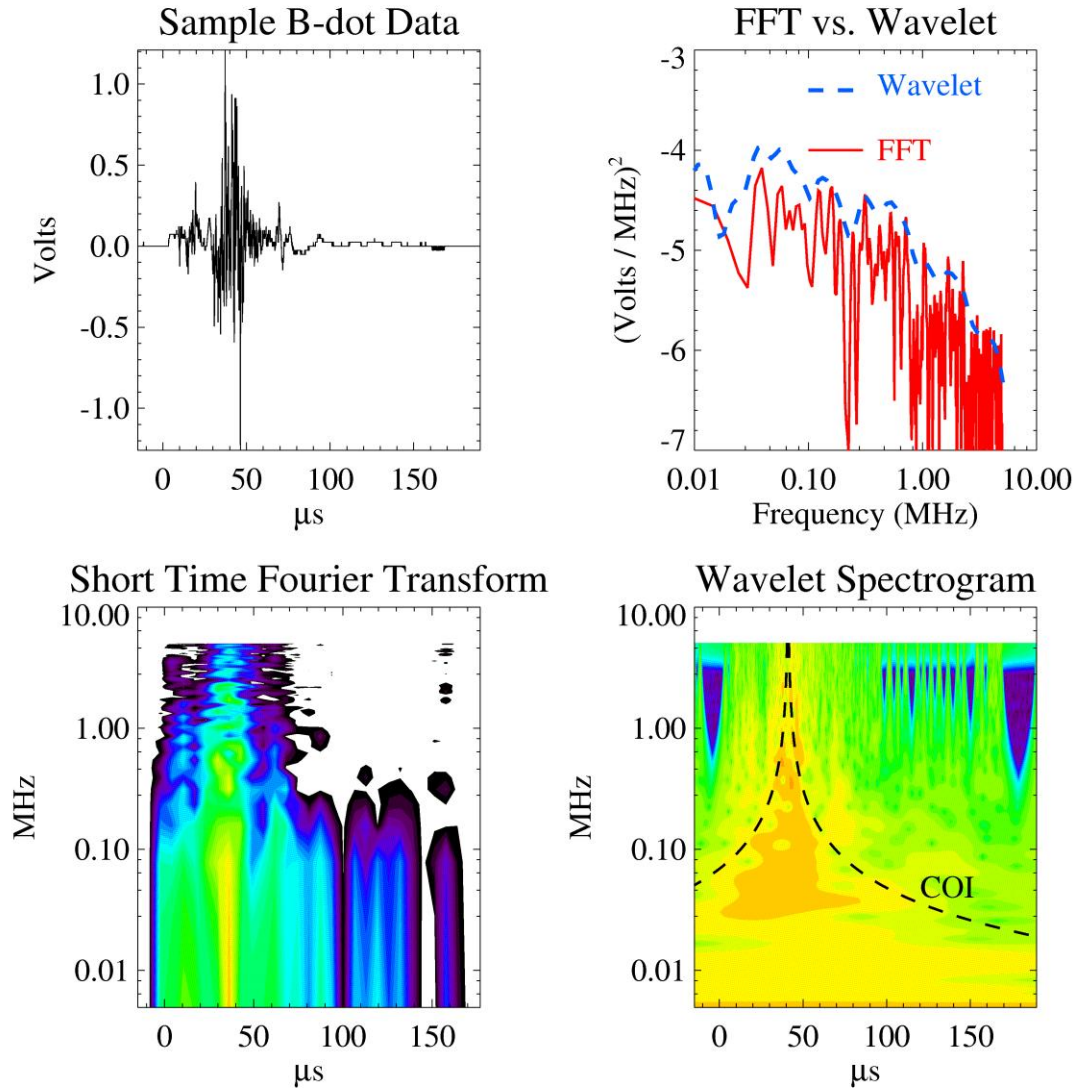


Figure 5.4: Spectral analyses of sample data from Shot 6500. The cone of influence, centered on a time of 41 microseconds in (d) shows the minimum length of time at each frequency that a signal must be present to be considered meaningful.

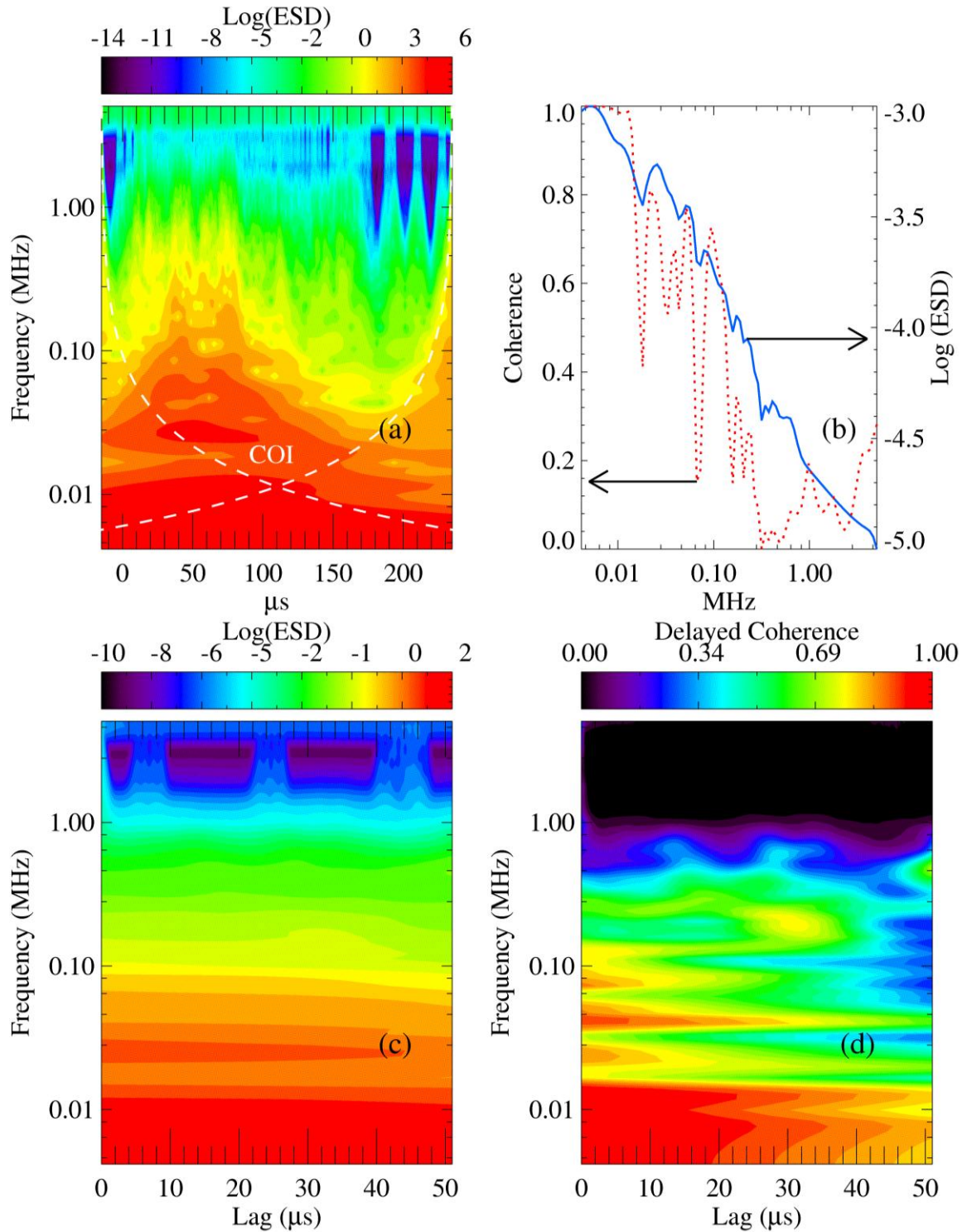


Figure 5.5: (a) Cross spectrogram, (b) cross spectrum and coherence, (c) delayed spectrum, and (d) delayed coherence. Edge effects are marked by the cone of influence (COI).

Higher order spectra linking three different frequencies can be measured by quantities called the bispectrum and bicoherence. These are defined by

$$Bispec(f_1, f_2) = X(f_1)X(f_2)Y^*(f_3) \quad (5.8)$$

and

$$bicoch((f_1, f_2) = \frac{|Bispec(f_1, f_2)|^2}{|X(f_1)|^2|X(f_2)|^2|Y(f_3)|^2} \quad (5.9)$$

where $f_3 = f_1 \pm f_2$. The bispectrum and bicoherence measure the amount of three wave coupling in signals x and y , and can be used to find nonlinear interactions. Analysis suggest that there is significant three wave coupling in the IFRC, the further analysis of which will be left for future work. Figure 5.6 (d) gives a taste of what can be measured, with a hint of coupling at $f_3 - f_2 = 250$ kHz (vertical feature). The two probes used are a B-dot probe located at $z = -8.5$, $r = 17$ cm looking at B_z and a Faraday cup located at $z = -30$, $r = 16$ cm. The bispectra and bicoherences are calculated over a time window from 25 to 75 microseconds.

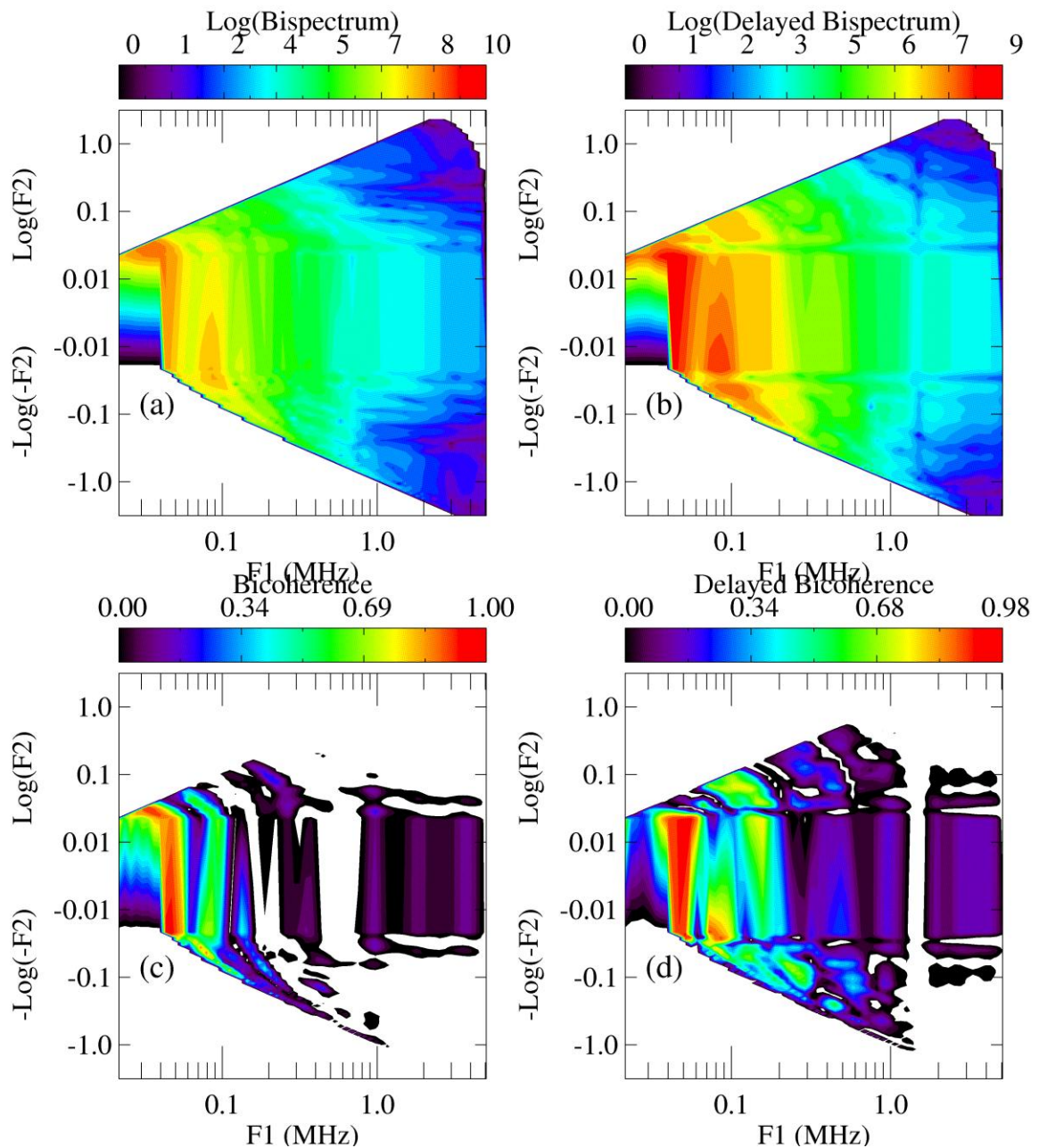


Figure 5.6: Bispectrum (a) and bicoherence (c) from Shot 6500 sample data. (b) Delayed bispectrum and (d) delayed bicoherence, formed by delaying the Faraday cup data 30 microseconds relative to the B-dot data. The value at each point on the contour plot is the power or coherence at the sum frequency of $f_1 + f_2$

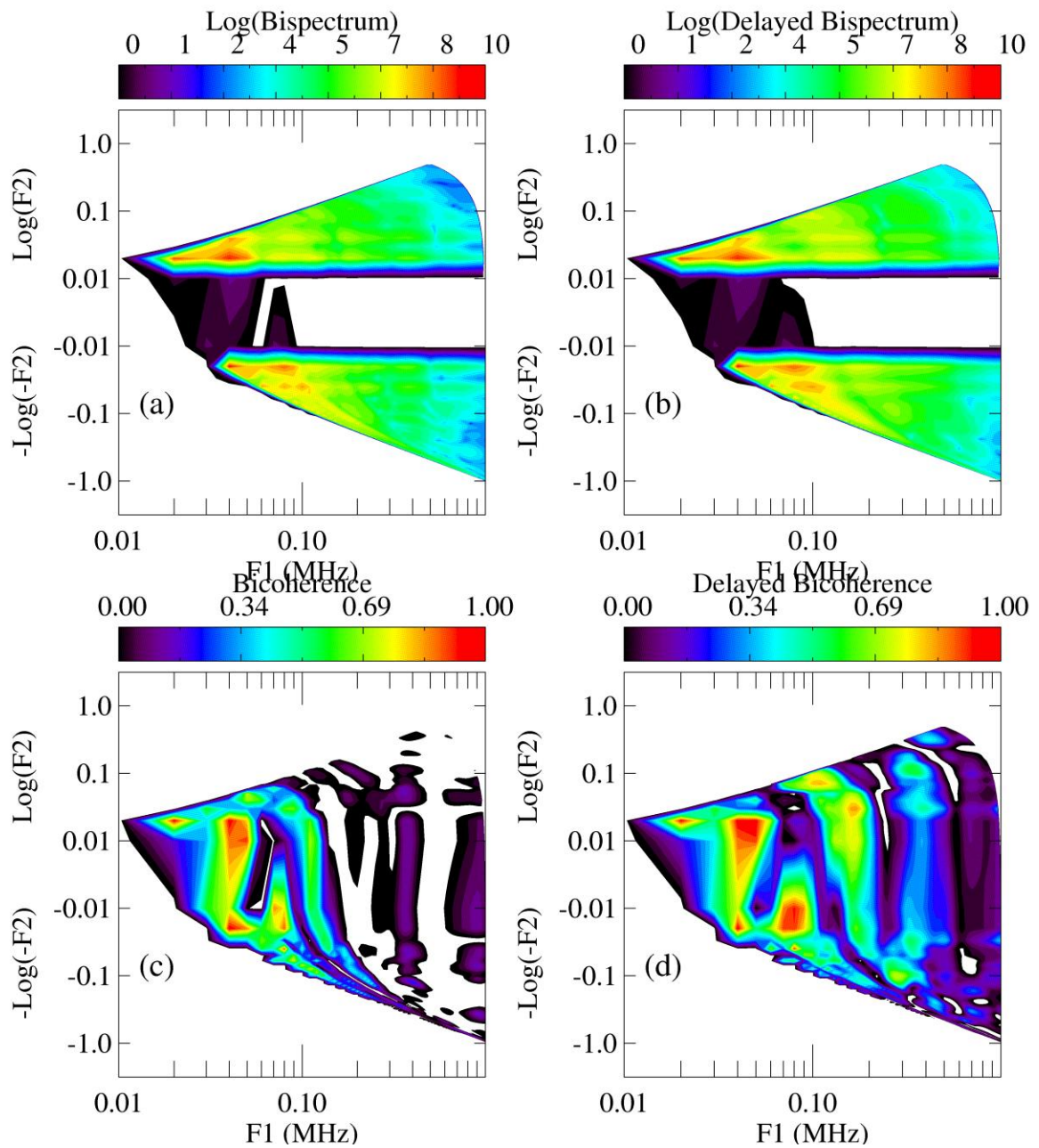


Figure 5.7: Same as Figure 5.6, but with linearly spaced frequencies.

Chapter 6: Basic Plasma Parameters

This chapter describes the measurable quantities that characterize the plasma in the Irvine Field Reversed Configuration (IFRC). General quantities covered in this chapter are the magnetic and electric fields, currents, temperature, and particle fluxes. Particular emphasis is placed on the time evolution of the two dimensional structures listed above. A summary of the general plasma parameters are listed in Table 6.1. Data in this chapter is taken from the *NCP* and *FCUP* datasets, encompassing a total of 233 shots.

Magnetic Field	$ B $	300 Gauss
Magnetic Pressure	$B^2/8\pi$	3.6E4 Pa
Plasma Density	n_0	5E14 cm ⁻³
Plasma Temperature	$T_e T_i$	~ 3eV
Average Beta	$8\pi\langle n(kT_e+kT_i)\rangle/\langle B^2\rangle$	~0.2 →0.6
Plasma Current	I_p	15 kAmps
Azimuthal Electric Field	E_θ	250 V/m

Table 6.1: Plasma Parameters

It will be shown that a field-reversed configuration is formed and maintained for approximately 50 microseconds, with closed flux surfaces and a large toroidal plasma current. A magnetic field in the toroidal direction, with strong axial and radial gradients is identified, as well as the radial and axial current densities that must be present. Large

particle losses are quantified by the Faraday cups with a total number of particles that is of the same order as the particle inventory.

6.1 Magnetic Fields

Magnetic fields in the IFRC are measured by the previously described arrays of B-dots that are placed at various locations in our plasma. The processes by which we convert voltages into estimates of the magnetic field at each probe location are summarized by Figure 6.1 and have been covered in depth in Section 4.1 and Chapter 5.

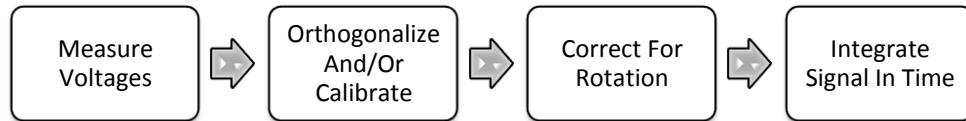


Figure 6.1: Process steps for magnetic measurements

Figure 6.2 shows the time evolution of the axial component of the magnetic field at the midplane ($z = 0$) and many different radial positions. The data come from the radial B-dot array and show the main features in the life and death of our field reversed configuration. The evolution can be broken into five phases, as shown in Figure 6.2 and Table 6.2. The first section is due to current discharge in the limiter coil, which produces predominantly axial fields, with some curvature near the ends of the limiter coil. Phase 2 captures the dynamic formation of the plasma current and its rapid evolution in time and space. Phase 3 shows a relatively stable field reversed configuration, which lasts for approximately 40 μs , after which the plasma currents and related magnetic fields begin to change their positions and magnitudes in Phase 4. Currents are still flowing in the limiter

coil after the plasma current is gone; Phase 5 records these field structures up to the end of our acquisition period.

Phase 1	Background Field Begins Ramping	0→19 μs
Phase 2	Fields Begin Reversal	19→27 μs
Phase 3	FRC Equilibrium	27→68 μs
Phase 4	FRC Decay	68→100 μs
Phase 5	Background Fields	100→End μs

Table 6.2: FRC Phases

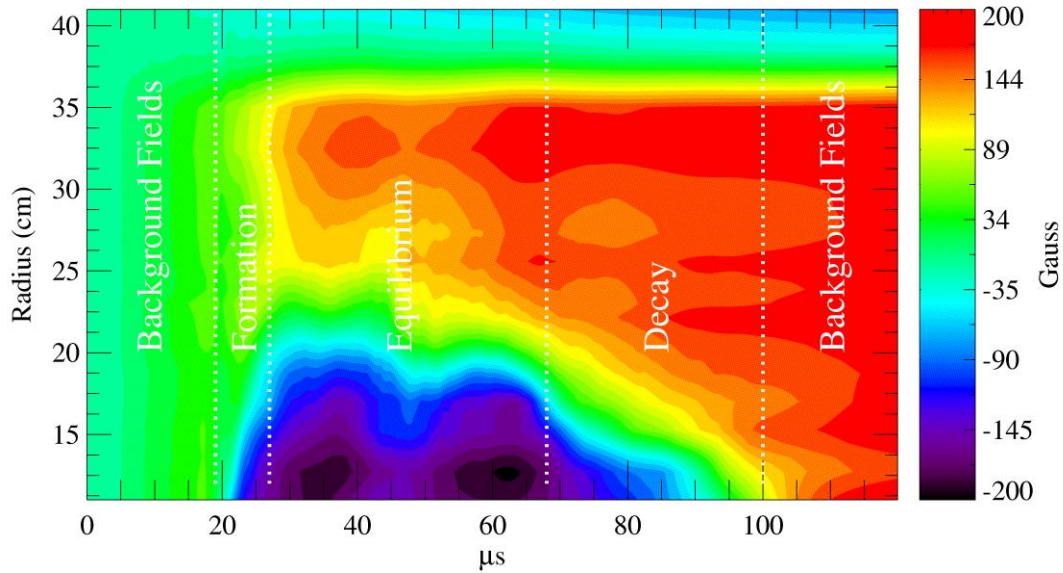


Figure 6.2: Evolution of the axial magnetic field at the midplane

The topology of the IFRC magnetic field, illustrated in Figure 6.3, is essentially that of a torus. The large plasma current flows primarily in the $-\hat{\theta}$ direction and can be thought of as a solenoidal current distribution. Field lines wrap around nested surfaces that are centered on the plasma current. The fields that the plasma current creates are approximately equal in magnitude to those created by the limiter coil, and point in the opposite direction. The inner solenoid threads through the center of the ‘doughnut’, while the limiter coil encloses it.

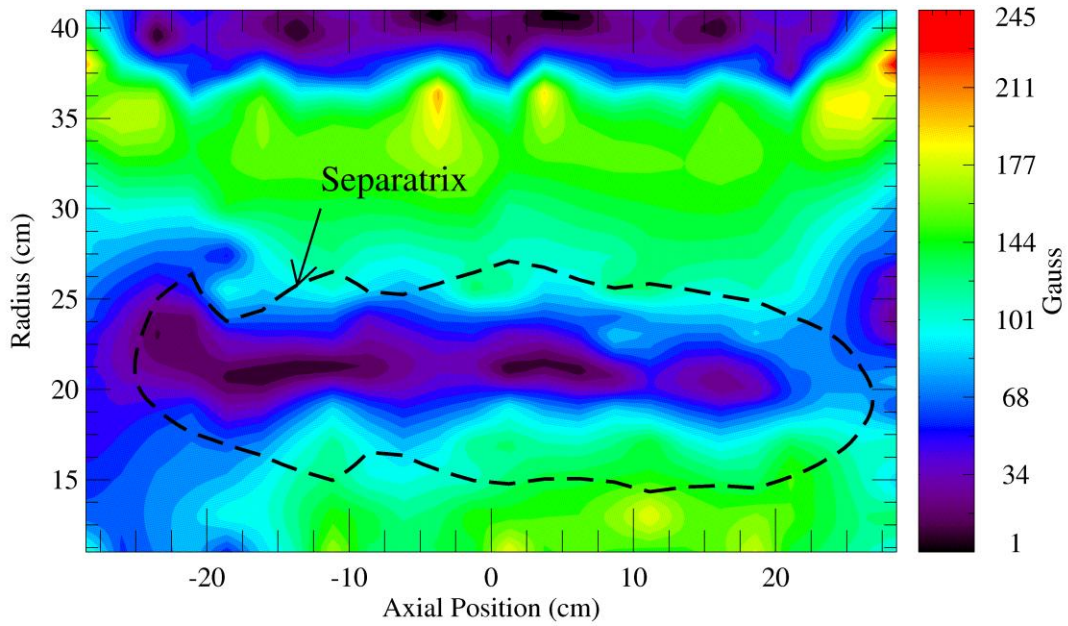


Figure 6.3: Magnitude of B at 43 microseconds

A quantity that defines the center of the FRC is the null position. The null position is the region near the radial center of the FRC where the current is largest and no magnetic fields are present. The radial location of the null at each axial and time position is estimated by finding points where the axial magnetic field changes signs from negative to positive. Multiple points where this criterion is satisfied are averaged together, in order to account for a current distribution with distinct radial peaks that are spaced near together. The end result is a list of (z, r) coordinates at each time period that map out the approximate peak of the azimuthal current. The null position is shown in Figure 6.4 at 43 microseconds, overlain on contour plots of the three magnetic field components. It has a rough correspondence with dividing lines in the B_θ and B_r plots.

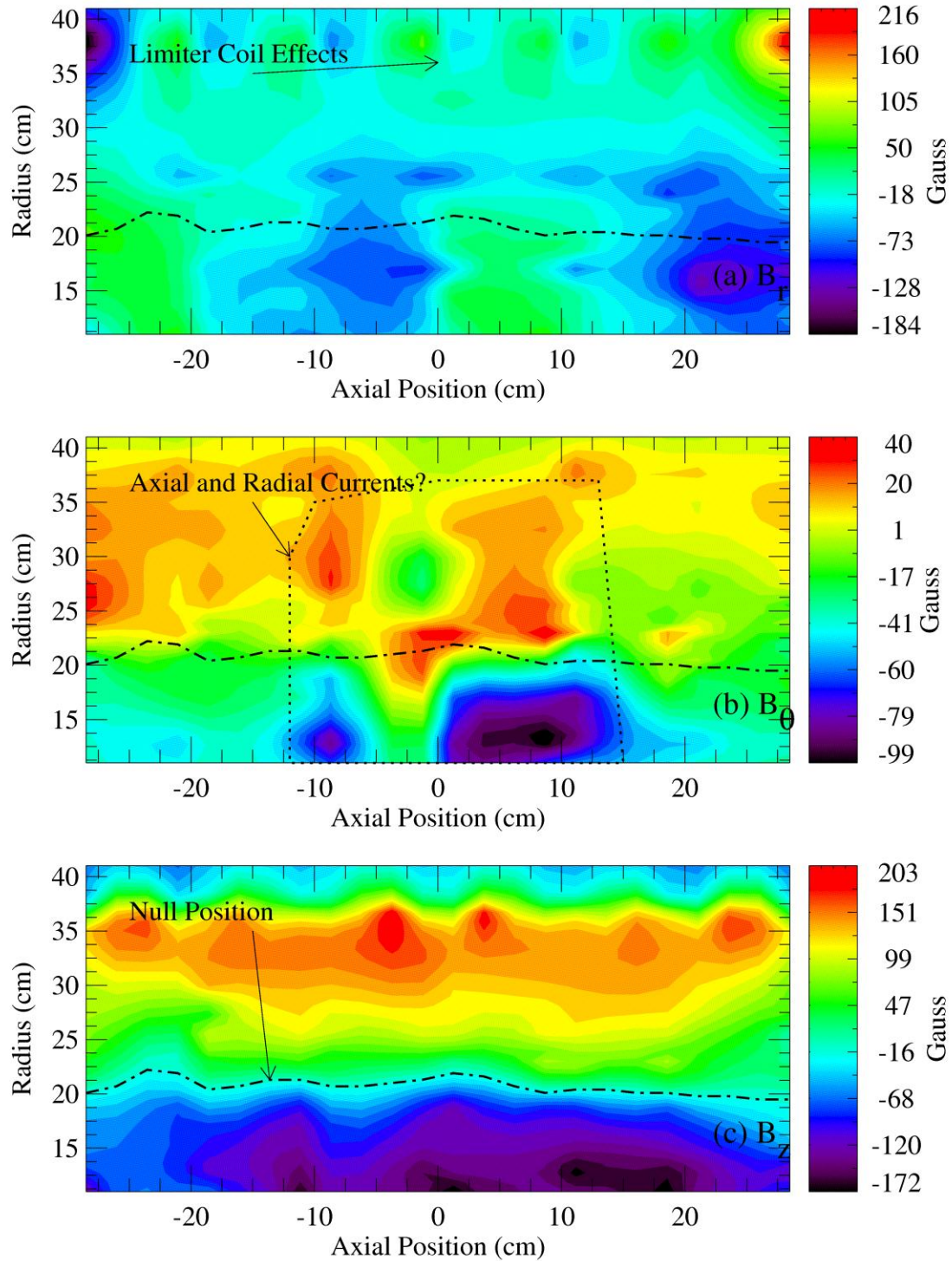


Figure 6.4: Magnetic field components (a) B_r , (b) B_θ and (c) B_z at 43 microseconds. Note especially the strong spatial variation of the toroidal magnetic field.

FRCs are generally assumed to have zero toroidal magnetic fields. The Irvine FRC does however have significant periods where there are dynamic changes in the

structure of B_θ as a function of position and time. The radial structure of B_θ is of particular interest, as this indicates the presence of non-azimuthal currents. These fields have been seen in other devices^{17 19 36}, and are possibly caused by the Hall effect.³⁸ The question naturally arises: What are the characteristics of the B_θ field, its associated current distribution, and possible sources of this non-ideal feature in the IFRC?

Figure 6.4 (b) shows the dataset averaged magnetic field structure of B_θ as a function of axial and radial position at 43 microseconds. This time is approximately 15 microseconds into the equilibrium phase of the discharge. Figure 6.2 shows that the axial magnetic field component is relatively stable at this time period, while Figure 6.3 shows the nested contours and general symmetry of the axial and radial field structure. The field structure of B_θ has an odd radial symmetry about the null position. This indicates that if axial currents are the sole source of the azimuthal magnetic fields, then the radial position of those currents is at approximately the same position as the toroidal current that forms the reversed axial fields. The axial symmetry of B_θ is not as obvious as its radial symmetry. This implies that if radial currents are responsible for the azimuthal field structure, their axial distribution is not centered on one sole position. For more discussion and plots of the derived current densities, see Section 6.3.

One way of characterizing the nature of the azimuthal magnetic field is by studying the spatial size of the amplitude variations at a particular time. The radial and axial scale lengths of B_θ are shown in Figure 6.5, and are produced by performing a two dimensional wavelet transform on the azimuthal field data at each time period. The result

of this analysis is a three dimensional array of the distribution of power as a function of radial scale length, axial scale length, and time. Figure 6.5 (a) shows the distribution of power at 43 microseconds. The dominant axial scale length is about 20 cm, with a bimodal radial distribution, centered on radial scales of approximately 13 and 26 cm. The scales are logarithmically spaced, with scale ranges of 0.6 to 29.5 cm in the radial direction and 4.9 to 55.4 cm in the axial direction. It is possible that the feature at a radial scale of 13 cm is an alias of the 26 cm feature, though the scale resolution is high enough to resolve both features. Figure 6.5 (b) is sum of the power distribution throughout the IFRC lifetime, with the same axial and radial scales as Figure 6.5 (a). The time period over which the signal is averaged is from 20 to 100 microseconds. The machine size is reflected in the power distribution, with a concentration of B_θ at radial and axial scales of 26 and 55 cm respectively. There is a large distribution in scales however, indicating that the processes that create the azimuthal field vary considerably in their spatial extent over the IFRC lifetime.

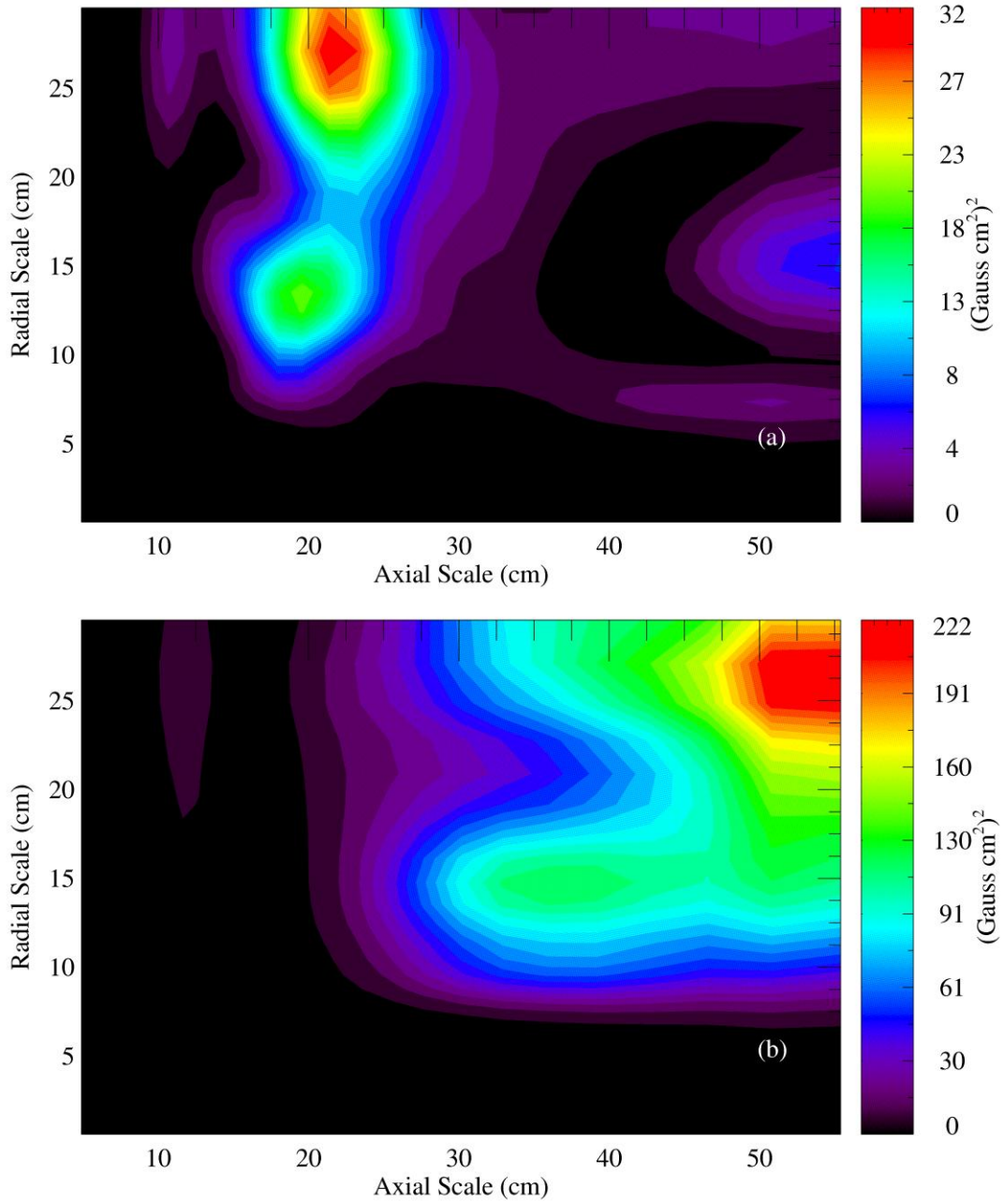


Figure 6.5: (a) B_θ scale lengths at 43 microseconds. (b) B_θ scale lengths averaged over the FRC lifetime.

A possible mechanism by which the azimuthal fields are generated is an oscillation in direction of the main plasma current. This current is predominately in the $-\hat{\theta}$ direction, but it is possible that it has a ‘wobble’ that periodically points in the axial direction. This axial component J_z of the current can be modeled as

$$J_z = \mathbf{J} \cdot \hat{z} \sim J_\theta \cos\left(\frac{2\pi t}{T_b}\right), \quad (6.1)$$

where T_b is a bounce period and J_θ is the azimuthal current. Figure 6.6 is a contour plot of B_θ data from shot 5672, which is located near the midplane at $z = -1.5\text{cm}$. Clearly visible are the periodic changes in magnetic field polarity at various radial positions. The bounce period for this shot is approximately 25 microseconds, with a total of at most two bounces before the FRC dies at about 80 microseconds.

Further evidence that the oscillations in B_θ are due to axial bounces of the azimuthal current is the radial anti-symmetry of the magnetic field about the null position. This indicates that for this shot at least, the center of the current channel that created the azimuthal magnetic field structure was located at approximately the same radial position as the current that created the axial fields.

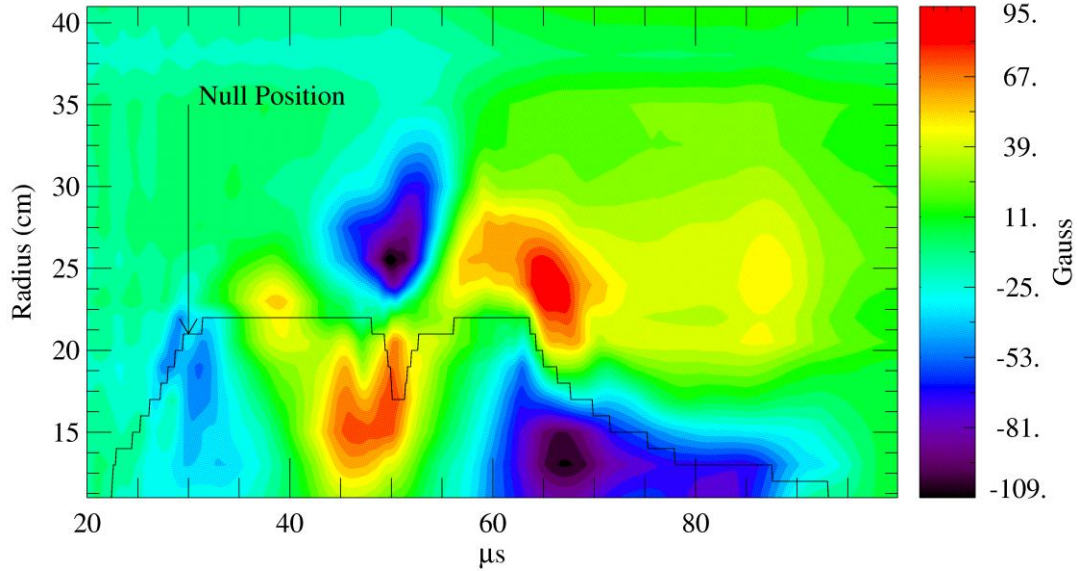


Figure 6.6: B_θ data from shot 5672. Approximate B_z null position is overlain for reference.

Variations of the wobble period in time can be captured in an average sense by summing the wavelet spectrogram over a number of probe locations. Figure 6.7 is a contour plot of the result of this technique; it illustrates the evolution of the distribution of B_θ from predominately long periods at the beginning of the FRC to a broad distribution of periods, and back again. The averaging region for this plot is a rectangular portion of the plasma volume from $z = -8.5 \rightarrow 8.5$ cm, and from $r = 11 \rightarrow 27.5$ cm, with a total of 605 probe instances used to create the plot.

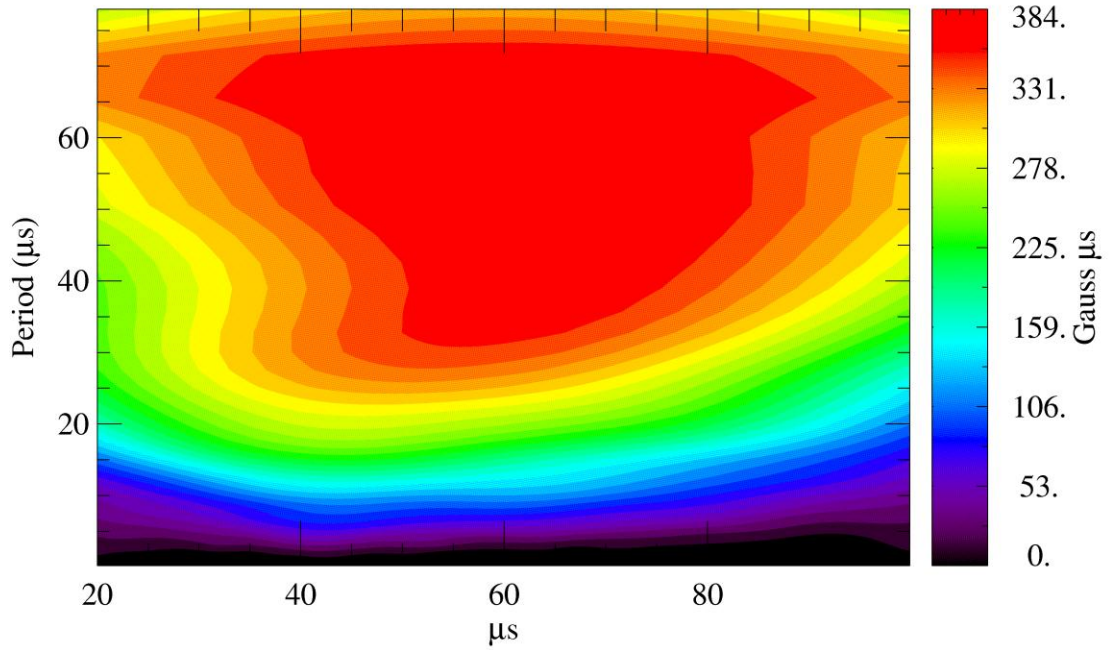


Figure 6.7: Evolution of average B_0 spectrogram, with the period being defined as the inverse frequency.

The average bounce period as a function of time for each shot in the dataset is calculated by

$$T_b = \frac{\int_{f_{min}}^{f_{max}} \frac{1}{f} WV(t, f) df}{\int_{f_{min}}^{f_{max}} WV(t, f) df}, \quad (6.2)$$

where $WV(t, f)$ is the wavelet transform of data from each individual probe. The various periods are plotted in Figure 6.8 in color, with the ensemble average and standard deviation of the entire dataset plotted in white. There is a large variation in bounce periods in the dataset, with periods ranging from 20 to 65 microseconds. The overall trend is a decrease in the period from 20 to ~ 40 microseconds followed by a constantly slowing bounce period as time increases.

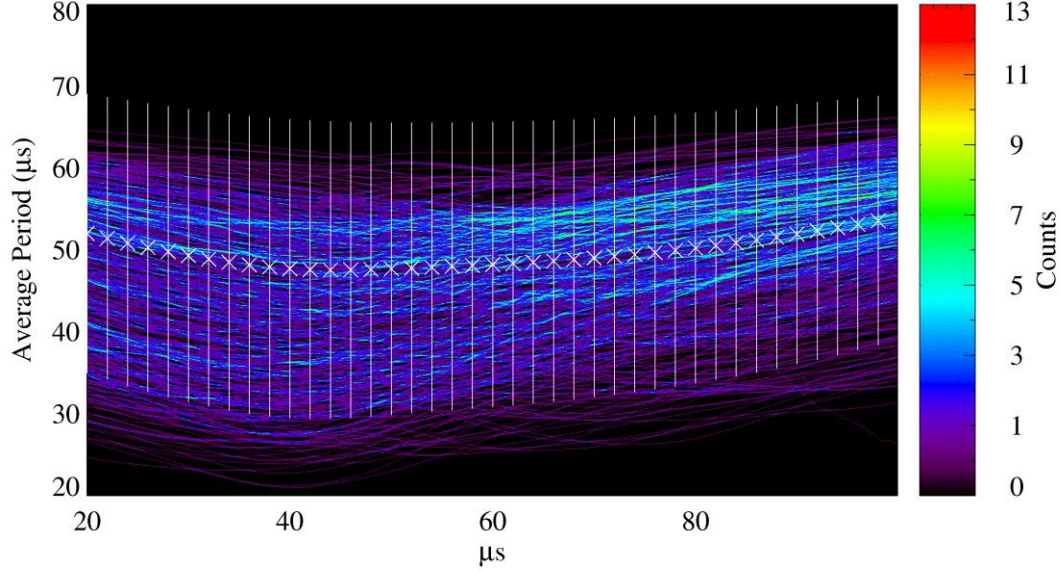


Figure 6.8: Average period of B_θ for the entire dataset.

6.2 Magnetic Flux

Axial magnetic flux surfaces are a complementary way to view and analyze the IFRC temporal and spatial evolution. The axial flux Φ at each position and time is derived from knowledge of the axial magnetic field values; this is written mathematically as

$$\Phi(Z, R, t) - \Phi(Z, r_a, t) = \int_{r_a}^R B_z(Z, r, t) * 2\pi r dr. \quad (6.3)$$

Integration is done in the radial direction, with the integrand being the axial magnetic flux B_z through an annulus of radius r at axial position z at time t . There is a constant of integration that must be defined for the magnetic flux in our system to be completely determined. This constant, denoted by $\Phi(Z, r_a)$, is the value of the flux at the point of a flux loop probe. The flux loops measure the time rate of change of the axial magnetic

flux; upon integration in time, we can use this derived flux as a boundary condition and uniquely specify the flux as a function of axial position, radial position, and time.

A minor problem with finding the boundary condition for the magnetic flux is that we only have three flux loops to provide local flux measurements. A key assumption that we make is that the axial magnetic flux is approximately constant just outside of the flux coil. Local magnetic field measurements do indicate that the fields are nearly all in the axial direction at that radial position. Flux loops measurements around the flux coil were attempted; each probe was destroyed as soon as plasma discharges were attempted, probably due to the large electric field with plasma shorting out the circuit.

The program that calculates the magnetic flux consists of the following steps. We first integrate radially each two dimensional spatial snapshot of the axial magnetic field; this produces the correct radial shape of the axial magnetic flux at each z position. The flux at each axial position must be shifted by some constant value to account for the flux that passes at radii less than our innermost probe. Our assumption of straight field lines at small radii allows us to need only one boundary condition for the flux. A flux loop near the midplane gives us the required constant by which we must shift our two dimensional flux map.

Figure 6.9 is a plot of the axial flux as a function of axial and radial position at 43 microseconds. The FRC is centered on the minimum value of the axial flux, and its extent can be estimated by the largest closed flux surface. This surface, called the

separatrix, has a constant value of Φ and does not intersect any external boundaries. The separatrix defines the boundary between regions of open and closed magnetic field lines, and roughly delineates the regions where the external currents are dominant from those where the plasma current is the main driver. An IDL program called *contour* outputs the (z, r) coordinates of each contour from a two dimensional plot, and also notes whether or not the contour path exits the plotting region. The separatrix is estimated numerically by finding the closed axial flux contour that has the maximal cross sectional area.

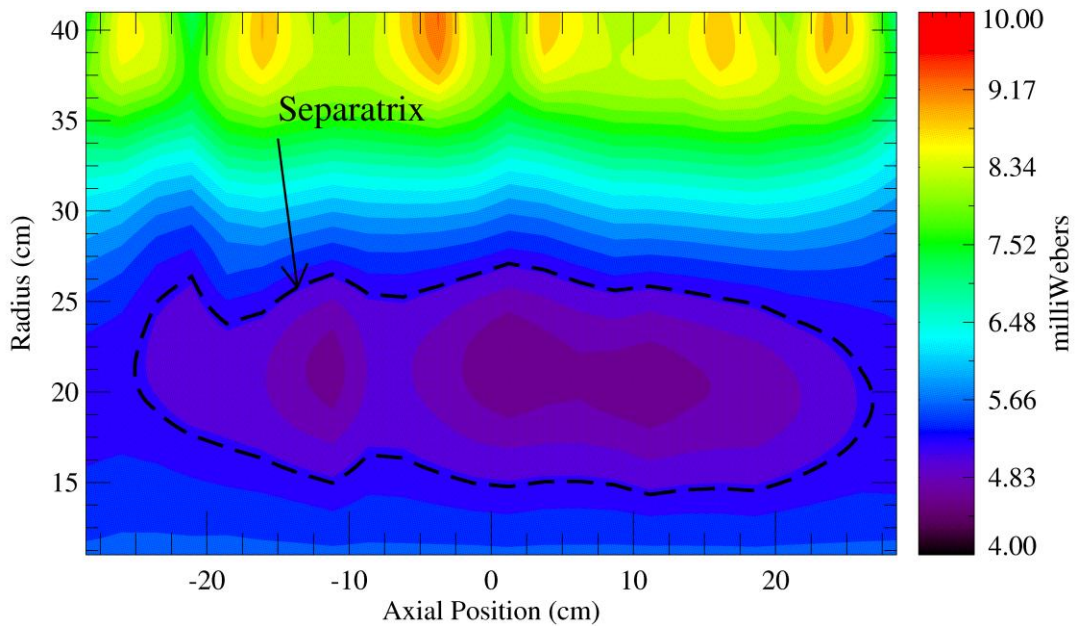


Figure 6.9: Axial Magnetic Flux At 43 Microseconds

So-called ‘sanity checks’ are very useful when combining data from different probes. One such check is to compare fluxes measured by the combination of the flux loops and B-dot probes to estimates of the fluxes produced by the measured currents that flow through our different field coils. To do this, the flux coil and limiter coil are modeled as a series of current loops that closely approximate their actual positions. Analytic expressions for the radial and axial magnetic fields can be numerically evaluated

for the simulated current rings to help us find the fluxes at any particular point for a given current. These constants can then be used in conjunction with the actual measured currents to find what the magnetic fluxes should be in the absence of plasma.

The flux coil is modeled by 80 current rings, spaced axially every 1.25 cm with a radius of 10 cm. Each ring carries $\frac{1}{4}$ of the total current, as the flux coil is formed by four wires in parallel. The limiter is simulated by six groups of six rings. All limiter rings have a radius of 38 cm; rings in each group are spaced 1 cm apart from each other, with the center of each group separated by 10 cm from the next. The currents flowing in the six groups were measured while the machine was open, and used to find the division of the total current between the six straps. The radial and axial magnetic fields and axial fluxes are then found at many axial and radial positions for an input current of one ampere per coil. Figure 6.10 illustrates the structure of the measured and simulated magnetic field magnitudes with both the flux and limiter coils discharging. Note in particular the radial and axial similarities. The comparison is completed by measuring the actual fluxes produced by the limiter and flux coils, and normalizing them by the currents that produce them. Figure 6.11 shows the different profiles at the axial midplane as a function of radius. The overall trends are similar; however the actual magnitudes do differ by a significant percentage, especially in the case of the limiter coil flux profile. The differences are most likely due to the lack of inclusion of the large metal end plates. Induced mirror currents in these plates are likely to alter the flux profiles from their theoretical values.

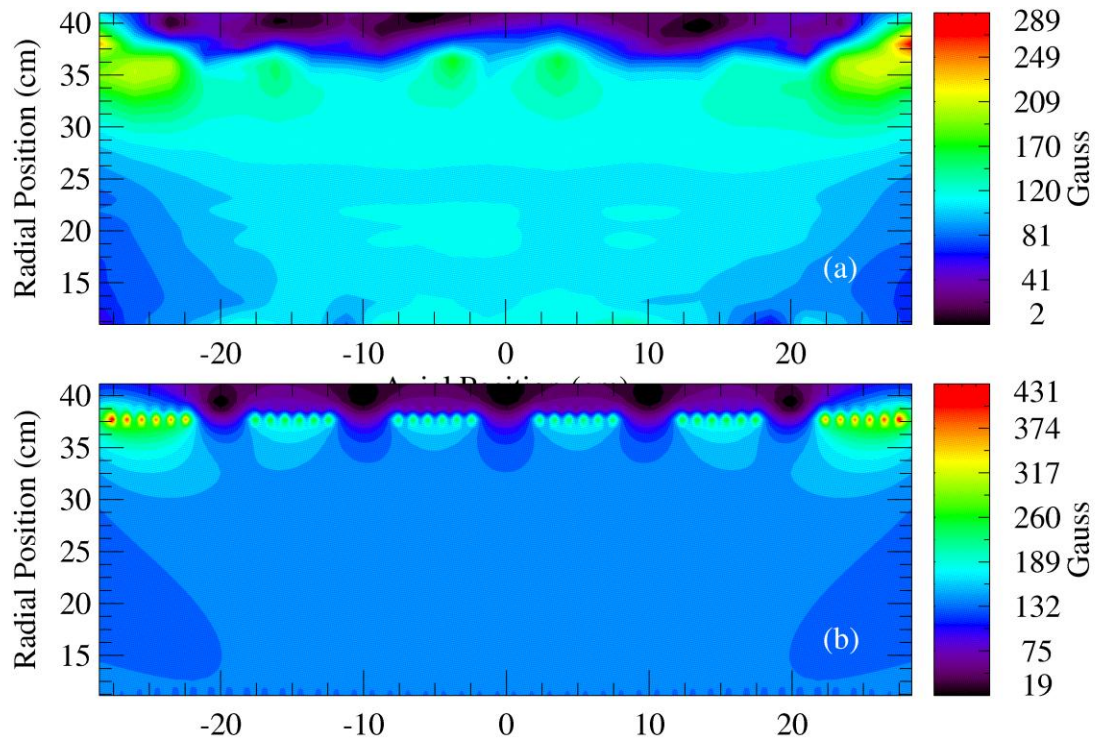


Figure 6.10: (a) Measured and (b) analytic magnetic field magnitudes

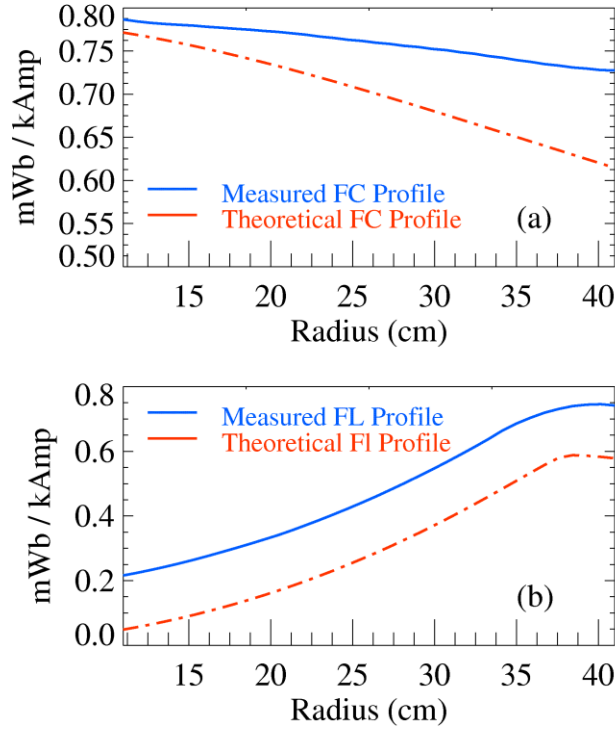


Figure 6.11: (a) Theoretical and measured axial flux profiles produced by the flux coil at $z = 1.5$ cm. (b) Midplane theoretical and measured flux profiles for the limiter coil. Note: experimental measurements are made with no plasma present.

A way to visualize the response of the plasma to the flux coil is by plotting the excluded flux, Φ_{ex} . This is the difference between the flux without plasma and the flux with plasma, written as

$$\Phi_{ex}(z, r, t) = \Phi_0(z, r, t) - \Phi_{plasma}(z, r, t). \quad (6.4)$$

Here, Φ_0 is the flux from the field coils without plasma and Φ_{plasma} is the measured flux during a plasma shot. This can be found for all points where magnetic field measurements are made. Radial distortions of the flux profiles are evident in Figure 6.12(a); this becomes even clearer in Figure 6.12(b). The excluded flux shows that the plasma is quite a good conductor and has an inner boundary very near the flux coil radius.

Another way to estimate the excluded flux is by finding the amount of flux contained inside the separatrix. This is written as

$$\Phi_{ex}(z, r, t) = \Phi_c(z, t) - \Phi_{plasma}(z, r, t), \quad (6.5)$$

where Φ_c is a measurement of the flux at the separatrix position which is assumed to lie along the flux coil. Figure 6.12(c) is a plot of the flux inside the separatrix, and has a similar magnitude and spatial-temporal profile as Φ_{ex} in Figure 6.12(b).

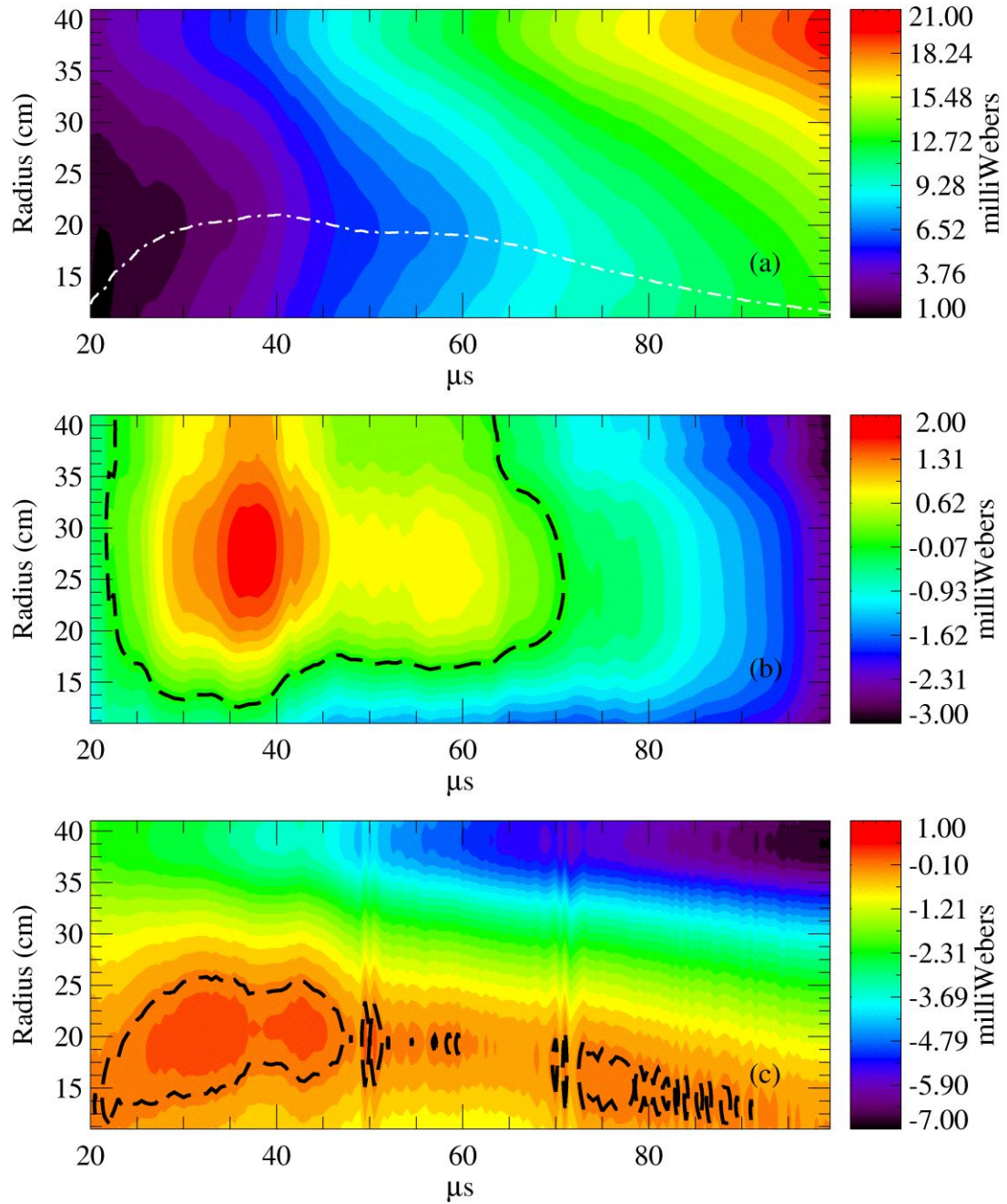


Figure 6.12: (a) Time evolution of the axial flux Φ_{plasma} at the midplane with null position. (b) and (c) Evolution of Φ_{ex} measured by two different methods, with a dashed line at the contour of zero milliWebers.

6.3 Current Density

Distributions of current in space give rise to the magnetic fields that we measure. Much information can be discovered by inverting our magnetic measurements to find the current density distribution in our plasma.

The current density J is related to the magnetic field B by Ampere's Law,

$$\nabla \times \mathbf{B} = \mu_0 \mathbf{J}. \quad (6.6)$$

We may neglect the displacement current, as it is many orders of magnitude smaller than the free current. The terms in the curl on the left hand side are listed in Table 6.3. Derivatives in the $\hat{\theta}$ direction cannot be determined, as we do not have probes that are positioned at different azimuthal positions. Inspection of the curl terms shows us that only the current density in the $\hat{\theta}$ direction is possible to find completely, given our diagnostic limitations.

Curl Component	Direction	Possible To Find?
$\frac{1}{r} \frac{d}{dr} (r B_\theta)$	\hat{z}	Yes
$\frac{1}{r} \frac{d}{d\theta} (B_r)$	$-\hat{z}$	No
$\frac{d}{dz} (B_r)$	$\hat{\theta}$	Yes
$\frac{d}{dr} (B_z)$	$-\hat{\theta}$	Yes
$\frac{1}{r} \frac{d}{d\theta} (B_z)$	\hat{r}	No
$\frac{d}{dz} (B_\theta)$	$-\hat{r}$	Yes

Table 6.3: Curl components of \mathbf{B} in cylindrical coordinates

The inputs to the $+\hat{\theta}$ component of the current density calculation are the interpolated two dimensional B_r and B_z arrays at each time slice. Derivatives are calculated with the *deriv* function in IDL, which performs the numerical differentiation

by 3-point Lagrangian interpolation. Once the appropriate derivatives are calculated, both two-dimensional arrays are added together to produce the current density array. This process is repeated for all different time periods; the result of this calculation is a three-dimensional array of the current density J_θ as a function of axial position, radial position, and time.

Figure 6.13 shows a plot of the current density at 43 μs . Prominent features include the plasma current near the midplane with a center at approximately 20 cm. Also visible are the currents that are flowing in the limiter coil at a radius of 38 cm. The current ring is obviously broken into multiple filaments that are separated axially from each other. This may be an artifact due to the sampling points at which the fields are measured, or may be an actual measurement of main ring splitting into several smaller rings.

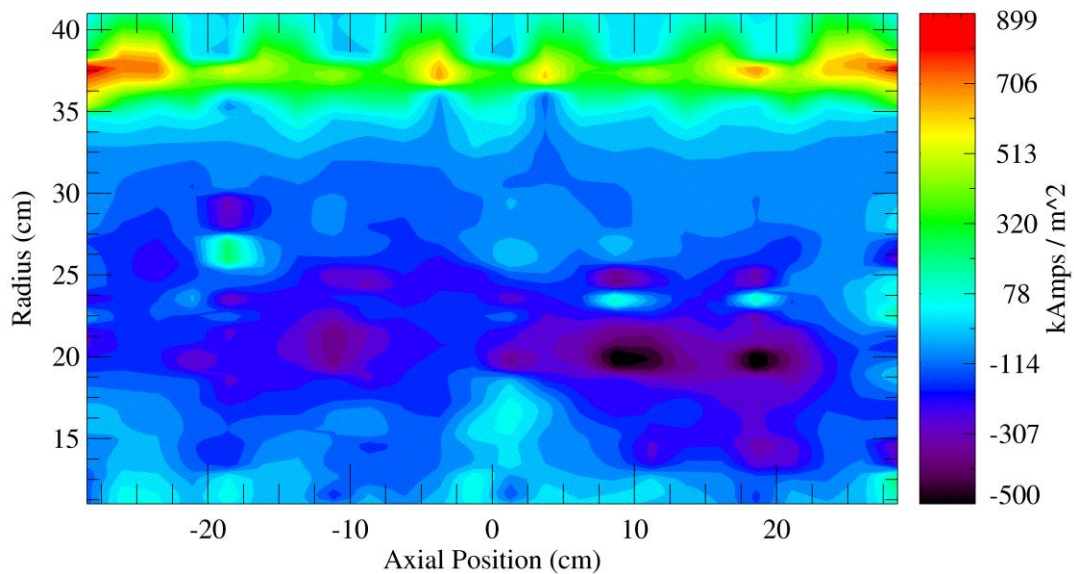


Figure 6.13: J_θ in the z-r plane at 43 microseconds.

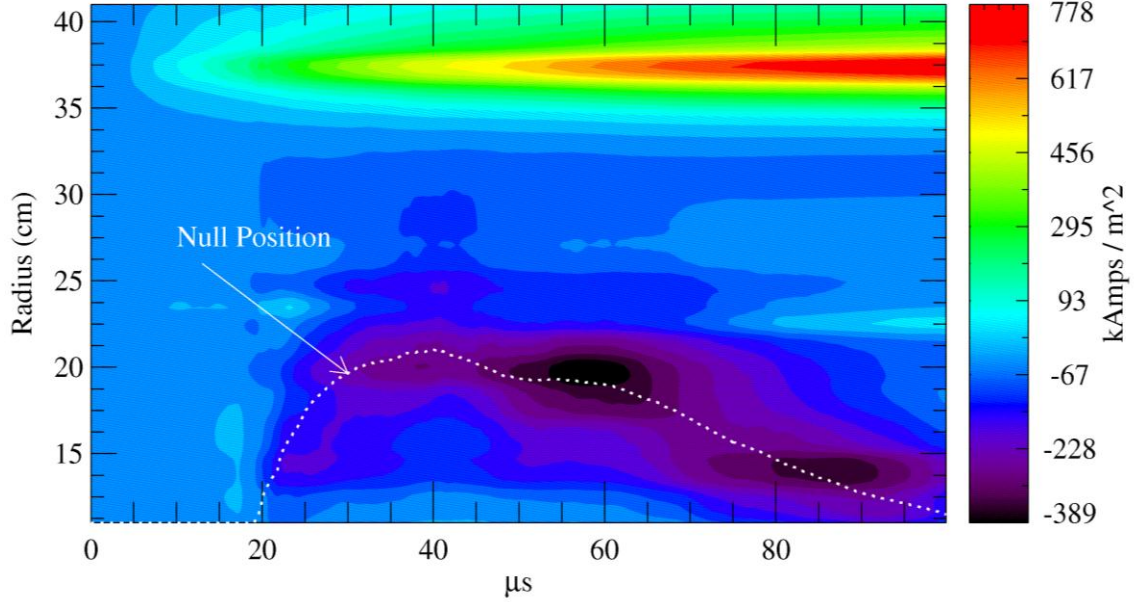


Figure 6.14: Axially averaged J_θ as a function of time and radial position

Figure 6.14 is a contour plot of the axially averaged J_θ , produced by

$$\bar{J}_\theta(r, t) = \frac{1}{z_{max} - z_{min}} \int J_\theta(z, r, t) dz. \quad (6.7)$$

The center of the current distribution in the $-\hat{\theta}$ direction lines up well with the estimation of the null position. Features to note are the rapid radial motion outwards of the current channel, with a velocity approaching $1 \text{ cm}/\mu\text{s}$, as well as the constant increase of the current carried by the limiter coils, located at $r = 38 \text{ cm}$. The current density stays increases only slightly after reaching its maximal radial position, which can be explained by a balance between the driving electric field from the flux coil and the electric field produced by the plasma resistivity. It is possible that the currents supplied to the limiter coil became too large for radial pressure balance to be maintained, which led to the subsequent implosion from 50 microseconds on to the time of FRC death near 90 microseconds. It is likely that clamping the limiter current's magnitude at 50 microseconds with a crowbar would have extended the FRC lifetime.

Another ‘sanity check’ that is done is a comparison between currents calculated from B-dot measurements and currents measured by other devices. Our main Rogowski coil measures the plasma current I_p , while a smaller Rogowski coil monitors the current $I_{limiter}$ that flows through the limiter coil. The integration of the current density J_θ over the plasma cross section A gives a second estimate of the total toroidal current I_θ . The two methods, written as

$$\int_A J_\theta(z, r) dA = I_\theta = I_p + I_{limiter} , \quad (6.8)$$

should equal each other if everything is working properly. As Figure 6.15 shows, the two different methods of measuring currents in our plasma agree quite well with each other. Integration over the two dimensional space of the current density provides the best agreement to the actual measured currents, and should be used rather than a simple summation formula in similar situations where double integration is desired.

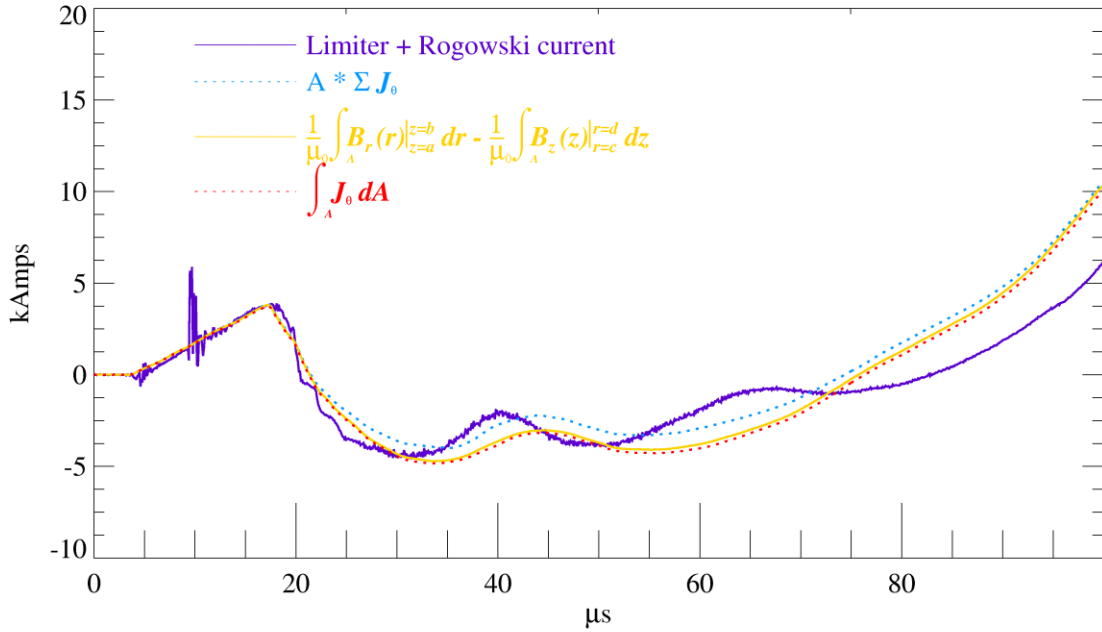


Figure 6.15: Comparison of toroidal currents measured directly and inferred from magnetic field measurements. Three methods of current estimation from magnetic field measurements are shown.

Radial and axial current densities are not present in the classical picture of an FRC, as they indicate deviations from purely poloidal magnetic fields. It should not be assumed however that these currents are zero, especially when experimental data exist that can confirm or deny their presence. Missing toroidal gradients in B_r and B_z do not allow for a complete calculation of J_z and J_r . It is probable however that the toroidal variations of these quantities are small, which implies that the axial and radial currents are primarily determined by the axial and radial gradients of B_θ . Limits can be put on the magnitudes of J_z and J_r by estimating the amount of charge that enters the plasma volume as a function of time. This is done by modeling several different charge distributions in our plasma and comparing the potentials that are created to an actual measurement of the plasma floating potential. If the currents flowing into the plasma calculated solely from

variations in B_θ are sufficient to account for the charge build up in the plasma, we can discount the missing gradient terms entirely.

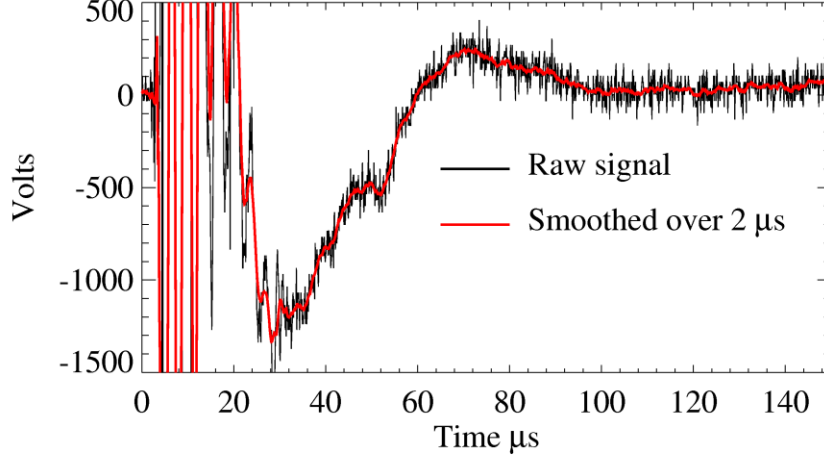


Figure 6.16: Floating potential measurement

The first model for the charge distribution in our plasma is a constant density distributed over the plasma volume. The potential V due to this can be written as

$$V = \frac{\rho_0}{\epsilon_0} \int \frac{rdrd\phi dz}{\sqrt{(z - z_0)^2 + r^2 + r_0^2 - 2rr_0\cos(\phi - \phi_0)}} \quad (6.9)$$

where ρ_0 is the charge density, ϵ_0 is the vacuum permittivity, the coordinates of the reference point are (r_0, ϕ_0, z_0) , and the integral is done from $r = 0.11 \rightarrow 0.38$ m, $\phi = 0 \rightarrow 2\pi$ radians, and $z = -0.3 \rightarrow 0.03$ m. Evaluation of this integral with a reference point of $(r_0, \phi_0, z_0) = (0.25, 0, 0.5)$ and a sample charge density of $1 \frac{C}{m^3}$ results in a potential of approximately 4.8×10^{10} volts. Since we measure a floating potential that is -1000 volts or less, the actual charge density must be approximately $-20 \frac{nC}{m^3}$. This equates to a charge density imbalance of about $10^{11} e^- / m^3$, for a total charge in our plasma volume of about -5 nC.

The second model consists of a Gaussian distribution in both the axial and radial directions. Mathematically, this charge distribution is written as

$$\rho(r, z) = \rho_0 \exp\left(-\frac{(r - 0.25)^2}{2 * 0.07^2} - \frac{(z)^2}{2 * 0.15^2}\right). \quad (6.10)$$

The potential from this charge distribution is once again found by integration over the plasma volume, written as

$$V = \frac{1}{\epsilon_0} \int \frac{\rho(r, z) r dr d\phi dz}{\sqrt{(z - z_0)^2 + r^2 + r_0^2 - 2rr_0 \cos(\phi - \phi_0)}} \quad (6.11)$$

For this charge distribution and the same reference point of $(r_0, \phi_0, z_0) = (0.25, 0, 0.5)$, the peak charge density ρ_0 must be approximately $-64 \frac{nC}{m^3}$ to satisfy the floating potential measurement. This is equivalent to an imbalance in ions to electrons of about $4 \times 10^{11} e^- / m^3$ and a total charge in the plasma volume of -16 nC.

Both sample charge distributions give charge densities of the same order of magnitude for the measured floating potential voltage. The charge imbalance is also very small compared to the total plasma density, which is on the order of $10^{20} m^{-3}$.

The net current entering the plasma volume should be proportional to the time rate of change of the floating potential. Since we know that the total plasma charge is on the order of 10^{-8} Coulombs, and the peak rate of change is about 10^{-5} electrons/s, the peak current flowing into the plasma can only be approximately 10^{-3} Amperes. This is very small compared to the plasma current that forms the FRC, which has a peak magnitude of

more than 10^4 Amperes. This strongly suggests that any large calculated current densities in the radial and axial directions must be due to the lack of inclusion of toroidal gradients.

Figure 6.17 shows the total currents into two test volumes based on the incomplete calculations of J_r and J_z . The first test region encompasses the entire volume between the limiter and flux coils, with a surface area of 1.84 m^2 . Its axial and radial limits are $\pm 28.5 \text{ cm}$ and $11 \rightarrow 38.5 \text{ cm}$ respectively. The second encloses a smaller volume with $z = \pm 23.5 \text{ cm}$ and $r = 12.7 \rightarrow 36.7 \text{ cm}$, for a total area of $\sim 1.45 \text{ m}^2$. The calculated total currents into these volumes are much larger than the limits imposed by floating potential measurements; however, the average current densities at the two surfaces of 2.2 kA m^{-2} at A_1 and 1.7 kA m^{-2} at A_2 are both less than one percent of the maximum current density. This implies that the toroidal gradients are not necessary to include for a quantitative description of the current densities in the axial and radial directions near the plasma center, since the input currents at A_2 match the constraints placed on them.

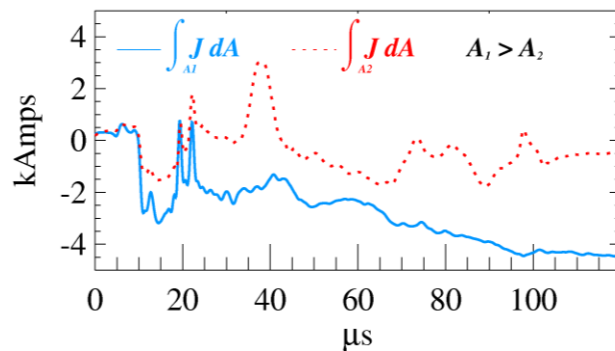


Figure 6.17: Total currents flowing into the plasma volume.

Figure 6.18 shows J_r and J_z at 43 microseconds. The current densities are calculated from the interpolated values of B_θ , and then smoothed in software, with axial,

radial, and temporal averaging of 3, 5, and 20 points respectively. This corresponds to averaging over 7 cm axially, 2 cm radially, and 2 microseconds in time. Local values of these current densities are comparable in magnitude to J_θ . Prominent features at this time include a large axial current density near $r = 20$ cm, with return currents at $r \sim 25$ cm and $r \sim 15$ cm. Also clearly visible in the axial current density plot are contributions from the limiter coil at some axial positions. This is most likely due to an incomplete or inaccurate rotation matrix calculation, though it is possible that axial currents are flowing along open field lines. The radial current density plot has regular axial and radial features. It is anti-symmetric about the point $(z, r) \sim (0, 25)$. This point corresponds to the axial center of the magnetic field null region, where the current and density are at their maximum values. This has been seen on other experiments^{19 36 37} and simulations^{38 39} and could be due to the Hall effect for a radial current.

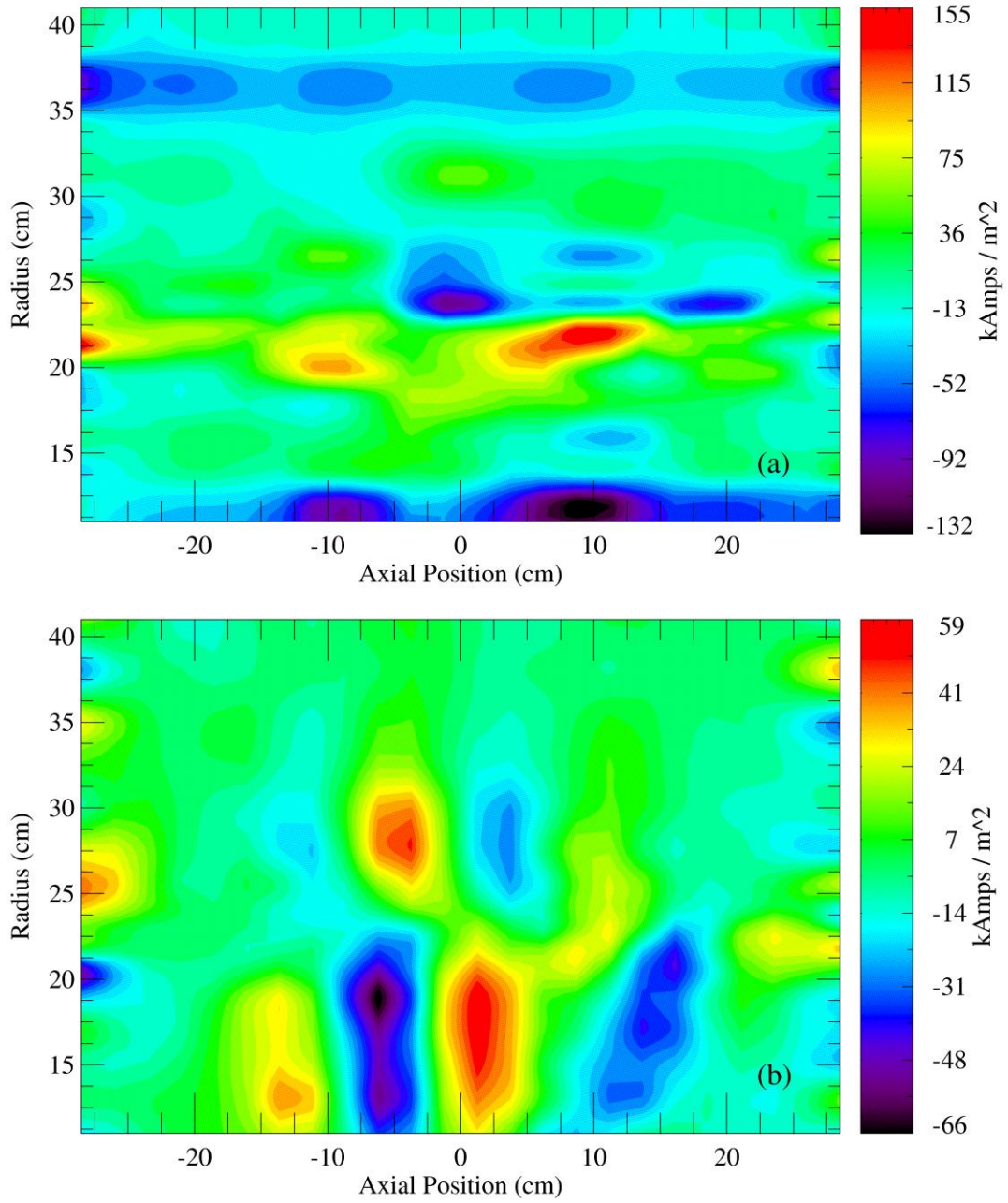


Figure 6.18: Current densities in the (a) Axial and (b) Radial directions at 43 microseconds. These calculations ignore toroidal gradients in B_z and B_r .

6.4 Inductive Electric Field

The electric field E in the plasma is found by an application of Faraday's Law in integral form,

$$\int \nabla \times \mathbf{E} \cdot d\mathbf{a} = \oint \mathbf{E} \cdot d\mathbf{l} = -\frac{d}{dt} \int \mathbf{B} \cdot d\mathbf{A} = -\frac{d\Phi}{dt} \quad (6.12)$$

This equation relates the change in time magnetic flux Φ to the electric field \mathbf{E} around the loop that encloses it. Only the theta component of the electric field can be fully resolved by this technique, as the bounding paths of the loop integral are not well defined due to magnetic field sampling in only a two-dimensional plane.

E_θ is derived by knowledge of the loop voltage V_{loop} at a radius a , as well as the radial profiles of the axial component of B-dot. This is written as

$$E_\theta(r, z) \cong \frac{V_{loop}}{2\pi a} - \frac{1}{2\pi r} \int_a^r \frac{dB_z}{dt} 2\pi r' dr', \quad (6.13)$$

where the integrand is evaluated at each axial location separately. The loop voltage as measured by the flux loop at the midplane provides a boundary condition, subject to the assumption that there is very little axial variation in the electric field at large radii. This is probably a valid assumption, since the three flux loops present show an axial variation of 5% or less.

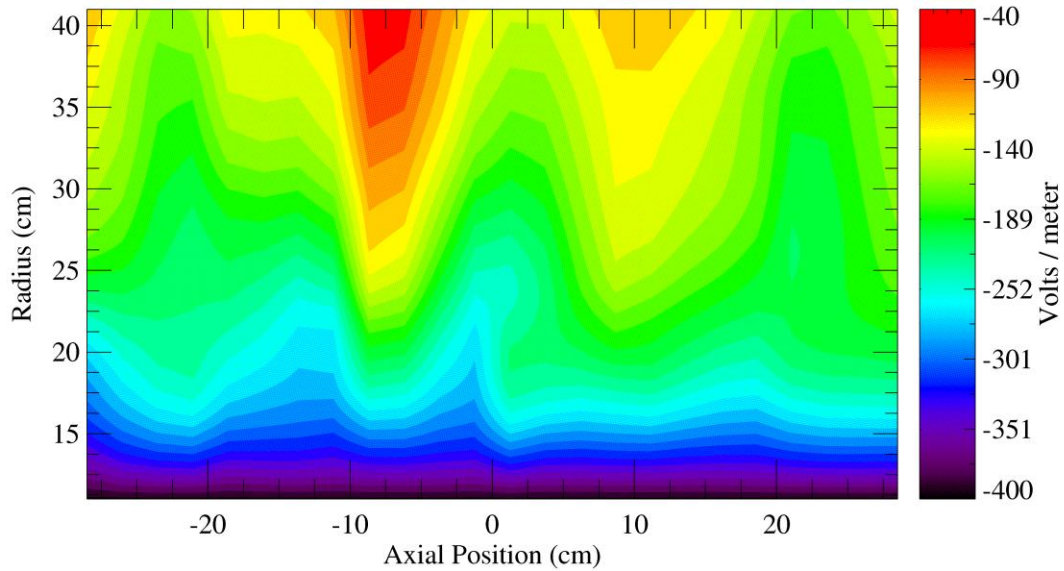


Figure 6.19: E_θ measurement at 43 microseconds

Figure 6.19 shows a plot of the toroidal electric field E_θ . The field is entirely in the $-\hat{\theta}$ direction at this time, with a nearly monotonic decrease in magnitude with increasing radial position. There are axial inhomogeneities at approximately ± 10 cm that are not expected based on the field coil geometry that is present in our system. They are possibly due to the assumption of straight field lines at the inner flux coil. Measurements of the loop voltage at more axial positions would provide a better set of boundary conditions; three positions were all that were acquired for this dataset. The fields generally remain in the $-\hat{\theta}$ direction throughout the discharge, though there are brief period of time where the fields are locally reversed. The axially averaged value of E_θ is shown in Figure 6.20. Temporal variations of more than $200 \text{ V/m}/\mu\text{s}$ are present at particular radial positions. When averaged over the cross sectional plane, as shown in Figure 6.21, the loop voltage is entirely in the negative toroidal direction. The dramatic

changes in time indicate that the plasma is strongly affecting the electric field that is produced by the inner flux coil.

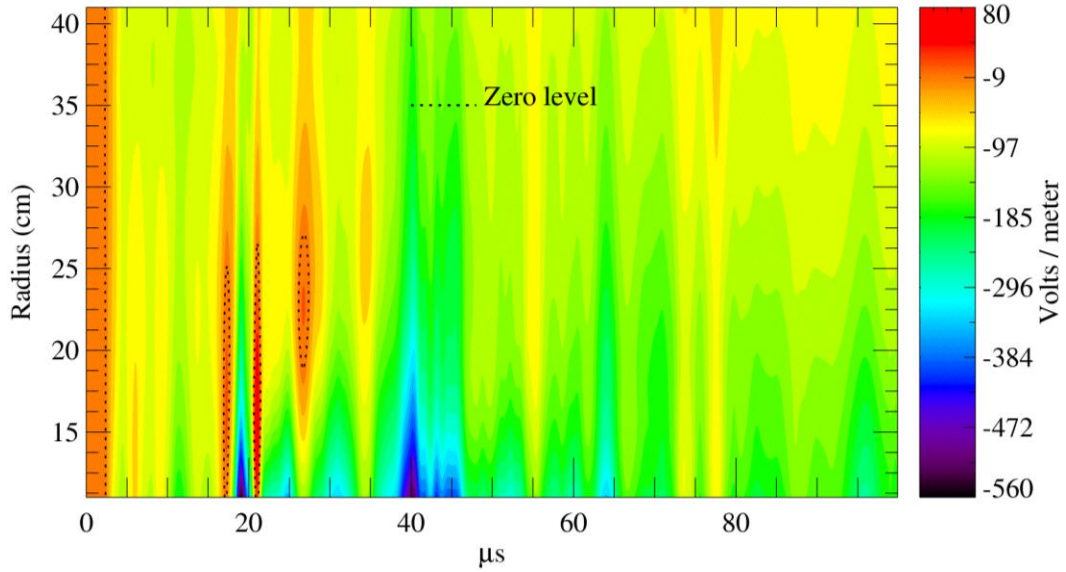


Figure 6.20: Axially averaged E_θ as a function of time and radial position. The dotted line marks the contour where the electric field is equal to zero.

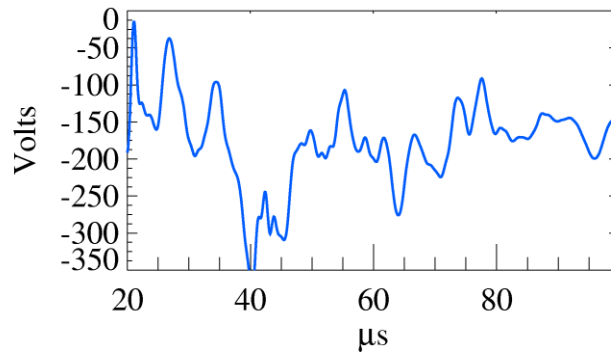


Figure 6.21: Average loop voltage

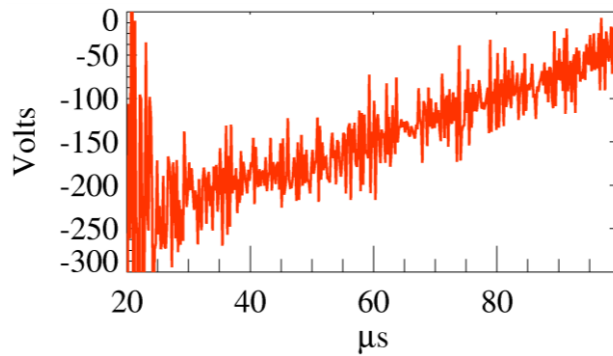


Figure 6.22: Theoretical loop voltage

The electric field as measured can be compared to theoretical profiles produced by the field coils in the absence of plasma. This is done by using the measured currents flowing through each coil during plasma shots and the resultant fields that are produced from the simulated field coils (See Section 6.2.) The axial symmetry about the midplane is apparent in Figure 6.23, as should be expected given the symmetric design of the simulated coils. The average loop voltage that the simulated field coils produce is shown in Figure 6.22. While the overall magnitudes of the two voltages are similar, deviations of more 100% occur at many times. This further illustrates the effect that the plasma has on the applied electric field.

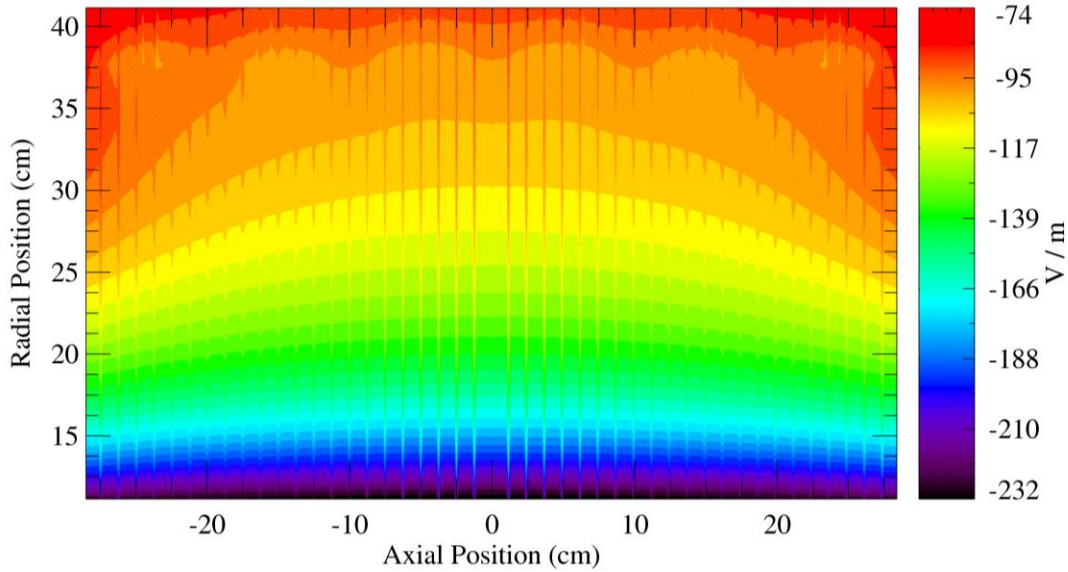


Figure 6.23: Theoretical E_θ based on measured currents at 43 microseconds

6.5 Plasma Temperature

Estimates of the ion and electron temperatures are key ingredients in many descriptions of plasmas. Whether measured by Doppler broadening of line radiation or by direct measurements of neutral particle energies, the concept of an average

temperature is one of the most fundamental ways that plasma can be characterized. We do not have local measurements of the temperature, since triple probes did not perform adequately on the IFRC. This leaves spectroscopy as the only means available of measuring the plasma temperature. As will be discussed, Doppler broadening of spectral lines has several challenges that make interpretation difficult.

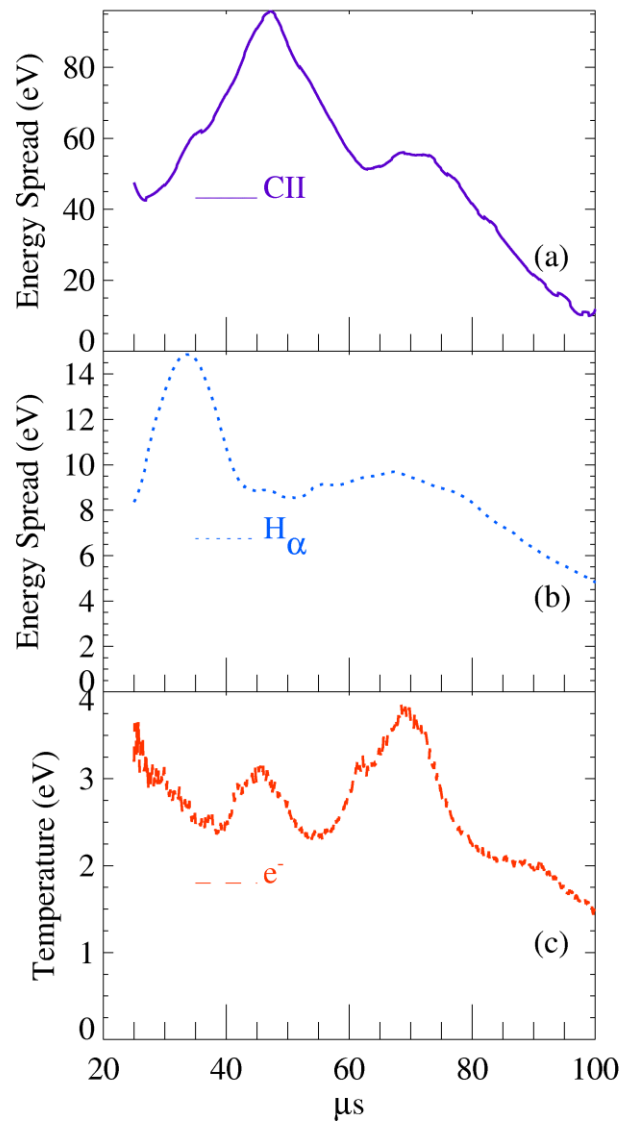


Figure 6.24: Velocity spreads measured by Doppler shifts for (a) singly ionized carbon and (b) neutral hydrogen. (c) Electron temperature from line ratio.

The velocity spreads of neutral hydrogen and singly ionized carbon are shown in Figure 6.24 (a) and (b). Also shown is the electron temperature estimated by line ratio measurements. These plots have been estimated from a compilation of 249 shots. The electron temperature, shown in Figure 6.24 (c), shows relatively small absolute changes in time, though the percentage changes between the minimum and maximum measured approach 100%.

The ion ‘temperatures’ inferred from Doppler broadening are not physically reasonable, and become more unreasonable as the source particle mass increases. These ‘temperatures’ are much higher than expected, considering that very little neutral and no ionized helium emission was observed. Even the hydrogen ‘temperature’ is too large, given that the measured intensity does not decrease with time. The ionization fraction may be estimated from the Saha equation, which can be written as

$$\frac{x^2}{1-x} = \frac{\exp(-13.6/kT)}{n\lambda_{dB}^3}, \quad (6.14)$$

where x is the ionization percentage, kT is the plasma temperature, n is the ratio of hydrogen neutrals to ions, and λ_{dB} is the electron deBroglie length. Assuming n in the range of 10^{10} to 10^{15} cc^{-1} , hydrogen is completely ionized to better than 1 part in a million by 2.58 eV. It is quite hard to believe that the intensity would stay approximately constant as a function of time (see Figure 6.25), given that the radiation emitted is proportional to the neutral density, which if anything should be dropping in time.

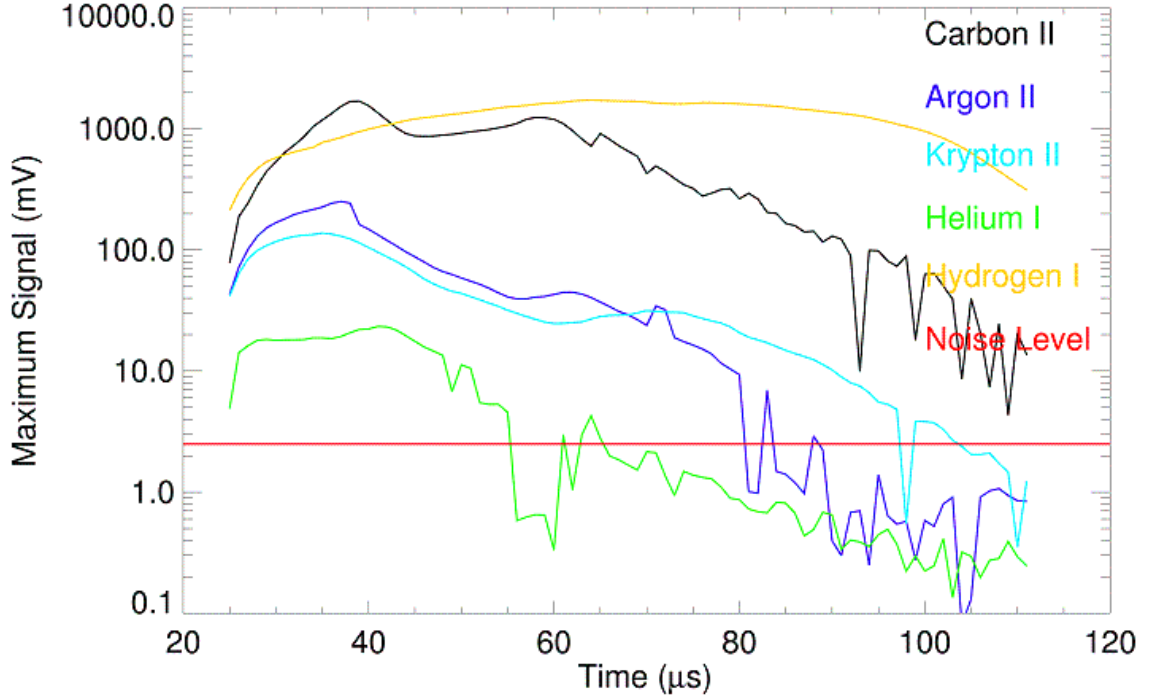


Figure 6.25: Average intensities for various spectral lines³¹

A plausible picture that could explain the suspiciously high ion ‘temperatures’ is that there is a bulk radial motion as well as random thermal motion. The viewing chord of the spectrometer could intersect the radial motion such that the spatial distribution of velocities could contribute to the observed broadening. The relationship between broadening sources can be modified to include a term related to bulk motion of a particular species. This is written as

$$\Delta\lambda_{observed} = \sqrt{\Delta\lambda_{thermal}^2 + \Delta\lambda_{inst.}^2 + \Delta\lambda_{stark}^2 + \Delta\lambda_{bulk}^2}, \quad (6.15)$$

where the broadening due to bulk motion has been removed from the thermal term. This equation can be rewritten as

$$\Delta\lambda_{thermal} = \sqrt{\Delta\lambda_{observed}^2 - \Delta\lambda_{bulk}^2 - .09}, \quad (6.16)$$

where the values for the instrumental and stark broadening terms have been input. The fluid velocity of carbon ions necessary to produce a Doppler shift equivalent to a 100 eV thermal distribution is nearly the same as the thermal velocity of hydrogen, approximately 2.8 cm/ μ s if the hydrogen ‘temperature’ is correct. It is most likely that the ionized carbon does not actually have zero temperature; Equation 6.16 gives the relationship between velocity and temperature combinations that could produce the observed broadening of the spectral line.

One plausible guess for the ion temperatures is that they are equal to the electron temperature, and all other broadening is due to bulk motion along the line of sight. The bulk velocities estimates of carbon and hydrogen are shown in red in Figure 6.26 (a). Note especially that the velocities of both ion species are within 50% of each other throughout the FRC lifetime, and have similar decaying trends as time increases.

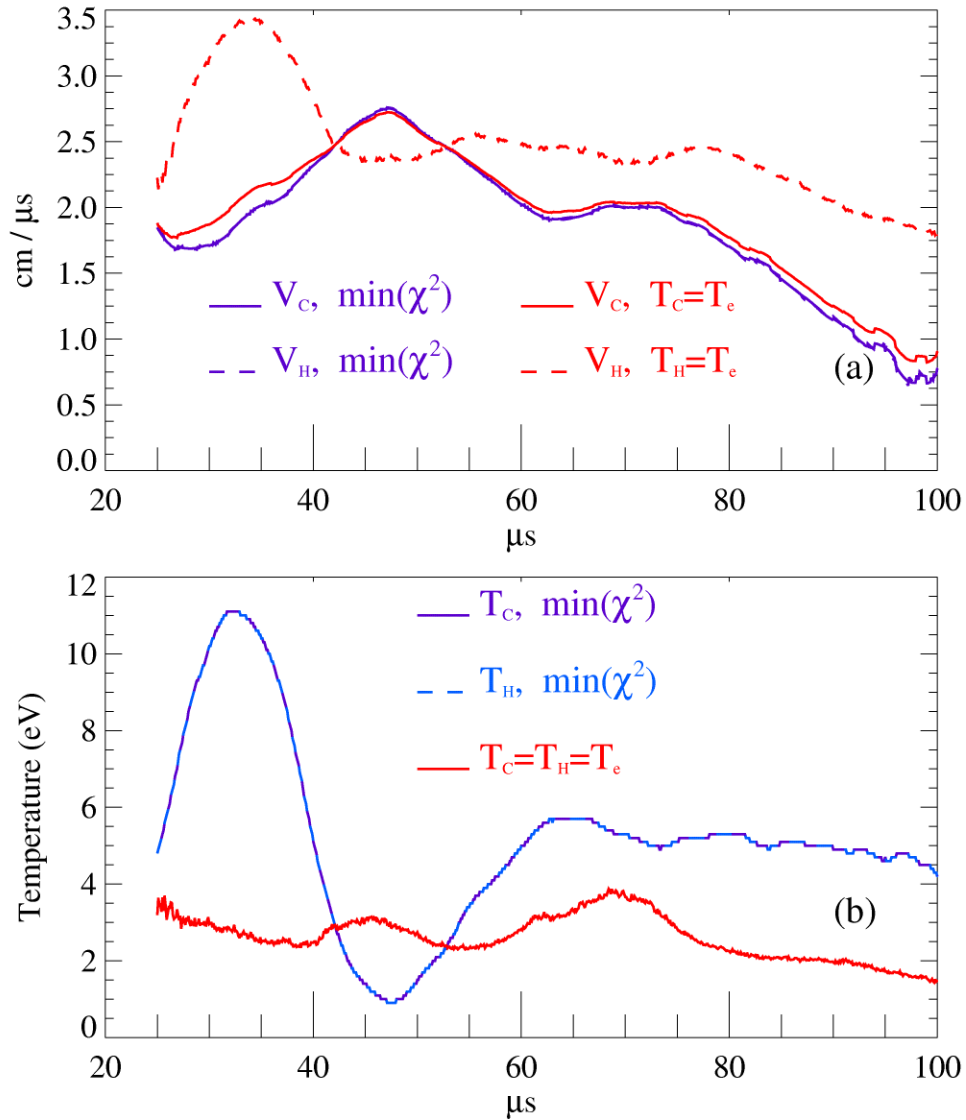


Figure 6.26: (a) Estimates of fluid velocities that give rise to erroneously large ion temperatures. (b) Ion temperatures after subtraction of line of sight broadening.

Another method of estimating temperatures and velocities of hydrogen and carbon is to allow the temperature of each species to vary in time. The purple traces in Figure 6.26 (a) show the two ion velocities, with the temperature and velocity differences minimized at each time. Both the temperatures and velocities are essentially identical in

this model, though the temperature evolution seems unlikely to actually occur in the IFRC.

Both methods of bulk ion velocity estimation result in similar magnitudes and temporal evolutions. The question arises: What are possible sources of a radial acceleration that could give rise to the velocities necessary to account for the observed broadening? One possibility could be the radial $\mathbf{E} \times \mathbf{B}$ drift. The azimuthal electric field that forms the FRC and drives the plasma current is present throughout most of the discharge. The interactions of ions with this field and the axial magnetic fields formed by the plasma current will produce a bulk drift towards the magnetic null, with a magnitude of approximately

$$V_{\text{ExB}} \sim \frac{200 \text{ V/m}}{.01 \text{ T}} = 2 \frac{\text{cm}}{\mu\text{s}}. \quad (6.17)$$

Another possible source could be the radial electric field that should be present in the equilibrium rigid-rotor FRC description. This field has not been measured to date; the magnitude is based solely on the analytical solution. As shown in Figure 2.2, the magnitude of E_r should vary (unmeasured) from -100 V/m to over 400 V/m for typical IFRC parameters. Assuming an electric field of 100 V/m or greater, it would take approximately 2 μs and 2 cm to accelerate a proton up to 2 $\text{cm}/\mu\text{s}$. A singly ionized carbon atom would take about 25 μs and 25 cm to reach 2 $\text{cm}/\mu\text{s}$. These timescales are short enough compared to the IFRC lifetime that it is possible that the radial electric field could be responsible for the necessary velocities, though the distance necessary to accelerate a carbon ion approaches the system size.

Collisional drag between protons and carbon ions could provide another mechanism of acceleration that would shorten the travel distance of carbon ions. For temperatures in the range of 3 eV and densities in the range of 10^{12} to 10^{13} particles / cc, the collision frequency between protons and singly charged carbon ions is approximately 10^5 to 10^6 s⁻¹.⁴⁰ A velocity difference of 1 cm/ μ s between the two ion species results in an acceleration on the order of 10^9 to 10^{10} m s⁻², which is the same magnitude as that resulting from an electric field of 100 V/m.

The effect of a chord intersecting a population of particles with a constant radial velocity has the net effect of creating a relatively flat spectral shape near the unperturbed wavelength smoothly increasing to two peaks at $\lambda_0 \pm \lambda_0 V_r/c$. One can imagine a varying spatial velocity profile more realistic than a constant that would still produce a broadened spectral signature. Figure 6.27 shows two different H_α profiles that are the result of a particular line of sight intersecting a population of particles with a constant outward radial velocity of 2 cm/ μ s. The line of sight is taken to be a chord stretching from -30 to 30 cm with a vertical offset of 25 cm. The solid curve results from an equal number of particles at every position along the chord, while the dotted curve is produced by a rigid-rotor distribution that peaks at a radius of 22 cm and has a width of 7 cm, similar to predicted FRC density distributions. Both distributions have zero broadening from thermal motion. Also plotted is the broadened profile due to a 2 eV thermal distribution. The broadening due to bulk motion and the line of sight is quite comparable in magnitude to typical thermal temperatures in the IFRC.

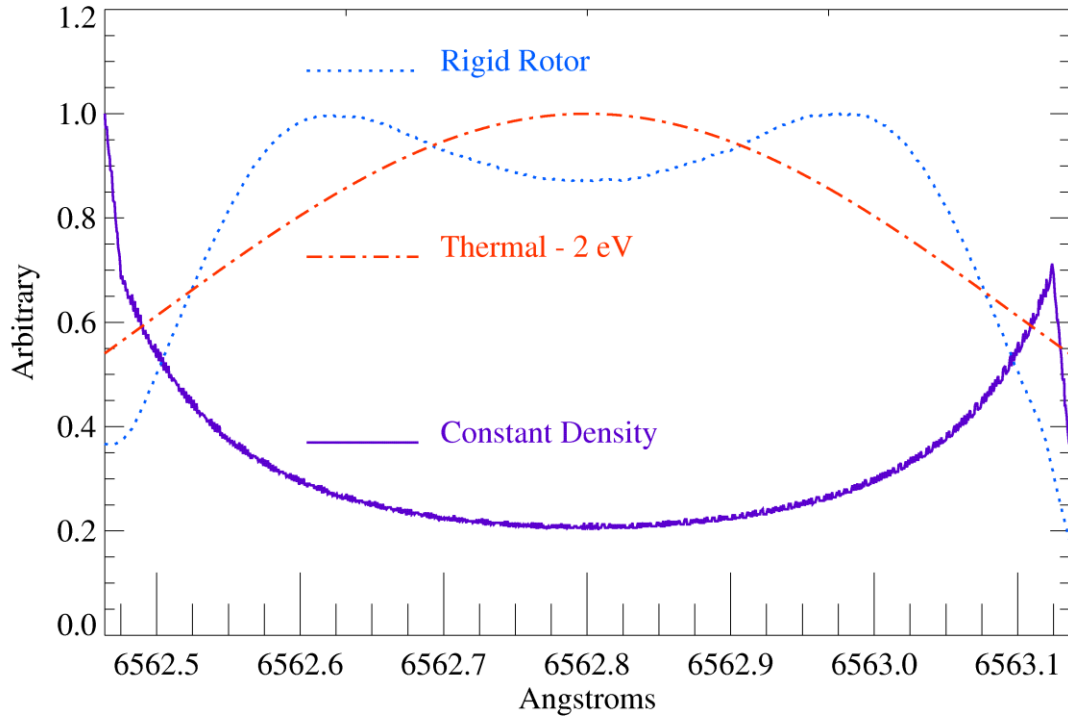


Figure 6.27: Doppler broadened profiles for two analytic densities with a thermal distribution for reference.

In summary, the measured amount of Doppler broadening implies ionic temperatures that are physically unreasonable. It is considered to be quite likely that line of sight effects due to bulk motions of the ions contributes strongly to the observed amount of broadening. Since we cannot measure these bulk motions, the electron temperature will be used from throughout this thesis as an estimate for all ionic temperatures.

6.6 Faraday Cup

The performance of a fusion device is often qualified by how well it confines particles. This is usually measured by the particle loss rate from the plasma when compared with the particle inventory, with the goal of most experiments to minimize

these losses. The particle losses out the axial end planes of the IFRC are measured by an array of five Faraday cups spaced every 5 cm from 11 to 31 cm. The data presented were compiled over a sequence of 187 shots, with the differences between the two datasets being the charging voltage on the plasma gun capacitor bank. The normal charging voltage of 12 kV was studied for 80 shots, while a higher voltage of 16 kV was sampled 107 times with a goal of increasing the plasma density.

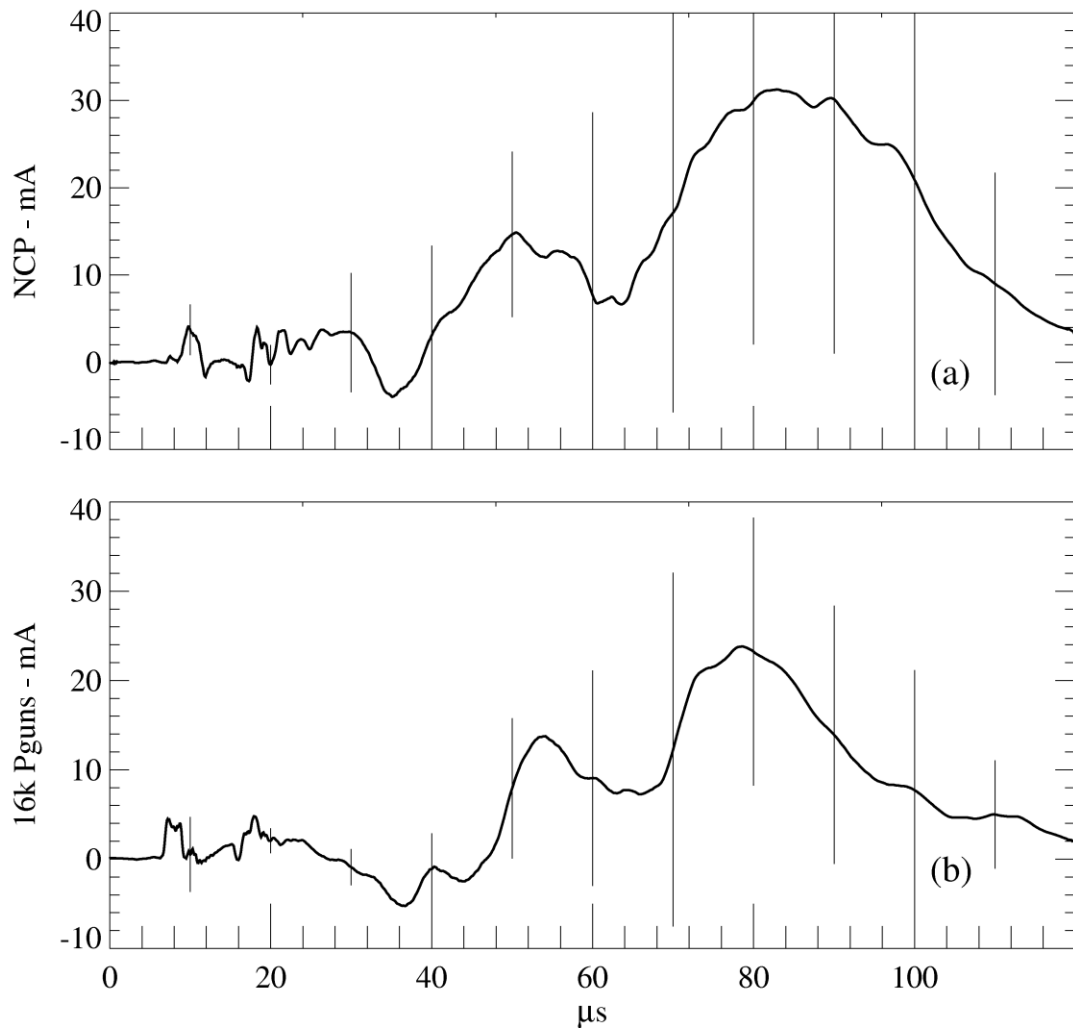


Figure 6.28: Faraday cup data at $r = 16$ cm. (a) Average of 80 shots, with the plasma gun charging voltage at 12 kV. (b) Plasma guns at 16 kV, 107 shot average.

The average signal of one Faraday cup is shown in Figure 6.28. There is substantial variability in the losses from shot to shot, indicated by the error bars. While the cups are biased negatively at -48 volts to collect ions, there is an average negative current from 30-44 microseconds measured by four of the five probes, graphically shown in Figure 6.29. This could be due to rapid changes in the floating potential or expulsion of fast electrons. The amplitude of the losses tracks the position of the null with time and peaks at a slightly larger position. This means that most of the particles lost from the IFRC originate on the outer edge of the plasma rather than near the flux coil, and suggests that open field lines which surround the separatrix guide particles out the end of the machine.

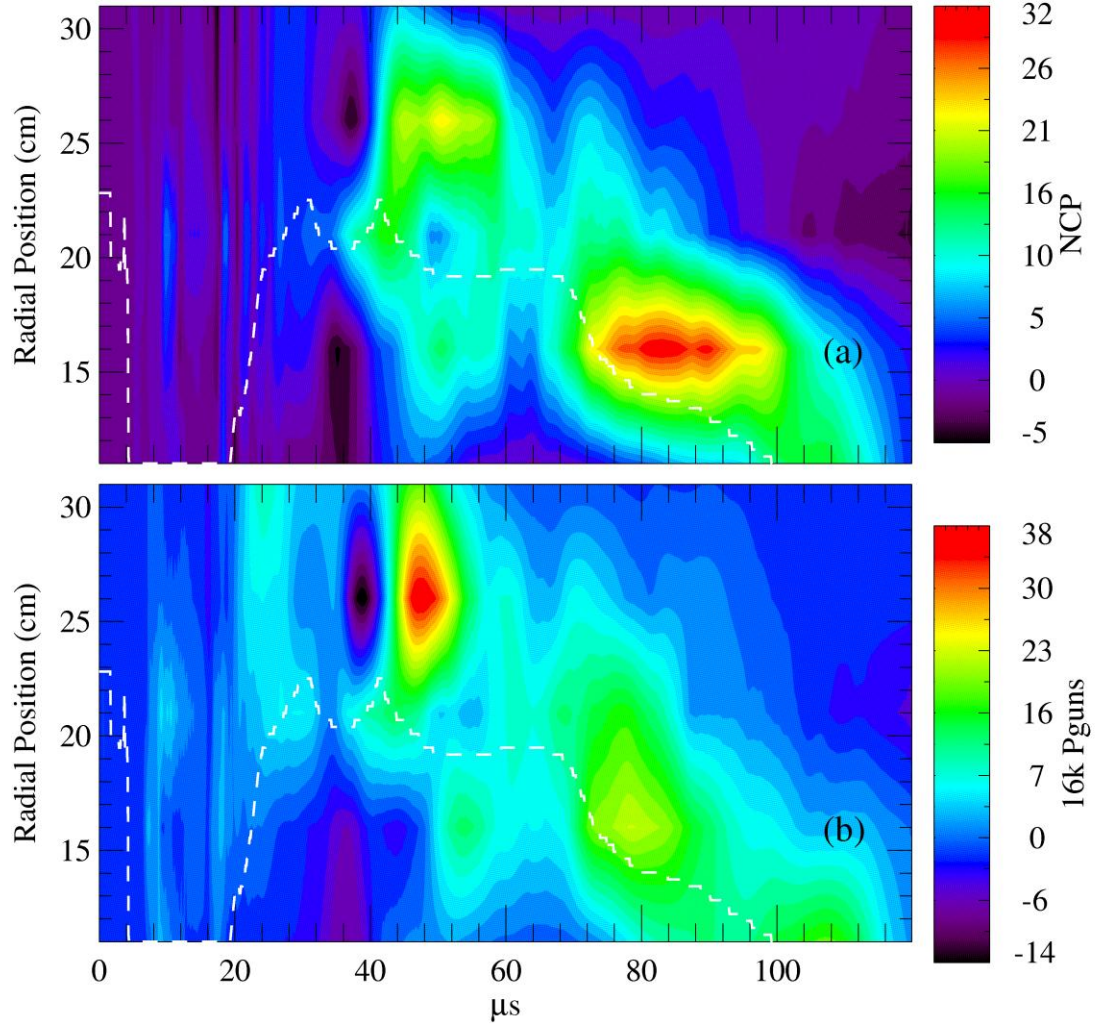


Figure 6.29: Radial and temporal evolution of average Faraday cup signals for (a) *FCUP* dataset and (b) *FCUP16k*. Approximate position of the magnetic null is shown by the dashed line.

The total amount of particles lost out one end of the machine is estimated by radially integrating the Faraday cup signals at each time and then integrating in time.

This is written as

$$N_{loss}(t) = \frac{2\pi}{\Delta\Omega} \int_0^t d\tau \int_{11}^{31} \frac{I(r, \tau)}{eA} 2\pi r dr, \quad (6.18)$$

where e is the unit charge, A is the area of each Faraday cup, and $2\pi/\Delta\Omega$ corrects for the acceptance angle of the each cup with a value of approximately 110. The losses

calculated here are probably an underestimate for two reasons. First, radial losses are not measured at all. While probably small compared with the axial losses, they should be measured in the future to provide a more accurate account of particle transport. Second, the negative currents measured from ~32-40 microseconds actually reduce the calculated value of lost particles. Though this is completely unphysical, the magnitude and duration of this negative current is relatively small compared with the overall discharge which will not change our estimates of the lost particles appreciably.

The two datasets have similar time and spatial evolutions indicating that the overall discharge does not change much when the plasma gun voltage is increased. The larger charging voltage does cause the particle loss rate to peak earlier in time than the *NCP* case, with a larger negative current preceding it as well. It is also interesting that the total particle losses are about the same, as shown in Figure 6.30. It is unclear whether the increased voltage did increase the plasma density; the negative currents at ~35-40 microseconds in Figure 6.30 (b) could be masking more losses.

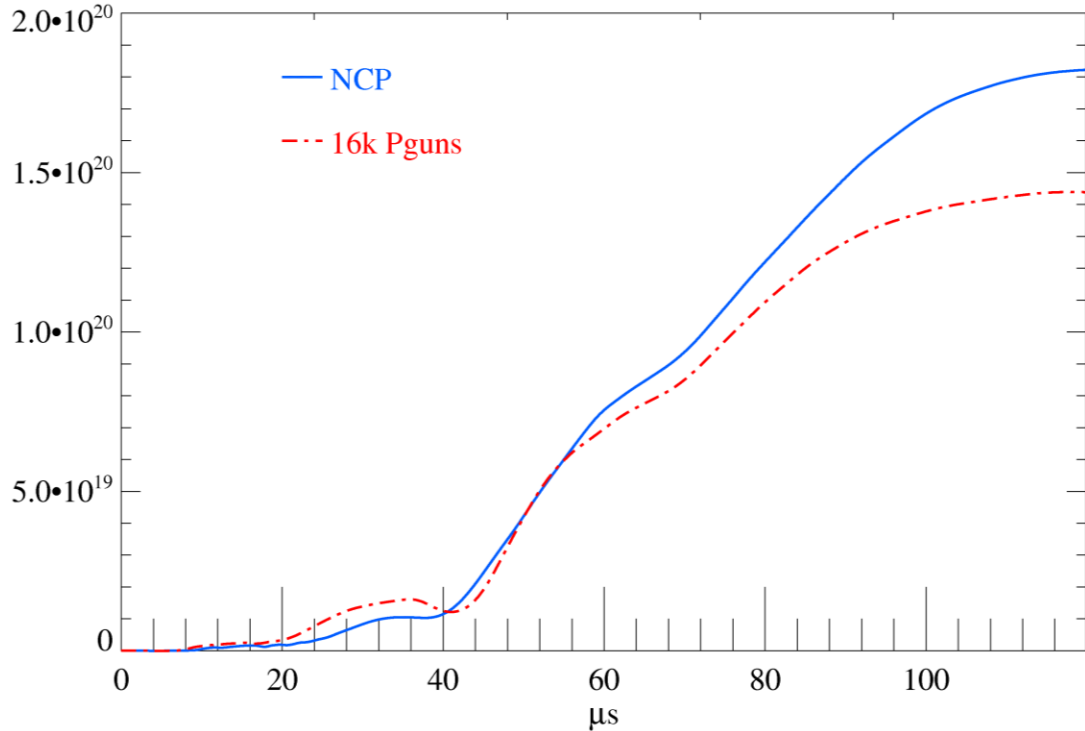


Figure 6.30: Particle loss out one end plane for two datasets

The Faraday cup signals have identified a large pathway for energy losses in the IFRC, and hints that the source may be open field lines at the plasma edge. This subject will be revisited in Chapter 10 by studying the correlations between magnetic fluctuations and the particle losses.

6.7 Summary of Basic Parameters

Magnetic field measurements indicate that an FRC was formed and maintained for approximately 50 microseconds. The estimates of the poloidal flux indicate closed field lines, surrounded by open field lines that guide lost particles out the axial end planes. The measured magnetic fields, and estimated magnetic flux, current density, and electric field agree well with theoretical profiles for the measured currents in the field coils. This agreement bolsters the faith in the measurements. The IFRC does have large

toroidal magnetic fields that vary strongly with time and position. These fields arise spontaneously, and could be due to a periodic wobble in the toroidal plasma current.

Chapter 7: Secondary Quantities

Armed with the knowledge of the magnetic and electric fields, current density, plasma temperature, and particle fluxes, we can begin to derive important information that guides our understanding of the behavior of our particular FRC. Parameters that will be described in this chapter include the following: plasma pressure, average beta, and the radial component of the Poynting vector. From the thermal pressure, the density and particle inventory will be derived, using temperature measurements from spectroscopy. These variables are necessary for a complete understanding of the distribution of energy and power flows that will be discussed in Chapters 8 and 10.

7.1 Plasma Pressure

The plasma pressure p is due predominately to the thermal energy of the plasma, and can be written

$$p = \sum_i n_i kT_i \sim n(kT_e + kT_i), \quad (7.1)$$

where n is the plasma density, kT_e is the electron temperature, and kT_i is the hydrogen temperature. Both the temperature and density may be functions of position, though in practice it is assumed that the temperature is constant. This assumption is based on past experimental evidence that have indicated relatively flat temperature profiles inside the separatrix of FRCs. Direct measurements of the local plasma density do not exist on the IFRC; triple probe measurements did not give physical results, most likely due to large fluctuations in the floating potential. Density estimates based on pressure balance were

consistent with interferometer data in the past;⁴¹ for the sequence of shots on which this thesis is based however, no interferometer data are available. Due to these issues, plasma pressure must be inferred from other estimates, such as radial pressure balance and ion saturation current measurements.

The statement of radial pressure balance can be written as a balance between the pressure gradient force and the magnetic $J \times B$ force, written as

$$\nabla p = J \times B, \quad (7.2)$$

or

$$\nabla \left(p + \frac{B^2}{2\mu_0} \right) = (\mathbf{B} \cdot \nabla) \mathbf{B} / \mu_0. \quad (7.3)$$

This is just a simplification of the generalized Ohm's Law equation (Equation 8.1) in the limit of infinite conductivity and zero electric field and fluid velocity. Equation 7.3 can be simplified to look at the radial component only, and is given by

$$\frac{d}{dr} \left(\mu_0 p + \frac{B_\theta^2 + B_z^2}{2} \right) = B_z \frac{dB_R}{dz} - \frac{B_\theta^2}{r}. \quad (7.4)$$

Since the magnetic field structure is known, we next integrate both sides of Equation 7.4 and solve for the radial profile of the plasma pressure at each axial position. The integration constant at each axial position is found by solving the axial pressure balance equation and using the derived axial profile at the maximum radial position to add the appropriate constant to the radial profiles at each axial position. Finally, another constant value is added to the resultant 2D pressure profile such that the minimum pressure at each time is always greater than or equal to 0.1 Pa. This method produces pressure profiles at 43 microseconds as shown in Figure 7.1 (a).

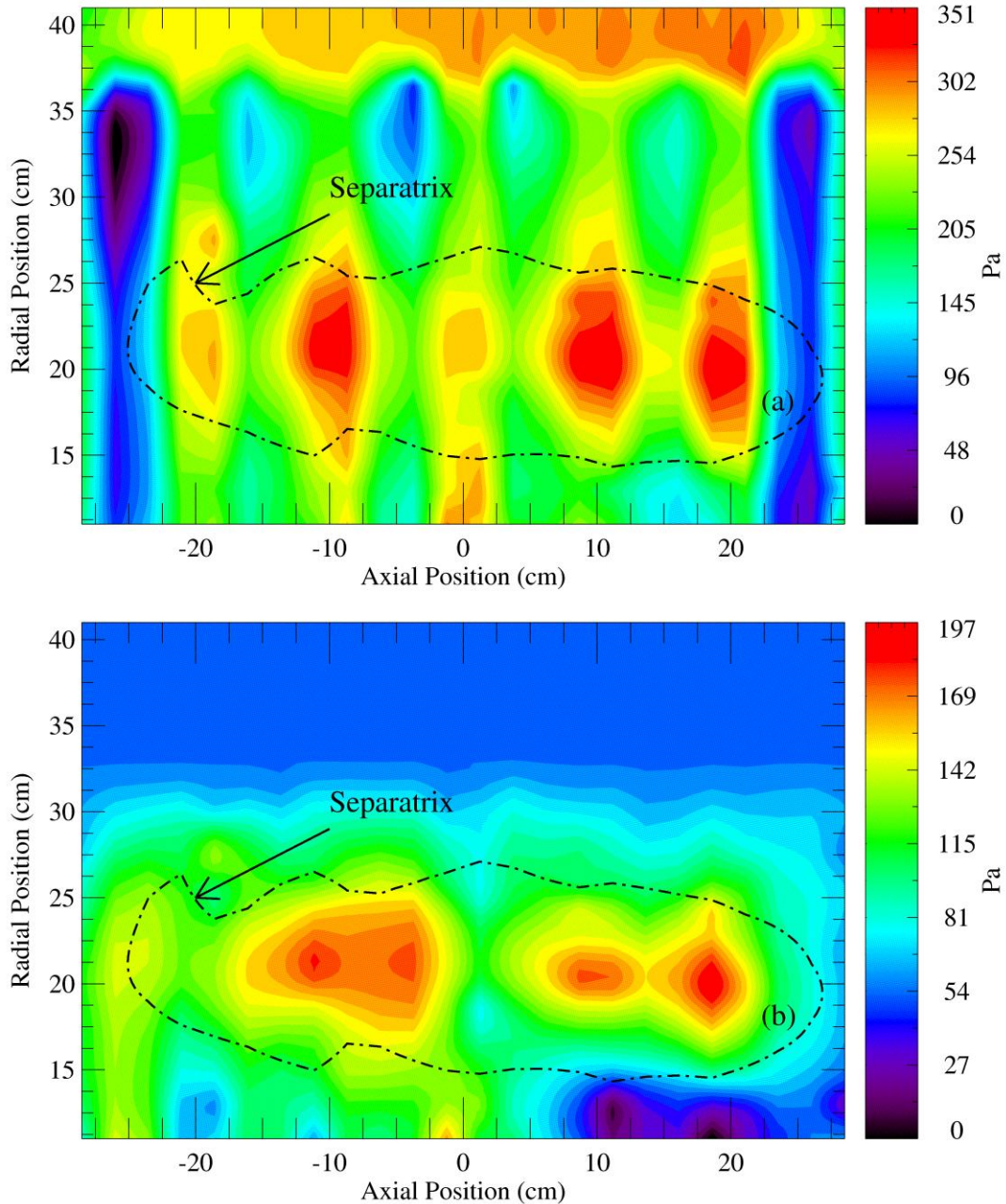


Figure 7.1: (a) Plasma pressure from radial force balance with constants found from axial force balance at 41 cm. (b) Pressure derived from $J_{plasma} \times B$, where J_{plasma} clips the derived current densities outside of 32 cm.

The periodic variations of the density with axial position are partly due to the analysis technique. The assumption of straight field lines near the null is not always correct, as stray fields have been measured there with magnitudes of approximately 10-20

Gauss. The plots of magnetic energy density do show that there is an axial separation of the density into two or more rings that split and merge as the discharge progresses. See Figure 6.3 for example, noting in particular the axial variations where the magnitude of the magnetic field is small.

An alternative method which produces more physically reasonable plots is to use only the plasma current to derive the plasma pressure. This is done by clipping the current densities at radii near the limiter coil. The rationale behind this is that the measurements of the magnetic field are not sampled sufficiently near the limiter coil where their gradients are very large. This results in the unphysical picture of large plasma densities on open field lines near the limiter coil, as shown in Figure 7.1 (a) at radial positions of 35 cm and greater. The radial clipping point of ~32 cm is estimated by finding the radial position where the total current measured by gradients in the magnetic fields is equal to the measured limiter current. Equation 7.2 is then solved by integrating in r , assuming that the pressure is constant at the maximal radial position, and then shifting the resulting 2D array by a constant to ensure that the pressure is still greater than or equal to 0.1 Pa. The profiles produced by this method (see Figure 7.1 (b)) have less variation in axial position than the first method, and do not lead to large densities on open field lines.

The third method consists of making localized measurements of the ion saturation current along many radial points. The ion saturation current, given by Equation 4.8, is proportional to the plasma density and the square root of the plasma temperature. With

prior knowledge of the temperature, this current measurement can be unfolded to yield the local density and plasma pressure, written as

$$n = \frac{I_{sat}}{eAc_s} \quad (7.5)$$

and

$$p = n * \sum kT. \quad (7.6)$$

Ion saturation measurements were only made at the axial midplane. This precludes them from two dimensional reconstructions. These measurements show that the density derived from radial pressure balance has a similar radial and temporal evolution at the axial midplane. Since the two measurements agree fairly well, only the pressure measurements based on force balance will be used from here on, as they provide a more complete picture of the spatial distribution of the plasma density.

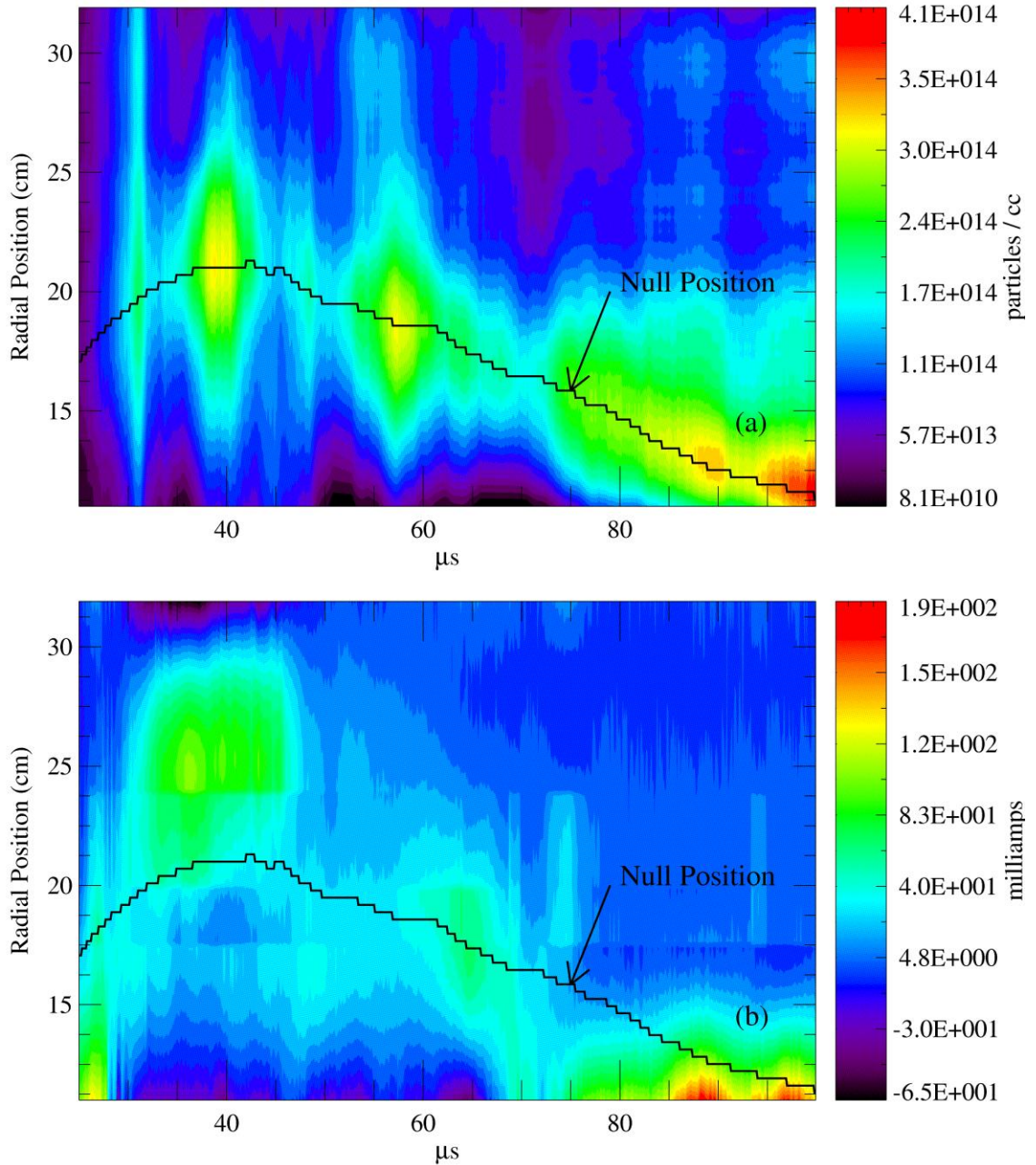


Figure 7.2: (a) Plasma density evolution as inferred from force balance, and (b) Ion saturation measurements along the same radial chord. Note: Measurements are from different sets of shots.

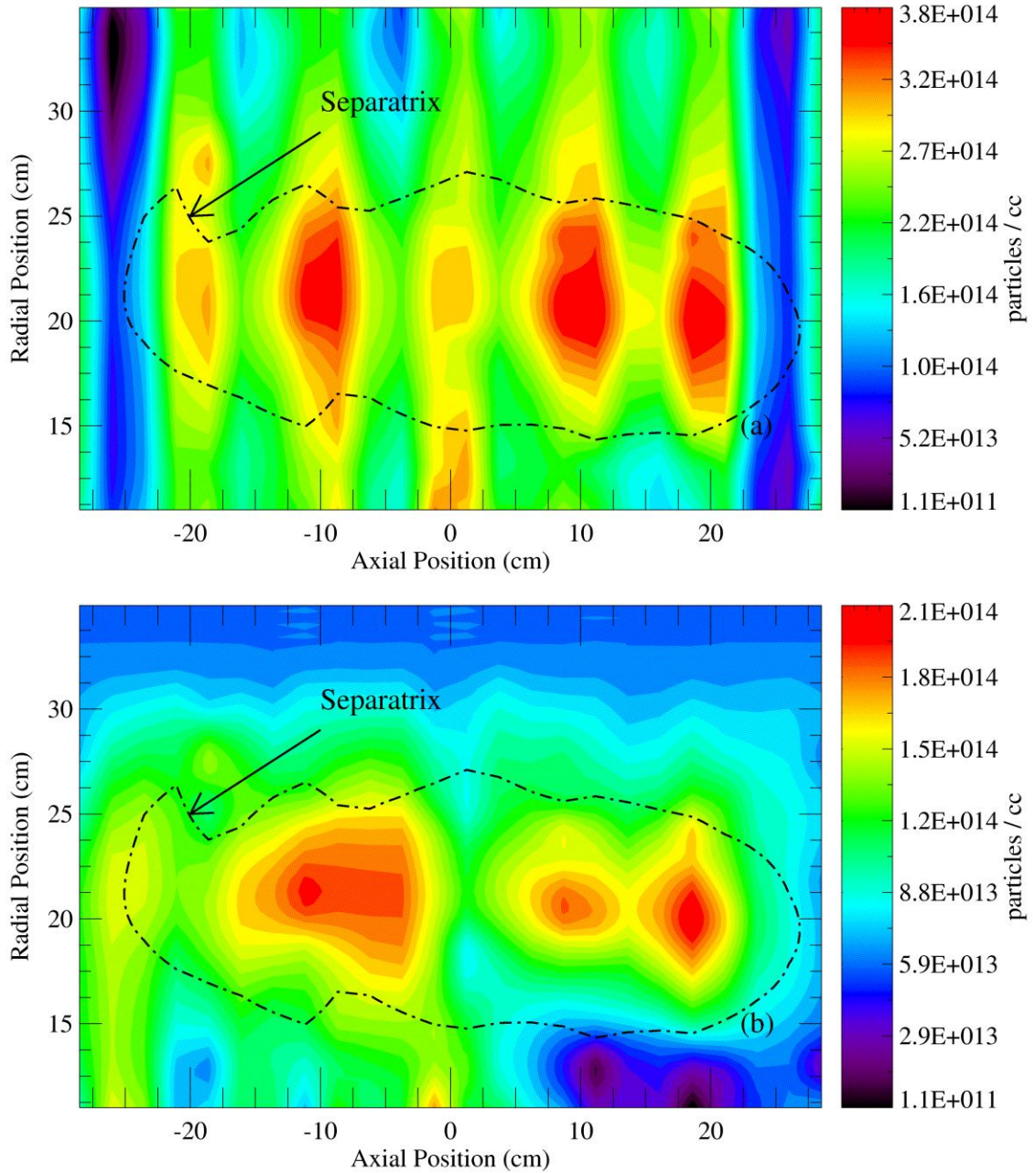


Figure 7.3: Density profile in R-Z plane at 43 microseconds

Figure 7.3 is a contour plot of the densities derived by the two force balance methods at 43 microseconds. Note in particular how the second method, using only the plasma current, results in a profile that peaks inside of the estimated separatrix position.

With estimates of the spatial distribution of the plasma density, the total particle inventory N can be estimated. This is simply the volumetric integral of the density under the assumption of azimuthal symmetry and is written as

$$N = \int_A n(r, z) 2\pi r dr dz, \quad (7.7)$$

where A is cross-sectional area in the R-Z plane. From this plot, it is apparent that the estimated particle losses in Figure 6.30 are probably too large by a factor of 5-10, as the inventory has a peak value at 55 microseconds of only 4.5×10^{19} , while the losses were estimated to be greater than 2×10^{20} . The large increases and decreases are consistent with poor particle confinement, though the assumptions of pressure balance, temperature isotropy, and zero toroidal variations could affect the inventory calculation as well.

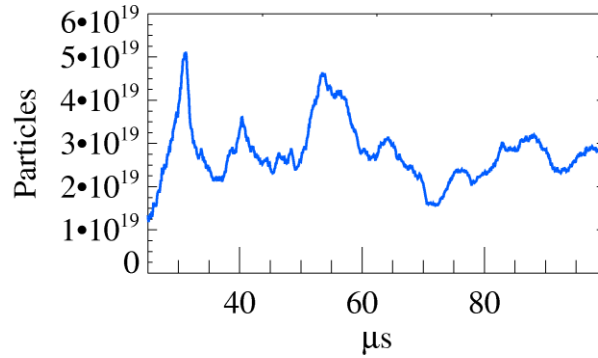


Figure 7.4: Particle inventory

7.2 Average Beta

Magnetic field and density measurements can be cast into a form that allows an estimate of the volume averaged plasma beta. This section discusses how the equations are formulated, the data that are necessary, and concludes with a plot of the time evolution of the volume averaged beta.

The ratio of thermal to magnetic pressure is called beta, written as

$$\beta = \frac{nkT}{B^2/2\mu_0}. \quad (7.8)$$

This quantity can be defined as a ratio of local values or as an average taken over some spatial domain. Global averages make more sense on field-reversed configurations, due to the wide ranges of density and magnetic field values that are present in typical systems. Local values of beta range from zero, where no plasma is present, to infinity where the magnetic field is equal to zero. The volume averaged beta $\langle\beta\rangle$, which is the preferred measure, is calculated by integrating the numerator and denominator of Equation 7.8 separately, and then taking the ratio. The numerator integral is equal to $\int pdV$, while the denominator is equal to the total magnetic energy. Experimentally measured profiles are used for both integrations; Figure 7.5 shows the resulting time evolution of $\langle\beta\rangle$.

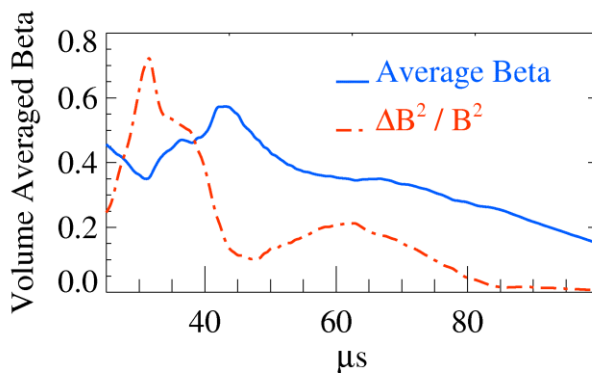


Figure 7.5: Volume averaged beta

Also included in Figure 7.5 is the change in stored magnetic energy between the plasma dataset and that of background fields only, normalized by the background magnetic field energy. To zeroth order, the extra magnetic energy when plasma is

present is equivalent to the thermal energy, while the background fields remain unperturbed. The overall magnitudes of the two estimates of the volume averaged beta are similar, as are the temporal evolutions.

7.3 Poynting Vector

The Poynting vector S describes how electromagnetic energy moves through space, and is written as

$$\mathbf{S} = \frac{1}{\mu_0} \mathbf{E} \times \mathbf{B}. \quad (7.9)$$

The radial component of this vector depends on the axial and toroidal components of the electric and magnetic fields. Since E_z is assumed to be zero, or at least much smaller than the other terms, the radial profiles of S_r are given by

$$S_r = \frac{1}{\mu_0} E_\theta B_z. \quad (7.10)$$

An obvious feature of the spatial distribution is the division into two radially separated regions, graphically depicted in Figure 7.6. Power generally is directed towards the magnetic field null, though there are brief periods in time where the direction is reversed. This is to be expected, given that the IFRC is a driven system with power delivered from the field coils to the plasma. The null position marks the average radial point where incoming flux is annihilated and converted into thermal energy.

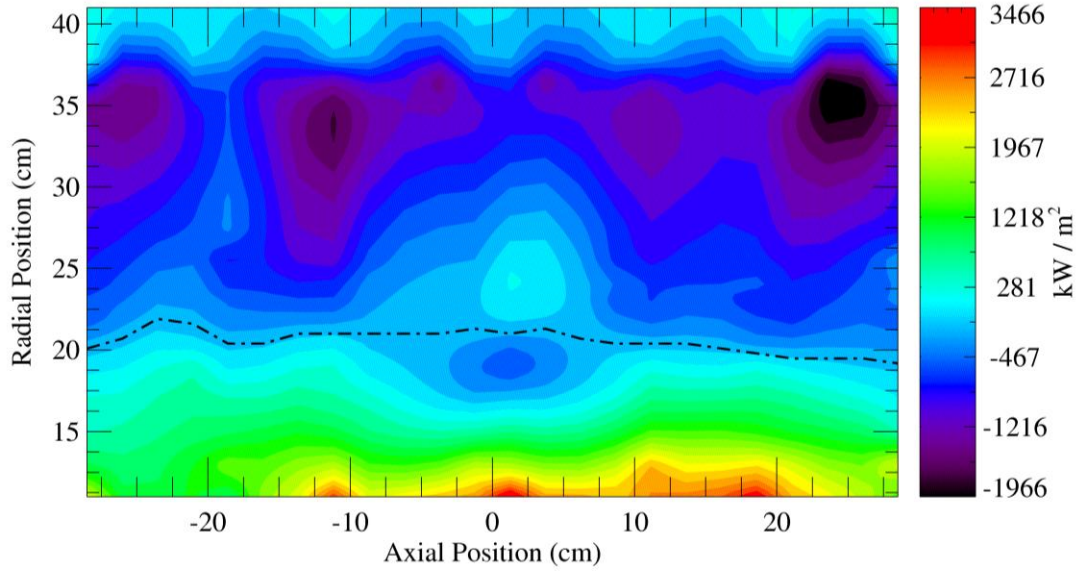


Figure 7.6: Spatial structure of the radial Poynting vector at 43 microseconds. Null position is shown by the black dashed line.

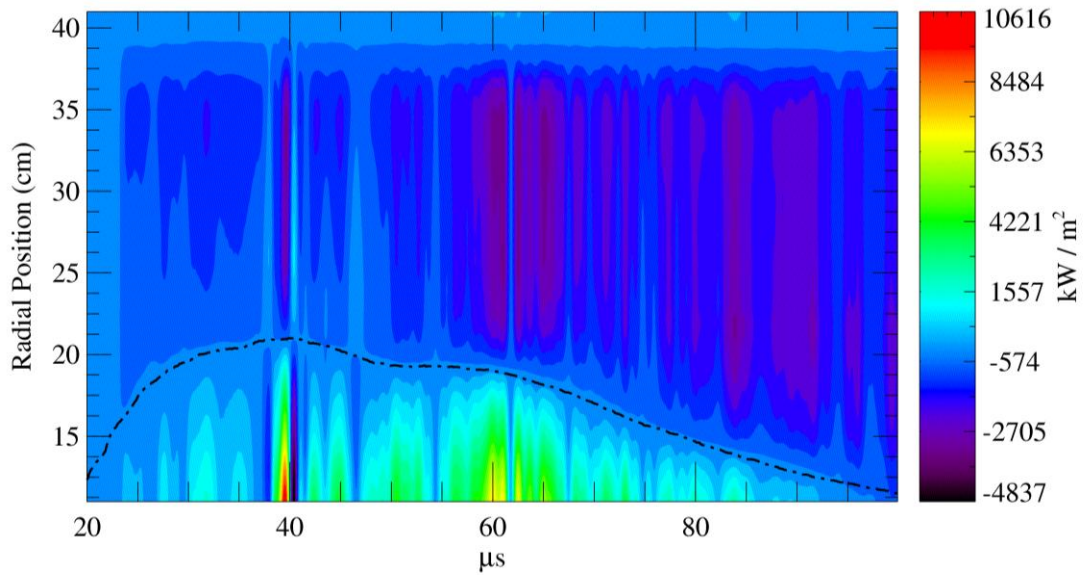


Figure 7.7: Time evolution of the axially averaged radial Poynting vector. Null position is shown with the dashed black line. Note that the two plots of the Poynting vector do not have the same amplitude scales.

Chapter 8: Plasma Resistivity and Power Balance

The generalized Ohm's Law in plasma is derived from a two fluid description of the momentum equation, and can be written as

$$\mathbf{E} + \mathbf{v} \times \mathbf{B} = \eta \mathbf{J} + \frac{\mathbf{J} \times \mathbf{B}}{ne} - \frac{\nabla p}{ne} \quad (8.1)$$

where terms that are small have already been dropped. New terms are the plasma fluid velocity \mathbf{v} and resistivity η . This equation states that the electric field in the plasma frame (left side of Equation 8.1) is balanced by three terms on the right hand side, due to plasma resistance $\eta \mathbf{J}$, the Hall term $(\mathbf{J} \times \mathbf{B})/ne$, and gradients in the thermal pressure $\nabla p/ne$. This chapter begins with estimates of the plasma resistivity, based on knowledge of the field components, density profiles, and plasma temperature that have been found in previous chapters. An estimate of the ohmic power is found, and comparisons are made to the input power found from the Poynting vector at the plasma edge. The thermal and electromagnetic components of energy stored in the plasma, and various loss terms are estimated. Finally, the energy confinement time is estimated and compared to measurements from other experiments. It will be shown that the dominant means of energy loss on the IFRC is through particle transport, with a correspondingly low energy and confinement time.

8.1 Plasma Resistivity

The generalized Ohm's Law (Equation 8.1) is a vector equation, and should hold for any particular component. An analysis of the toroidal component is the simplest and

most accurate, since the electric field and current density can be evaluated completely in that direction. At the magnetic field null, the magnetic field and pressure gradient are approximately zero. This means that we can drop the $\mathbf{v} \times \mathbf{B}$ term, the Hall term, and pressure gradient term from Equation 8.1, leaving us with a linear relationship between the toroidal electric field and current density. When the current density is the independent variable, the constant of proportionality is called the resistivity, and is given by

$$\eta = \frac{E_{\theta}(z, r = r_{null})}{J_{\theta}(z, r = r_{null})}. \quad (8.2)$$

This method, while analytically valid, is somewhat prone to numerical errors, such as when the electric field or current density reverses sign. Different averaging conditions lead to slightly different values of the calculated resistivity. Figure 8.1 shows three different averaging estimates, as well as the Spitzer resistivity calculated for the estimated values of the density and temperature in the IFRC. The first method averages E_{θ} and J_{θ} over a 1.5 cm radial region centered on the magnetic null for each axial position, and then averages these values over the axial extent of the plasma before taking the ratio. The second method expands the averaging regions to encompass the entire toroidal cross-section. This is equivalent to performing a two dimensional integral of E_{θ} and J_{θ} over the radial and axial positions. The current density integration is the same as the toroidal plasma current, which is measured by the Rogowski coil. The integration of the electric field is done numerically, and the ratios are then taken at each time period.

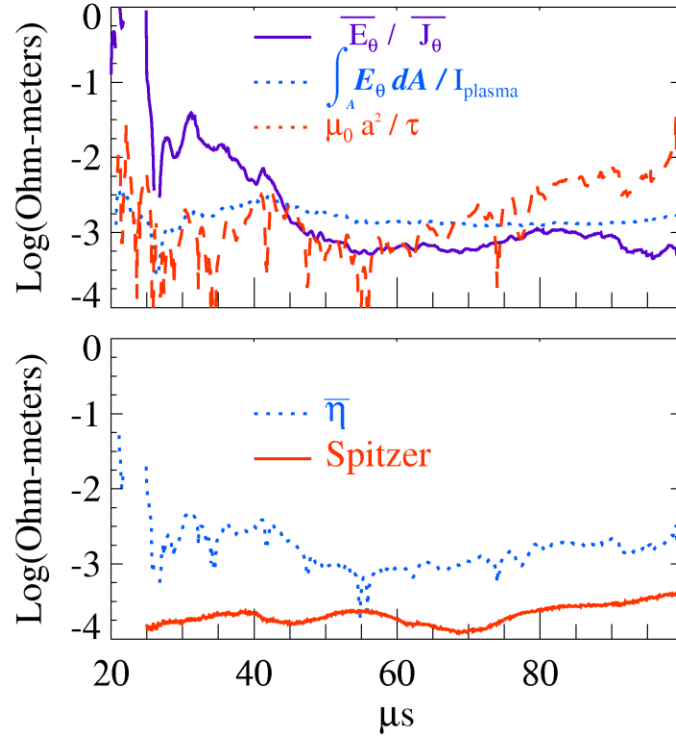


Figure 8.1: (a) Time evolution of the plasma resistivity by three different methods. (b) Comparison between averaged resistivity and Spitzer resistivity.

The third method⁴² exploits the relationship between the resistivity and diffusivity. The diffusion of magnetic fields into the plasma can be estimated by measurements of the magnetic scale length a_1 and flux diffusion time τ . The magnetic scale length is estimated numerically at each axial position by

$$a_1 = \frac{\text{Max}(|B|)}{\nabla B(\text{null})}. \quad (8.3)$$

The flux diffusion time estimate is a bit more involved; it is given by a balance between magnetic fluxes input by the external field coils and flux losses due to resistive decay at the field null. The system of equations that describe this can be written as

$$\dot{\Phi}_{ex} = \int (\text{Input} - \text{Loss}) dt, \quad (8.4)$$

$$Input = \frac{d\Phi_c}{dt}, \quad (8.5)$$

$$Loss = \frac{\Phi_{ex}}{\tau}, \quad (8.6)$$

$$\Phi_c = \int_0^{separatrix} 2\pi B_z r dr, \quad (8.7)$$

and

$$\Phi_{ex} = \int_{separatrix}^{null} 2\pi |B_z| r dr. \quad (8.8)$$

Here Φ_c is the flux present at the separatrix while Φ_{ex} is the axial flux that is trapped in the FRC. This model describes exponential decay of the trapped flux, characterized by time τ , with the inclusion of a driving term given by $d\Phi_c/dt$.⁴² By taking the time derivative of Equation 8.4 after substitution of Equations 8.5 and 8.6, it can be solved for the decay time yielding

$$\tau = \frac{\Phi_{ex}}{\dot{\Phi}_c - \dot{\Phi}_{ex}}. \quad (8.9)$$

Since the total flux Φ_0 is given by the sum of Φ_c and Φ_{ex} , Equation 8.9 can be recast as

$$\tau = \frac{\Phi_0(null) - \Phi_0(separatrix)}{\dot{\Phi}_0(null)}. \quad (8.10)$$

Equations 8.9 and 8.10 can be used interchangeably, depending on which is simpler to use. For the data analysis here, Equation 8.10 was used to derive the decay time of the flux. The diffusivity D_B , which has the usual form of $length^2 / time$, is given by

$$D_B = \frac{a_1^2}{\tau}, \quad (8.11)$$

and the resistivity is related to the magnetic diffusivity by

$$\eta = \mu_0 D_B. \quad (8.12)$$

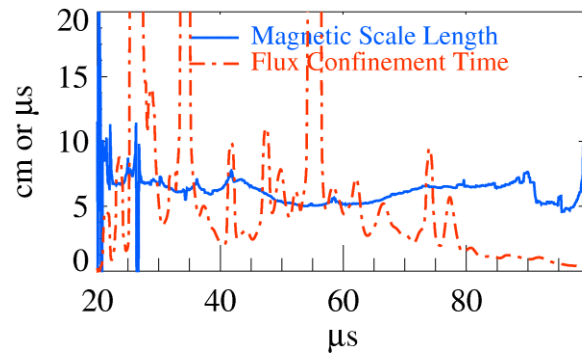


Figure 8.2: Spatial and temporal scales of the magnetic flux

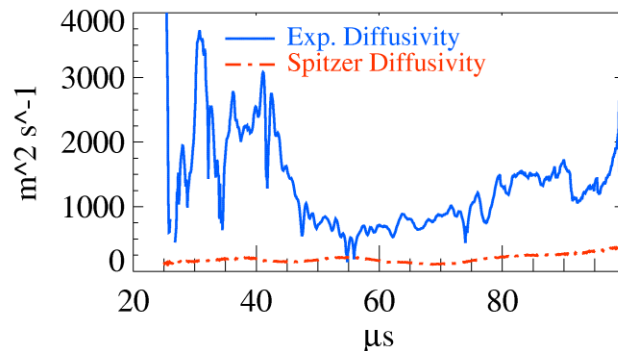


Figure 8.3: Magnetic diffusivity at the field null. Solid line is the value derived from magnetic field data, while the dashed line is the Spitzer value based on temperature and density estimates.

All three estimates of the resistivity as listed in Figure 8.1 agree fairly well with each other from approximately 40 microseconds through 70 microseconds. This is about all that can be expected, given that the FRC is formed at about 30 microseconds and begins dying at around 70 microseconds. As Figure 8.4 clearly shows, the measured resistivities differ from the Spitzer value by factors of 2-20. These differences are not unexpected given the history of similarly large differences measured on many other machines.^{43 46 51} It is actually somewhat surprising that the calculated values are so close to each other during the FRC lifetime.

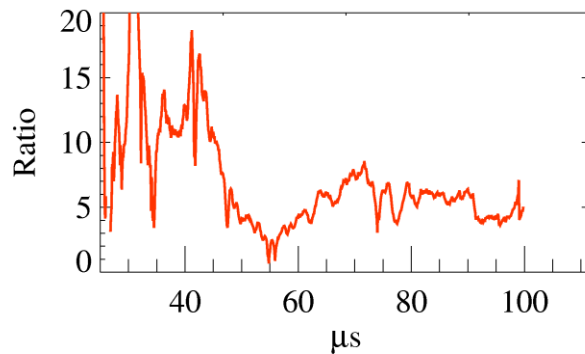


Figure 8.4: Ratio of measured resistivity to Spitzer value

The temporal variations in the resistivity can be partially explained by changes in the plasma density near the null region. Decreases in density in reconnecting regions have been correlated with increasing resistivity on the MRX device⁴⁴; this general pattern is also observed on the IFRC, and is illustrated in Figure 8.5. The three methods of measuring the resistivity, shown in Figure 8.1, are averaged together either geometrically or arithmetically, and plotted against the density at the null position in the axial center of the IFRC. The resistivity and density values are taken from a time window of $t = 30$ to 90 microseconds, which encompasses the equilibrium and decay stages of the FRC.

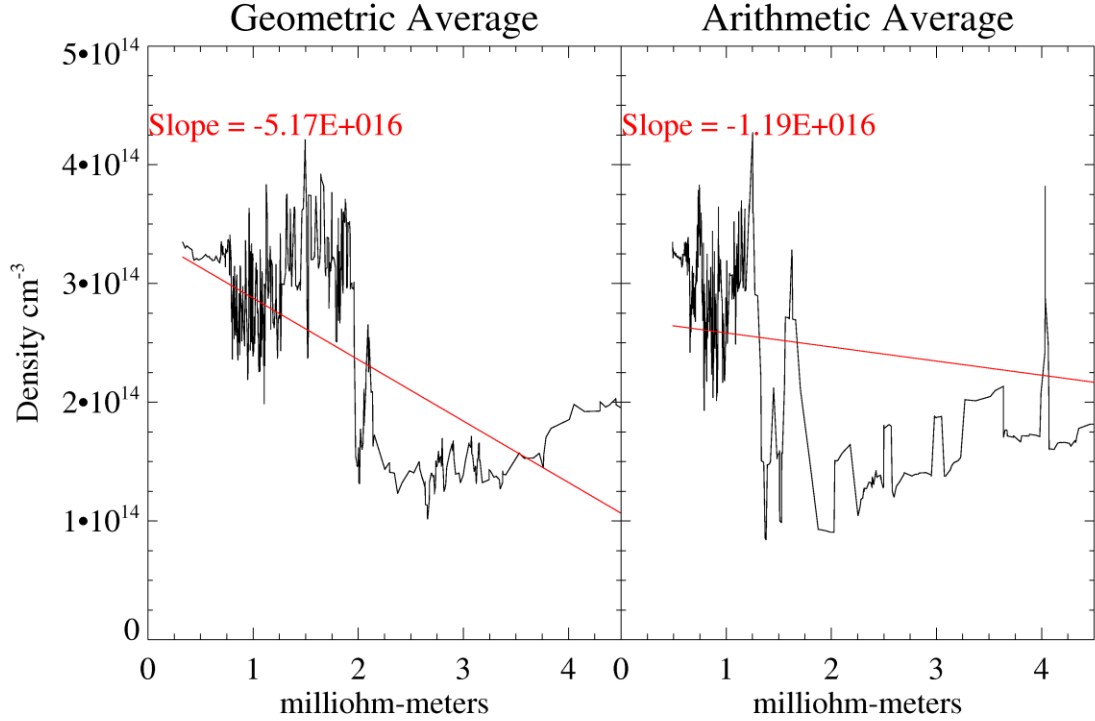


Figure 8.5: Variation of density at the null for two different resistivity estimates. Red lines are linear fits to the data.

The plasma resistance R_P is given by the ratio of the average loop voltage to the plasma current measured by the Rogowski coil, or

$$R_P = \langle V_{Loop} \rangle / I_{Rogowski} . \quad (8.13)$$

The temporal evolution of this quantity is given by Figure 8.6; it compares favorably with the resistance calculated by the (geometric) average resistivity, given by

$$R_\eta = \eta 2\pi r_{null} / (3a_1 * 10a_1). \quad (8.14)$$

In Equation 8.14, the length is estimated by the circumference of the plasma at the null radius and the axial and radial extent of the cross section is estimated to be $10 a_1$ and $3 a_1$ respectively where a_1 is the magnetic scale length. Both measurements agree in both magnitude and time evolution, which further supports the resistivity measurements.

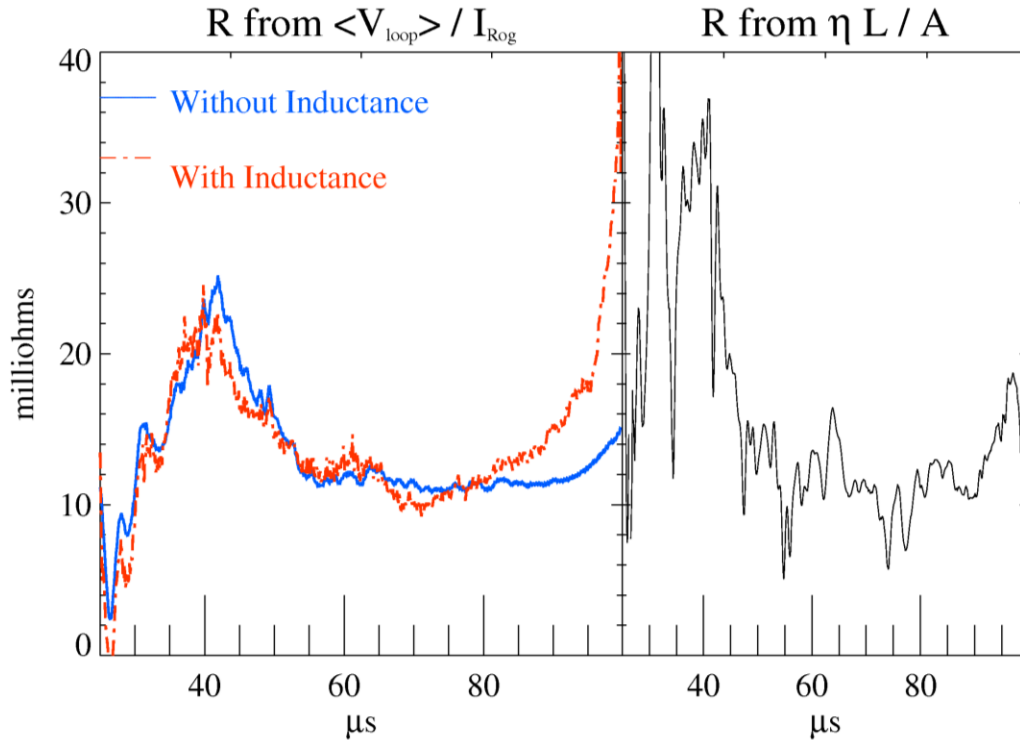


Figure 8.6: Average plasma resistance estimates. Plasma inductance is taken to be the ratio of the stored magnetic energy to the square of the plasma current.

8.2 Power Balance

Stored energy in plasma is divided into two main groups: electromagnetic energy and thermal energy. Studies of how the energies vary in time determine key plasma characteristics, such as the energy and particle confinement times, and help to quantify the quality of a particular experiment. An analysis of all channels that have significant power flows is beyond the scope of this thesis. That being said, there is enough information to evaluate a few of the terms in the power balance equation.

The electromagnetic power balance equation measures how the energy stored in electric and magnetic fields in plasma changes with time, and is given by

$$\frac{\partial W_{EM}}{\partial t} = - \int_A \mathbf{S} \cdot d\mathbf{A} - \int_V \mathbf{J} \cdot \mathbf{E} dV - P_{Radiation} . \quad (8.15)$$

Here \mathbf{S} is the Poynting vector, which estimates electromagnetic energy entering volume V that is encompassed by area A that is delivered by the field coils. \mathbf{J} and \mathbf{E} are the current density and electric field and together determine the amount of energy lost to resistive (ohmic) heating of the plasma. $P_{Radiation}$ lumps together power lost by all other radiative mechanisms, and the electromagnetic energy W_{EM} is given by

$$W_{EM} = \frac{1}{2} \int_V dV (\mathbf{H} \cdot \mathbf{B} + \mathbf{E} \cdot \mathbf{D}). \quad (8.16)$$

In this analysis, W_{EM} is taken to be solely comprised of the magnetic energy. This simplification ignores the energy stored in electric fields; for this assumption *not* to be valid, the electric field magnitude would have to be on the order of 3 MV/m for a relative permittivity of 1. While the permittivity may be larger, it is unlikely to be large enough for the observed electric fields of less than 1 kV/m to contribute much to the stored electromagnetic energy.

The thermal energy W_{TH} that is stored in the plasma can be written as

$$W_{TH} = \frac{3}{2} N \sum_m kT_m, \quad (8.17)$$

where N is the total number of particles in the test volume, and kT_m is the usual temperature for species m .

It is estimated by pressure balance analysis and has a rate of change given by

$$\frac{\partial W_{TH}}{\partial t} = \int_V \mathbf{J} \cdot \mathbf{E} dV - P_{Transport} , \quad (8.18)$$

where $P_{Transport}$ is a loss term containing all conducted power and power carried by particles that leave the system, with the resistive heating measured by $\int \mathbf{J} \cdot \mathbf{E} dV$ is a source term.

When Equations 8.15 and 8.18 are added together, the change in total energy W contained by the FRC can finally be stated as

$$\begin{aligned} \frac{\partial W}{\partial t} &= \frac{\partial W_{EM}}{\partial t} + \frac{\partial W_{TH}}{\partial t} \\ &= - \int_A \mathbf{S} \cdot d\mathbf{A} - P_{Transport} - P_{Radiation} . \end{aligned} \quad (8.19)$$

This mathematically states that the energy input to the plasma is solely from the electric and magnetic fields created by the flux coil and limiter coil, while losses are due to radiation, particle transport, and heat conduction.

The various terms defined in Equations 8.15 - 8.18 are shown in Figure 8.7. For this plot, the cross sectional area covers the axial positions between the mirror coils and radial positions between the flux and limiter coils, with z between ± 28.5 cm and r from 11-38 cm. The Poynting vector is determined by the values of E_θ and B_z at the maxima and minima radial positions. The magnetic and thermal energies are of the same order of magnitude; this is a characteristic of high beta devices of which the FRC is an example. The thermal energy is largest from 40 to 65 microseconds; this corresponds with the

equilibrium phase of the IFRC. The electromagnetic energy generally rises throughout the discharge as the current rises in the limiter coil. This is an undesirable feature of the IFRC design, as it results in radial pressure imbalances which cause the plasma to radially implode. As noted in Chapter 6, clamping the limiter current at a lower value would probably improve the lifetime of the IFRC.

The input power measured by the Poynting vector is matched closely by the ohmic heating term for most of the discharge, and shows that most of the energy delivered by the flux and limiter coils is dissipated by the plasma resistance with relatively little going to increase the magnetic fields. It should be emphasized that the ohmic heating term and power input term, while based on overlapping measurements, are calculated separately. That they agree so well with each other further supports the conclusions drawn from the measurements.

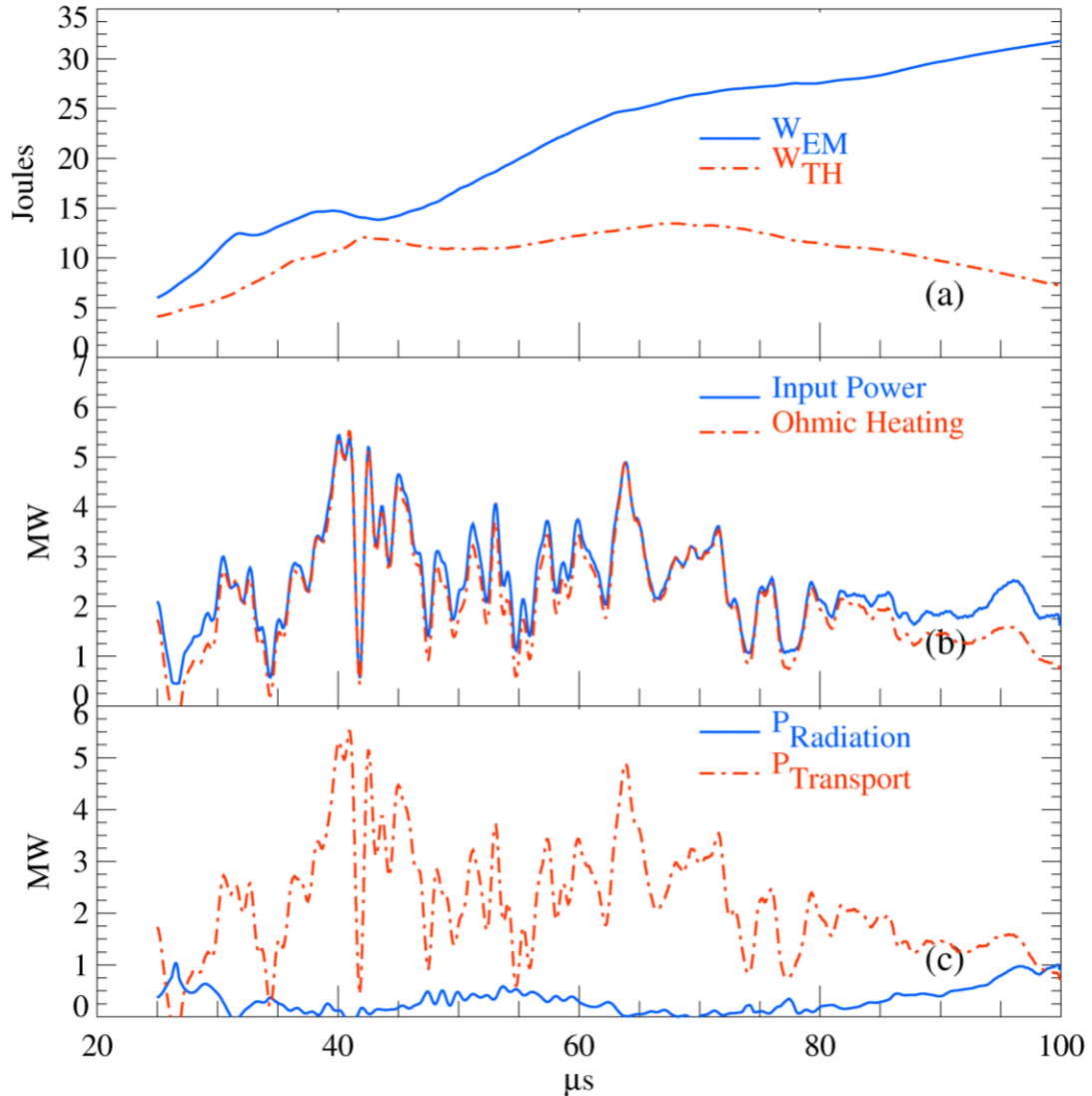


Figure 8.7: Power and energy estimates from the entire plasma volume. (a) Magnetic field and thermal energies, (b) input power and ohmic heating, and (c) estimates of power lost to radiation and plasma transport.

The loss terms in Equations 8.15 and 8.18 are the only terms not defined by measurements, and can thus be solved for. They are shown in Figure 8.7 (c) and illustrate the large amount of power carried by plasma transport. This is the dominant energy loss channel on most FRCs, and is particularly true in this instance as well. The radiated power is quite small, as should be expected since the plasma temperature is quite low. An independent calculation⁴⁵ of the power radiated by singly ionized carbon for

$n_e = 3E13 \text{ cm}^{-3}$, $n_{\text{carbon}} = 1E13 \text{ cm}^{-3}$, $T_e = 3\text{eV}$, and a volume of $2.5E4 \text{ cm}^3$ predicts a radiated power on the order of 750 kW, which is quite similar to the rough estimates derived in this chapter.

The terms in the power balance equations are estimated again in Figure 8.8 for a control volume defined by the separatrix. This quantifies how much energy is stored inside the closed field lines of the FRC and the various source and sink terms that govern the rate of change of the energies. The thermal energy is generally larger than the magnetic energy, which implies that within the region of closed field lines, the IFRC achieves an average beta of at least 1. This can be explained by noting that the separatrix position, as calculated numerically by finding the largest closed poloidal flux contour, may be an underestimate of the trapped flux volume. Integrating over a larger spatial extent would lower the beta, as the largest thermal pressure regions are already included in the current estimate. The rapid decay of stored energy from 38 microseconds onward is due to the steadily decreasing volume inside the calculated separatrix, and is a witness to the breakup of the IFRC into axially separated current rings and mostly open field lines.

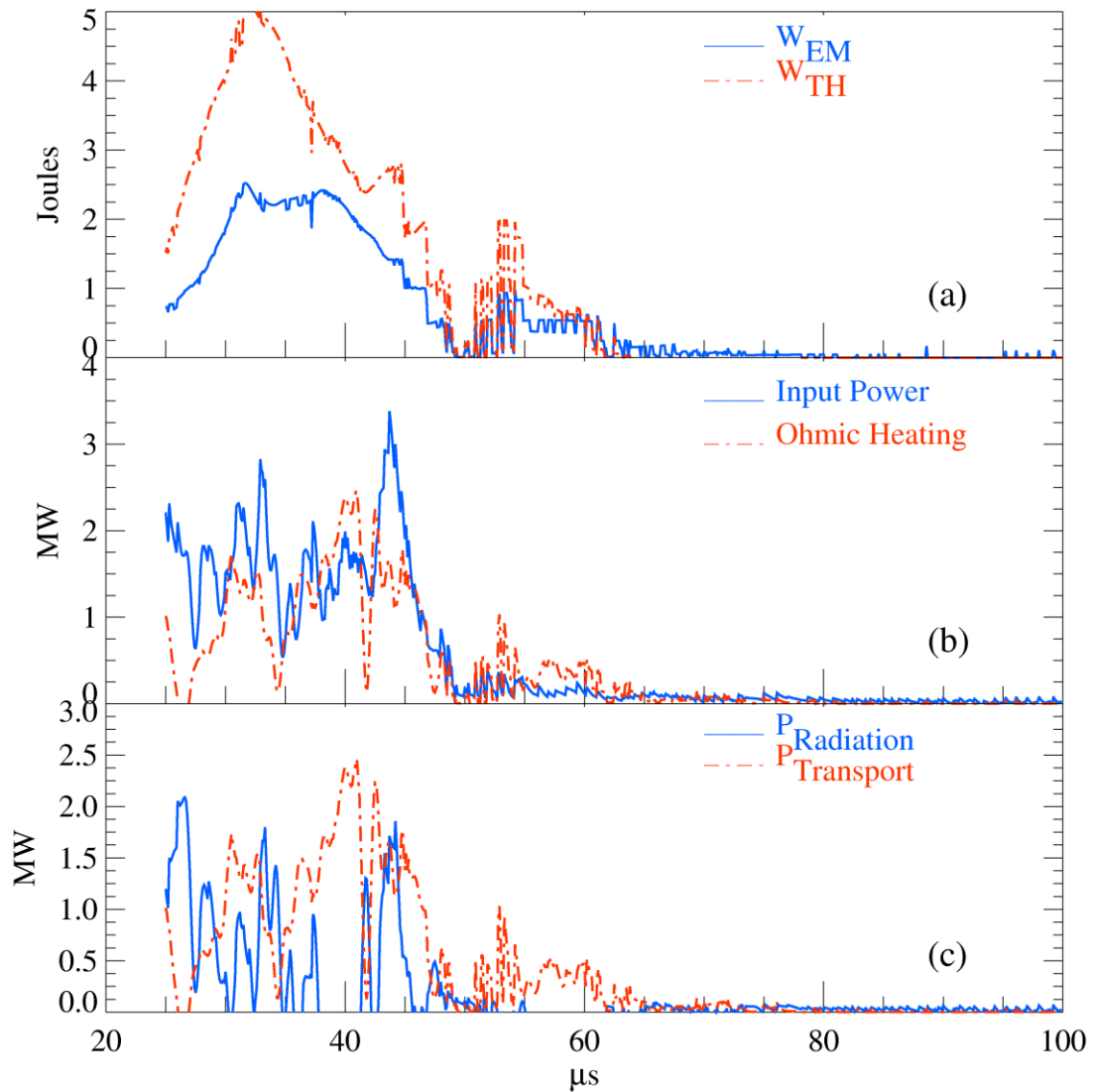


Figure 8.8: Power and energy estimates inside the separatrix. (a) Magnetic field and thermal energies, (b) input power and ohmic heating, and (c) estimates of power lost to radiation and particle loss.

Another sanity check on the various derived powers lends more support to their values. First, the input power to the plasma in the form of the Poynting vector is checked. The total amount of stored energy in the capacitor banks, listed in Table 3.4, is approximately 18.2 kJ. Of this, only the 5.4 kJ stored in the flux and limiter banks are available as energy inputs after the plasma guns produce the initial plasma. For the given

rise times of the field coils of ~ 110 microseconds, the maximum power that can be applied to the plasma is approximately 50 megawatts, much larger than the power levels observed. This is explained however by the large amount of power that goes into creating the magnetic field inside of the flux coil solenoid. For the measured value of flux coil inductance of $19.5 \mu\text{H}$, peak current of 13 kA, and rise time of 110 microseconds, the peak power creating the solenoidal B field is approximately 47 MW at 55 microseconds. Losses occur in the transmission lines, ignitrons, and capacitors themselves which also lowers the amount of energy that can be delivered to the plasma. The flux coil itself has a resistance of 50 milliohms which ignores losses in the capacitor bank and ignitron switch. The power dissipated in the lines peaks at 110 microseconds when the flux coil current is largest, with a magnitude of at least 8 MW. From this, measured input powers of 3-5 MW are what should be expected given the experimental design of the machine.

The thermal losses of 3-5 MW can be checked by comparisons with particle losses measured by the array of Faraday cups at one axial end of the machine. This calculation takes the measured currents by the Faraday cup array at one axial end of the machine and estimates the number of particles lost out each end plane, corrected for the measurement angle of each cup. This is necessary since lost particles will not have only axial velocities; the actual solid angle of each cup is approximately 0.054 steradians, which is less than one percent of the possible 2π steradians in which the velocities could lie. The loss rate is then multiplied by the electron temperature derived from spectroscopy to find the power carried out of the plasma by particles. The results are

shown in Figure 8.9, with $P_{Transport}$ smoothed over a 5 microsecond window. Immediately evident is the similar temporal evolutions; the Faraday cups accurately measure the transport losses, with a delay time of approximately five microseconds. The magnitudes are quite similar, which is a bit surprising given the uncertainties in how much of the velocity distribution the Faraday cups sample and the lack of any inclusion of radial particle losses.

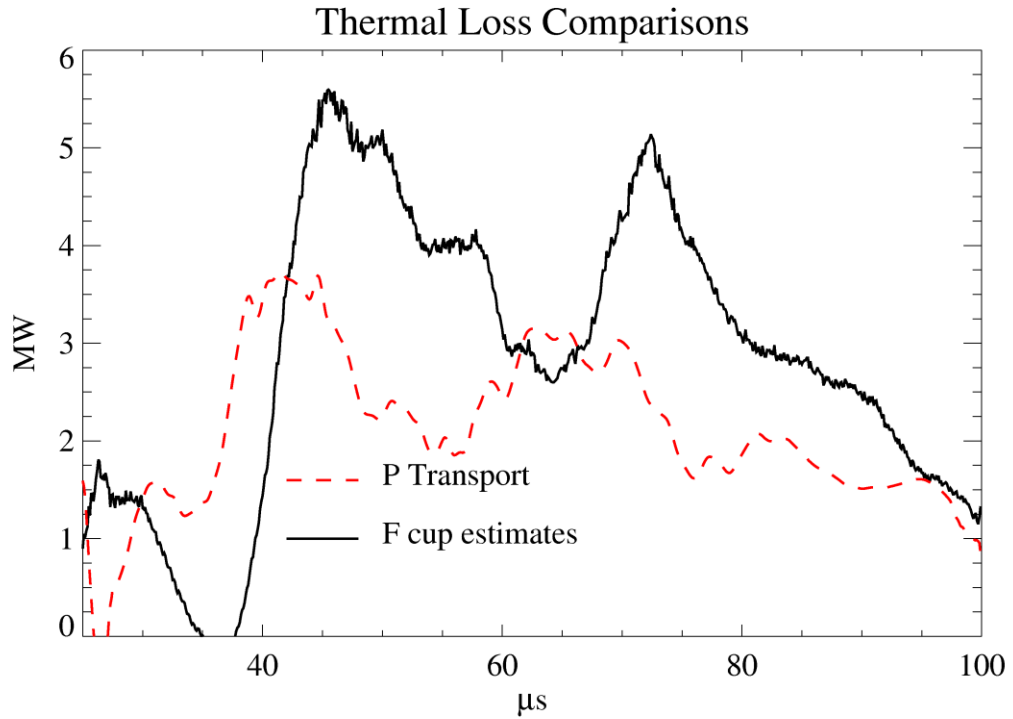


Figure 8.9: Comparisons of thermal losses.

8.3 Confinement Times

Armed with knowledge of the stored energy in the plasma and the loss rate, the energy confinement time τ_E can simply be calculated as¹⁴

$$\tau_E = \frac{W_{TH}}{P_{Transport}} \quad (8.20)$$

For thermal energy measured in Joules and power measured in megawatts, the confinement time is units of microseconds. Knowledge of the particle inventory N from pressure balance and the particle loss rates \dot{N} measured by the Faraday cups also allows an estimate of the particle confinement time τ_N . It is defined as

$$\tau_N = \frac{N}{\dot{N}} \quad (8.21)$$

Both quantities are shown as functions of time in Figure 8.10. Both time scales are quite short compared with the 40 microseconds over which field reversal is maintained.

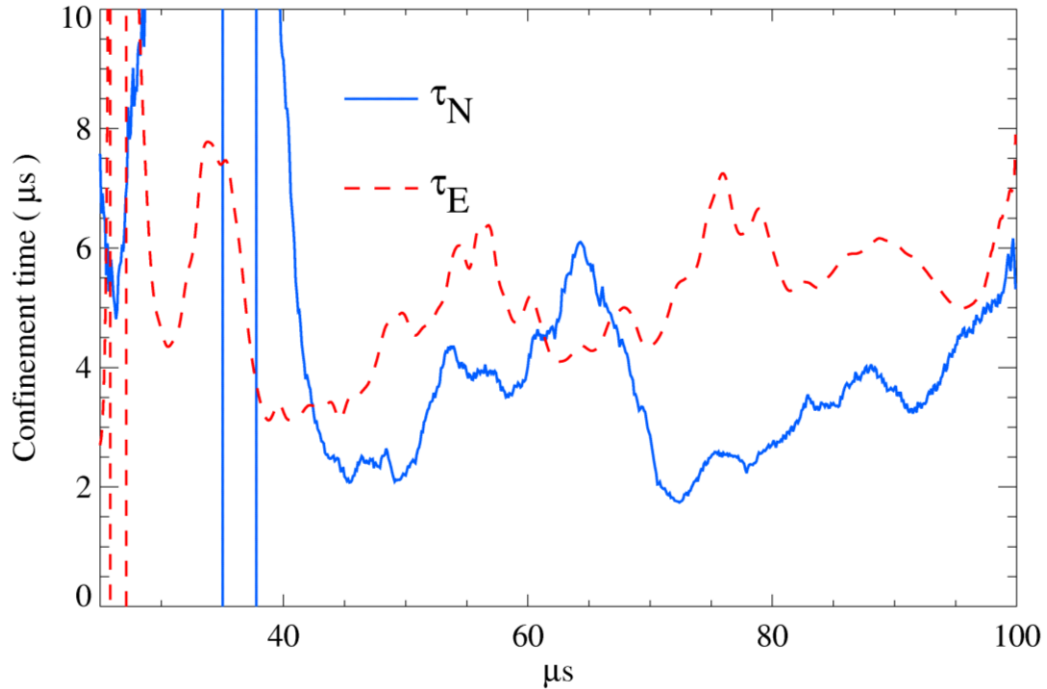


Figure 8.10: Confinement times

8.4 Discussion

Multiple methods have yielded similar results of the plasma resistivity and resistance. When compared with the Spitzer value, the measured resistivity is anomalously large, a feature seen in almost all plasma devices. It does fall into the same ranges seen on other FRC devices, such as on the TS-4 device⁴⁶ and the MRX

experiment.⁴³ Chapter 9 will discuss measurements of fluctuations that have been proposed to be the cause of the anomaly.⁵¹

The particle and energy confinement times are quite short, at only 10-20% of the IFRC equilibrium time. As shown in the LSX review paper¹⁴ and refined by Ryzhkov⁴⁷, particle confinement times in microseconds have been shown to vary with the separatrix radius and ion gyroradius as

$$\tau_N \sim 21 \frac{r_{sep}^2}{\rho_{i0}^{1.6}}, \quad (8.22)$$

while the energy confinement time scales as

$$\tau_E \sim 13 \frac{r_{sep}^2}{\rho_{i0}^{1.35}}, \quad (8.23)$$

The separatrix radius for this analysis is taken to be the distance from the flux coil to the last closed flux surface near the limiter coil, and has a distance of approximately 15-20 cm. The ion gyroradius for a peak field of ~100 Gauss and temperature of 4 eV is equal to 2 cm. Predictions of over 1 millisecond result from these scaling. From this, it is obvious that the IFRC does not confine energy or particles very well when compared with higher power machines.

Chapter 9: Spectral Analysis

Spectral analysis of B-dot data has identified spatially localized fluctuations from the hydrogen cyclotron frequency up to the lower hybrid frequency range. Subjects included in this chapter are the time averaged spectra of the magnetic field components, their spatial distribution and temporal variations, and the classification of the fluctuations by possible characteristic modes.

All analysis of the spectral content is done by the continuous wavelet transform, described in Chapter 5.8. This tool allows both time resolved and average spectra to be found. Averages are done by first calculating the spectra for each probe, and then averaging the results together.

9.1 Magnetic Field Spectra: Radial Array

The ensemble average of the spectra of each magnetic field component is shown in Figure 9.1. Also shown are the spectra with the power due to background fields only subtracted out. The measured spectra are almost entirely dependent on the presence of plasma, with a small contribution to the B_z and B_r spectra below ~ 50 kHz. The peaks at 2.5 and 5.0 MHz are due to the discrete nature of sampled data at a sampling frequency of 10 MHz.

The spectra do not have a simple variation of amplitude with frequency. A power law fit seems to be the most appropriate fitting function since the spectra is

predominately linear on a log-log plot. B_z has a power law decay of amplitude with frequency, with an exponent of -3.08 in the region of 100 kHz to 2 MHz. B_r and B_θ have slightly steeper decays in this frequency range, but have a much lower decay power below 100 kHz. The lack of any peaks in the spectra shows that the fluctuations do not have a characteristic oscillation frequency when averaged over spatial and time windows. Temporal inhomogeneities in the spectra can only be seen by looking at the spectrogram of data; this allows the power at various frequencies to be localized in time.

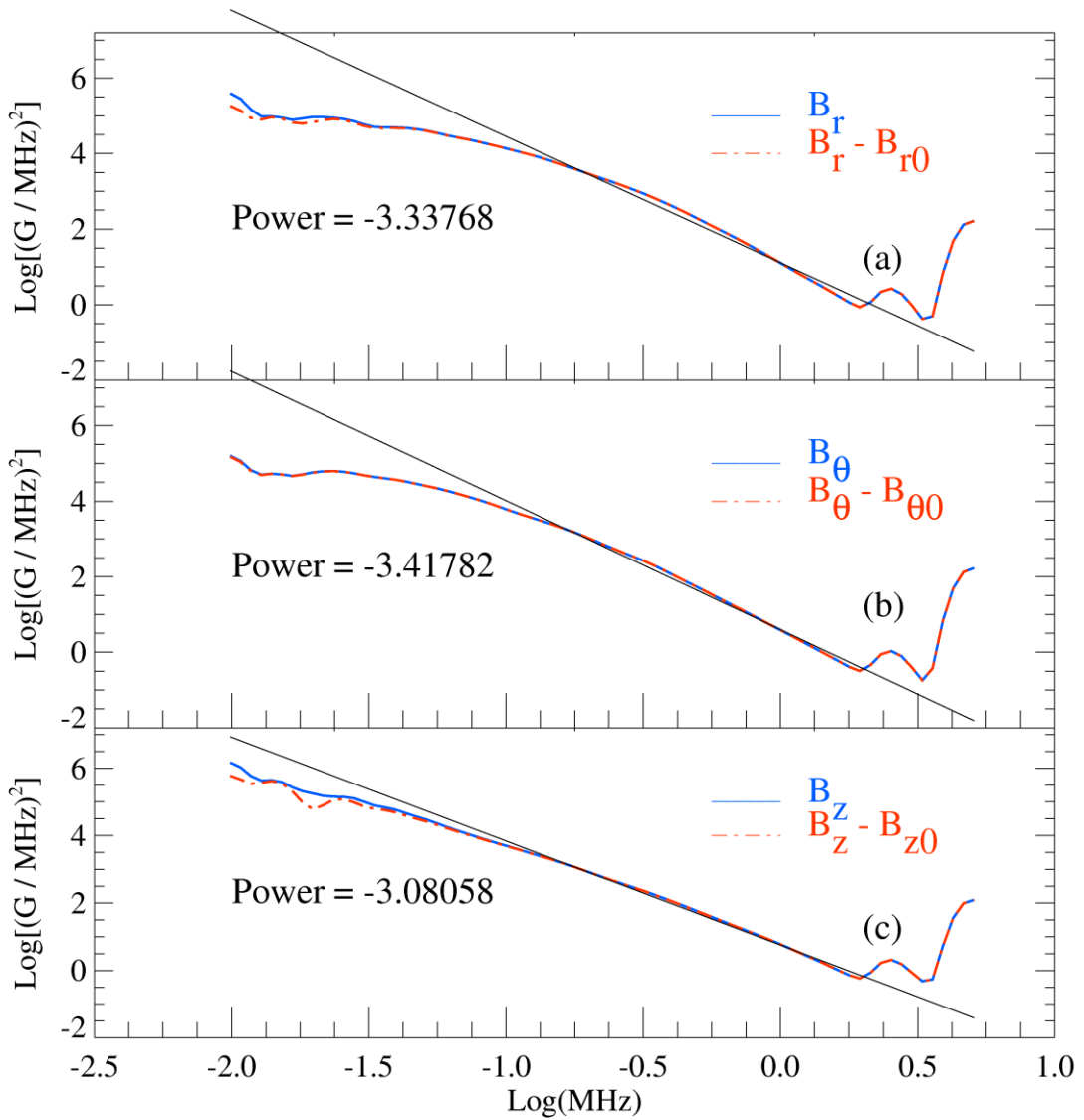


Figure 9.1: Magnetic spectra for (a) B_r , (b) B_θ , and (c) B_z .

Background spectra subtracted for each of the three components are also shown. Note: Spectra are based on spectrogram data from 20-90 microseconds.

The average time evolution of the spectra is shown in Figure 9.2. These plots show that the frequency at peak power does vary with time; it is only when averaging over the FRC lifetime that we get the power law decay. The prominent feature at 20 microseconds near 500 kHz is due to noise pickup from the flux coil. The shape of this feature is indicative of a time signal that has high frequency components and does not last very long. The apparent increase in amplitude at higher frequencies as time progresses is a natural result of the changing window sizes of the wavelet transform. Since low frequencies have long time windows, they ‘see’ the noise first with higher frequencies ‘seeing’ the noise at later times as their windows overlap. This concept is graphically demonstrated in Figure 9.3. The step discontinuity creates a v-shaped pattern in time-frequency space, with similar features occurring at the starting and ending times due to the finite number of samples in the test waveform. The dashed lines mark a ‘cone of influence’ or COI³⁵, below which the spectrogram cannot be fully trusted. Mathematically, the COI is determined by how quickly the wavelet decays in time at a particular frequency. For the analyses presented here, the COI has a width in time equal to $2\sqrt{2} / \text{frequency}$. The test signal at 470 kHz shows clearly, even though the signal to noise ratio is only two.

Figure 9.2 has a reference COI centered on a time of 41 microseconds. While there is some similarity between the shape of the spectrograms and the effects of a step function, it is apparent that there is a significant amount of power that occurs outside of

the COI. This indicates that the fluctuations last long enough to have their amplitude and frequency unambiguously identified. It also indicates that the fluctuations do not last for many periods, which means that the frequency content is non-stationary.⁴⁸ Fluctuations are present during the entire FRC equilibrium phase, with peak amplitudes occurring from approximately 35 to 60 microseconds. All three components have highly peaked spectra during the majority of the IFRC lifetime (27 to 68 microseconds,) with average frequencies of over 100 kHz.

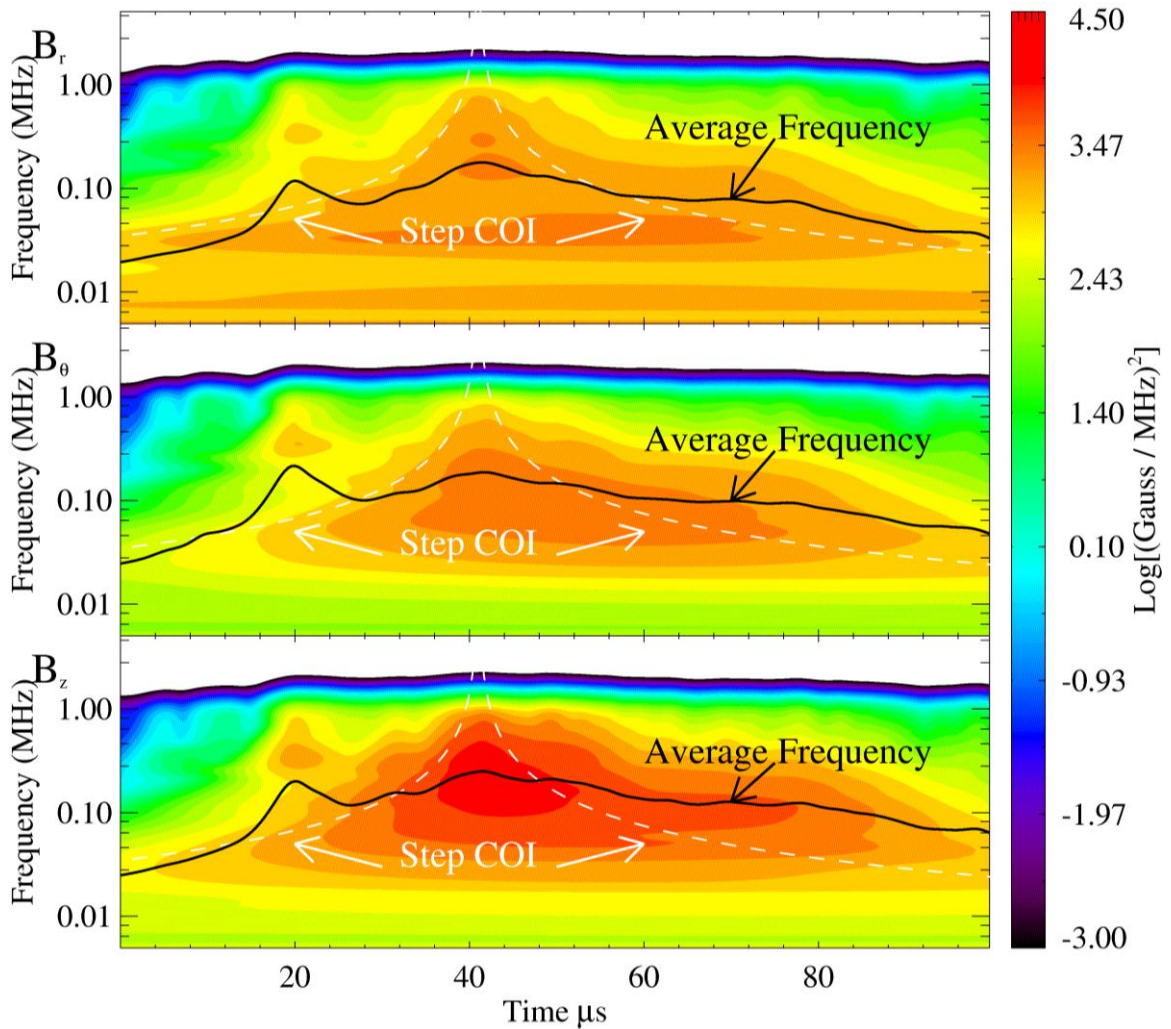


Figure 9.2: Average spectrograms for the three magnetic field components. Average power-weighted frequency for each component is overlaid, as well as a cone of influence *COI* indicating the length of time for each frequency to be well defined. Inputs are filtered B-dot signals, with low pass frequency of 1 MHz.

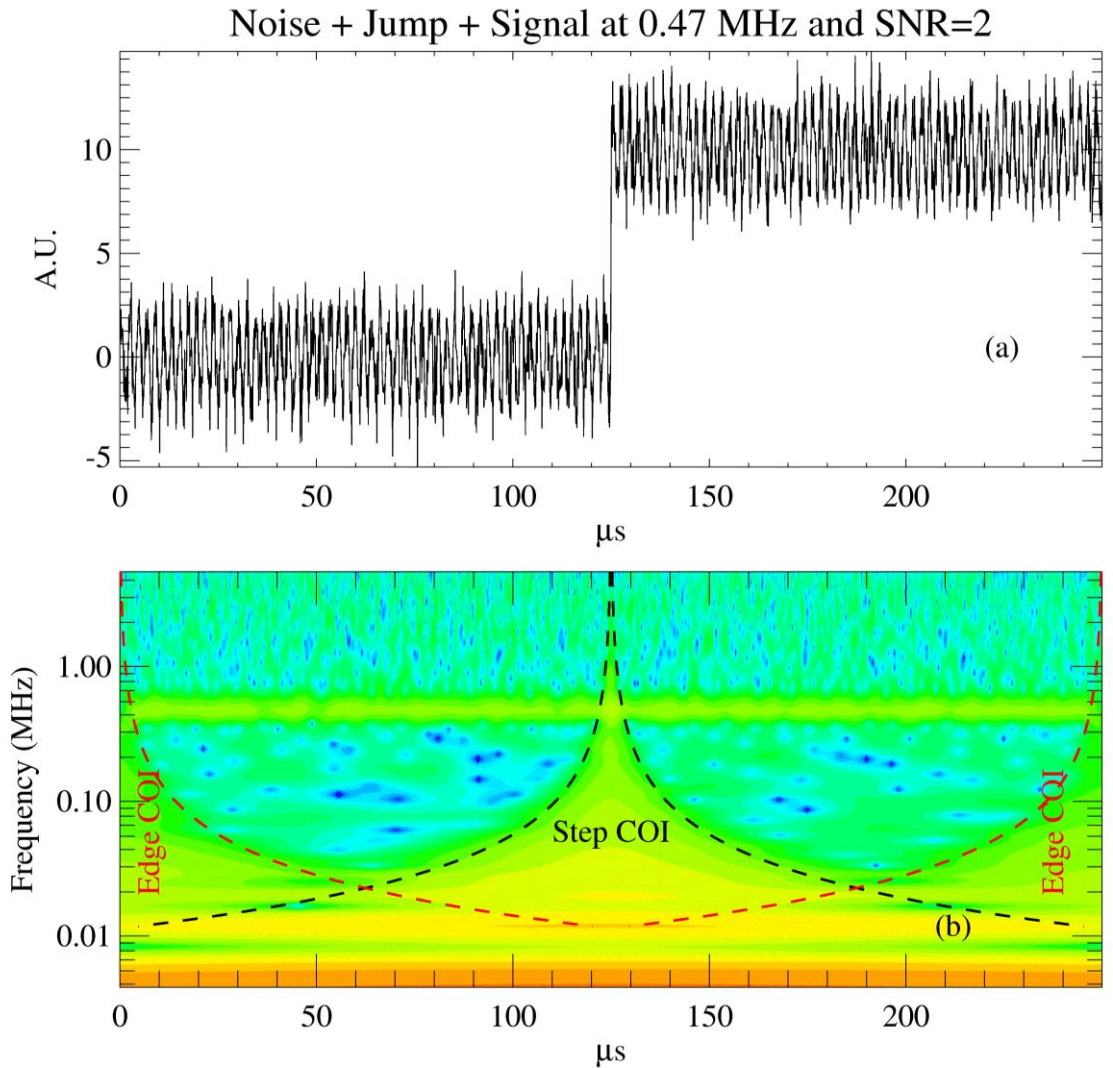


Figure 9.3: (a) Step function with SNR of 10 and signal with SNR of 2. (b) Spectrogram of the data, with cones of influence demarcating edge effects and the step discontinuity.

The axially averaged radial distribution of power in three different frequency bands is shown in Figure 9.4. The power distribution is generally centered on the null position, with an approximate width of 10-15 cm. This is similar in size to the scale length of the radial gradients in the equilibrium B_z field. It is interesting to note that the fluctuation power is largest in B_r , especially in the 0.25 to 0.5 MHz band. We do see

splitting and merging of the azimuthal current ring throughout the average NCP discharge; the larger power in B_r is a direct result of these variations.

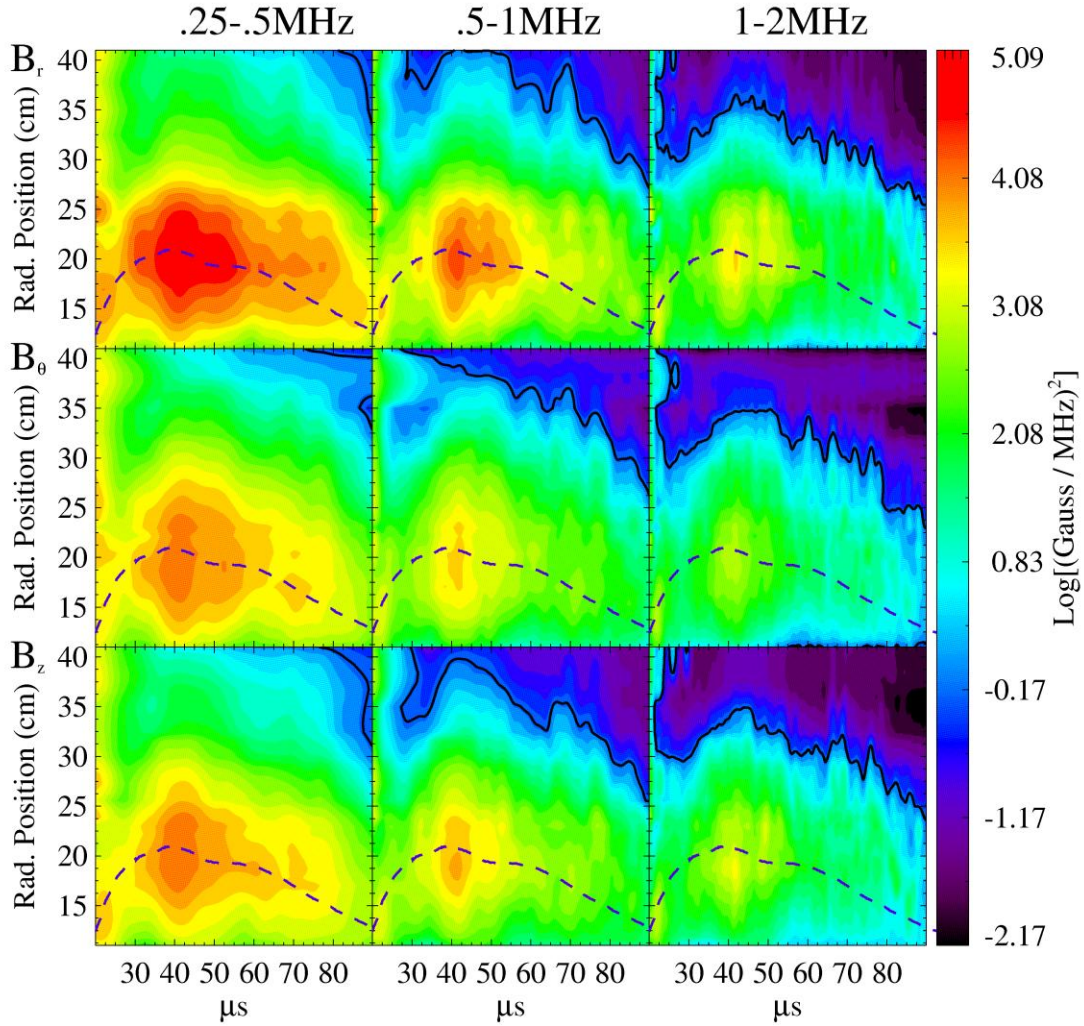


Figure 9.4: Amplitude of magnetic fluctuations in three frequency bands as a function of time and radial position. Dashed line is the approximate position of the null.

The spatial variation at 43 microseconds is shown in Figure 9.5. The fluctuations are generally symmetric about the midplane, centered on the null, and exist primarily inside of the separatrix. The fluctuation amplitudes have decreasing magnitudes as the magnetic field strength increases.

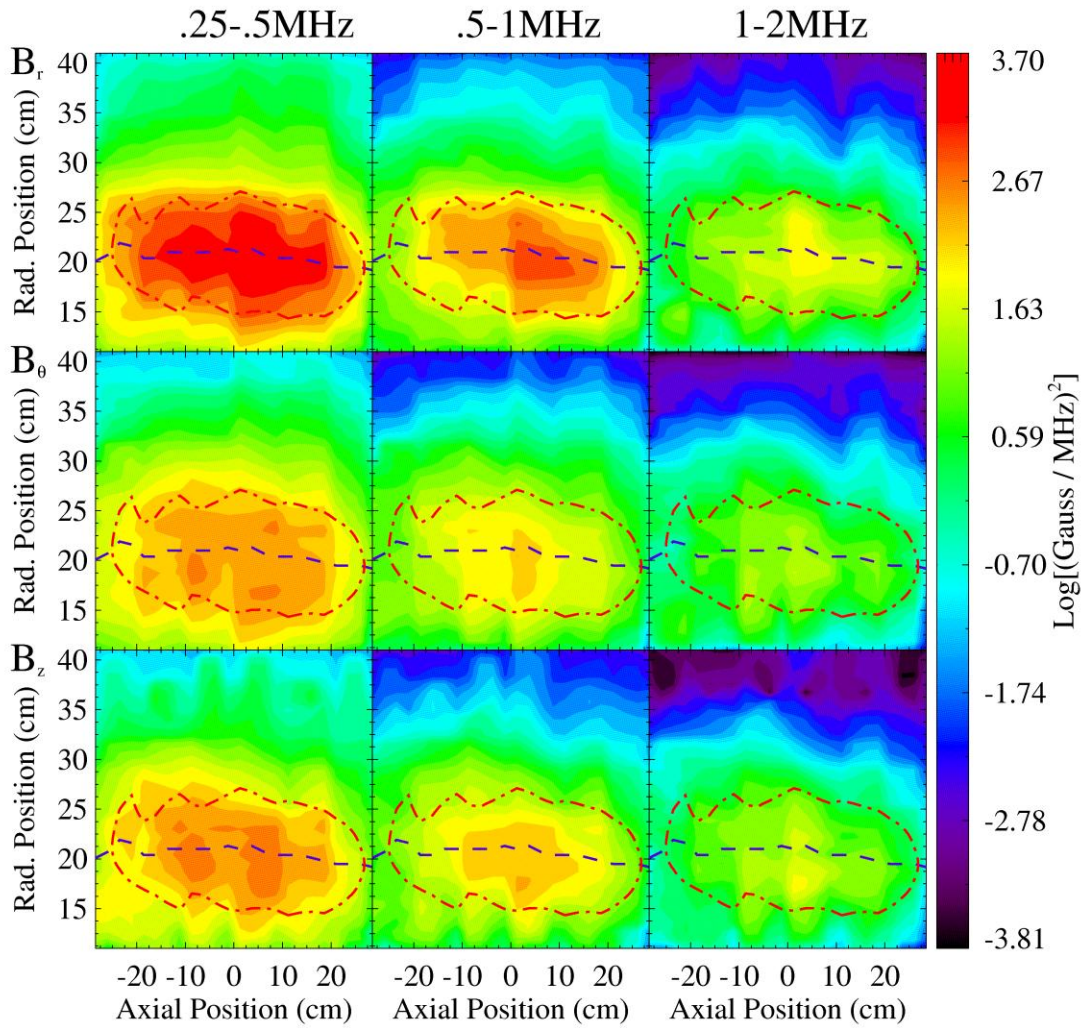


Figure 9.5: Spatial variation of magnetic fluctuations in three frequency bands as a function of axial and radial position at 43 microseconds. Null position is marked with a dashed line, and the separatrix is marked with a dash-dot line.

The variation of the shapes of the spectrograms with frequency for each component is shown in Figure 9.6. The spectrogram from 0.25 to 0.5 MHz is taken to be the reference distribution that the spectrograms in the other two frequency bins are compared to. The plots in Figure 9.4 are produced by first dividing each reference plot in Figure 9.4 by its maximum value. The plots in the two right columns are then divided by their value at the same time and position where their reference plot maximum occurred.

If the radial and temporal evolutions are identical as the frequency increases, the right two columns would be identically equal to 1.0, or 0 on a logarithmic scale. This is not the result that we see. Regions where the resulting contour is greater than zero are where the power at a particular time, frequency, and radial position is relatively higher than the reference case. Likewise, regions less than zero indicate relatively less power than the low frequency reference. Fluctuations in the two higher frequency bins generally peak later in time than the lowest bin for the radial and axial components. The radial fluctuations in the 1-2 MHz bin also are relatively stronger farther out in radial position than the lowest frequency bin. This would indicate that the fluctuations in the 0.25 to 0.5 MHz bin are more tightly confined to the null region, while higher frequencies are present over a wider range of radial positions. Changes in the radial field at large radii could lead to changes in the local flux contours from open to closed; this is consistent with the Faraday cup measurements (see Chapter 6) that do indicate that the peak losses occur predominately at larger radii.

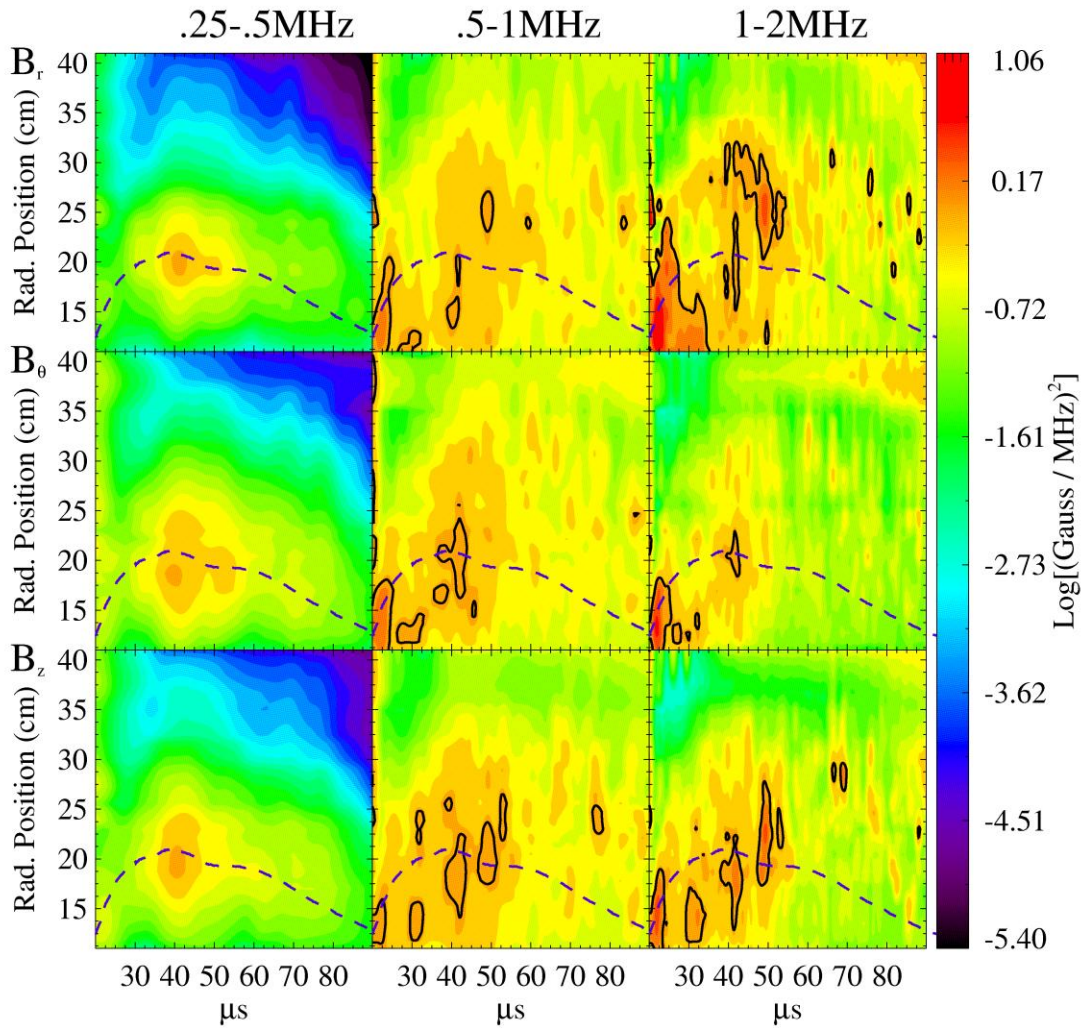


Figure 9.6: Spatial variation of the normalized magnetic spectra in three frequency bands as a function of time and radial position. Null position is marked with the dashed line and the zero contour is marked with the solid black line.

A similar analysis is done for the distribution of power in the axial and radial dimensions at 43 microseconds. This comparison of profiles shows regions where the power is relatively more concentrated. The power in the two higher frequency bands is distributed over a larger area than the 0.25-0.5 MHz band; this indicates that though the power decreases with frequency, the fluctuations are present over more of the plasma. An interesting feature in the 1-2 MHz bin for all three components is a structure that has

a periodicity of three moving along the separatrix. This possible mode structure will be discussed more fully in Chapter 10.

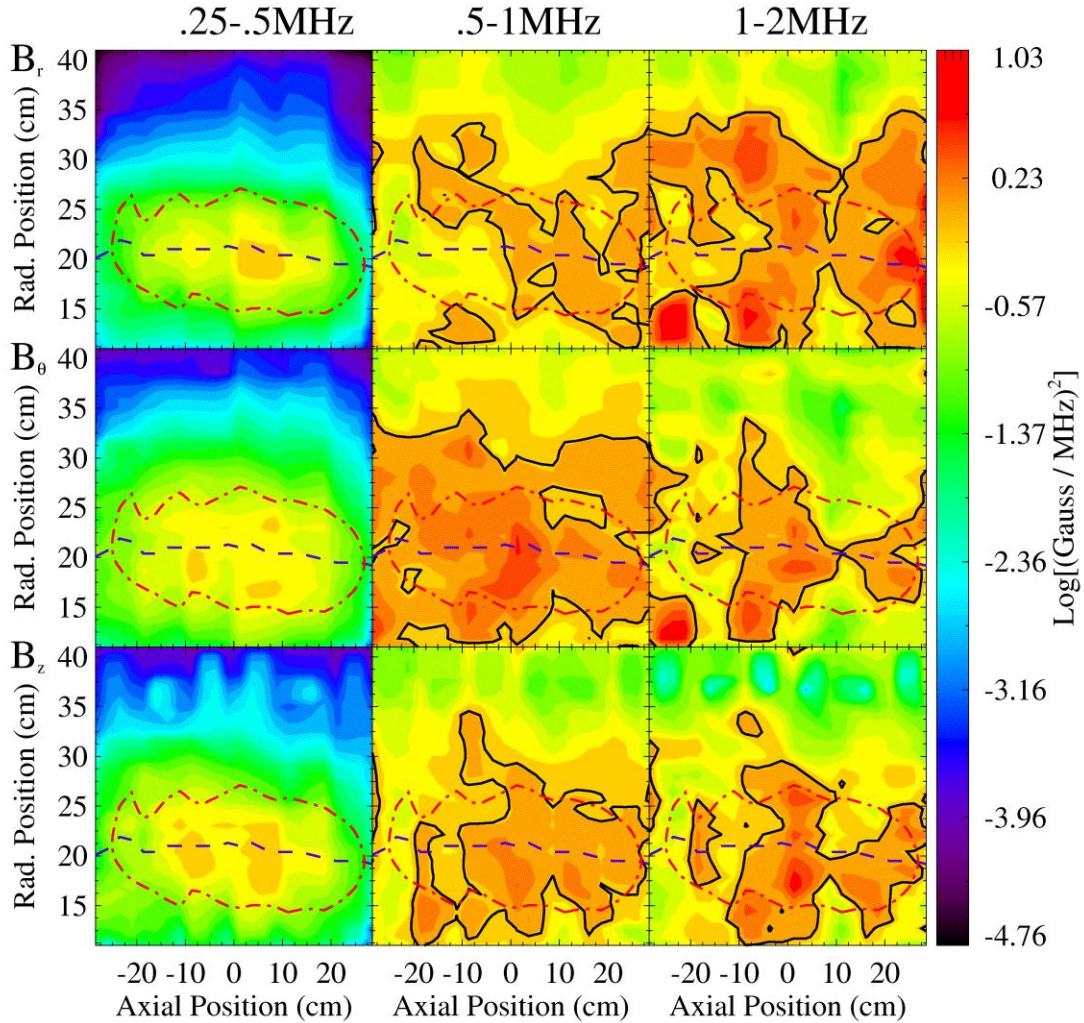


Figure 9.7: Spatial variation of the normalized magnetic spectra in three frequency bands as a function of axial and radial position at 43 microseconds. Null position is marked with a dashed line, and the separatrix is marked with a dash-dot line. Solid black line indicates the contour equal to zero.

The spectrograms of Figures 9.2 and 9.4 prove that the time evolution of the magnetic fields in the IFRC is nowhere near stationary in a statistical sense. The manner in which the signals at particular times, frequencies, and positions are related to each

other has many possible outcomes. One interesting one is that the time signal of a particular probe may sample a frequency ‘chirp’ in time. This could be due to the dispersion of a particular wave or a change in the plasma parameters that affect the particular fluctuation.

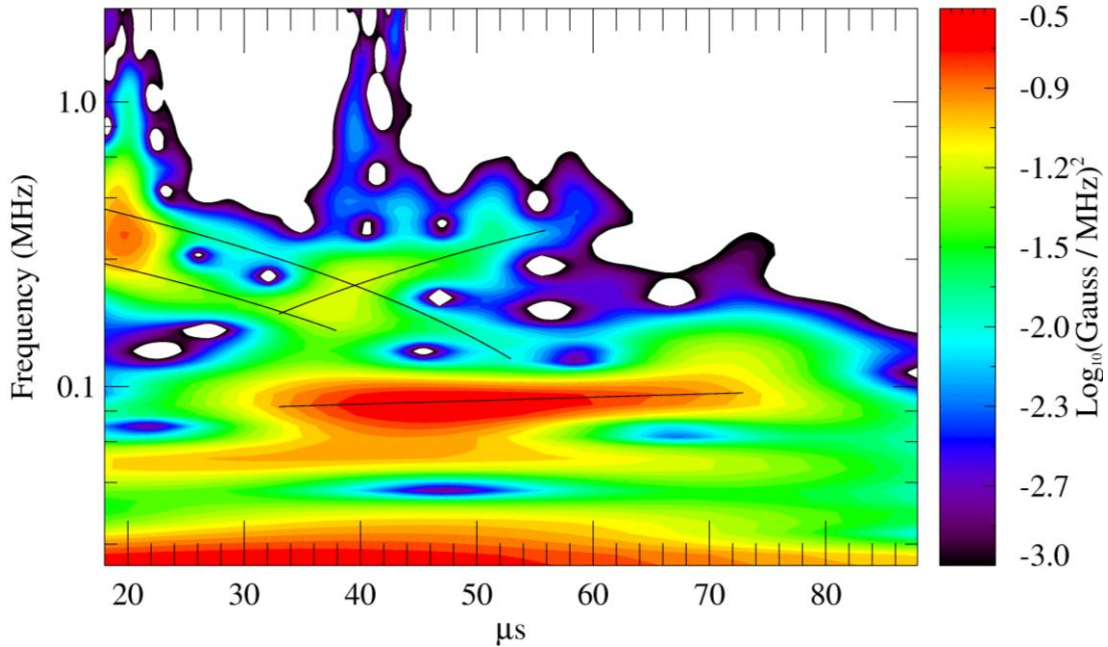


Figure 9.8: Four chirps present in Shot 5672 at $r = 32.5$ cm

Figure 9.8 is a spectrogram from a single B_z probe from Shot 5672. There are four apparent chirps that are present in this data. All of them last for many wave periods; this rules out sharp discontinuities at a particular time leading to COI broadening. A model for a chirp can be written as

$$chirp(t) = A(t) * \cos \left(\left[f_0 + \frac{df}{dt} * t \right] t \right), \quad (9.1)$$

where $A(t)$ is the amplitude, f_0 is a starting frequency, and df/dt is a frequency shear rate. The different parameters are listed in Table 9.1. The four chirps have total frequency changes over their lifetime ranging from 44 to 117 percent.

	Start Frequency (kHz)	Frequency Shear (kHz / μ s)	Frequency Change (%)
Chirp 1	420	-10	-80.95
Chirp 2	270	-6	-44.44
Chirp 3	280	7	60
Chirp 4	85	2.5	117.65

Table 9.1: Chirp parameters

Unfortunately, the chirps that are present in the data do not have the same temporal and spatial locations in every shot, nor do they always have the same chirp parameters. Identification of chirps to this point has been done by identifying them from a single time trace and manually fitting linear functions to fit the peaks in the resulting spectrogram. Until an automated identification program can be implemented, further analysis of chirp properties in this dataset will be left for future work.

9.2 Magnetic Field Spectra: RF B-dot

The frequency content of magnetic field fluctuations measured by B-dot arrays has been completed, but the data are limited in frequency resolution and range by the relatively low frequency response of 1 MHz of the B-dot probes, as well as the slow sampling rate of 10 MHz of the digitizers. Higher frequencies have been measured by a single B-dot probe (RF B-dot) with an upper frequency limit of approximately 40 MHz and digitized by a 200 MHz 12 bit digitizer.⁴⁹ Measurements were taken at various radial positions at an axial location of $z = -10$ cm. Figure 9.9 is produced from an ensemble of 84 shots covering nine radial positions. Of particular note is the variation of fluctuation amplitude with position. The majority of the power is bracketed by two different characteristic frequencies; the lower hybrid frequency serves as an upper bound, with the hydrogen cyclotron frequency bracketing the lower frequency edge of the power

distribution. The lower hybrid frequency, denoted f_{lh} , is defined as the local value of the geometric mean of the ion and electron cyclotron frequencies. These measurements are consistent with the radial probe array results, while extending the frequency range to unambiguously identify the upper frequency bound of fluctuations.

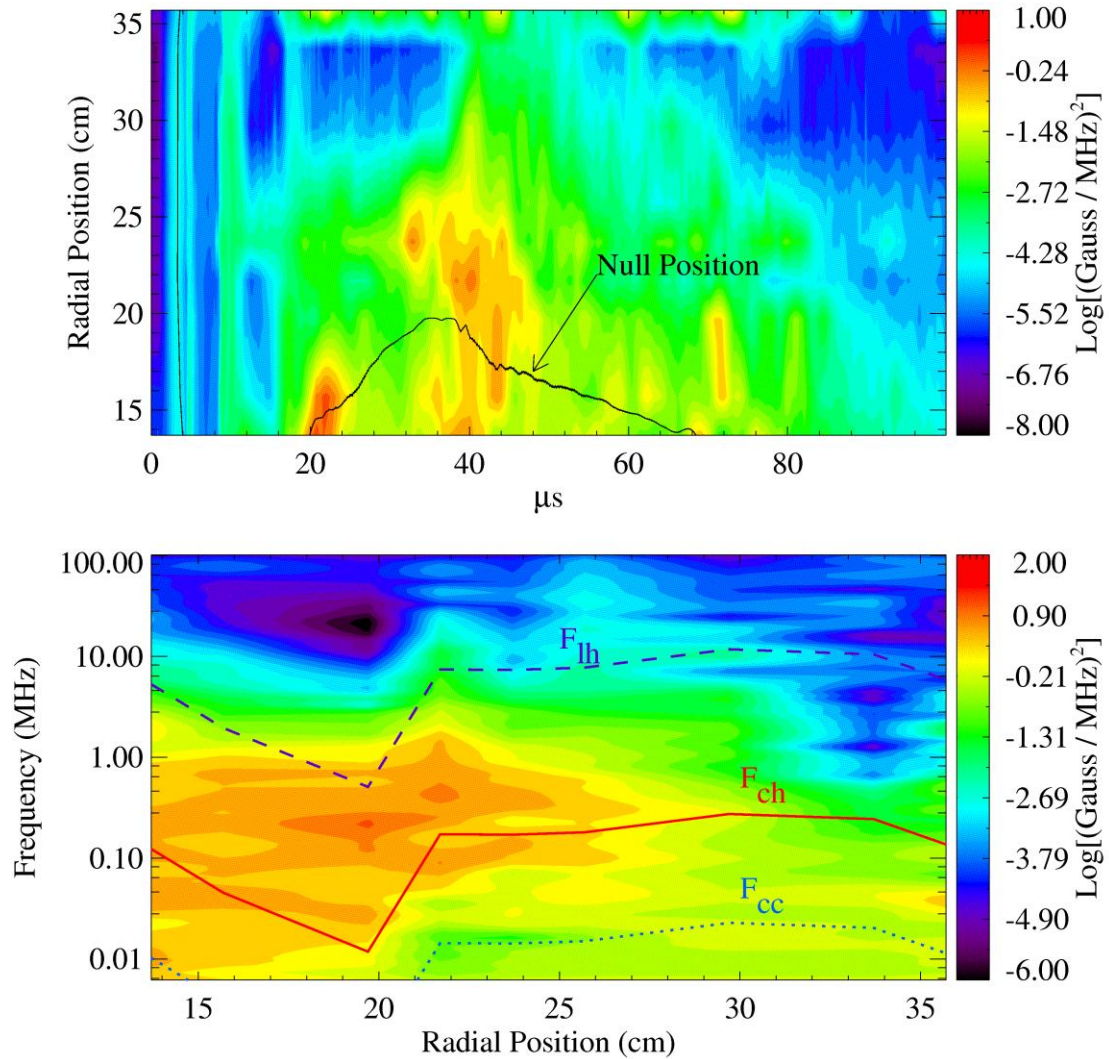


Figure 9.9: Top: spectrogram of RF B-dot data, averaged from 1 to 20 MHz. Bottom: radial distribution of spectrum at $t = 40$ microseconds. The lower hybrid, hydrogen cyclotron, and carbon cyclotron frequencies are also plotted. Note: the three frequencies use local values of B_z , which passes through zero near 20 cm but is not identically equal to zero at the sampled points.

Delving a bit deeper into the spatial structure of the power distributions, Figure 9.10 shows spectrograms where the amplitude is equal to the sum of the power at the local value of the hydrogen cyclotron frequency and the lower hybrid frequency. Figure 9.10 (a) is produced by summing the total power that is within the range of 0.8 to 3.5 times the local hydrogen cyclotron frequency. There are distinct peaks in the power away from the null position from 40 to 50 microseconds, with peak powers following the null position before and after this time range. As Figure 9.11 shows, the radial gradient in the axial magnetic pressure has a similar spatial and temporal structure as Figure 9.10 (a). Since the plasma is in radial pressure balance, peaks in the gradient of the magnetic pressure also correspond to peaks in the gradient of the thermal pressure. Both mechanisms are sources of free energy which can drive instabilities.

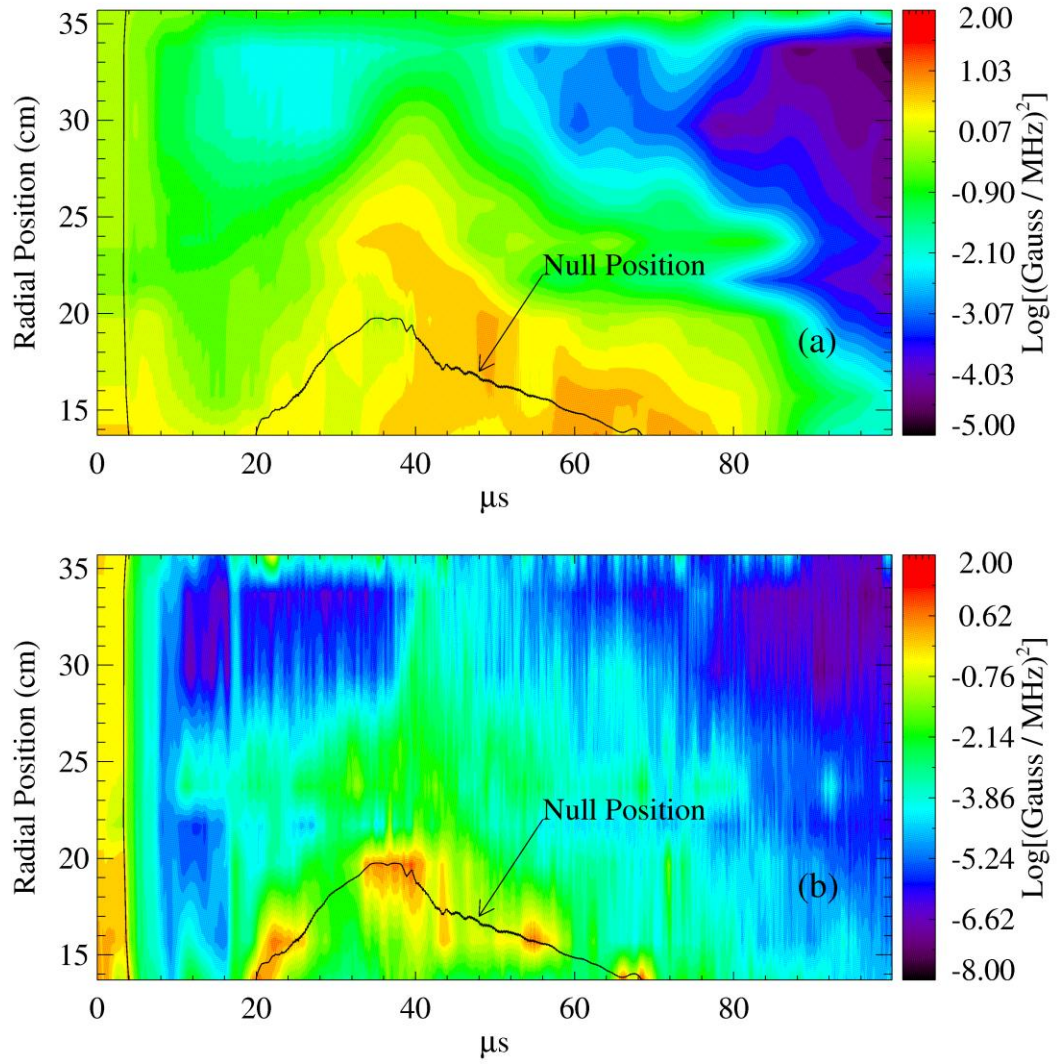


Figure 9.10: Total power at the local (a) hydrogen cyclotron frequency and (b) lower hybrid frequency as a function of radial position and time.

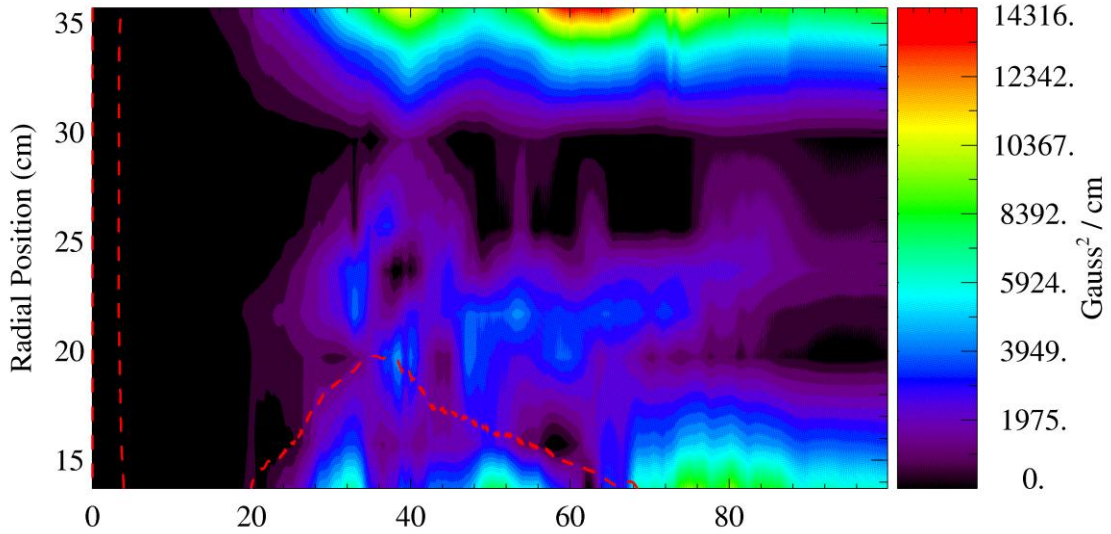


Figure 9.11: Absolute value of ∇B^2 . Approximate null position is shown by the dashed line. Edge effects at $r > 30$ cm can be ignored.

The majority of the power in the lower hybrid frequency band tracks the position of the null, and has a radial width of less than 5 cm. Given that the spectrum peaks between the hydrogen cyclotron (f_{ch}) and lower hybrid (f_{lh}) frequencies, and that the power in this range is centered near the magnetic null, it is quite likely that these measurements are of lower hybrid drift instability (LHDI) turbulence.^{50 51 52} This instability is characterized by a dependence on large plasma beta, with a broad frequency spectrum also peaking between f_{ch} and f_{lh} .

There is a secondary peak in the lower hybrid power at $r = 24$ to $r = 30$ from 25 to 60 microseconds. The plasma parameters are quite different in this region, with a lower density and higher B field. This could indicate another region of instability, which has yet to be characterized.

The data measured by the RF B-dot probe agree fairly well with magnetic field measurements made by the movable B-dot array. Fluctuations are still generally centered on the null position, and have a similar spectrogram evolution in time-frequency-position space. As Figure 9.12 illustrates, the spectra in the *RF B-dot* dataset agrees fairly well over a wide frequency range, and peaks at the same frequency as the spectra derived from the Radial B-dot array. The sharp break in the radial array spectra is due to software filtering of the time traces, with a low pass frequency of 1 MHz. The RF B-dot spectrum has larger amplitude at lower frequencies, likely due to sampling near the axial midplane where fluctuations are much stronger. The radial array includes field measurements near the plasma edges, and even outside of the limiter coil where no plasma is present.

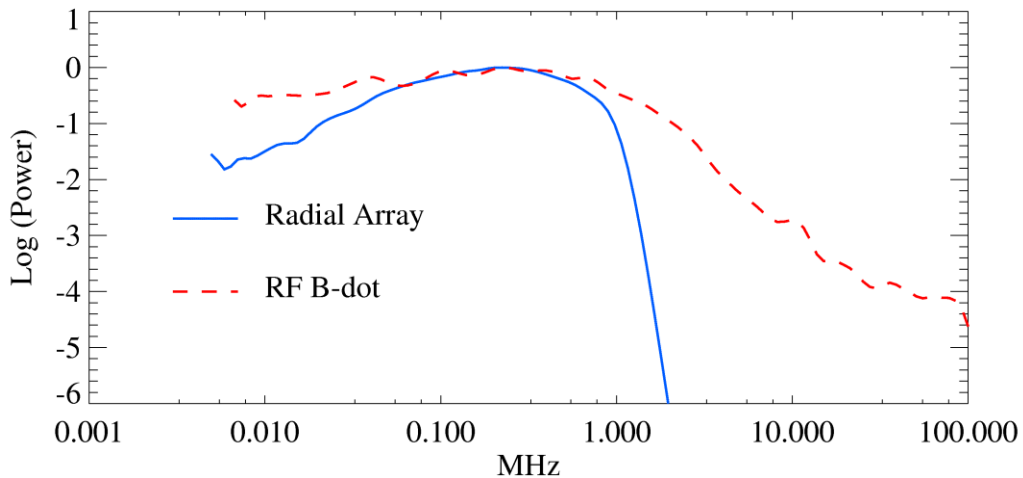


Figure 9.12: Comparison of magnetic fluctuation spectra measured by two different probe types. Spectra measured at $t = 40$ microseconds. Note: the spectra are normalized to each have a maximum value of 1.

9.3 Capacitive Probe Spectra

High frequency fluctuations are also measured with a capacitive probe at the same radial and axial locations as the RF B-dot probe. The radial and temporal distribution of

power in the range of 1-40 MHz is shown in the top plot of Figure 9.13. When compared with Figure 9.9, it is immediately obvious that the capacitive probe is much more sensitive to shot noise at the start of the discharge, as seen by the large amount of power at $t = 20$ microseconds. There is still measurable power during the discharge, especially from 35 to 40 microseconds and near 60 microseconds, however the overall distribution does not have as strong of a spatial variation as the RF B-dot data. This indicates that for the frequency range of 1-40 MHz, the electric and magnetic fields do not have a constant ratio, with relatively more power present in the magnetic field near the null position.

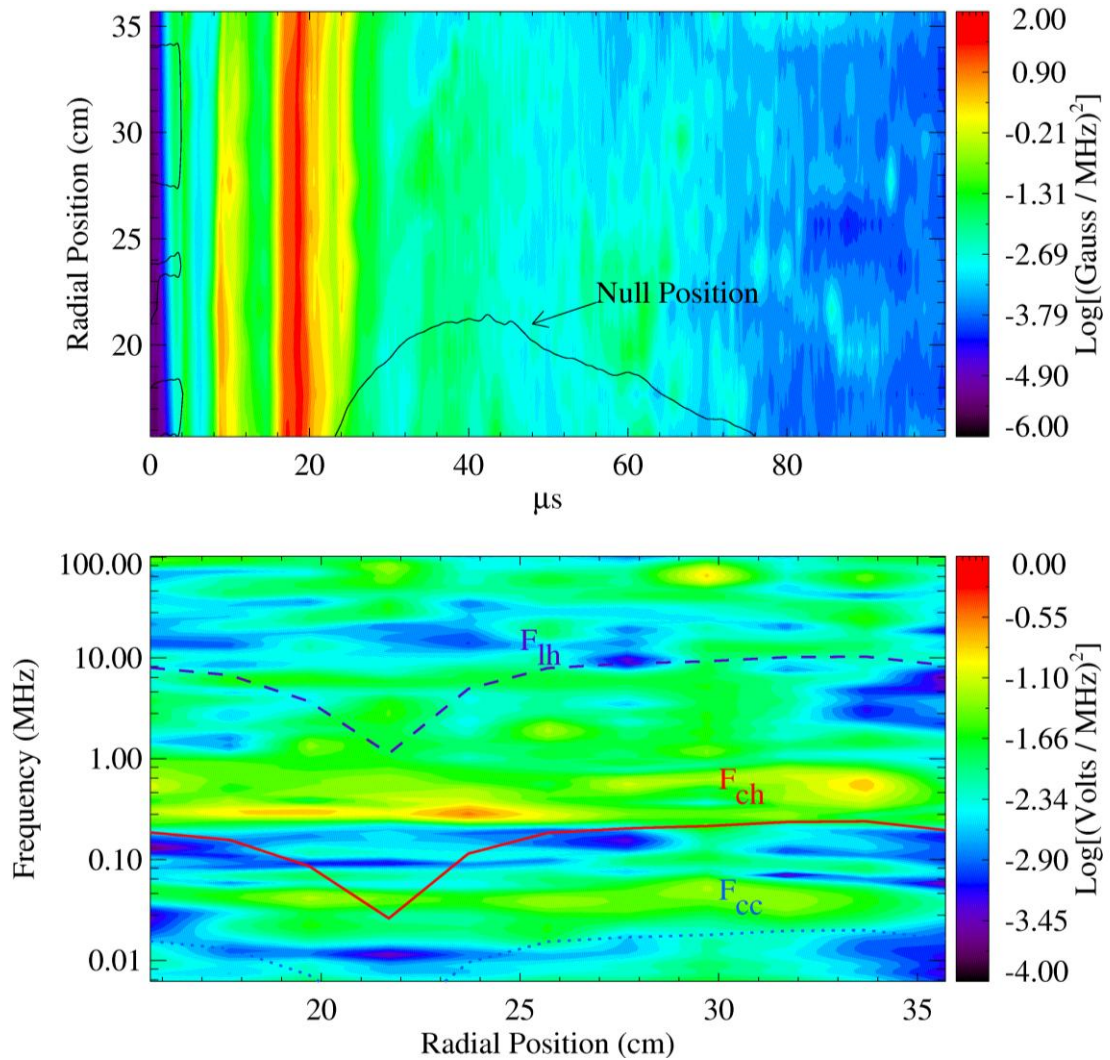


Figure 9.13: Top: spectrogram of capacitive probe data, averaged from 1 to 20 MHz. Bottom: radial distribution of spectrum at $t = 40$ microseconds. The lower hybrid, hydrogen cyclotron, and carbon cyclotron frequencies are also plotted.

The lower plot of Figure 9.13 shows the distribution of power as a function of radial position and frequency. Evident here are strong peaks in power at frequencies between 3 and 5 times the local hydrogen and carbon cyclotron frequencies. When compared with the bottom plot of Figure 9.9, it is apparent that the spectrum is concentrated around fewer frequencies.

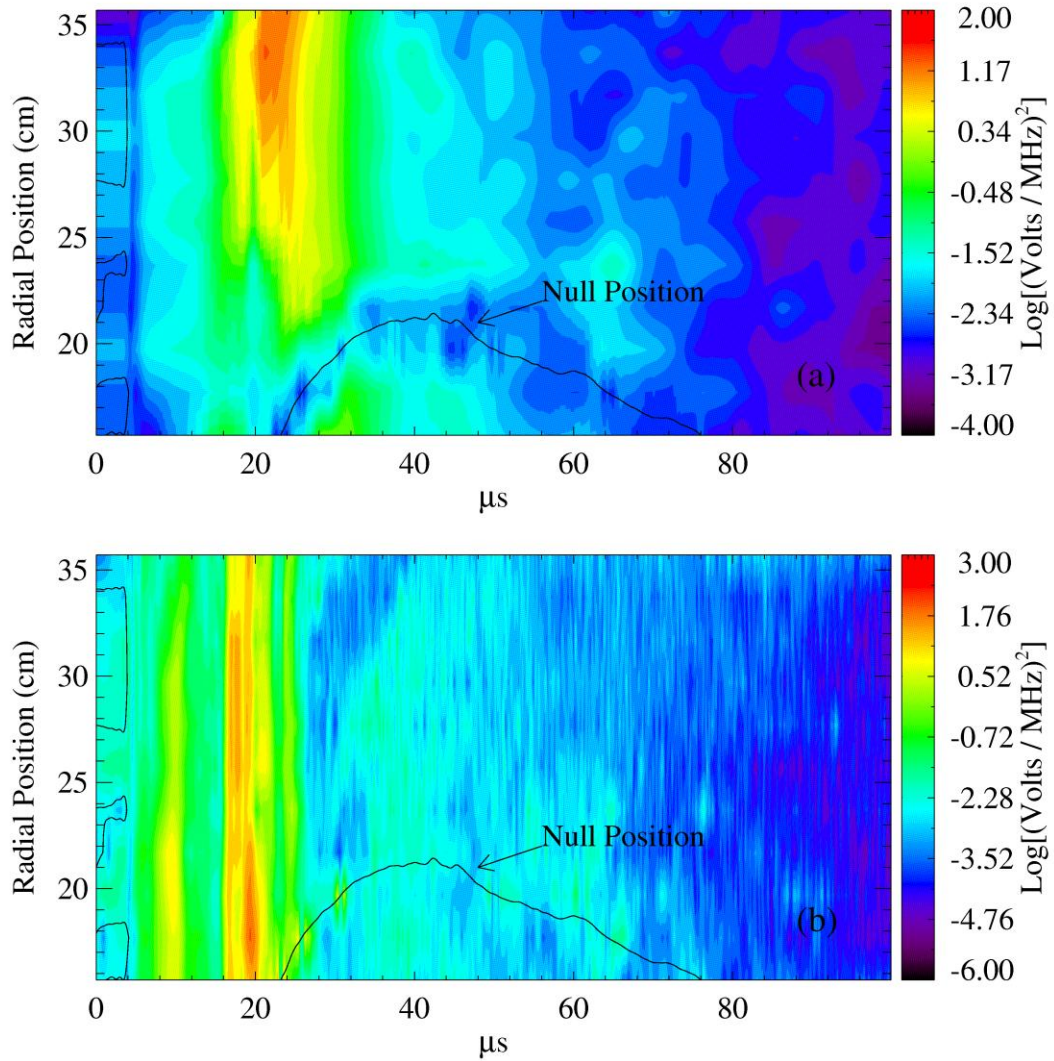


Figure 9.14: Total power near the local (a) hydrogen cyclotron frequency and (b) lower hybrid frequency as a function of position and time from the capacitive probe dataset.

Figure 9.14 is produced in the same way as Figure 9.10. Once again, power peaks away from the null position in the local hydrogen cyclotron frequency range. It has a stronger dependence on separation distance from the null than the magnetic fluctuations, and seems to be largest where the gradient of the magnetic field pressure is largest. The region of time to focus on is from $t = 40$ microseconds onward, as the capacitive probe signal is highly contaminated with shot noise occurring at $t = 20$ microseconds.

The power in the lower hybrid range does have peaks near the null position from 30 to 35 microseconds, but has a much wider radial width than the magnetic fluctuations after this time range. The conclusion to be drawn from this data is that the electric field near the lower hybrid frequency does not have a strong spatial dependence; power is present in this frequency range over a majority of the radial extent of the IFRC, with only slight correlation to the magnetic field minima. It is intriguing that power in the lower hybrid range is measured by both the capacitive and magnetic probe at $r = 24\text{-}30$ cm.

9.4 Discussion

Fluctuation measurements and their change with frequency have two different reasons that make them believable. First, the probes making the initial measurements are all calibrated as a function of frequency. Second, the spectra of different probes agree with each other. This is unlikely to occur by chance.

It is difficult to vary the charging parameters that lead to a good field-reversed configuration. In particular, the lack of control and independent measurement of the density limited the amount of parameter space that could be explored. It would be very interesting to find how the fluctuations parameters (spatial location, amplitude, frequency) change as global variables such as the peak magnetic field, particle inventory, and temperature are changed. This will have to be left for the future.

Chapter 10: Correlations

As discussed in Chapter 6, the particle losses out the axial end planes is quite large when compared with the particle inventory; these losses serve as the primary mechanism of energy losses in the IFRC, described in Chapter 8. In Chapter 9, fluctuations were characterized as being centered near the null with the largest amplitudes lying between the hydrogen cyclotron and mean gyrofrequency. These observations will be shown in this chapter to be strongly correlated and imply that changes in the magnetic field topology allow particles to stream along open field lines at the thermal velocity.

Topics covered in this chapter include the correlations between magnetic field probes, derived quantities such as the current density, and Faraday cups. The important observation of correlations between the magnetic fluctuations and particle losses as measured by the Faraday cups is the topic of the first section. Large scale symmetries between magnetic field components, spatial mode structures of the axial field at various frequencies, and correlations between different frequency fluctuations are discussed in the second section. Variations of the magnetic field properties with inferred quantities such as the electric field and current density are covered in the final section

A brief word about the magnitude of the correlations is appropriate. The similarity of two groups of measurements can be quantified by the correlation coefficient.⁵³ In this thesis, the measurements are either functions of time, space, or both. The minimum number of points that are ever used is 550, which result from the averaging

of many (~ 10) sequences of data that have the same ‘location’. Aggregates of similar measurements increase the number of points over which correlations are made to well over 10,000. Tests of the significance of a particular correlation value strongly depend on the number of points used in the analysis; in this thesis, significance levels are measured by a two-tailed T-test which quantifies the likelihood that two variables are correlated. As an example, two variables with 550 points are significant better than 99% of the time if their correlation value exceeds 0.11.

Due to the random nature of fluctuations, and the many possible spatial positions that lost particles could originate, it is highly unlikely that a correlation value near 1 would ever be measured between the magnetic field data and particle losses. Statistical significance estimates based on the number of measurements and the assumption of a normal distribution do strongly imply that the correlations between losses and fluctuations are significant, though masked by noise. As illustrated in Figure 10.5, a signal to noise ratio of 5 is enough to reduce the overall correlation between two identical signals to a value of 0.5 or less. Larger SNR ratios are highly desired, but cannot be achieved without measuring particle losses and fluctuations on an infinitely small grid.

10.1 Magnetic Field and Faraday Cups

Correlations between Faraday cup data and magnetic field data are shown in Figures 10.1, 10.2, and 10.3. The window over which correlations are found is from $t = 15$ to 70 microseconds in the magnetic field data, with lags of up to 30 microseconds added to the Faraday cup time window. The correlation is found as a function of lag and

probe combinations for each field component. Since the probes are not all at the same positions, lag (delay time) is not the most appropriate variable to visualize the resulting correlations. Velocity defined as the absolute separation between probe pairs divided by the time delay is a more appropriate variable, since a roughly constant velocity that links fluctuations in magnetic field properties to measured signals in a Faraday cup will cause the averaged correlations to be grouped more tightly together.

The process by which Figure 10.1 is created consists of the following steps. Magnetic field data is correlated with a sliding window of Faraday cup data and the correlation is found at each lag. The velocity at each lag and probe separation is also computed and stored in a separate array. The correlations and velocities are stored for all probe combinations and shots. The velocity array is then binned with a histogram function to find the number of counts and the array positions in the correlation array where the velocity linking probe pairs is a particular value. Using these positions, which assemble points from many shots, lags, and probe pairs, the correlation array is binned with another histogram function to find the number of counts that have a particular velocity and correlation. This is shown in the top row of Figure 10.1. This second histogram can be thought of as distributing the number of counts in each velocity bin into the appropriate correlation bin.

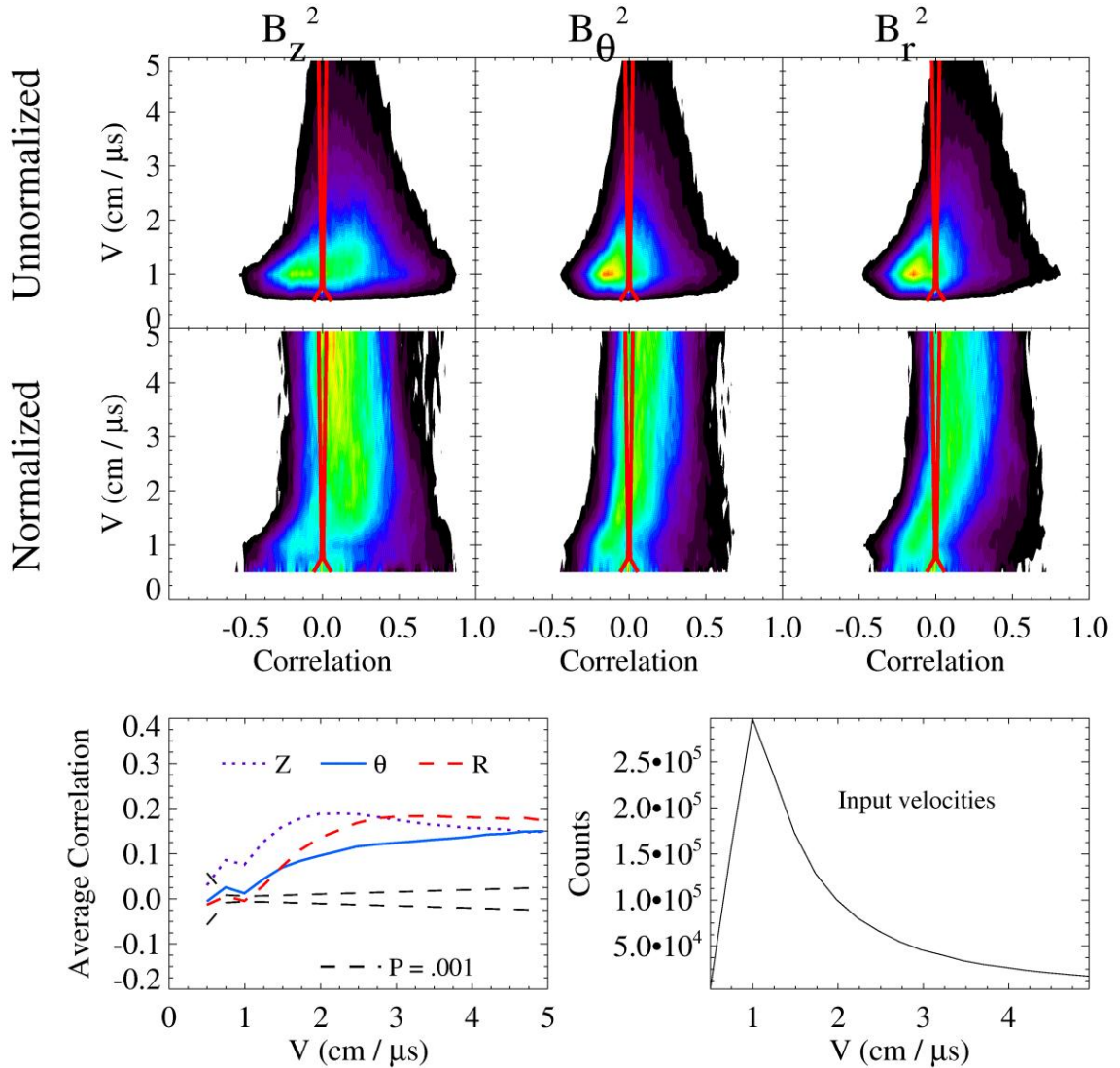


Figure 10.1: Average velocities between components of B^2 and Faraday cup signals from the same dataset. Straight lines are significance levels at $P=0.001$ for the number of counts in each velocity bin.

Due to the discrete positions of the magnetic probe array, the numbers of possible velocities linking probe pairs are not distributed evenly in velocity space. This is because the average distance is on the order of 30 cm, while the lags range from 0 to 30 microseconds. The lower right plot shows the input distribution of velocities, which is the result of the first histogram. The middle row of Figure 10.1 is made by normalizing

the top row by the number of counts in each velocity bin. The bottom left plot shows the average correlation at each velocity for the three different magnetic field components.

The largest correlations of the Faraday cup data are seen between B_z^2 and B_r^2 , with a velocity at peak correlation of approximately 2-3 cm/microsecond. The overall correlation is significant at higher than $P = .001$ for all velocities greater than approximately 0.8 cm/microsecond. The wide range of velocities that have significant correlation coefficients is indicative of significant variability in plasma parameters between shots and as a function of position. In spite of this variability, the average velocity linking magnetic field fluctuations and the Faraday cup signals seems quite plausible. The thermal velocity is approximately 1.5-2 cm/microsecond, while the Alfvén velocity is 3 cm/microsecond for $B = 100$ Gauss and $n = 5 \times 10^{13}$ cm⁻³, which are both quite similar to the highest correlated velocity.

A possible explanation for the correlation between particle losses and changes in the magnetic field is that local changes in the strength of the radial and axial fields cause closed field lines to become open and connected to the Faraday cups. Particles then stream down the open field lines at speeds typical of the hydrogen thermal velocity; the Alfvén velocity cannot be completely ruled out as a characteristic particle velocity since regions of the plasma exist where the measured velocities are of the same magnitude as the local Alfvén velocity.

The dataset containing Faraday cup data does not contain a complete mapping of the magnetic fields. The radial probe array was placed at only three of the twelve possible axial locations (-8.5, -1.5, and 1.5 cm). To compare average responses of the Faraday cup over a broader range of axial and radial positions, the average Faraday cup response is correlated with the average magnetic fields from the NCP dataset. The velocity connecting particle losses and changes in the magnetic fields is once again defined by the lag and the separation between probe pairs, with the position of the averaged Faraday cup signal taken to be the midpoint of the array of five probes, located at $z = -30$ cm, $r = 21$ cm.

Figure 10.2 shows the results of correlation analysis between the averaged Faraday cup signal and the averaged values of B^2 . After normalization, all three components of B^2 show significant correlations, peaking at a velocity of approximately 1.5 cm/microsecond. The correlations between B_z^2 and the averaged Faraday cup signal are particularly strong, peaking at an average correlation more than 0.5. This is equivalent to saying that over half of the average particle losses are coincident with changes in the axial magnetic pressure measured at a discrete number of points.

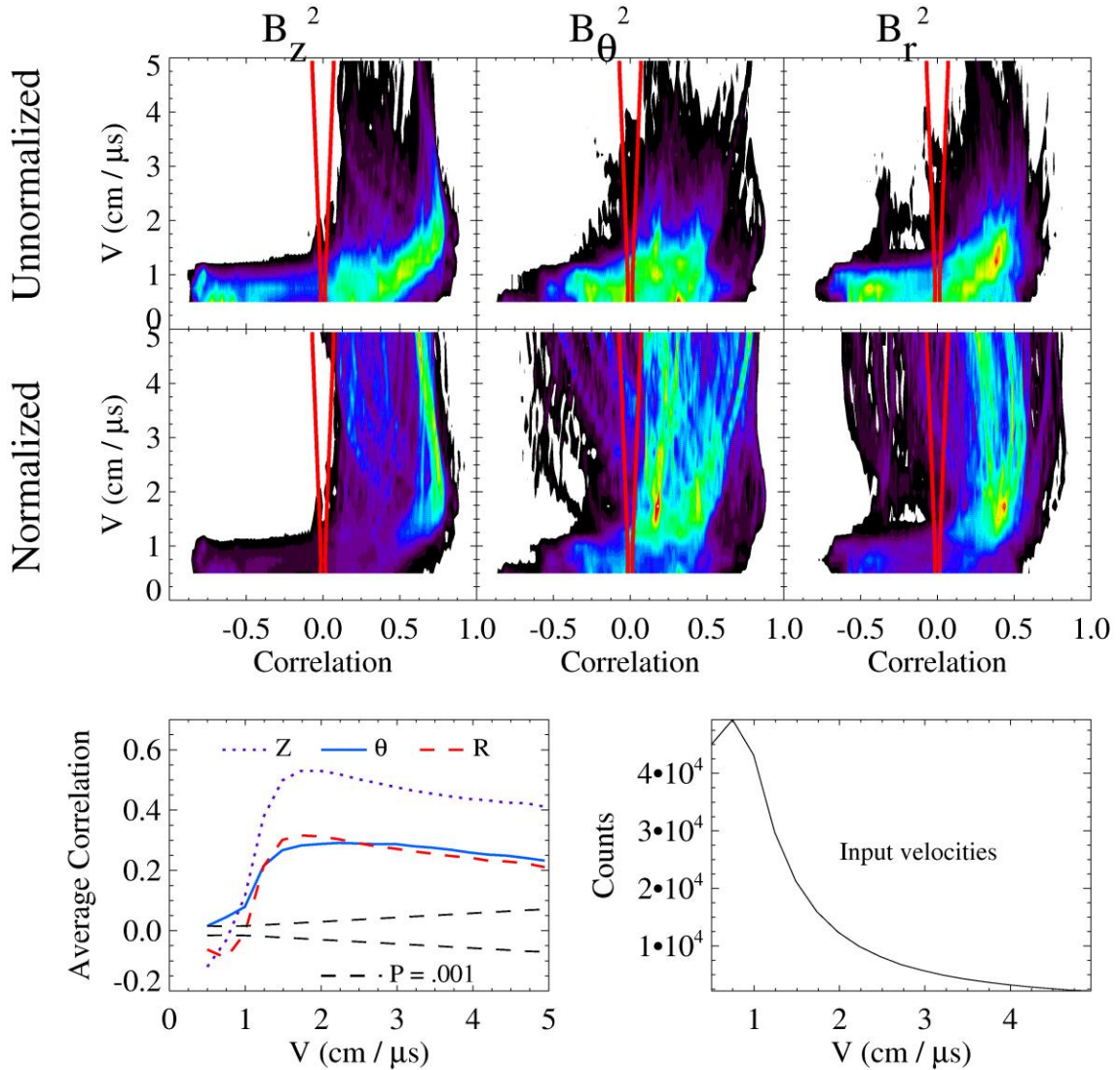


Figure 10.2: Average velocities between components of B^2 and Faraday cup signals. Magnetic field data and Faraday cup data are not from the same shots. Straight lines are significance levels at $P=0.001$ for the number of counts in each velocity bin.

The correlations between axial gradients in the magnetic pressure components and the averaged Faraday cup signal are shown in Figure 10.3. The use of the larger magnetic dataset allows the axial gradients at various locations to be more accurately determined than is possible from the smaller Faraday cup dataset. The average correlations are much lower than the B^2 cases, though still significant for the radial and

axial components. The velocity at peak correlation is slightly lower for the axial pressure gradient case, when compared to variations in the local magnetic pressure itself. It seems likely that the lower linking velocity and the much lower overall correlation is a sign that the force acting on plasma due to gradients in the magnetic pressure do not have as strong an effect on the particle losses measured by the Faraday cups. Instead, breaking field lines caused by variations in the local current density allow formerly confined particles to stream along the now open magnetic field lines and out the axial ends of the machine.

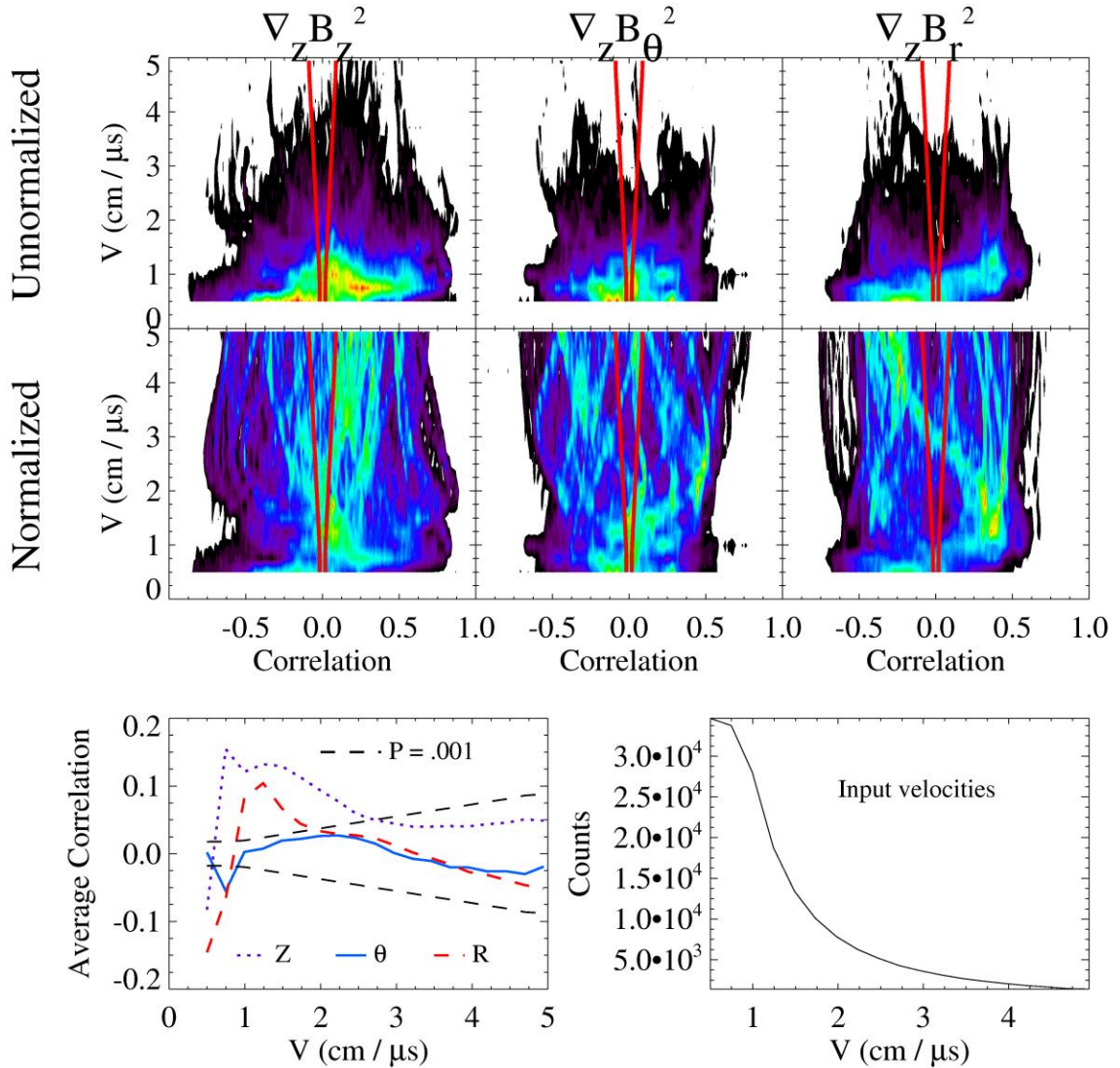


Figure 10.3: Average velocities between axial gradients of B^2 and the average Faraday cup signal. Magnetic field data and Faraday cup data are not from the same shots. Straight lines are significance levels at $P=0.001$ for the number of counts in each velocity bin.

The last two variables checked for correlations with the average Faraday signal are the radial and axial components of the Poynting vector given by $E_\theta B_z$ and $E_\theta B_r$. The radial Poynting vector has a strong correlation to the particle losses, with a similar average velocity as the correlations with B_z^2 . The Poynting vector is quite similar to the $E \times B$ particle drift; it is possible that fluctuations in the Poynting vector cause particles to

become unconfined when the radial component of their velocity exceeds some threshold value determined by the depth of the potential in which they are trapped.⁷

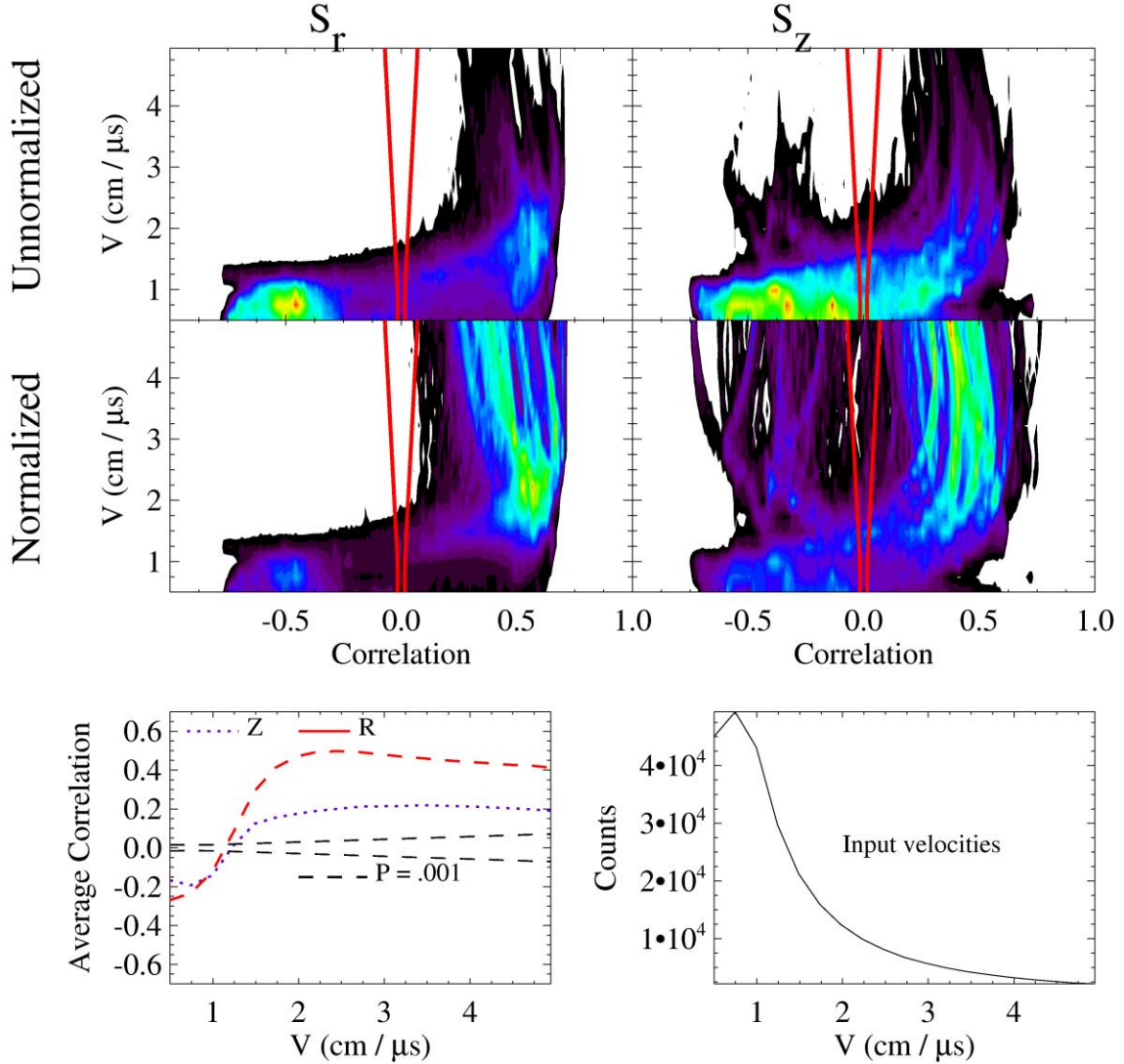


Figure 10.4: Average velocities between components of the Poynting vector and the average Faraday cup signal. Straight lines are significance levels at $P=0.001$ for the number of counts in each velocity bin.

This analysis method can be checked by creating fake data at the B-dot positions that have an identical waveform as the resultant Faraday cup signal. The data at each spatial point is taken to be a Gaussian function that peaks earlier in time than the output

signal, with the delay dependent on the probe separation and a randomly chosen velocity. Random noise is added to both the fake Faraday cup and B-dot signals, with a signal to noise ratio (SNR) of 5 or 10. The results of this simulation are shown in Figure 10.5. The bottom plots have a peak correlation at the linking velocity, with the correlation going to zero as the difference in velocities increases. Smaller SNRs lead to overall smaller correlation values, but correct localization of the velocity. This shows that this analysis tool works well, especially when the SNR is large.

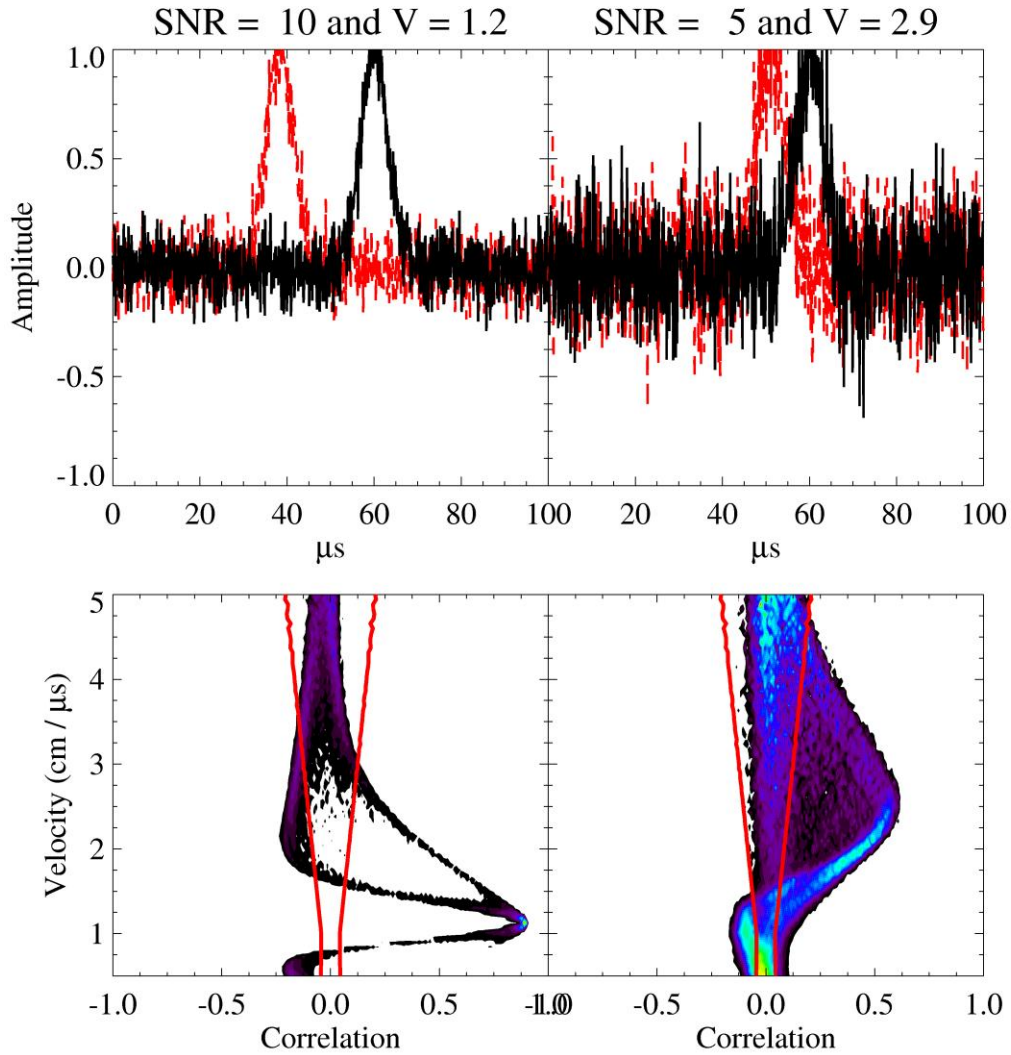


Figure 10.5: Estimates of the characteristic velocity linking spatially separated probes for two different signal to noise ratios and velocities. The top plots show sample B-dot (in red) and Faraday cup (in black) signals separated by 25 cm. The input for the bottom two plots are distributed over a 2-D spatial grid, similar in size to the locations of the magnetic probes.

A clear correlation between B_z^2 and particle losses has been shown; an important question is the identification of locations where lost particles originate. The assumption is that regions highly correlated to particle losses are where those particles originated. To do this, the spatial profiles of correlation at the velocity which maximizes the overall correlation between B^2 and the average Faraday cup signal are shown in Figure 10.6.

These plots are created by averaging the correlation at each position over the number of lags that lie within a certain velocity range.

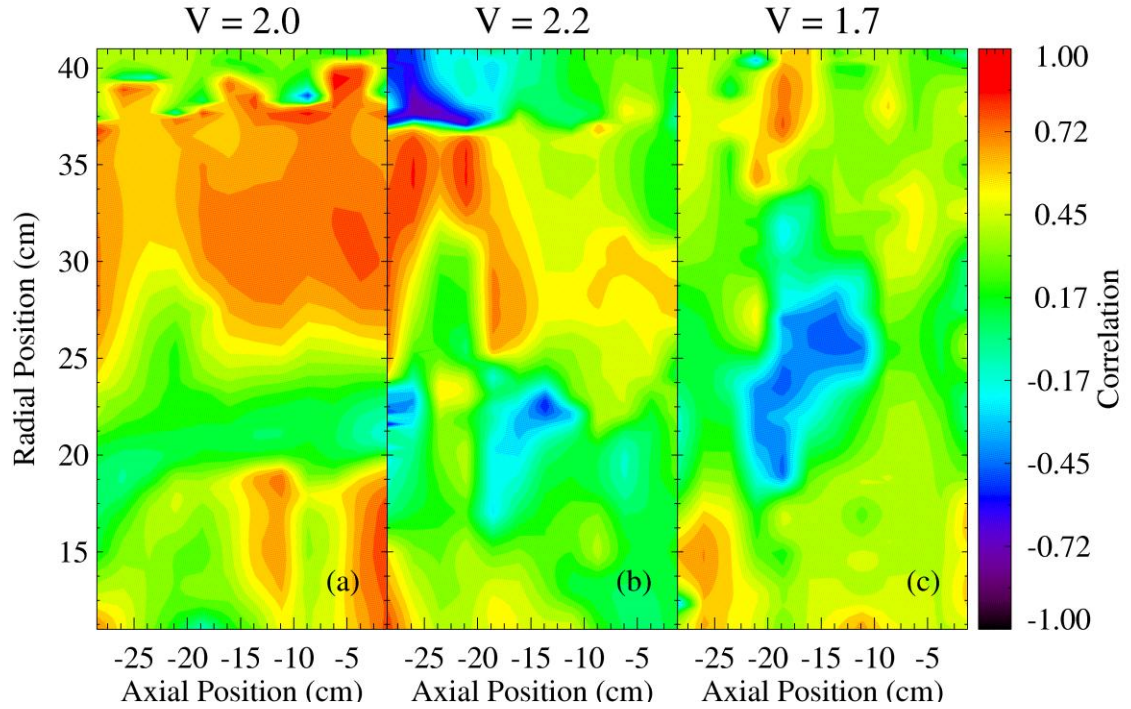


Figure 10.6: Spatial variations of the correlation at maximum correlated velocity between the average Faraday cup signal for (a) B_z^2 , (b) B_θ^2 , and (c) B_r^2 .

The overall correlation is strongest for B_z^2 , with three distinct regions evident. The correlation is large and positive at radii greater than 27 cm and less than 18 cm, and becomes more positive nearer the axial midplane at $z = 0$. This is consistent with the proposition that open field lines allow particles to leave the machine and be collected by the Faraday cup. The region of smallest correlation occurs from 18 to 27 cm, and overlaps where closed field lines are present. The other two components of B^2 also show similar spatial variations, but have lower correlation. The spatial variations of correlations between the radial Poynting vector and particle losses in Figure 10.7 (a) look quite similar to Figure 10.6 (a). The structure of the axial component does not have any obvious pattern to it, and consists of strongly positive *and* negative regions. The most

positive regions are near the separatrix position, but it is unclear why negative regions are present so near them.

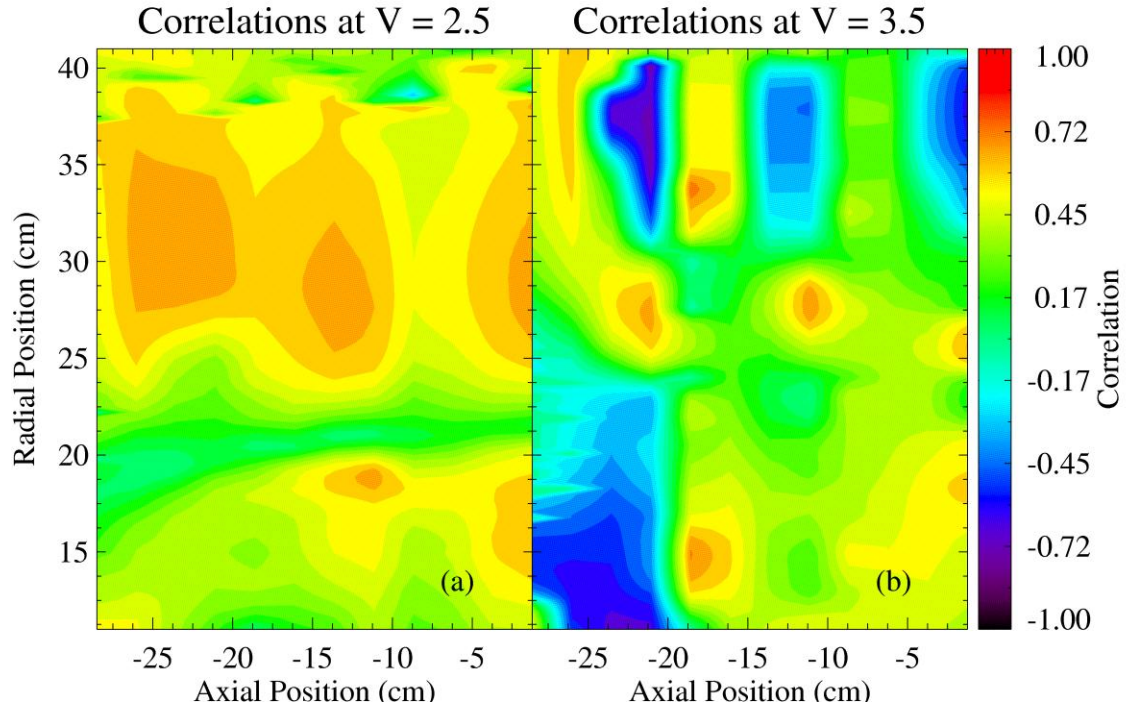


Figure 10.7: Spatial variations of the correlation at maximum correlated velocity between the average Faraday cup and (a) S_r and (b) S_z .

On examination of Figures 10.6 and 10.7, it is apparent that there can be strongly correlated regions of space at a given velocity, concurrent with regions of low correlation. The plots of Figures 10.1-10.4 distribute these measurements by their correlation value, which show the wide variability in the correlation value. It is possible that even the plots that show a relatively low average correlation do have well demarcated spatially correlated regions. This will be left to future endeavors.

The correlation between magnetic fluctuations and the average Faraday cup signal is actually significant and has a different spatial structure than the overall correlation

between B^2 and particle losses. Figure 10.8 shows the regions of strong correlation for the three magnetic field components in three different frequency bands. The time window at each spatial point is from 25 to 70 microseconds, slightly shorter than the previous studies (15-70 microseconds.) The black line indicates the correlation level that is necessary for significance at the $P=0.001$ level. From this plot, it is evident that there are strong correlations between fluctuations at frequencies between 100 - 800 kHz. These frequencies generally lie between the hydrogen and mean gyro frequencies, with peak amplitudes near the magnetic null.

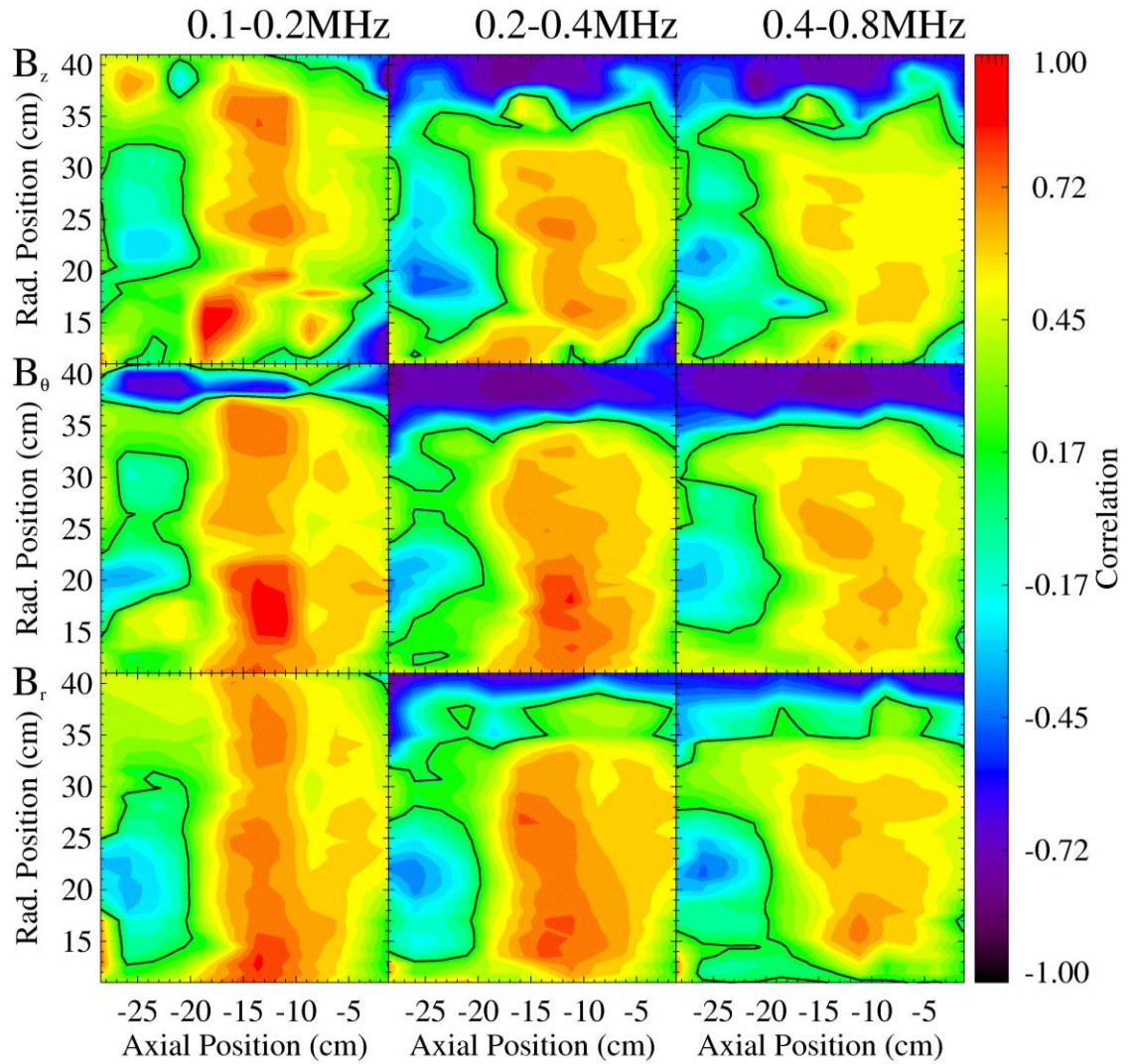


Figure 10.8: Correlations between particle losses and magnetic fluctuations. Linking velocity is 2.5 cm/microsecond.

10.2 Magnetic Field Correlations

Equilibrium calculations for the magnetic fields in FRCs have specific predictions about the relationships between different field components, specifically that the radial and axial magnetic fields for closed contours surrounding the plasma current. Correlation studies can show whether the different components do vary in the expected way. Coherent changes can also be studied, which can lead to mode structure identification.

The correlation coefficient between various magnetic field components as a function of axial and radial position is shown in Figure 10.9. The general features of the FRC topology can be seen in Figure 10.9 (c), with regions near $z = \pm 20$ cm showing strong positive and negative correlations between the radial and axial components of the magnetic field. Since the axial field is (on average) an odd function about the null position and the radial field is an odd function about the midplane, the quadrupolar structure in the 2-D plane centered on $z \sim 0, r \sim 20$ does show the expected symmetries.

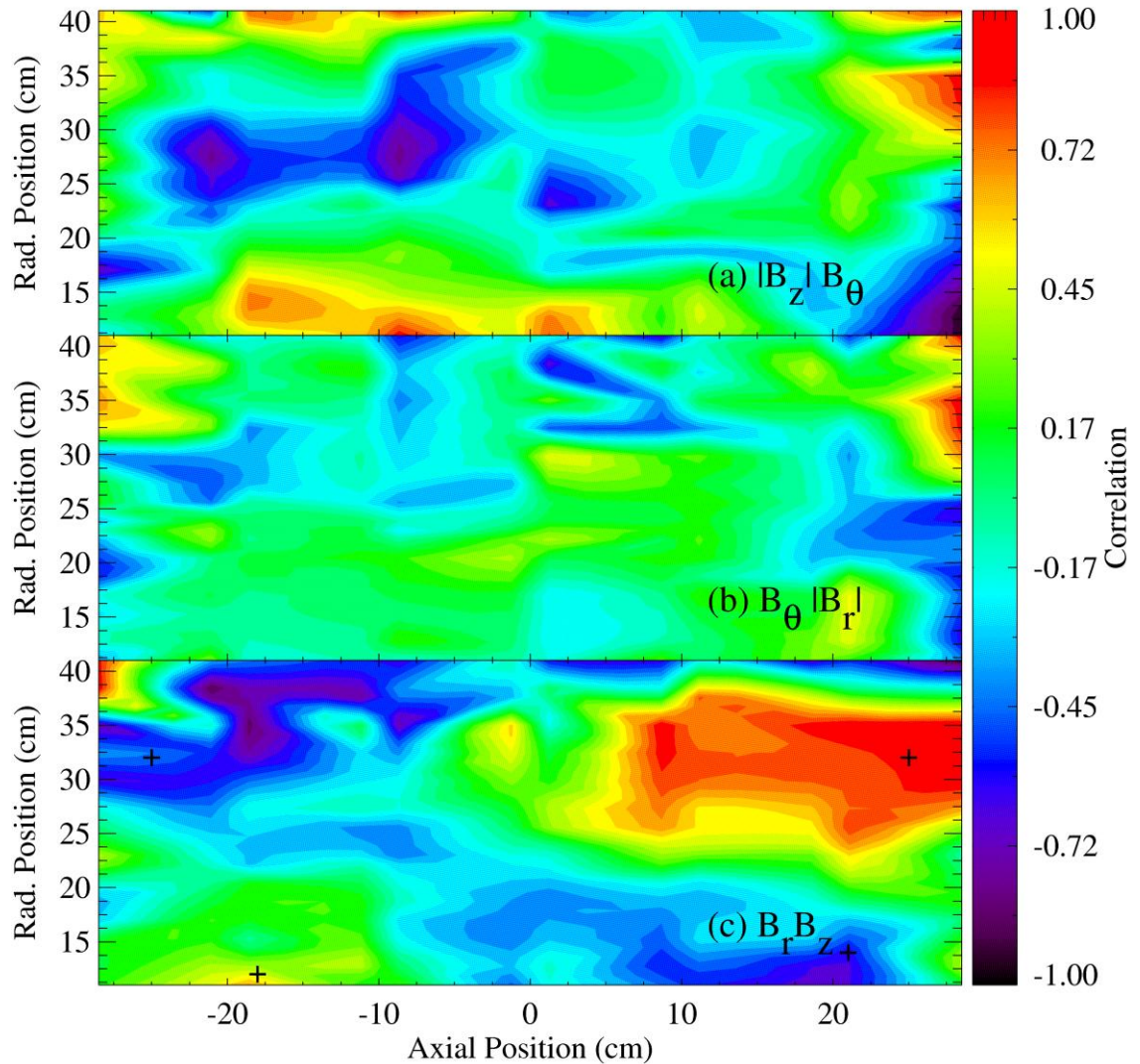


Figure 10.9: Correlations between magnetic field components. Time period for correlation is from 35 to 50 microseconds. The spatial extent of the FRC is approximated by the positions of the crosses.

Figure 10.9 (a) and (b) are complicated due to the azimuthal magnetic field. The correlation between B_θ and the absolute values of B_z is large and antisymmetric about the null. This indicates that the toroidal field itself is antisymmetric about the null position. The axial ends on both (a) and (b) are mostly symmetric about the midplane, with a small quadrupolar region in Figure 10.9 (b) near the midplane from $z \sim -5$ to 5 and $r \sim 17$ to 28 .

Figure 10.10 is a good example of the relationship between spectral and correlation analyses. The upper left two plots show the axial and radial variation of the real part of the cross spectrum between a reference B_z -dot probe located at ($z = 0$, $r = 11$ cm) with other B_z -dot probes located throughout the 2-D plane, written as

$$Re(E_{xy}) = |XY^*| \cdot \cos(\theta_{xy}), \quad (10.1)$$

where θ_{xy} is the cross phase between the reference and test probe, defined by

$$\theta_{xy} = \text{atan}\left(\frac{\text{Im}[XY^*]}{\text{Re}[XY^*]}\right), \quad (10.2)$$

and X and Y are the Fourier transforms of time traces x and y . The time window over which the cross spectra are calculated is from $t = 35$ to 60.6 microseconds, and the spatial structure of two different frequencies are shown.

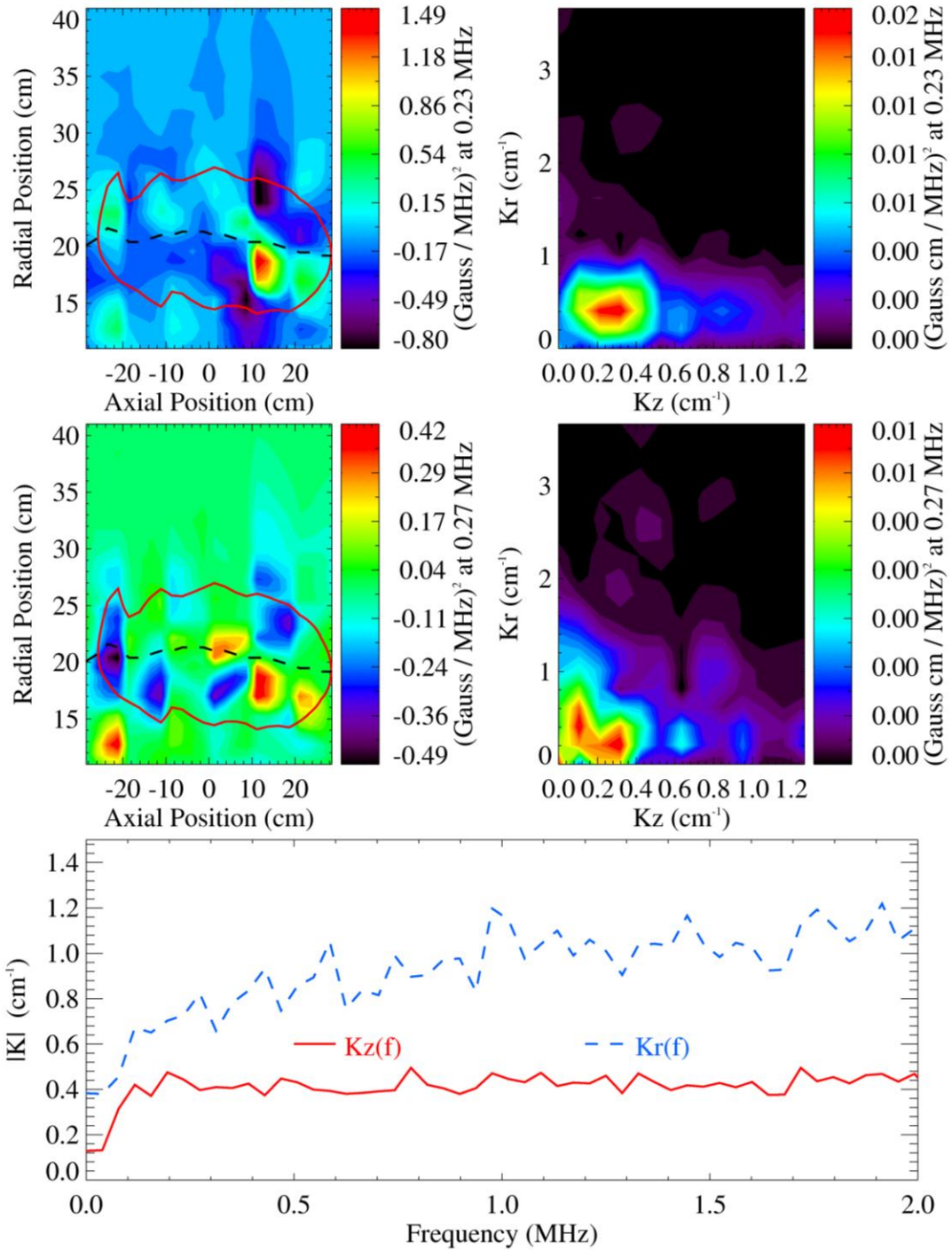


Figure 10.10: Possible B_z mode structure at 230 and 270 kHz at 47.8 microseconds, with power distribution in K_r and K_z at the same frequencies. Reference probe is at $z = 0$ cm, $r = 11$ cm. Approximate separatrix and null positions are noted on the mode structure plots.

Regularly spaced periodic spatial amplitude variations in the cross spectrum near the position of the separatrix exist, with average axial and radial wave numbers K_z and K_r of 0.4 and 0.8 cm^{-1} respectively. The power distribution with wave number is shown in the upper right two plots, and is calculated by taking the spatial Fourier transform of the cross spectra in the plots on the left side. The average values of each component of K are found by using the power distribution as the weighting function, and written as

$$\langle K(f) \rangle = \sum K_i * E_{xy}(k_z, k_r, f) / \sum E_{xy}(k_z, k_r, f), \quad (10.3)$$

where the summation is done over K_z and K_r . The variation of K_z and K_r with frequency is shown in the bottom plot. There is a general increase in k_r , while k_z stays approximately constant. This intriguing result suggests a mode structure that has perturbations around the separatrix position.

While Figure 10.10 shows periodic variations in space at several frequencies, a necessary question to ask is whether or not the fluctuations are part of a coherent mode or due to random turbulence in this frequency range. This can be answered by looking at the time variation of the mode structure. The period of a wave with frequency 235 kHz is ~ 4.25 microseconds. By looking at different time windows encompassing at least one period, the modes ought to go from a maximum to a minimum and back. A comparison of the averaged real component of the power to the total power in a frequency range will also determine whether or not the fluctuations are adding coherently.

The temporal variations of the spatial mode structures are shown in Figure 10.11. The time window is kept at a fixed length of 12.8 microseconds, with a start time that is

swept from 0 to 80 microseconds in increments of 0.2 microseconds. The time stamp of each window is taken to be the time at the window center, i.e. a start time of 0 microseconds is assigned a time stamp of 6.4 microseconds. The phase and spatial position modes do not change much in time. Also, the percentage of power that is repeatable from shot to shot is quite small compared with the total power, on the order of 2 percent or less. This proves that the phase of the fluctuations is mostly random which is a characteristic of turbulence. While it is possible that there are coherent modes present on the IFRC, they do not appreciably contribute to the measured amplitude of fluctuations when averaged over a large number of discharges. This could be due to variations of the plasma parameters which determine the wavelength and frequency of the modes.

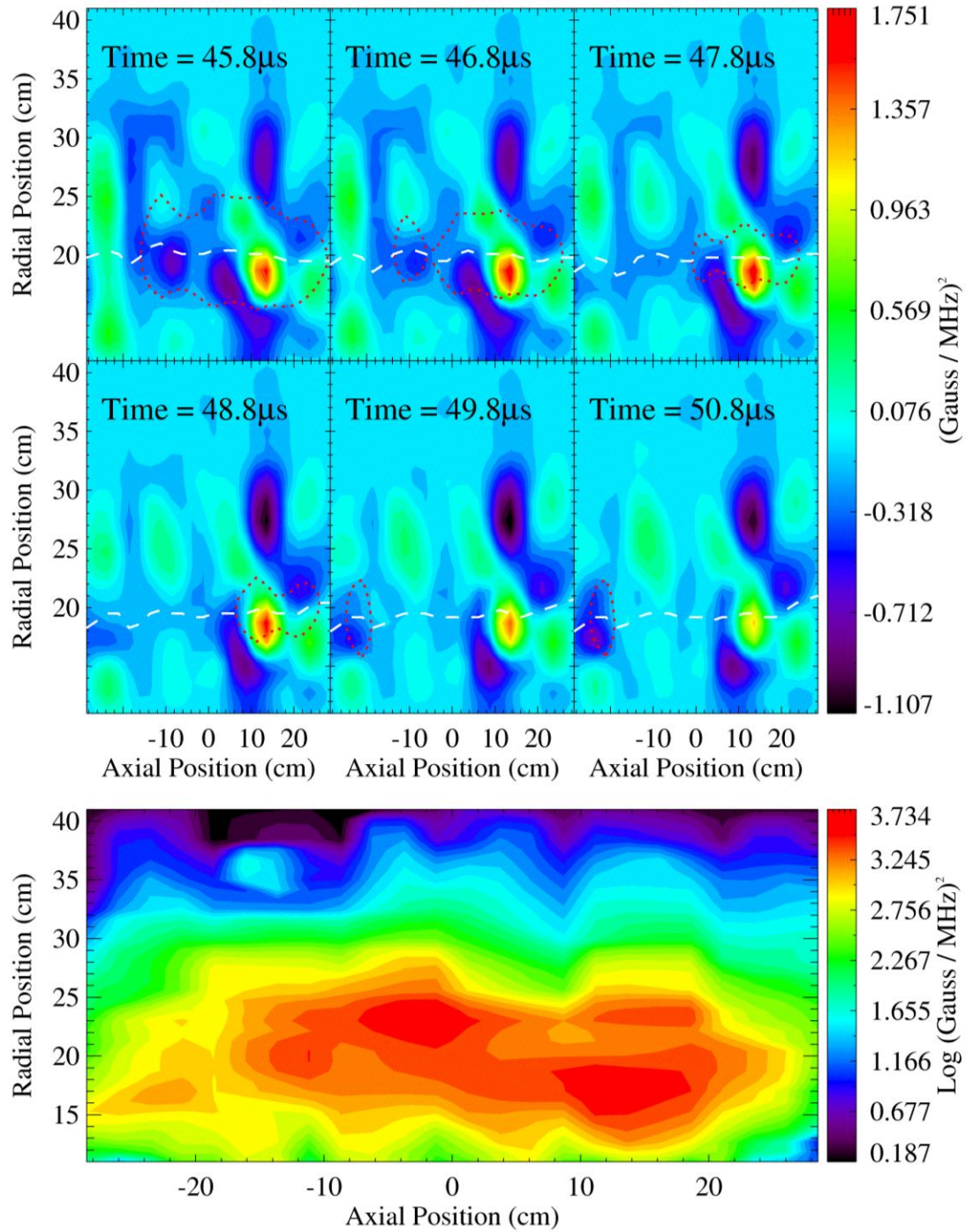


Figure 10.11: Top plots: Time evolution of mode structure at 235 kHz. Bottom plot: Total power of axial magnetic field fluctuations at 235 kHz and 47 microseconds. Note that the bottom plot has a logarithmic amplitude scale.

10.3 Magnetic Field and Derived Quantity Correlations

The similarity between spatial distributions of the magnetic field and current density is measured by the spatial cross correlation of the two quantities. Figure 10.12 shows the time evolution of the correlations between the various components of B^2 and J , as well as the correlations between components of $J \times B$. We would expect that the azimuthal component of the current density J_θ would be anti-correlated with $B_r^2 + B_z^2$ since the magnetic fields are caused by the current. This is indeed what is seen in Figure 10.12(a), plotted with the dotted line. Once significant azimuthal current begins to flow, at around $t = 30$ microseconds, the correlations become strong and negative. The correlations of B^2 with the other two components of J are not nearly as strong, though still fairly significant at some times. The negative correlation of $B_\theta^2 + B_z^2$ with J_r , and the positive correlation of $B_r^2 + B_\theta^2$ with J_z imply that the azimuthal magnetic field is most likely caused by radial currents. This follows from the fact that magnetic fields and the currents that create them do not generally have the same spatial structure.

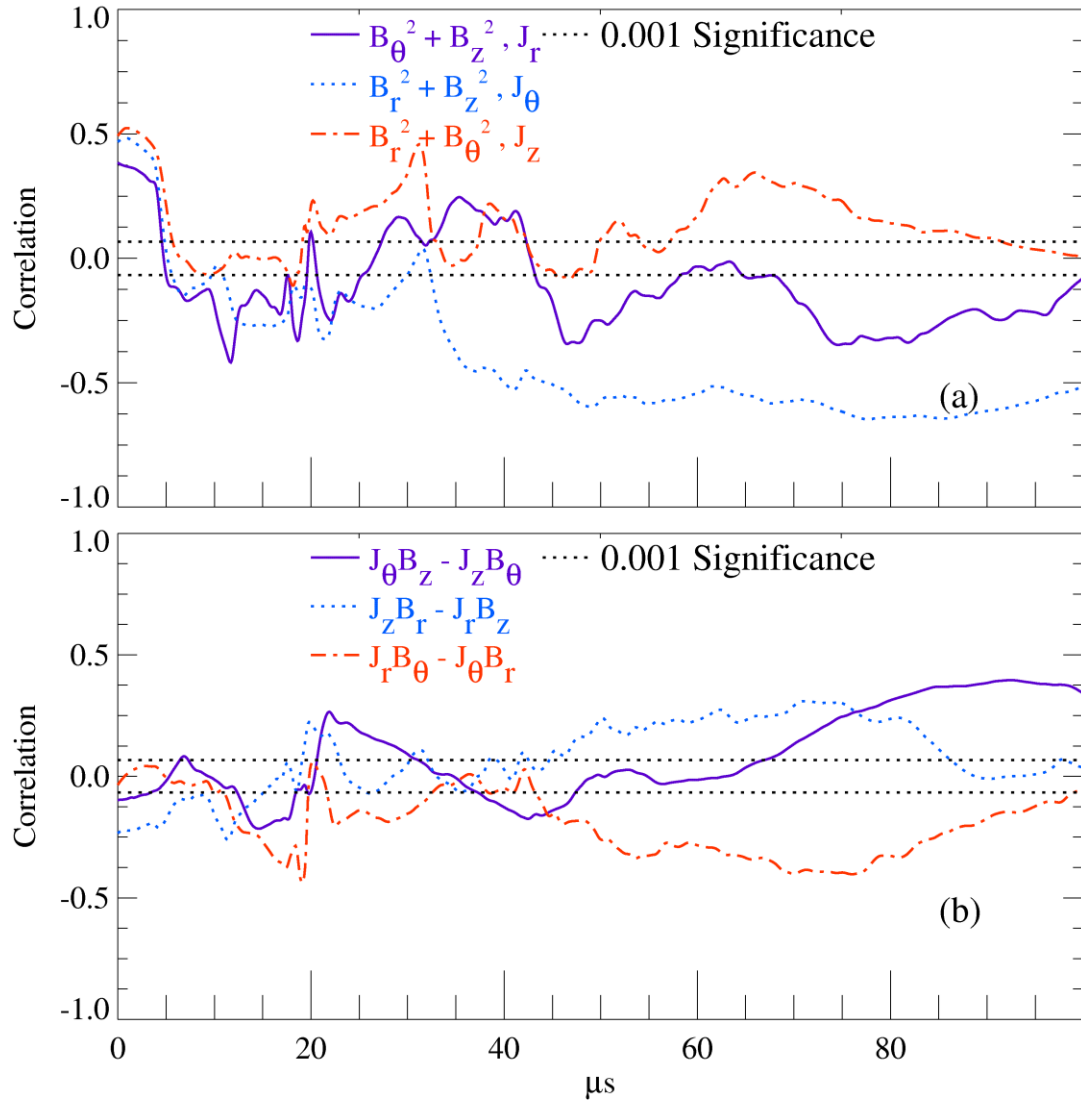


Figure 10.12: Spatial correlation of magnetic field and current density components. Top plot correlates magnetic energy with appropriate current density. Bottom plot correlates force balance components.

The small correlations from $t = 25$ to 45 microseconds on the bottom plot of Figure 10.12 shows that the Hall term is relatively small for this time period. The radial component, given by the solid line, is quite small after 30 microseconds until the equilibrium phase is over, which occurs near 70 microseconds. The axial component, denoted by the dashed line, begins to deviate from zero by 50 microseconds. This is

confirmed by observations of the azimuthal current density splitting into several pieces and wobbling back and forth.

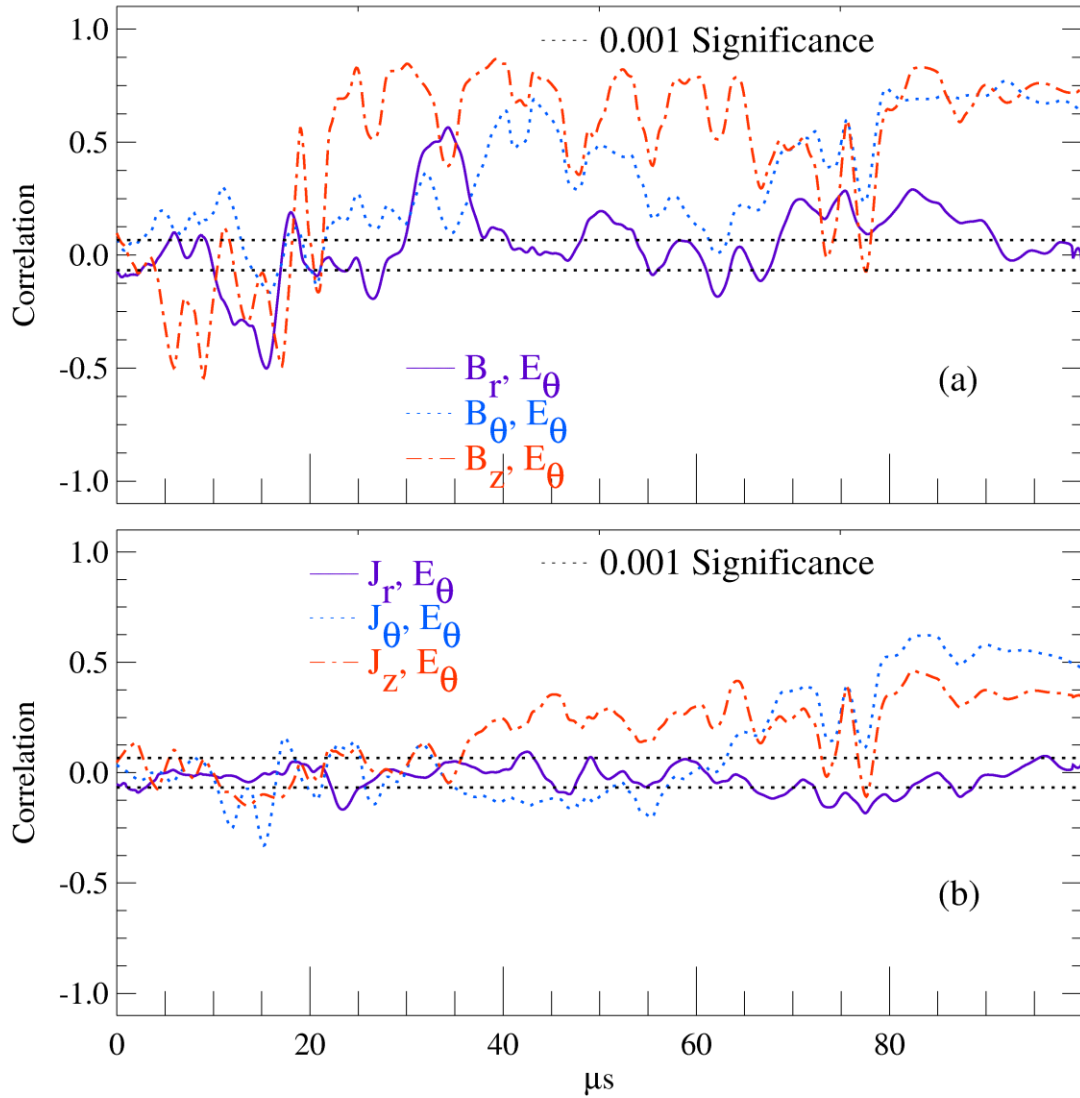


Figure 10.13: Spatial correlations of E_θ with B and J components

The correlation between E_θ and B_z is quite strong, due to their similar radial profiles. Both have their most negative values nearest the flux coil, with increasing values at greater radii. The other two components of B have strong correlations that exhibit large changes in time. The peak in $E_\theta - B_r$ near 35 microseconds occurs when the IFRC reaches its maximum null position and trapped flux; field lines are also breaking

and moving from open to closed as the flux builds. The concurrent drop in the other two correlations is intriguing, though the cause is unknown. The peak in $E_\theta - B_\theta$ correlation near 40 microseconds occurs when the azimuthal field fluctuations are largest and implies that the field structures are quite similar. The overall correlations of E_θ with components of J are quite small for the majority of the discharge, with no obvious conclusions to be drawn.

Chapter 11: Conclusions and Final Remarks

11.1 Summary

This thesis has quantified what is known about the Irvine Field-Reversed Configuration device. Reversed magnetic fields are regularly produced and observed; spatial mapping of the three dimensional nature of these fields has revealed the following results:

- Axial and radial magnetic fields form closed poloidal flux contours, surrounded by open field lines, with maximum field strength of approximately 200 Gauss.
- Toroidal magnetic fields that are of similar magnitude to the reversed field with strong spatial and temporal gradients.
- The measured fields and fluxes in the absence of plasma are comparable in strength and spatial distribution to theoretical models of currents in the field coils that confine and drive the discharges.

The magnetic field measurements have been used to derive estimates for the plasma current density and toroidal electric field. Cross checks show that the calculated current from B-dot measurements agrees well with the sum of the plasma current and limiter coil current measured by Rogowski coils.

The IFRC is a low temperature device, though it does achieve a high volume averaged beta. The input power measured by the radial Poynting vector is transferred to the plasma by resistive heating. Particle losses out the axial ends of the machine agree very well with the estimates of the power lost by particle transport. These large losses

are consistent with the small observed increases in the thermal stored energy. As a direct consequence of the large losses by transport, the particle and energy confinement times are much shorter than the discharge length.

There is a substantial amount of power in magnetic fluctuations that have a frequency between the hydrogen cyclotron and mean gyrofrequencies. These fluctuations are strongest where the magnetic field is lowest, an observation similar to those made on other machines.⁵⁰⁻⁵² The Faraday cups measure correlated signals with changes in the magnetic fields. The strongest correlations are with the B_z^2 and the absolute value of the radial Poynting vector, and are highest near the estimated separatrix position. This indicates that changes in the topology of the poloidal magnetic fields allow particles with a velocity of approximately 2 cm/microsecond to stream along open field lines which exit the confinement region at each end of the machine. Correlations are also high between particle losses and magnetic fluctuations with frequencies in the hydrogen cyclotron to mean gyrofrequency range. These correlations peak near the null, where the amplitude of the fluctuations is largest, and indicate that turbulence in this region is correlated with particle loss.

Whenever possible, ‘sanity checks’ were done to test whether a particular analysis method produced physically reasonable results. These checks, such as those performed on the plasma current in Chapter 6.3 and the input power in Chapter 8.2, have all consistently agreed with each other.

11.2 Discussion

Theoretical and experimental studies of stability and confinement properties of field-reversed configurations have focused primarily on low-frequency MHD modes and global instabilities.^{5 23 24} While these modes can be present in different experiments, methods such as multi-pole stabilization¹⁷ have been designed to reduce or eliminate these global disruptions. What has not yet been solved is the problem of anomalously high particle transport rates that constrain particle and energy confinement times for this topology. Particle transport must be reduced for FRCs to be a viable fusion reactor candidate.

While the IFRC device is not at the cutting edge of experimental design, the combination of a high beta region of plasma surrounded by open field lines is a feature that defines all FRCs. It seems likely that loss mechanisms present on this experiment will be present on all experiments that share this topology. It has been established in Chapter 8 that power losses in the IFRC are dominated by particle transport as shown in Figure 8.9. Macroscopic estimates of the particle diffusion rate in Figure 8.3 are much larger than those given by the Spitzer resistivity, and are consistent with the power loss calculations. This loss channel will likely account for a smaller percentage of the total power losses on higher temperature machines but any information that may lead to a better understanding of particle transport losses should be applicable no matter the size of the experiment.

It has been noted that the lower hybrid drift instability⁵⁴ could be the cause of the anomalous resistivity observed in FRCs and reconnecting current sheets.^{43 51} While this instability is electrostatic, magnetic field fluctuations have been observed^{51 52} between the ion and mean gyro frequencies. Some theoretical work on electromagnetic fluctuations in this frequency range^{55 56 57} has indicated that magnetic fluctuations can be unstable in high beta regimes, such as near the center of field-reversed configurations. As shown in Chapter 9, fluctuations in this frequency band are observed on the IFRC, with spatial locations restricted to high beta regions, frequencies in the expected range, and amplitudes of up to 10% of the peak magnetic field. The strength and spatial locations of the correlations between particle losses and fluctuations, shown in Figures 10.6 through 10.8, indicate that the likely cause of the observed particle transport on the IFRC is due to electromagnetic turbulence ejecting particles from regions near the null onto open field lines which exit the containment region. The observation of these fluctuations on other machines makes it likely that this particle loss mechanism is a general feature of the field-reversed configuration.

In summary, the key results of this thesis are the following:

- Power losses are dominated by particle transport. (Figure 8.9)
- Magnetic fluctuations of appreciable amplitude between the hydrogen and mean gyrofrequencies are present near the magnetic null. (Figures 9.4, 9.5, and 9.9)
- Particle losses are correlated to the magnetic fluctuations as well as to changes in the confining equilibrium magnetic fields. (Figures 10.6-10.8)

11.3 Future Work

The primary measurement device in this thesis is the humble B-dot probe. While many conclusions can be drawn from the temporal and spatial variations of the magnetic field in plasma, an independent measurement of the plasma density, temperature, and electric field would greatly improve the understanding of the plasma characteristics of the IFRC. This effort would be greatly aided by the development of a different plasma source; a direct link between the plasma and plasma gun electrodes precluded the local measurement of temperature and density by triple probes.

This thesis is based on a set of charging parameters that were empirically observed to produce reversed fields in the IFRC. An exhaustive survey of parameter space was not performed; in particular our lack of control over the initial plasma density precluded a study of the dependence of fluctuations and particle losses on equilibrium magnetic field strength and peak density. These dependencies as well as plasma characteristics such as the confinement times, stored energy, and power flows should be addressed in a future work.

High frequency magnetic fluctuations measured on this machine have similar characteristics to those of other experiments; the precise nature of this instability such as its dispersion relation and parametric dependence on macroscopic plasma parameters has yet to be fully characterized on the IFRC. Toroidal variations have been completely ignored in this work. Future study should include correlation measurements between particle losses and changes in the magnetic field, electric field, and density as function of

spatial location to fill in the path between fluctuations in the center of the plasma and losses measured at the axial ends. Finally, comparisons should be made between the observed characteristics of particle losses on this machine and available theoretical models in order to guide our understanding of how energy and particles are confined in a field-reversed configuration.

Bibliography

-
- ¹ U.S. Department of Energy. Energy Information Agency. (2009, May 27). “International Energy Outlook 2009.” (DOE/EIA-0484(2009)). Washington, DC: U.S. Government Printing Office. Retrieved December 28, 2009 from the World Wide Web: <http://www.eia.doe.gov/oiaf/ieo/pdf/table1.pdf>.
- ² U.S. Department of Energy. Energy Information Agency. (2009, March 3). “World Proved Reserves of Oil and Natural Gas, Most Recent Estimates.” Retrieved December 28, 2009 from the World Wide Web: <http://www.eia.doe.gov/emeu/international/reserves.html>
- ³ U.S. Department of Energy. Energy Information Agency. (2009, March 3). “Table A4. World Oil Consumption by Region, Reference Case, 1990-2030.” Retrieved December 28, 2009 from the World Wide Web: http://www.eia.doe.gov/oiaf/ieo/pdf/ieoreftab_4.pdf
- ⁴ U.S. Department of Energy. Energy Information Agency. (2009, March 3). “Table A2. World Total Energy Consumption by Region and Fuel, Reference Case, 1990-2030.” Retrieved January 6, 2010 from the World Wide Web: http://www.eia.doe.gov/oiaf/ieo/pdf/ieoreftab_2.pdf
- ⁵ M. Tuszewski. “Field reversed configurations.” *Nuclear Fusion*, **28** (1988) 2033
- ⁶ A. Qerushi. “Particle and Energy Transport in a Field Reversed Configuration.” PhD thesis, University of Florida (2000)
- ⁷ N. Rostoker and A. Qerushi. “Equilibrium of field-reversed configurations with rotation. I. One space dimension and one type of ion.” *Phys. Plasmas*, **9** (2002) 3057
- ⁸ L.C. Steinhauer. “Improved analytic equilibrium for a field-reversed configuration.” *Phys. Fluids B*, **2** (1990) 3081
- ⁹ A. Shiokawa, S. Okada, et al. “Spontaneous Appearance of Toroidal Field in Field Reversed Configuration Plasma.” *Japanese Journal of Applied Letters Part B* **30** (6B): L1142-L1144. (1991).
- ¹⁰ W. Pierce, R. Maqueda, et al. “Initial Results From Parallel Coil Operation of the Coaxial Slow Source Field Reversed Configuration Device.” *Nuclear Fusion* **33**(1): 117-132 (1993)
- ¹¹ R. Farengo, R. Brooks. “Plasma-Heating and Dynamics in the Coaxial Slow Source.” *Nuclear Fusion* **32**(1): 67-80 (1992)
- ¹² K. McKenna, W. Armstrong, et al. “Field-Reversed Configuration Research at Los Alamos.” *Nuclear Fusion* **25**(9): 1317-1319 (1985)
- ¹³ T. P. Intrator, et al. *J Fusion Energy* **28** (2009) 165–169
- ¹⁴ A. Hoffman, L. Carey, et al. “The Large-S Field-Reversed Configuration Experiment.” *Fusion Technology* **23**(2): 185-207 (1993)
- ¹⁵ A.L. Hoffman, H.Y. Guo, R.D. Milroy and Z.A. Pietrzyk. *Nuclear Fusion* **43** (2003) 1091-1100
- ¹⁶ H. Guo. “Recent Results on Field Reversed Configurations from the Translation, Confinement and Sustainment Experiment.” *Plasma Science and Technology* **7** (2005) 2605
- ¹⁷ S. P. Gerhardt, et al. “Equilibrium and stability studies of oblate field-reversed configurations in the Magnetic Reconnection Experiment.” *Physics of Plasmas* **13**, 112508 (2006)
- ¹⁸ S. P. Gerhardt, et al. “Inductive sustainment of oblate field-reversed configurations with the assistance of magnetic diffusion, shaping, and finite-Larmor radius stabilization.” *Physics of Plasmas* **15**, 022503 (2008)
- ¹⁹ C. D. Cothran, et al. *J. Fusion Energy* **26** (2007) 37
- ²⁰ C. D. Cothran, et al. *Geophysical Research Letters* **32** (2005) L03105
- ²¹ S. Okada, et al. *Nuclear Fusion* **45** (2005) 1094–1100
- ²² S. Okada, et al. *Nuclear Fusion* **41** (2001) 625-629
- ²³ M. Tuszewski, D.P. Taggart, R.E. Chrien, D.J. Rej, R.E. Siemon, and B.L. Wright. “Axial dynamics in field-reversed theta pinches. II: Stability.” *Physics of Fluids B, Plasma Physics*, **3**(10):2856, (1991)
- ²⁴ M. A. Rosenbluth, M.N. Bussac. “MHD stability of spheromak.” *Nuclear Fusion* **19**(4):489, (1979)
- ²⁵ “Multi-Gauge Controller Instruction Manual”, *Varian vacuum technologies*. Doc. No. 699908091 Revision Y. February 2007
- ²⁶ <http://www.bitscope.com>
- ²⁷ A. Van Drie. [Lab2000](#)

-
- ²⁸ C.A. Romero-Talamás *et al.* “Multielement magnetic probe using commercial chip inductors.” *Review of Scientific Instruments*, **75** (2004) 2664
- ²⁹ D. Pace. (2008, October 31). “Example of Langmuir Probe Analysis.” Retrieved November 30, 2009 from the World Wide Web: <http://www.davidpace.com/physics/graduate-school/langmuir-analysis.htm>.
- ³⁰ M. A. Lieberman, A. J. Lichtenberg. “Principles Of Plasma Discharges And Materials Processing.” New York, NY, USA: *John Wiley & Sons, Inc.*, 1994. 282. Print.
- ³¹ W.S. Harris. “Ion Flow Measurements And Plasma Current Analysis In The Irvine Field Reversed Configuration.” PhD Dissertation, University of California, Irvine, 2009
- ³² FFT help file. Retrieved April 17, 2010 from the World Wide Web: http://www.astro.umass.edu/~tangsk/documents/idl_html_help/F4.html
- ³³ WV_CWT help file. Retrieved April 17, 2010 from the World Wide Web: http://idlastro.gsfc.nasa.gov/idl_html_help/WV_CWT.html
- ³⁴ B. Ph. van Milligen, E. Sanchez, T. Estrada, C. Hidalgo, B. Branas, B. Carreras and L. Garcia. *Phys. Plasmas* **2** (1995) 3017
- ³⁵ C. Torrence, G. P. Compo. “A Practical Guide to Wavelet Analysis.” *Bull. Amer. Meteor. Soc.*, **79**, 61–78
- ³⁶ H. Y. Guo, A. L. Hoffman, K. E. Miller, and L. C. Steinhauer, *Phys. Rev. Lett.* **92** (2004) 245001
- ³⁷ Y. Ono, T. Matsuyama, K. Umeda, and E. Kawamori, *Nuclear Fusion* **43** (2003) 649
- ³⁸ R. D. Milroy, and J. U. Brackbill, *Phys. Fluids* **29** (1986) 1184
- ³⁹ Y. A. Omelchenko, M. J. Schaffer, and P. B. Parks, *Phys. Plasmas* **8** (2001) 4463
- ⁴⁰ J.D. Huba. *NRL Plasma Formulary*. Naval Research Laboratory, Washington, DC (2007)
- ⁴¹ F. Brandi, F. Giammanco. “Harmonic interferometry in the visible and UV, based on second- and third-harmonic generation of a 25 ps mode-locked Nd:YAG laser.” *Optics Letters*, **33**(18):2071, (2008)
- ⁴² R. Raman. “Physics Results from the initial operation of a Slow FRC Source.” PhD Dissertation, University of Washington, (1990)
- ⁴³ Ji, H., M. Yamada, S. Hsu, and R. Kulsrud, “Experimental test of the Sweet-Parker model of magnetic reconnection.” *Phys. Rev. Lett.*, **30** (1998) 3256
- ⁴⁴ R. Kulsrud, H. Ji, W. Fox and M. Yamada. *Phys. Plasmas* **12** (2005) 082301
- ⁴⁵ A. Qerushi. private communication. June 2, 2010
- ⁴⁶ E. Kawamori *et al.* *Nuclear Fusion* **47** (2007) 1232
- ⁴⁷ S. Ryzhkov. <http://fti.neep.wisc.edu/pdf/fdm1102.pdf> Retrieved May 16, 2010 from the World Wide Web.
- ⁴⁸ http://en.wikipedia.org/wiki/Stationary_process
- ⁴⁹ ZT431 PCI Digitizer / Digital Storage Oscilloscope (DSO). ZTEC Instruments. Retrieved May 11, 2010 from the World Wide Web: <http://www.ztecinstruments.com/zt431-pci/>.
- ⁵⁰ H. Ji, *et al.* *Phys. Rev. Letts.* **91** (2004), 115001
- ⁵¹ T. A. Carter, *et al.* “Measurement of Lower-Hybrid Drift Turbulence in a Reconnecting Current Sheet.” *Phys. Rev. Letts.* **88** (2002) 015001
- ⁵² R. L. Stenzel and J. M. Urrutia. “Electron magnetohydrodynamic turbulence in a high-beta plasma. I. Plasma parameters and instability conditions.” *Phys. Plasmas* **7** (2000) 4450
- ⁵³ “Correlation and dependence.” *Wikipedia* <http://en.wikipedia.org/wiki/Correlation> Retrieved May 17, 2010 from the World Wide Web
- ⁵⁴ R. Davidson, N. Gladd, C. Wu, and J. Huba, *Phys. Fluids* **20**, 301 (1977).
- ⁵⁵ R. Farengo, P. N. Guzdar, and Y. C. Lee, *Phys. Fluids B* **1**, 1654 (1989)
- ⁵⁶ R. Farengo, P. N. Guzdar, and Y. C. Lee, *Phys. Fluids* **31**, 3299 (1988)
- ⁵⁷ A. Y. Chirkov and V. I. Khvesyuk, *Phys. Plasmas* **17**, 012105 (2010)